Helsinki University of Technology. Laboratory of Aerodynamics.
Series A
Teknillinen korkeakoulu. Aerodynamiikan laboratorio.
Sarja A
Espoo 2004, FINLAND

NEW TWO-EQUATION TURBULENCE MODEL FOR AERODYNAMICS APPLICATIONS

Report A-21

Antti Hellsten

Dissertation for the degree of Doctor of Science in Technology to be presented with due permission of the Department of Mechanical Engineering, for public examination and debate in Auditorium K216 at Helsinki University of Technology (Espoo, Finland) on the 20th of February, 2004, at 12 noon.

Helsinki University of Technology
Department of Mechanical Engineering
Laboratory of Aerodynamics

Teknillinen korkeakoulu
Konetekniikan osasto
Aerodynamiikan laboratorio

Distribution:
Helsinki University of Technology
Laboratory of Aerodynamics
P.O.Box 4400
FIN-02015 HUT
Tel. +358-9-451 3421
Fax. +358-9-451 3418

ISBN 951-22-6933-3 (print), 951-22-6934-1 (pdf, available at http://lib.hut.fi/Diss/)
ISSN 1456–6982

Printed in Otamedia Oy
Espoo 2004, FINLAND
Typeset on 27th January 2004 using LaTeX

Abstract

Two-equation turbulence modelling for computational fluid dynamics and especially for analyses of high-lift aerodynamics applications is studied in depth in this thesis. Linear Boussinesq-type modelling is abandoned and a more sophisticated explicit algebraic Reynolds stress modelling (EARSM) approach is chosen as a constitutive relation between the turbulent stress tensor and the mean-velocity gradient and turbulent scales. The proposed techniques to extend the EARSM method for significantly curved flows are critically discussed and assessed.

The main focus of this study is on development of a new scale-determining two-equation model to be used with the EARSM as a constitutive model. This new $k - \omega$ model is especially designed for the requirements typical in high-lift aerodynamics. In the model development, attention is especially paid to the model sensitivity to pressure gradients, model behaviour at the turbulent/laminar edges, and to calibration of the model coefficients for appropriate flow phenomena. The model development is based on both theoretical studies and numerical experimenting. A systematic study is carried out to find the most suitable operational second scale-variable for this model. According to this study, ω itself was chosen. The developed model is finally assessed and validated for a set of realistic flow problems including high-lift aerofoil flows.

Keywords: Computational fluid dynamics, turbulence modelling, high-lift aerodynamics, k-omega model, explicit algebraic Reynolds stress model

Foreword

This study has been funded mostly by the Finnish Technology Agency (TEKES) within the TURBU-projects (1995–2000 and 2000–2003). Part of this work has been made within the HiAer Project (High Level Modeling of High Lift Aerodynamics). The HiAer project is a collaboration between DLR, ONERA, KTH, HUT, TUB, Alenia, EADS Airbus, QinetiQ and FOI. The project is managed by FOI and is partially funded by the European Union (Project Ref: G4RD-CT-2001-00448). The support from TEKES and EU for this work is gratefully acknowledged.

This work has been carried out in the Laboratory of Aerodynamics at Helsinki University of Technology. I want to warmly thank my former and current supervisors Professor (emeritus) Seppo Laine and Professor Jaakko Hoffren. Prof. Seppo Laine was the supervisor and instructor of this study until he retired in the end of November 2002. Prof. Jaakko Hoffren then became my supervisor, while Prof. Seppo Laine unselfishly continued as the instructor of my work. I am grateful to both my supervisors for their positive and encouraging attitude towards my work with turbulence modelling, a topic about which relatively little was known in the laboratory at the time I started this work. I want to thank also Prof. Timo Siikonen who not only taught me the fundaments of computational fluid dynamics, but he has also coordinated the national turbulence-modelling research projects under which most of this work has been conducted.

I take this opportunity to thank all my colleagues over the years. First, I want to thank my former colleagues Dr. Petri Kaurinkoski, Dr. Patrik Rautaheimo and Mr. Esa Salminen. I enjoyed a lot of the time we worked together. Moreover, this work would not have been possible without their kind and patient support with the computers, software, and numerous other items. Besides this, Patrik taught me a lot about turbulence modelling in the beginning of my studies. I want to thank my colleagues Mrs. Tellervo Brandt, Mrs. Katariina Salo, and Mr. Kyösti Kaarlonen without forgetting Lic. Tech. Petri Majander and Dr. Mizanur Rahman for their help in countless number of issues and for fruitful discussions. Mr. Mikko Korhonen and Dr. Reijo Lehtimäki deserve special thanks. Mikko's support has been vitally important as he has devoted a lot of his time to the laboratory's computer systems and kept the computers running. Reijo has helped me a lot by creating many of the high-quality computational grids needed in this study.

I also want to acknowledge Mr. Bo Fagerström for taking care of the financial duties of my research projects, and Ms. Mervi Ritvala, Ms. Tytti Nyman, Mr. Martti Alatalo, and Mrs. Tarja Matsuoi for providing me their help in numerous practical matters.

Last but not least, I am deeply grateful to my dear wife Satu, who has been patient enough to support me during all the years this work has taken, and to our lovely children Jaakko and Kaisla. I dedicate this thesis to you with love.

Espoo, September 1, 2003

Antti Hellsten

Contents

Nomenclature

A	constant in the decay law of grid-generated turbulence
$A_0, \ldots, A_4$, A_3'	model coefficients in Reynolds stress modelling
$A_{\mathcal{X}_i}$, $A_{\mathcal{U}}$, $A_{\mathcal{K}}$, A_{Φ}	convection-related coefficients in self-similar equations
B	constant in the logarithmic velocity law
C	various model coefficients (specified by subscripts)
C_p	pressure coefficient $(p - p_\infty)/(\frac{1}{2}\rho_\infty U_\infty^2)$
D	cylinder diameter
$\frac{\mathrm{D}}{\mathrm{D}t}$	material derivative $\frac{\partial}{\partial t} + u_k \frac{\partial}{\partial x_k}$
$\mathcal{D}_{ij}$, $\mathcal{D}_{ij}^{(a)}$	turbulent plus molecular transport (diffusion) of the Reynolds stress component $\overline{u_i'u_j'}$ and of a_{ij}, respectively
$\mathfrak{D}$	a formal total transport operator
F_1	mixing function in Menter's $k - \omega$ models
$\mathcal{F}_{ij}$	nondimensional Reynolds stress redistribution tensor, $\mathcal{F}_{ij} = \Phi_{ij}/\varepsilon$
G	filter function
H	channel height
H_{12}	shape parameter, $H_{12} = \delta_1/\delta_2$
I_t	first invariant of tensor t_{ij}
II_t, II_a, II_S, II_Ω	second invariants of tensors t_{ij}, a_{ij}, S_{ij}, and Ω_{ij} (or Ω_{ij}^*), respectively
III_t, III_a, III_S	third invariants of tensors t_{ij}, a_{ij}, and S_{ij}, respectively
IV	tensor invariant defined as $S_{kl}\Omega_{lm}\Omega_{mk}$ (or $S_{kl}\Omega_{lm}^*\Omega_{mk}^*$)
L	generally a length-scale; also plate length
M_{ijkl}	fourth-rank tensor defining $\Phi_{ij}^{(r)}$ as $\Phi_{ij}^{(r)} = M_{ijkl}\partial U_k/\partial x_l$
$\mathcal{M}_{ijkl}$	nondimensional M_{ijkl}, $\mathcal{M}_{ijkl} = M_{ijkl}/k$
N	number of individual samples in an ensemble; also a shorthand notation in the EARSM expression, $N = A_3 + A_4 P/\varepsilon$
$\mathcal{N}_T$	nondimensional eddy viscosity in self-similar equations
P	production of k; also mean pressure
P_{ij}	production of the Reynolds stress component $\overline{u_i'u_j'}$
P_1, P_2	shorthand notation in the EARSM expression
Q	source term; also shorthand notation in the EARSM expression
$\mathcal{Q}$	source term of self-similar equations

R	second scale variable in $k-R$ models, $R \sim k^2/\varepsilon$; also radius
Re	Reynolds number
S	scalar measure of mean strain rate $S=\sqrt{2S_{ij}S_{ji}}$
$\vec{\mathcal{S}}$, $\mathcal{S}_k$	surface-area vector of a computational control volume (cell)
S_{ij}	mean strain-rate tensor nondimensioanlized by the turbulent time scale
S_R	auxiliary function in the rough-wall expression for ω_w
T	averaging time
$T_j^{(k)}$	turbulent transport of k
T_{ijk}	turbulent transport of the Reynolds stress component $\overline{u_i'u_j'}$
$T_{ip'}$, $T_{q'j}$	transformation matrices between coordinate systems
T_l	inner product of gradients of the turbulent scale variables
U	one of the Cartesian mean-velocity components U_i, $U=U_1$
$\mathbf{U}$	mean velocity vector
U_b	bulk velocity
$\mathcal{U}$	nondimensional velocity variable in self-similar equations
V	general velocity-scale; also a tensor invariant defined as $S_{kl}S_{lm}\Omega_{mn}\Omega_{nk}$ (or $S_{kl}S_{lm}\Omega^*_{mn}\Omega^*_{nk}$); and also volume of a computational cell
$\mathcal{V}$	transverse convective velocity in self-similar equations in general and also in the idealized edge problem in particular
W	azimuthal velocity component in the combustor flow
$\mathcal{X}_i$	vector of unknown variables in self-similar problems
a_1	Bradshaw's structural parameter, $a_1=-a_{12}$
a_{ij}	Reynolds stress anisotropy tensor $a_{ij}=\overline{u_i'u_j'}/k-(2/3)\delta_{ij}$
b	half width of a wake
c	chord length of an aerofoil
c_f	skin-friction coefficient $\tau_w/(\frac{1}{2}\rho_\infty U_\infty^2)$
c_d	drag coefficient
c_l	lift coefficient
d	distance to the nearest wall point
f	a ramp-function $f=\max\left[(\delta_0-y)/\delta_0;0\right]$ in power solutions of the idealized edge problem
f_{β^*}	an auxiliary function in Wilcox's $k-\omega$ model
f_{mix}	mixing function for the model coefficients
g	second scale variable in $k-g$ models, $g \sim \sqrt{k/\varepsilon}$
h	wire spacing of turbulence-generating grid
k	kinetic energy of turbulent motion per unit mass
k_s^+	sand-roughness height k_s scaled by the viscous length-scale, $k_s^+=k_s u_\tau/\nu$
$\mathcal{K}$	nondimensional turbulent energy in self-similar equations
kl	second scale variable in $k-kl$ models, $kl \sim k^{5/2}/\varepsilon$
l	second scale variable in $k-l$ models, $l \sim k^{3/2}/\varepsilon$

l_T	turbulent length-scale, $l_T \sim l$
l_{mix}	turbulent mixing length
m, $\tilde{m}$	exponents of k in the generalized second-scale formulation
m'	shorthand notation in the generalized second-scale formulation
n, $\tilde{n}$	exponents of ε in the generalized second-scale formulation
n'	shorthand notation in the generalized second-scale formulation
n_u, n_k, n_ω	exponents of the power solutions to the idealized edge problem
p	pressure
q	exponent in the decay law of grid-generated turbulence
r	radial coordinate
s	curvilinear wall-following coordinate
s'_{ij}	fluctuating part of the strain-rate tensor
t	time
$\overline{u'_iu'_j}$	Reynolds stress tensor
$\overline{u'u'}$, $\overline{u'v'}$, $\overline{v'v'}$	$= \overline{u'_1u'_1}$, $\overline{u'_1u'_2}$, $\overline{u'_2u'_2}$, respectively
$\overline{u'_iu'_ju'_k}$	turbulent transport of the Reynolds stress component $\overline{u'_iu'_j}$ by fluctuating velocity field, *i.e.* T_{ijk} minus pressure diffusion
u_τ	friction velocity, $u_\tau = \sqrt{\tau_w/\rho}$
v_T	turbulent velocity-scale
x	one of the Cartesian coordinates x_i, $x = x_1$
$\mathbf{x}$	Cartesian coordinates x_i
$\mathbf{x}'$	displaced location vector in two-point correlations
y	one of the Cartesian coordinates x_i, $y = x_2$; also wall-normal coordinate
y^+	wall-normal coordinate scaled by the viscous length-scale, $y^+ = yu_\tau/\nu$

Greek Symbols

Γ	circulation; also argument of f_{mix}
Γ_1, Γ_2, Γ_3	arguments of f_{mix}
Δ	Clauser's delta, $\Delta = U_e\delta_1/u_\tau$; also increment of a variable
Π	Coles' wake-strength parameter
Π_{ij}	Reynolds stress redistribution tensor
Φ_{ij}, $\Phi^{(s)}_{ij}$, $\Phi^{(r)}_{ij}$, $\Phi^{(w)}_{ij}$	pressure-strain correlation, its slow, rapid, and wall parts
Ω_{ij}	mean vorticity tensor
$\Omega^{(r)}_{ij}$	vorticity modification by curvature, $\Omega^{(r)}_{ij} = -\epsilon_{ijk}\omega^{(r)}_k$
Ω^*_{ij}	apparent net vorticity tensor, $\Omega^*_{ij} = \Omega_{ij} - \tau\Omega^{(r)}_{ij}/A_0$
α	angle of attack; also second scale variable, $\alpha \sim k\varepsilon$
$\beta_1, \ldots, \beta_{10}$	coefficients in the explicit tensor expression for the Reynolds stress anisotropy

β_T	nondimensional pressure-gradient in boundary layers, $\beta_T = (\delta_1/\tau_w)\mathrm{d}p/\mathrm{d}x$
β^*	model coefficient, $\beta^* = a_1^2 \approx 0.09$
γ	model coefficient in $k-\omega$ models
δ	thickness of a turbulent shear layer
δ_0	length-scale of the idealized edge problem
δ_1	displacement thickness of a turbulent shear layer
δ_2	momentum thickness of a turbulent shear layer
δ_{ij}	Kronecker's delta
ε	dissipation rate of turbulent kinetic energy k
ε_{ij}	dissipation rate of $\overline{u_i'u_j'}$
ϵ_{ijk}	permutation tensor
ζ	second scale variable in $k-\zeta$ models, $\zeta \sim \varepsilon^2/k^2$
η	transverse similarity coordinate
θ	angular coordinate of the U-bend geometry
κ	von Kármán constant of the logarithmic velocity law
κ_l	slope of the mixing-length distribution in the logarithmic layer
λ	growth exponent of the homogeneous shear flow
μ	dynamic viscosity
μ_T	dynamic eddy viscosity
ν	kinematic viscosity, μ/ρ
ν_T	kinematic eddy viscosity, μ_T/ρ
ν_k, $\nu_{\tilde{\omega}}$, $\nu_{\phi\phi}$, $\nu_{\phi k}$	shorthand notation for various diffusivities
$\boldsymbol{\xi}$	spatial separation vector in two-point correlations
ξ	streamwise similarity coordinate
ρ	fluid density
σ	model coefficients of diffusive terms (specified by subscripts)
τ	turbulent time-scale, $\tau = k/\varepsilon$; also shear stress; and also second scale variable in $k-\tau$ models, $\tau \sim k/\varepsilon$
ϕ	general second scale variable, $\phi \sim k^m\varepsilon^n$
φ	second scale variable in $k-\varphi$ models, $\varphi \sim \varepsilon/k^{1/2}$
χ	argument of f_{β^*} in Wilcox's $k-\omega$ model
ω	second scale variable in $k-\omega$ models, $\omega \sim \varepsilon/k$
$\tilde{\omega}$	perturbed definition for ω, $\tilde{\omega} \sim \varepsilon^{1\pm\delta_\varepsilon}/k^{1\pm\delta_k}$ with δ_ε and δ_k being small perturbations of the order of 0.1
$\omega_k^{(r)}$	rotation rate vector of the local basis of a curvilinear streamline-coordinate system

Subscripts

e	value just outside the edge of a turbulent flow
f	free-stream value
pw	fictive potential-flow value on the wall
w	wall value

∞	farfield value
1,2	references to model coefficient sets 1 and 2, *i.e.* inner and outer model coefficients

Superscripts

$+$	variable scaled by viscous length and velocity scales, ν/u_τ and u_τ, respectively
$'$	fluctuating quantity
(eq)	equilibrium value
(ex)	higher-order residual of a polynomial truncated to first order
(T)	turbulent
(V)	viscous

Abbreviations and Acronyms

APG	adverse pressure gradient
ARSM	algebraic Reynolds stress model
BSL	Menter's baseline $k-\omega$ model
CC	curvature correction/corrected
CC-WJ	curvature corrected Wallin-Johansson EARSM based on ARSM derived in a suitable streamline coordinate system
CFD	computational fluid dynamics
DES	detached-eddy simulation
DNS	direct numerical simulation
EARSM	explicit algebraic Reynolds stress model
EVM	eddy-viscosity model
GLM	general linear model for the Reynolds stress redistribution tensor
GQLM	general quasi-linear model (an extension of GLM)
iWJ	Wallin-Johansson EARSM based on ARSM derived in the inertial coordinate system (standard WJ-EARSM)
MUSCL	monotonic upwind schemes for conservation laws
LES	large-eddy simulation
LRR	Launder-Reece-Rodi RSM
LRR-IP	a simplified "isotropization of production" version of the LRR
RANS	Reynolds-averaged Navier Stokes (equations)
RSM	differential Reynolds stress model
SST	Menter's shear-stress transport model
SSG	Speziale-Sarkar-Gatski RSM
TNT	Kok's $k-\omega$ model for turbulent/non-turbulent interfaces
WJ	Wallin-Johansson EARSM
ZPG	zero pressure gradient

1 Introduction

Experimental testing and research using wind tunnels have been very important tools in aircraft design throughout the history of aviation. Actually, one could claim that the success of the Wright brothers' 1903 Flyer and their later developments was at least partially owing to the elaborate surveys they carried out using their small wind tunnel. The experimental wind-tunnel work has, indeed, been an unavoidable part of aircraft design and aeronautical research work since those historic times, the centenary which we are now celebrating. While being much more viable than direct flight testing, experimental wind-tunnel work is, however, very expensive and time consuming. Thus, some kind of more cost-effective alternative techniques replacing the wind-tunnel experiments would be a great advantage for the aeronautical industry.

Great expectations have been set on the computational fluid dynamics (CFD) methods during the computer era of the past few decades. Computational methods have, indeed, rendered some of the wind-tunnel testing unnecessary, but only a part of it. The computational methods that have been utilized in the aircraft industry during the last few decades have mostly been crude approximative methods with severe limitations in terms of modelling the physics of real fluid flow. Potential-flow solvers coupled with boundary-layer methods can be mentioned as representative examples of such methods. The physically correct and general mathematical model for fluid flow at Reynolds numbers relevant to aeronautics, and almost all engineering, is a highly nonlinear system of partial differential equations known as the Navier-Stokes equations. The mathematical nonlinearity of these equations has its roots in the physics of fluid flow. Fluid flow, except at extremely low Reynolds numbers, is a nonlinear dynamical system, which in certain circumstances shows chaotic-like behaviour. All this nonlinear physics is inherently described by the Navier-Stokes equations. It is quite clear that no analytical solutions can be found for such a complex system for any practical problems. Moreover, the numerical solution of such a system is not straightforward. The influence of the physical as well as mathematical nonlinearity is most often seen in the fact that almost all flows of engineering interest are at least partially turbulent, *i.e.* unsteady, three-dimensional, randomly fluctuating, and highly vortical down to very small scales in space and time. The appearance of shock waves in supersonic flows is another salient footprint of the nonlinearity. Shock waves can be satisfactorily handled with the present numerical methods, but turbulence must be filtered away by means of so-called Reynolds averaging in almost all engineering flow problems due to the enormous computational work the direct solution of turbulent motion would require. The equations and the numerical solution algorithms do not prevent the direct numerical simulation of turbulent flows (DNS) from being performed in principle. DNS is, indeed, nowadays used for low Reynolds number flows in simple geometries for scientific rather than engineering purposes. In principle, only the huge computer capacity requirement prevents its use for engineering problems. The solution of Reynolds averaged Navier-Stokes (RANS) equations is the best available option for most aerodynamical problems these days and in the near future.

The RANS approach is physically much more realistic than the potential-flow methods and other highly simplified models of fluid flow. On the other hand, it is a much more elaborate and time-consuming approach, and therefore it has only recently started to drift into the designers' toolboxes. It may be mentioned as an example that the high-lift devices and configurations of the most recent major all-new civil-transport aircraft, Airbus A-380, are designed, at least partially, using the RANS-CFD methods, except in the preliminary design phase [1]. About ten years ago, when the aerodynamic design of Boeing 777 aircraft was carried out, no RANS methods at all were utilized in its high-lift design [2]. Of course, the RANS methods are also used in longer-term high-lift aerodynamics-related research work, where the time-scales are much larger than in the design work.

Although being superior over the simpler methods in terms of physical realism, the RANS methods, however, involve one major weakness — the effects of the turbulent motion on the mean flow are unknown and must be modelled. The influence of turbulence is seen as a new term in the equations. This term is the divergence of a second-order correlation tensor of the fluctuating parts of each velocity component. This correlation tensor is known as the Reynolds stress tensor, and it is the object that needs to be modelled. The accuracy and reliability of turbulence modelling is one of the major limiting factors, among the large computing times, of efficient exploitation of the RANS-based CFD methods in high-lift aerodynamics problems in the aircraft design work. While computer performance seems to continue to rapidly increase, the accuracy and reliability of turbulence modelling has to be improved to really meet the designers' needs and thus to strengthen the value of the RANS methods as design tools. This is the goal of this study.

The turbulence modelling presently employed in aerodynamics is usually based on two-equation models employing a linear relationship between the Reynolds stress and the mean strain-rate tensors. This relationship is known as the generalized Boussinesq model. This may be a too restricting assumption in complex problems typical in high-lift aerodynamics, because a multitude of different flow phenomena may be present in a single problem. Therefore, turbulence modelling with a wider range of applicability than the Boussinesq models must be sought. Differential Reynolds stress modelling (RSM), in which a modelled transport equation is solved for each stress component, is in principle a more general class of models with a wider range of applicability. RSMs are, however, considered a too complex approach for the industrial high-lift aerodynamic design work. On the other hand, the two-equation models can be extended for a wider range of applicability by developing more advanced nonlinear relations between the stress tensor and the mean-velocity gradient and the turbulent scales. These relations are generally called constitutive models. The two-equation turbulence models can be thought to consist of two more or less separate parts: the scale determining model, which provides scalar information about the turbulence, and the constitutive model, which determines the Reynolds stress tensor. Explicit algebraic Reynolds stress models (EARSM) are an interesting and promising subset of nonlinear constitutive models. In this approach, part of the higher-order description of physical processes on the RSM-level is transferred onto the two-equation modelling level. The EARSM approach is considered to be a suitable type of constitutive modelling for the present purposes.

Most of the existing two-equation scale-determining models are designed in conjunction with the linear constitutive modelling. This fact may compromise the performance of the model when combined with an EARSM or another nonlinear constitutive model. The aim of this study is to develop a new two-equation scale-determining model to be used purely with an EARSM as the constitutive model. The model is designed to be utilized mainly for aerodynamic problems, especially for high-lift aerodynamics. This does not mean that the model is unsuitable for all other flow problems, but the focus will be kept in flow phenomena that have an important role in typical high-lift aerodynamics problems. The goal is that the model becomes mature enough to be taken into practical use within a very short time frame. Therefore, too complex or revolutionary modelling techniques should be avoided. The approach is to first select a suitable starting-point scale-determining model, and then to completely recalibrate it for the present purposes in conjunction with the selected EARSM constitutive model. Further development of the EARSM is also explored in this study.

A general overview of turbulent flows, on the concept of RANS and turbulence modelling is first given in Chapter 2. The most important flow phenomena in a typical high-lift aerodynamics problem are reviewed in Chapter 3. Also, the requirements and challenges that these flow situations pose for turbulence modelling, and the capabilities of different existing models to cope with these flows is discussed. The starting-point model is selected from the grounds of this review. It turned out that a $k-\omega$-type model of the form developed by Menter [3] seems to be the most promising starting point. Also, the elementary flow cases used in the development, calibration, and validation is chosen in accordance with the review in Chapter 3. Chapter 4 includes a description of the numerical solution methods used in the various computations made in this study. The novel contributions and developments of this study are reported in Chapters 5 and 6. Chapter 5 first describes the selected baseline constitutive model, *i.e.* the EARSM developed by Wallin and Johansson [4]. After this, the proposed techniques to extend the algebraic stress modelling approach for curved flows, including the recently proposed strain-rate based technique by Wallin and Johansson [5], are discussed in depth. This method is also validated for some two- and three-dimensional flows where the curvature effects on turbulence are important. Theoretical analysis concerning the $k-\omega$ model is conducted in Chapter 6 in order to get a better understanding on how the model coefficients influence the model behaviour. The theoretical work also provides explicit constraints which are extremely useful in the calibration process. Most of the existing $k - \omega$ models are reviewed in the light of the theoretical analysis, and most of them are shown to be unsuitable to be combined with any nonlinear constitutive model. The actual recalibration is carried out after the theoretical part using the selected elementary flows and the derived constraints. A separate study about a possible alternative operational scale variable in the form $\phi = k^m \varepsilon^n$ is conducted in Chapter 6. This involves formulation of a set of criteria for such an alternative variable and theoretical derivation of constraints for the parameters m and n to satisfy the posed criteria. It is, however, concluded that the original $k - \omega$ formulation ($m = -1$ and $n = 1$) is optimal for the $k - \omega$ models, because it leads to the simplest and numerically least troublesome form of the equations. Finally, in Chapter 7, the model is preliminarily assessed for a few practical two-dimensional flow cases including high-lift aerofoil flows.

2 On Turbulent Flows and Turbulence Modelling

2.1 What Is Turbulence?

Anyone who has ever stopped for a moment to watch, say, smoke rising from a chimney, or any other large-scale flow occurring in every-day life, knows that such flows do not follow any smooth deterministic patterns. Instead, such flows in most situations have a very complex irregular behaviour — these are called turbulent flows. Flows with shear strain or thermal buoyancy are likely to be turbulent always when inertial effects in the flow are large enough in comparison to viscous damping. This is the case in the majority of flows of practical interest. Only slow small-scale flows, such as a candle flame, do not share this behaviour, and they are known as laminar flows. But, as pointed out by Tennekes and Lumley [6]: *“in fluid dynamics laminar flow is the exception, not the rule.”*

The inertial forces increase with increasing fluid density ρ, and with square of the velocity scale V of the flow. The magnitude of the viscous effects increase with the dynamic viscosity of the fluid μ, but depends only linearly on V. The inertial forces are proportional to the inverse of the length-scale L while the viscous forces depend on $1/L^2$. A nondimensional measure of the ratio of the inertial and viscous forces can be formulated using these four variables. This parameter is known as the Reynolds number named after Osborne Reynolds, a great scientist of the 19th century. The Reynolds number Re is defined as

$$Re \equiv \frac{\rho V^2/L}{\mu V/L^2} = \frac{\rho V L}{\mu} = \frac{VL}{\nu} \tag{2.1}$$

where $\nu = \mu/\rho$ is the kinematic viscosity. The Reynolds number takes usually quite large values in flows of engineering or other practical interest. For instance, Re may get a value of tens of millions in the flow past a wing of a typical transport aircraft.

Turbulent flows are always time-dependent and three-dimensional, and the flow variables such as the velocity vector or pressure fluctuate randomly. For instance, Bradshaw [7] describes turbulence as:

> *“Turbulence is a three-dimensional time-dependent motion in which vortex stretching causes velocity fluctuations to spread to all wave lengths between a minimum determined by viscous forces and a maximum determined by the*

boundary conditions of the flow. It is the usual state of fluid motion except at low Reynolds numbers.”

Turbulence is an efficient mixing agent. For instance, it mixes different gases in combustion processes so that combustion becomes much more efficient. Turbulent flows are also diffusive and dissipative. The former means that turbulence spatially spreads everything the flow contains including turbulence itself. The latter means that turbulence increases losses of mechanical energy. Hence, turbulence may have either positive and negative consequences from the engineer’s point of view.

From the mathematical point of view, the nonlinear convective terms in the Navier-Stokes equations, *i.e.* momentum transport equations, are related to the nonlinear dynamics of fluid flow. The nonlinear dynamics features all the instability phenomena and turbulence that characterize fluid flow. Owing to this nonlinearity, no general analytical solutions to Navier-Stokes equations are known.

The wide spectrum of scales in both time and space is a characteristic feature of turbulent motion. The individual structures of turbulent flow are called eddies. The concept of eddy is somewhat loosely defined. It could be associated with a vortex, but usually the word “eddy” is used for any identifiable disturbance with some length-scale estimate roughly charaterizing its spatial extent. Thus, rather than being a single vortex line, an eddy can be kept as a vortical disturbance. See Tennekes and Lumley [6] for a more detailed discussion. The spectrum width of turbulent motion depends on the Reynolds number as may be understood from the above citation. The largest eddies are of the size of the flow, for instance the width of a shear layer. The largest eddies are not affected by viscosity if the Reynolds number is sufficiently large. Large eddies interact with the mean flow and with the other eddies of comparable length scales. The mean-flow strain-rate is the agent of the energy supply for turbulent motion by means of stretching the largest turbulent eddies when the vorticity associated with such an eddy happens to be suitably oriented relative to the mean-flow strain-rate. Large eddies are usually highly anisotropic, because the mean strain-rate prefers certain directions. Straining intensifies the vorticity of the strained eddies because the angular momentum must be conserved. This way, the turbulent eddies continuously obtain energy from the sheared mean flow. Similarly, the eddies stretch each other, because different eddies contain vorticity and strain rate in varying directions. As the eddies stretch each other, smaller eddies are produced and fed with energy. This cascade process goes on towards smaller and smaller length scales until the Reynolds number associated with the eddies becomes so small that friction damps out the motion and dissipates the energy into heat. The length, velocity, and time scales related to the dissipative motion are known as Kolmogorov scales. The dissipative small-scale eddies do not much depend on the mean-flow strain-rate. Significant interaction takes place only between eddies of comparable length scales. Therefore, small eddies are much more isotropic than large ones. Thus, there are at least two different kinds of eddies in turbulent flows with a moderate or high Reynolds number: the large eddies that interact with the mean flow but do not show any significant viscous dissipation, and the small eddies that do not have direct interaction with the mean flow and are responsible for the viscous dissipation. If the Reynolds number is high enough, there will also be an intermediate range of eddies that depend neither on mean flow nor on viscosity. This part of the turbulent energy-spectrum is known as the inertial subrange.

The wide spectrum of scales renders direct numerical simulation (DNS) of turbulent motion impractical for almost all engineering purposes. Today, DNS is applied to low Reynolds-number flows in simple geometries. DNS is useful for turbulence research, and it also provides reference data for turbulence modellers. In DNS, all the details down to the dissipative motion must be resolved with sufficient accuracy. The amount of required computational work and storage space increases rapidly with the Reynolds number. Hence there is no reason to believe that DNS will become a practical flow-simulation tool for aeronautical engineering within any reasonable time frame.

The nature of the large eddies or structures depends on the mean flow details. There seems to be identifiable types of large structures characteristic for certain mean flows. For instance, planar mixing-layers are dominated by nearly two-dimensional Brown-Roshko rollers and braid regions between the rollers [8]. As another example, the streamwise vortices and the low-speed streaks between them in flows near solid walls are worth mentioning. Such eddies are called coherent structures. The appearance and the properties of the coherent structures usually strongly vary from one mean flow to another. This is one of the reasons why it is extremely difficult to construct a general turbulence model that would work properly for a wide range of different flows. This difficulty, related with the coherent structures, gives motivation to try simulating only the large-scale motion using some kind of model for the effects of the small-scale motion that has first been filtered away from the transport equations. This concept is known as the large eddy simulation (LES). It has shown encouraging potential for certain kinds of flows. However, LES is still restricted to relatively low Reynolds numbers, and it has not yet reached a sufficiently mature level for routine engineering use. In most of the aeronautical engineering problems, LES is still very far from becoming a practical tool.

2.2 Reynolds-Averaged Navier-Stokes Equations

In turbulent flows, the flow variables can be decomposed into the mean and fluctuating parts. This is known as the Reynolds decomposition. For instance, in the cases of stationary mean flow, the velocity field can be expressed as

$$u_i(x_i,t) = U_i(x_i) + u_i'(x_i,t) \tag{2.2}$$

where u_i is the instantaneous velocity component, u_i' is the fluctuating part, and U is the mean velocity which can be defined, *e.g.* as a long-time average

$$\overline{u_i}(x_i) = U_i(x_i) = \lim_{T\to\infty} \frac{1}{T} \int_t^{t+T} u_i(x_i,t)\mathrm{d}t \tag{2.3}$$

The long-time Reynolds average given by (2.3) is not sensible in flows with some kind of nonturbulent unsteadiness, such as transient or periodic behaviour. In such situations, a more general decomposition and averaging approach is needed. The ensemble average is defined as

$$\overline{u_i}(x_i,t) = U_i(x_i,t) = \lim_{N\to\infty}\frac{1}{N}\sum_{1}^{N} u_i(x_i,t) \tag{2.4}$$

Now, the mean field is defined as an average of a large number of realizations of the flow in question, and thus the mean field may be a function of time. Phase averaging is a special case of the ensemble average valid for strictly periodic flows. In this case, each cycle can be taken as an individual realization. The conventional time averaging, the ensemble averaging, and the phase-averaging approaches lead to the same system of Reynolds-averaged equations for incompressible flows.

For compressible flows, the density weighted Favre averaging

$$\widetilde{u}_i = \frac{\overline{\rho u_i}}{\overline{\rho}} \tag{2.5}$$

is a more useful concept than the traditional Reynolds averaging. In this study, the equations are written using the traditional Reynolds-averaging concept instead of the Favre averaging, although the mean-flow solution method used in Chapters 5 and 7 is suitable for compressible flows. The interest here is mainly in only slightly compressible flows, and thus it is thought to be justified to ignore the compressibility in turbulence modelling. In general, however, Favre's density weighting can be applied to each of the averaging concepts to extend the averaging for compressible flows. Thus, the same RANS-equations are valid for compressible flows with forced unsteadiness as well as for stationary compressible flows.

Substituting the decomposition (2.2) for velocity and pressure into the transport equation for momentum

$$\frac{\partial u_i}{\partial t} + u_k\frac{\partial u_i}{\partial x_k} = -\frac{1}{\rho}\frac{\partial p}{\partial x_i} + \frac{\partial}{\partial x_k}\left(\nu\frac{\partial u_i}{\partial x_k}\right) \tag{2.6}$$

yields

$$\begin{aligned}\frac{\partial}{\partial t}(U_i+u_i') + (U_k+u_k')\frac{\partial}{\partial x_k}(U_i+u_i') &= -\frac{1}{\rho}\frac{\partial}{\partial x_i}(P+p') \\ &+ \frac{\partial}{\partial x_k}\left(\nu\frac{\partial}{\partial x_k}(U_i+u_i')\right)\end{aligned} \tag{2.7}$$

Averaging this and taking into account that $\overline{u'} = 0$ and $\overline{U} = U$, the Reynolds-averaged momentum equation

$$\frac{\partial U_i}{\partial t} + U_k\frac{\partial U_i}{\partial x_k} = -\frac{1}{\rho}\frac{\partial P}{\partial x_i} + \frac{\partial}{\partial x_k}\left(\nu\frac{\partial U_i}{\partial x_k}\right) - \frac{\partial}{\partial x_k}(\overline{u_i'u_k'}) \tag{2.8}$$

is arrived at. The last term is new compared with (2.6) and it arises from averaging the nonlinear convection term of the fluctuating velocity. It is divergence of a correlation tensor known as the Reynolds stress tensor. If the energy equation is needed, as is the case in compressible flows and in incompressible flows with variable temperature, then also correlations between the fluctuating velocity and temperature will arise in the energy equation. The same happens with all necessary transport equations for any scalar fields of interest. These terms are generally known as scalar fluxes and their modelling is beyond the scope of this work.

2.3 Equation for the Reynolds Stress Tensor

The exact transport equation for the Reynolds stress tensor is derived from the transport equation for the fluctuating velocity component u_i' obtained by subtracting (2.8) from (2.7). This equation is multiplied by another fluctuating velocity component u_j' and averaged. The same equation written for u_j' is then multiplied by u_i', averaged and the resulting equations are added together. As a result of this, a transport equation system for $\overline{u_i'u_j'}$ is obtained

$$\begin{aligned}\frac{\mathrm{D}\overline{u_i'u_j'}}{\mathrm{D}t} = & \underbrace{-\overline{u_j'u_k'}\frac{\partial U_i}{\partial x_k} - \overline{u_i'u_k'}\frac{\partial U_j}{\partial x_k}}_{=P_{ij}} - \underbrace{2\nu\overline{\frac{\partial u_i'}{\partial x_k}\frac{\partial u_j'}{\partial x_k}}}_{=\varepsilon_{ij}} + \underbrace{\frac{1}{\rho}\overline{p'\left(\frac{\partial u_i'}{\partial x_j}+\frac{\partial u_j'}{\partial x_i}\right)}}_{=\Phi_{ij}} \\ & + \underbrace{\frac{\partial}{\partial x_k}\left(-\overline{u_i'u_j'u_k'} - \frac{1}{\rho}\left(\delta_{ik}\overline{p'u_j'} + \delta_{jk}\overline{p'u_i'}\right) + \nu\frac{\partial\overline{u_i'u_j'}}{\partial x_k}\right)}_{=\mathcal{D}_{ij}}\end{aligned} \tag{2.9}$$

or its shorthand notation

$$\frac{\mathrm{D}\overline{u_i'u_j'}}{\mathrm{D}t} = P_{ij} - \varepsilon_{ij} + \Phi_{ij} + \mathcal{D}_{ij} \tag{2.10}$$

The term designated as production, P_{ij}, is the rate at which energy is fed from the mean flow to each stress component. The vortex stretching mechanism discussed in Section 2.1 is responsible for this process. The production term can be computed directly from the stress and the mean-flow strain-rate components and thus needs no modelling.

The second term ε_{ij} is a viscous dissipative term. It is, however, not exactly consistent with the definition of the viscous dissipation of turbulent energy

$$k \equiv \frac{1}{2}\overline{u_k'u_k'} \tag{2.11}$$

According to *e.g* Ref. [6], the exact dissipation rate of k is defined as

$$\varepsilon \equiv \frac{1}{2}\nu\overline{\left(\frac{\partial u_k'}{\partial x_l} + \frac{\partial u_l'}{\partial x_k}\right)\left(\frac{\partial u_l'}{\partial x_k} + \frac{\partial u_k'}{\partial x_l}\right)} = 2\nu\overline{s_{kl}'s_{lk}'} \tag{2.12}$$

The dissipation rate ε is the rate at which the kinetic energy of turbulence (k) is dissipated into heat by viscosity. On the other hand,

$$\frac{1}{2}\varepsilon_{kk} = \nu\overline{\frac{\partial u_l'}{\partial x_k}\frac{\partial u_l'}{\partial x_k}} \neq \varepsilon \tag{2.13}$$

The trace of ε_{ij} divided by two is exactly equivalent with (2.12) only in case of homogeneous turbulence. In the context of RANS modelling, however, ε_{ij} is usually said to be the dissipative term. Similarly, half of its trace is assumed to be equal to ε, the viscous dissipation of k. The term ε_{ij} is actually a leftover of the total viscous term when part of that term is identified as the viscous gradient-diffusion, which is discussed below. In reality, the diffusive term takes a more complex form that cannot be evaluated explicitly. As the gradient-diffusion term is neat and can be computed explicitly without any modelling, it is attractive to keep the diffusive term in the simple gradient form, and to absorb the remaining part into the dissipative term. For more details of the viscous term, see *e.g.* Ref. [9]. In practice, the difference between the true dissipation ε and $\varepsilon_{kk}/2$ is believed to be negligible even in strongly inhomogeneous turbulence. Dissipation cannot be computed from available variables, hence it must be modelled.

Φ_{ij} can be called the redistribution term, because its trace is zero and thus it neither produces nor destroys mechanical energy. It merely redistributes the energy between the stress components. It is also commonly known as the pressure-strain term, because it is a correlation between fluctuating pressure and strain rate. In addition to the dissipation, the redistribution term needs to be modelled with care.

The remaining term $\mathcal{D}_{ij}$ has a form of divergence of a sum of three fluxes: the transport by velocity fluctuations, *i.e.* the triple velocity correlation $\overline{u'_i u'_j u'_k}$, the pressure transport flux, and the viscous flux of each stress component. The pressure diffusion originates from splitting the actual correlation between the fluctuating velocity and pressure into the above mentioned traceless pressure-strain correlation Φ_{ij} and the pressure diffusion as

$$-\left(\overline{u'_i \frac{\partial p'}{\partial x_j}} + \overline{u'_j \frac{\partial p'}{\partial x_i}}\right) = \underbrace{\overline{p' \left(\frac{\partial u'_i}{\partial x_j} + \frac{\partial u'_j}{\partial x_i}\right)}}_{\text{pressure-strain correlation}} - \underbrace{\left(\frac{\partial \overline{u'_i p'}}{\partial x_j} + \frac{\partial \overline{u'_j p'}}{\partial x_i}\right)}_{\text{pressure diffusion}} \tag{2.14}$$

The rationale behind this form is to isolate the traceless redistribution term. The pressure diffusion is usually believed to be small and its modelling is not considered as important as that of the other terms in (2.9) [10, 11]. This belief is critically reviewed in Section 3.5. The physical meaning of the flux terms is to spatially spread the energy associated with each stress component. From the mathematical point of view, they act similarly to molecular diffusion and usually all three terms are referred to as diffusive fluxes. It must be remembered, however, that this terminology is only relevant for the averaged equations. In reality, for instance $\overline{u'_i u'_j u'_k}$ is convective transport by turbulent velocity fluctuations; it originates from the convection term and does not depend on viscosity at all.

2.4 Reynolds Stress Closure Modelling

2.4.1 General Remarks

Differential Reynolds stress modelling (RSM), *i.e.* closing Eq. (2.10) by means of modelling unclosed terms, is virtually the most sophisticated level of RANS turbulence-modelling available for any practical simulations today. Modelling approaches of an even higher level of description are currently being studied. The structure-based turbulence modelling [12, 13] and two-point closures, see *e.g.* [14], may be mentioned as examples of such ideas. However, these concepts are still far from becoming practical engineering tools. The RSM approach aims at closing the system (2.10) in order to obtain a numerically solvable system of transport equations for each stress component and the dissipation rate of k. This is an attractive idea in principle, since all the physical processes governing the evolution of the stress tensor are involved in the equations. The important production term and also the convection by mean flow can be computed without modelling. This is the main motivation of the RSM approach. On the other hand, some very important terms must be modelled. Models for these terms may be complex, involving several coefficients to be calibrated, and derivation of some of these models is based on quite strong simplifying assumptions such as quasi-homogeneity of turbulence. Moreover, the results are often very sensitive to the details of modelling.

The basic concepts of the RSM were defined as early as in 1945 by Chou [15]. A few years later, Rotta made an important and lasting contribution to RS modelling [16]. In the 1970s the RSM gained more attention in the wake of the important work by Hanjalić and Launder [10] and by Launder *et al.* [11]. Since those years, many researchers have contributed to the field and proposed models of varying level of description and complexity.

2.4.2 Tensor Functions

Tensor functions are needed in modelling the unknown tensor-valued variables that appear in the Reynolds stress equations. The unknown terms must be closed in terms of the known variables. This does not mean that the available known variables are the only variables on which the unclosed terms depend on in reality. Part of the necessary information is simply lost in the Reynolds averaging, and the best that can be done in the context of RANS is to expand the unclosed terms as functions of the known variables only. Tensor-valued quantities must be modelled as isotropic tensor-valued tensor functions of the available tensor and scalar variables. This is because the coordinate-frame invariance must be preserved — the laws of physics do not depend on the orientation and the metrics of the chosen coordinate system.

Isotropy means here that the functional form of a tensor-valued tensor function does not depend on the coordinate system. In other words, let t_{ij}, and $q_{ij}^{(1)}, \ldots, q_{ij}^{(m)}$ represent the components of some tensors in a certain coordinate system with

$$t_{ij} = f(q_{ij}^{(1)}, \ldots, q_{ij}^{(m)}) \tag{2.15}$$

being valid in that system. If t'_{ij}, and $q'^{(1)}_{ij}, \dots, q'^{(m)}_{ij}$ represent the components of the same tensors in some other system, then

$$t'_{ij} = f(q'^{(1)}_{ij}, \dots, q'^{(m)}_{ij}) \tag{2.16}$$

must hold with f having exactly the same form as in (2.15).

In fact, the requirement of tensor-valued function simplifies the problem since polynomials are the only tensor-valued functions of tensors. Thus, an arbitrary tensor t_{ij} that depends on the other tensors $q^{(1)}_{ij}, \dots, q^{(m)}_{ij}$ may be formally expressed as

$$t_{ij}(q^{(1)}_{ij}, \dots, q^{(m)}_{ij}) = \sum_{k=1}^{\infty} \alpha_k T^{(k)}_{ij} \tag{2.17}$$

where $T^{(k)}_{ij}$ are various tensor groups, *i.e.* matrix products of the tensors $q^{(1)}_{ij}, \dots, q^{(m)}_{ij}$, and α_k are scalar coefficients that may depend on the scalar invariants of the $q^{(n)}_{ij}$-tensors. Fortunately, the number of linearly independent tensor groups is limited. All groups of higher than a certain order can be reduced to combinations of lower-order groups and scalar invariants according to the generalized Cayley-Hamilton theorem. Also, the number of irreducible invariants is always limited. The Cayley-Hamilton theorem states that a cubic product of a tensor t_{ij} with itself in three dimensional space can be expressed as

$$t_{ik}t_{kl}t_{lj} = \frac{1}{3} III_t \delta_{ij} + \frac{1}{2} II_t t_{ij} + I_t t_{ik} t_{kj} \tag{2.18}$$

where $III_t = t_{kl}t_{lm}t_{mk}$, $II_t = t_{kl}t_{lk}$, and $I_t = t_{kk}$ are the scalar invariants of t_{ij}. The right-hand side includes t_{ij} only in the second, first and zeroth powers. Thus, all third- and higher-order terms in any tensor polynomial can be reduced by successively applying this formula. For more details, see *e.g.* Refs. [17, 18].

Although the number of terms in any tensor polynomial representation is limited, the functional form of a representation is not yet closed. The expressions for the scalar coefficients α_k are still to be determined. A general approach is to expand the coefficient functions in terms of the invariants to some order. Coefficients of such expansions must then be determined using, *e.g.* physical constraints and empirical data. Constant coefficients, *i.e.* zeroth order expansions, are often used in the simplest-level modelling.

2.4.3 Terms that Need Modelling

The redistributive pressure-strain correlation Φ_{ij}, the dissipation tensor ε_{ij}, and the turbulent transport terms must be modelled. The redistribution tensor may be redefined by subtracting the deviatoric part of the dissipation tensor from it as

$$\Pi_{ij} = \Phi_{ij} - (\varepsilon_{ij} - \frac{2}{3}\varepsilon\delta_{ij}) \tag{2.19}$$

This way, all the traceless inter-component redistributive effects are lumped together. Note that ε is the dissipation rate of k and it must be modelled at the level of two-equation modelling as well. More or less similar modelling of ε may be used for RS- and two-equation modelling. In (2.9), the turbulent transport is embedded in the total transport $\mathcal{D}_{ij}$. The turbulent flux is given by

$$T_{ijk} = -\overline{u_i' u_j' u_k'} - \frac{1}{\rho}\left(\delta_{ik}\overline{p' u_j'} + \delta_{jk}\overline{p' u_i'}\right) \tag{2.20}$$

Using the definitions Π_{ij} and T_{ijk}, Eq. (2.10) may be rewritten as

$$\frac{\mathrm{D}\overline{u_i' u_j'}}{\mathrm{D}t} = P_{ij} - \frac{2}{3}\varepsilon\delta_{ij} + \Pi_{ij} + \frac{\partial}{\partial x_k}\left(T_{ijk} + \nu\frac{\partial\overline{u_i' u_j'}}{\partial x_k}\right) \tag{2.21}$$

where the terms that need modelling (Π_{ij} and T_{ijk}) are clearly separated from the other terms that are readily explicit in terms of the available variables and ε. Modelling of ε is discussed in the context of the two-equation modelling.

2.4.4 Redistribution Tensor

In the context of single-point RANS modelling, the redistribution tensor is assumed to be a function of the Reynolds stresses or the nondimensional anisotropy tensor

$$a_{ij} \equiv \overline{u_i u_j}/k - (2/3)\delta_{ij} \tag{2.22}$$

the mean-velocity gradient, and the scalars k and ε. The number of variables can be reduced by nondimensionalizing the mean-velocity gradient using the turbulent time-scale k/ε. Thus, the redistribution tensor may be formally written as

$$\Pi_{ij} = \varepsilon\mathcal{F}_{ij}\left(a_{ij}, \frac{k}{\varepsilon}\frac{\partial U_i}{\partial x_j}, \delta_{ij}\right) \tag{2.23}$$

It is convenient to split the velocity-gradient tensor into its symmetric and skew-symmetric parts, *i.e.* the nondimensional strain-rate and vorticity tensors defined as

$$S_{ij} \equiv \frac{1}{2}\frac{k}{\varepsilon}\left(\frac{\partial U_i}{\partial x_j} + \frac{\partial U_j}{\partial x_i}\right) \quad \text{and} \quad \Omega_{ij} \equiv \frac{1}{2}\frac{k}{\varepsilon}\left(\frac{\partial U_i}{\partial x_j} - \frac{\partial U_j}{\partial x_i}\right) \tag{2.24}$$

in order to make the necessary tensor algebra easier. Using S_{ij} and Ω_{ij}, (2.23) is rewritten as

$$\Pi_{ij} = \varepsilon\mathcal{F}_{ij}\left(a_{ij}, S_{ij}, \Omega_{ij}, \delta_{ij}\right) \tag{2.25}$$

where ε is used to nondimensionalize the tensor-valued function $\mathcal{F}_{ij}$ to be sought. $\mathcal{F}_{ij}$ depends also on δ_{ij}, since it is a tensor-valued function. The functional form of $\mathcal{F}_{ij}$ must satisfy the symmetry condition $\mathcal{F}_{ij} = \mathcal{F}_{ji}$ and its trace must be zero, $\mathcal{F}_{ii} = 0$. Locality in space and time has been assumed. This means that the model does not depend on the values elsewhere in space or values at previous times although in reality such dependencies may take place. In general, the redistribution term may depend also on the viscosity in the near-wall region. Therefore, the turbulent

Reynolds number $Re_T = k^2/(\varepsilon\nu)$ could be added as an argument of $\mathcal{F}_{ij}$. The brief discussion here, however, is limited to the case of a high Reynolds number where the influence of viscosity is negligible.

Usually, more attention is paid to modelling the pressure-strain correlation than to the dissipation anisotropy. One reason for this is that the dissipation anisotropy is usually quite small except near the walls. In most of the present-day models, *e.g* [11, 19], the latter term is thought to be embedded into the model for the pressure-strain term, which implies $\Pi_{ij} = \Phi_{ij}$. More recently, also separate models for the dissipation anisotropy have been proposed, see *e.g.* Refs. [20, 21]. The algebraic Reynolds stress modelling within this study is based on the former approach, and thus explicit modelling of the dissipation anisotropy is not discussed here.

Modelling of the pressure-strain term is based on the formal solution of the Poisson-equation for the fluctuating pressure in incompressible flow, see *e.g.* [22]

$$\nabla^2 p' = -2\rho \frac{\partial U_k}{\partial x_l}\frac{\partial u_l'}{\partial x_k} - \rho \frac{\partial^2}{\partial x_k \partial x_l}\left(u_k' u_l' - \overline{u_k' u_l'}\right) \tag{2.26}$$

This equation is linear in p', and includes two source terms of which only the first one depends on the mean-velocity gradient. This suggests that the complete solution is a sum of a harmonic solution that satisfies Laplace's equation $\nabla^2 p' = 0$, and two particular solutions called the slow and the rapid solutions. The rapid solution is driven by the source term that depends on the mean-velocity gradient. The word rapid indicates that this part responds immediately to a change in the mean-velocity gradient. Obviously, the velocity pressure-gradient correlation is also split into the harmonic, slow and rapid parts. The harmonic part is zero in homogeneous turbulence, and it is rather unimportant also in inhomogeneous flows except in the immediate vicinity of walls [23]. The slow part is independent of the mean-velocity gradient. Modelling of the slow part is much more straightforward than that of the rapid part. The derivation of the most commonly used redistribution models is found in most of the textbooks on turbulence modelling. The discussion here largely follows the book "Statistical theory and modeling for turbulent flows" by Durbin and Petterson-Reif [22].

Initially anisotropic turbulence has a tendency to return to isotropy in the absence of the mean-velocity gradient. This is because there is no directional forcing in such a situation (the turbulent energy will obviously decay at the same time, since there is no production). It is the slow term that is responsible for this return to isotropy process. The slow term is usually assumed to be a tensor function of only the anisotropy itself, besides δ_{ij}, as

$$\Phi_{ij}^{(s)} = \varepsilon \mathcal{F}_{ij}^{(s)}(a_{ij}, \delta_{ij}) \tag{2.27}$$

Therefore, it may be expanded as

$$\mathcal{F}_{ij}^{(s)} = -C_1 a_{ij} + C_1^n (a_{ik}a_{kj} - \frac{1}{3} II_a \delta_{ij}) \tag{2.28}$$

No independent higher-order terms exist because of (2.18). The coefficients C_1 and C_1^n may be functions of the invariants II_a and III_a. Some models include also strain-dependent parameters such as $P/\varepsilon = -a_{kl}S_{lk}$. The most popular model for the slow part is the simple Rotta model [16]

$$\mathcal{F}_{ij}^{(s)} = -C_1 a_{ij} \tag{2.29}$$

which ignores the nonlinear term. This is just a linear relaxation of a_{ij} towards zero. The second-order term is included in some models, *e.g* the SSG model by Speziale *et al.* [24]. It may, however, cause stiffness and thus troubles in numerical solution. The nonlinear term is often ignored in the model as it is usually of little importance in shear-dominated flows. The SSG model also features a shear-dependent coefficient C_1 as

$$C_1 = \frac{1}{2}\left(C_1^0 + C_1^1 P/\varepsilon\right) \tag{2.30}$$

The factor 1/2 is owing to the fact that the anisotropy tensor is scaled using $2k$ in Ref. [24].

Modelling of the rapid part is started from an equation obtained from (2.26) by dropping the slow part of the source term as

$$\nabla^2 p' = -2\rho \frac{\partial U_k}{\partial x_l}\frac{\partial u_l'}{\partial x_k} \tag{2.31}$$

The formal solution of this equation for homogeneous turbulence in unbounded space is obtained with the free-space Green function $1/(4\pi|\mathbf{x}-\mathbf{x}'|)$ as

$$p'(\mathbf{x}) = \frac{1}{4\pi}\iiint_{-\infty}^{\infty} \frac{2\rho}{|\mathbf{x}-\mathbf{x}'|}\frac{\partial U_k}{\partial x_l}\frac{\partial u_l'(\mathbf{x}')}{\partial x_k'}\mathrm{d}^3\mathbf{x}' \tag{2.32}$$

The mean-velocity gradient can be excluded from the integral by assuming homogeneous turbulence, which implies that also the mean-velocity gradient is constant in space. Next (2.32) is differentiated with respect to x_i and integrated by parts to obtain

$$\frac{\partial p'(\mathbf{x})}{\partial x_i} = \frac{\rho}{2\pi}\frac{\partial U_k}{\partial x_l}\iiint_{-\infty}^{\infty} \frac{1}{|\mathbf{x}-\mathbf{x}'|}\frac{\partial^2 u_l'(\mathbf{x}')}{\partial x_k'\partial x_i'}\mathrm{d}^3\mathbf{x}' \tag{2.33}$$

The $\mathbf{x}$-derivative is changed to $\mathbf{x}'$-derivative, which is possible because

$$\frac{\partial}{\partial x_i}\left(\frac{1}{|\mathbf{x}-\mathbf{x}'|}\right) = -\frac{\partial}{\partial x_i'}\left(\frac{1}{|\mathbf{x}-\mathbf{x}'|}\right) \tag{2.34}$$

Next, the rapid part of the velocity pressure-gradient correlation, which in homogeneous turbulence equals minus the pressure-strain correlation, see Eq. (2.14), can be formed as

$$\begin{aligned}
\Phi_{ij}^{(r)} &= -\frac{1}{\rho}\left(\overline{u_j'\frac{\partial p'}{\partial x_i}} + \overline{u_i'\frac{\partial p'}{\partial x_j}}\right) \qquad (2.35)\\
&= -\frac{1}{2\pi}\frac{\partial U_k}{\partial x_l}\iiint_{-\infty}^{\infty}\frac{1}{|\mathbf{x}-\mathbf{x}'|}\left[\overline{u_j'(\mathbf{x})\frac{\partial^2 u_l'(\mathbf{x}')}{\partial x_i'\partial x_k'}} + \overline{u_i'(\mathbf{x})\frac{\partial^2 u_l'(\mathbf{x}')}{\partial x_j'\partial x_k'}}\right]\mathrm{d}^3\mathbf{x}'
\end{aligned}$$

The right-hand side contains two-point correlations, although the velocity pressure-gradient correlation is a single-point correlation. This manifests one of the central difficulties in closing the Reynolds stress transport equations, especially their pressure-related terms. Pressure fluctuations influence at a distance but these effects have to be approximated using local values only. This fact, among the assumption of homogeneity, renders modelling of the pressure-terms quite vague. Owing to the assumed homogeneity, the two-point correlations are functions of the distance $\boldsymbol{\xi} = \mathbf{x} - \mathbf{x}'$ only. Moreover, $u_j'(\mathbf{x})$ and $u_i'(\mathbf{x})$ may be brought inside the derivative operators with respect to $\mathbf{x}'$ since they do not operate on these fluctuating velocity components as they are functions of $\mathbf{x}$ only. Eq. (2.35) may then be written as

$$\Phi_{ij}^{(r)} = -\frac{1}{2\pi}\frac{\partial U_k}{\partial x_l}\iiint_{-\infty}^{\infty}\frac{1}{|\boldsymbol{\xi}|}\left[\frac{\partial^2\overline{u_j'u_l'}(\boldsymbol{\xi})}{\partial x_i x_k} + \frac{\partial^2\overline{u_i'u_l'}(\boldsymbol{\xi})}{\partial x_j x_k}\right]\mathrm{d}^3\boldsymbol{\xi} \tag{2.36}$$

which may be formally written in terms of a fourth-rank tensor M_{ijkl} as

$$\Phi_{ij}^{(r)} = M_{ijkl}\frac{\partial U_k}{\partial x_l} = k\mathcal{M}_{ijkl}\frac{\partial U_k}{\partial x_l} \tag{2.37}$$

The remaining task is to construct a model for the fourth-order tensor $\mathcal{M}_{ijkl}$. This is accomplished by systematically expanding $\mathcal{M}_{ijkl}$ in powers of the anisotropy tensor. There are a few constraints for $\mathcal{M}_{ijkl}$. First, it must preserve the symmetry in i, j and its trace must be zero when contracted on $i = j$. When contracted on $j = k$, its trace must equal $2\overline{u_i'u_l'}$. In short:

$$\mathcal{M}_{ijkl} = \mathcal{M}_{jikl}; \quad \mathcal{M}_{iikl} = 0; \quad \mathcal{M}_{ijjl} = 2\overline{u_i'u_l'} \tag{2.38}$$

These constraints have been known since the times of Chou [15] and Rotta [16] although they did not attempt to construct models for $\mathcal{M}_{ijkl}$ explicitly [25]. As the dependence of $\Phi_{ij}^{(r)}$ on the mean-velocity gradient is expressed by (2.37) in the case of homogeneous turbulence, $\mathcal{M}_{ijkl}$ may be assumed to be a nondimensional function of a_{ij} only. W.C. Reynolds has shown that the most general expansion of the $\mathcal{M}_{ijkl}$ tensor in terms of a_{ij} that satisfies the constraints (2.38) contains 15 tensor groups up to the fourth[1] power of a_{ij} and 15 scalar coefficient functions that may depend on the anisotropy invariants and possibly also of the turbulent Reynolds number [25, 26]. By substituting such an expansion into (2.37) and applying the constraints (2.38), the complete expression for $\Phi_{ij}^{(r)}$ is obtained. This consists of eight tensor groups up to the third power in a_{ij}, and their coefficient functions. Despite this, most of the widely used models are linear in a_{ij}, and there are, indeed, grounds to claim that a model for $\Phi_{ij}^{(r)}$ should be linear in a_{ij}, see Refs. [25,27]. On the other hand, a high-order representation is needed to satisfy the strong realizability conditions. This means that linear models may in some extreme circumstances predict negative normal stresses. However, the algebraic Reynolds stress models

---

[1] Terms such as $a_{im}a_{mj}a_{kn}a_{nl}$ appear in the expansion since $\mathcal{M}_{ijkl}$ is a fourth-rank tensor. These cannot be further reduced, since they involve only quadratic *matrix* products.

discussed and used in this study are based on the so-called general quasi-linear model (GQLM)

$$
\begin{aligned}
\Phi_{ij}^{(r)} &= C_2 k S_{ij} + \frac{C_3}{2} k \left(a_{ik} S_{kj} + S_{ik} a_{kj} - \frac{2}{3} a_{kl} S_{lk} \delta_{ij} \right) \\
&- \frac{C_4}{2} k \left(a_{ik} \Omega_{kj} - \Omega_{ik} a_{kj} \right)
\end{aligned}
\tag{2.39}
$$

in which the C-coefficients may in general be functions of the anisotropy invariants and possibly also of the turbulent Reynolds number. All special cases of (2.39) with only constant coefficients form the class of general linear model (GLM). In fact, the majority of the widely used models, such as the LRR model by Launder *et al.* [11], its truncation known as the isotropization of production model (LRR-IP), and many others belong to this class.

Homogeneous turbulence has been assumed in the derivation of (2.36), although virtually all problems of practical interest are inhomogeneous. The developed models may be considered quasi-homogeneous models, *i.e.* they should be applicable to flows in which the turbulent quantities vary in space only relatively slowly. It is usually thought that the quasi-homogeneous models are applicable away from solid walls and inappropriate only near the walls. Solid walls have several effects on the pressure-strain term that have not been considered in the development of the quasi-homogeneous models. These are the kinematic wall-blocking effect, the low-Reynolds number effects, and possibly the contribution of the ignored harmonic part of the pressure. The wall-blocking effect is the most important of these, and it is usually modelled as an additional term $\Phi_{ij}^{(w)}$. This represents the non-local wall-echo of pressure fluctuations, and it depends on the wall-normal direction and distance. This fact makes its modelling rather cumbersome, especially for complex geometries.

It has been observed that the quasi-homogeneous modelling alone is sufficient for most purposes in high-Reynolds number aerodynamics if ε is modelled using an appropriate ω model-equation [28, 29]. Such an approach does not provide correct asymptotic near-wall behaviour of the turbulent quantities, but the mean velocity profile and the wall shear-stress can usually be predicted with sufficient accuracy. Also, the algebraic stress modelling studied and employed in this study is based on the quasi-homogeneous model only. Therefore, the wall effects and their modelling are not discussed here in more detail.

2.4.5 Turbulent Transport

Some kind of a gradient-diffusion model is usually selected for the turbulent transport plus pressure diffusion. The gradient transport models are based on the reasoning that the turbulent transport can be modelled as diffusion, because the fluctuating convective velocity field is quite random. Recall that molecular diffusion is also a kind of random transport at the molecular scales. It is usually assumed that the turbulent transport dominates over the pressure diffusion, and the latter is then thought to be absorbed into the model for turbulent transport. The generalized gradient diffusion model by Daly and Harlow [30]

$$T_{ijk} \approx C_s \frac{k}{\varepsilon} \overline{u_k' u_l'} \frac{\partial \overline{u_i' u_j'}}{\partial x_l} \tag{2.40}$$

which involves a vector-valued diffusivity, is probably the most popular of such models. More complex models that are symmetric with respect to all three indices have been proposed *e.g.* by Hanjalić and Launder [10]

$$T_{ijk} \approx C_s \frac{k}{\varepsilon} \left(\overline{u_i' u_l'} \frac{\partial \overline{u_j' u_k'}}{\partial x_l} + \overline{u_j' u_l'} \frac{\partial \overline{u_i' u_k'}}{\partial x_l} + \overline{u_k' u_l'} \frac{\partial \overline{u_i' u_j'}}{\partial x_l} \right) \tag{2.41}$$

Complete symmetry is, however, not a critical requirement since the flux will be contracted with the divergence operator $\partial/\partial x_k$.

A simpler scalar-diffusivity gradient-diffusion model can also be applied, see *e.g.* Refs. [28, 29]. This equals the eddy-viscosity concept and reads

$$T_{ijk} \approx \sigma_k \nu_T \frac{\partial \overline{u_i' u_j'}}{\partial x_k} \tag{2.42}$$

where σ_k is a model coefficient usually with a constant value and $\nu_T \sim k^2/\varepsilon \sim k/\omega$ is the eddy viscosity. Eq. (2.42) is used in the model developed in this study.

2.5 Two-Equation Modelling

2.5.1 Basic Formulation

In the concept of two-equation modelling, the idea of solving a transport equation for each stress component is replaced by some explicit constitutive relation. This means that the stress tensor is assumed to be an algebraic function of the local mean-velocity gradient and the two turbulent scale variables. These scale variables are then solved from the two transport equations of the model. This hypothesis is, of course, not generally valid, but the two-equation concept has, however, turned out to be a quite adequate level of modelling for many applications. The physical realism of two-equation modelling in more complex flows largely depends on the constitutive relation.

The two-equation turbulence models can be thought to consist of two more or less separate parts: the scale-determining model, and the constitutive model. The most popular constitutive model is the linear generalized Boussinesq eddy-viscosity model

$$\overline{u_i' u_j'} = -2\nu_T S_{ij} + \frac{2}{3} k \delta_{ij} = -2C_\mu \upsilon_T l_T S_{ij} + \frac{2}{3} k \delta_{ij} \tag{2.43}$$

where C_μ is usually constant 0.09 and υ_T and l_T are the turbulent scale variables: velocity scale and length scale, respectively. There are also more general nonlinear constitutive models, which include higher-order tensor products of the mean-flow strain-rate and vorticity tensors S_{ij} and Ω_{ij}, respectively. Explicit algebraic

Reynolds stress models (EARSM) are an important special class of these nonlinear constitutive models. This is because these models are derived from a differential Reynolds stress model by invoking the so-called weak-equilibrium assumption. The nonlinear constitutive modelling is discussed in more detail in Section 2.5.2, and in Chapter 5.

The scale-determining model consists of two modelled transport equations for the selected scale variables. The velocity scale is typically solved from the turbulent kinetic energy $k = \overline{u'_k u'_k}/2$, because its transport equation needs relatively little modelling. The exact transport equation of k is easily derived from (2.9) by taking half of its trace to obtain

$$\frac{\mathrm{D}k}{\mathrm{D}t} = -\overline{u'_i u'_j}\frac{\partial U_i}{\partial x_j} - \frac{1}{2}\varepsilon_{kk} + \frac{\partial}{\partial x_j}\left(T_j^{(k)} + \nu\frac{\partial k}{\partial x_j}\right) \tag{2.44}$$

The advantage of this equation over (2.10) is that it includes no redistribution term, thus only the dissipative term $\varepsilon_{kk}/2$ and the turbulent transport plus pressure diffusion have to be modelled. As explained above, $\varepsilon_{kk}/2$ is not exactly the viscous dissipation rate of k, except in homogeneous turbulence. In the following, it is assumed, however, that $\varepsilon_{kk}/2 = \varepsilon$ for the sake of simplicity. The difference is merely semantics in the context of modelling, where only crude generic models for this term are employed. The dissipation rate will be modelled using the second scale variable. Recalibration of a generic model equation for the second scale variable for the high-lift aerodynamics purposes is the principal goal of this study.

As in the context of RSM, gradient-diffusion models are used for the turbulent flux

$$T_j^{(k)} = \frac{1}{2}T_{jii} = -\overline{k'u'_j} - \frac{1}{\rho}\overline{p'u'_j} \tag{2.45}$$

which consists of the turbulent transport plus pressure diffusion. The simple eddy-viscosity-based gradient diffusion model

$$T_j^{(k)} \approx \sigma_k \nu_T \frac{\partial k}{\partial x_j} \tag{2.46}$$

is the only reasonable option with linear constitutive modelling. Nonlinear constitutive modelling gives more freedom for choosing the turbulent transport models, because also the normal-stress anisotropy is reasonably modelled. For instance, the Daly-Harlow model (2.40) [30] has been used in nonlinear two-equation modelling. In this study, however, the simpler scalar diffusivity approach (2.46) is chosen. It is assumed that (2.46) is usually adequate at the level of two-equation modelling. It also seems to be numerically more stable and robust, and it slightly reduces the coding effort in the implementation.

Substituting (2.46) for $T_j^{(k)}$ in (2.44), a simple model equation for k can be written as

$$\frac{\mathrm{D}k}{\mathrm{D}t} = P - \varepsilon + \frac{\partial}{\partial x_j}\left[(\nu + \sigma_k \nu_T)\frac{\partial k}{\partial x_j}\right] \tag{2.47}$$

where P is the production of k by the mean-flow gradients

$$P = -\overline{u'_i u'_j}\frac{\partial U_i}{\partial x_j} \tag{2.48}$$

The choice of the second scale variable is not that obvious, although ε has been the most popular choice since Jones & Launder published their $k-\varepsilon$ model [31], which then became very popular and is nowadays known as the standard $k-\varepsilon$ model. The exact dissipation equation is very difficult to model in comparison with the k-equation. This is especially the case in the near-wall region, see *e.g.* Rodi & Mansour (1993) [32].

Generic modelling is an alternative route to obtain models for the second scale variable. Most engineering models can be kept as generic models, also the standard $k-\varepsilon$ model. The word generic means here that we are not looking for a term-by-term modelled closure for the exact transport equation of ε or another scale variable derived from it. It is felt that the obstacles lying on the route to such a derivation are too high. Instead, the generic approach has usually shown to be a more efficient way to set up engineering models for the second scale variable.

It can be argued that the evolution of any second scale variable is governed by a certain limited set of physical processes. The simplest approach leads to an analogue with the transport equation of turbulent energy k. It includes four different terms representing the following physical processes: convection by the mean flow, production by the mean-flow gradients, viscous dissipation, and diffusion which actually consists mostly of turbulent random convection. The molecular diffusion is typically small in fully turbulent flows. Actually, it is misleading to speak about production of the second scale variable by the mean-flow gradients, since this variable is related to viscous dissipation, which is not directly produced by the mean-flow gradients. These two, however, are indirectly related since the spectral energy flux to the dissipative motion may be estimated as proportional to the production rate of k if the transport terms are not dominant over the production and dissipation.

After all, the idea of quite simplistic generic modelling is to hypothesize that the evolution of the second scale variable is basically governed by the very same physical processes as that of k. Assuming this, a transport model of similar form as (2.47) but dimensionally consistent with an arbitrary second scale variable ϕ can be set as

$$\frac{\mathrm{D}\phi}{\mathrm{D}t} = \frac{\phi}{k}\left(C_{\phi 1}P - C_{\phi 2}\varepsilon\right) + \frac{\partial}{\partial x_j}\left[(\nu + \sigma_\phi \nu_T)\frac{\partial \phi}{\partial x_j}\right] \tag{2.49}$$

In practice, the second variable is of the form of $\phi \sim k^m\varepsilon^n$. The success of this kind of model largely depends on the choice of the scale variable ϕ, or in other words on the choice of the parameters m and n. For instance, the standard ε model of Jones & Launder and Wilcox's ω model are special cases of (2.49), but they behave very differently from each other. This is not only because of the different calibration of their model coefficients, but also because transformations from one m, n-pair to another produces extra terms that depend on inner products of the gradients of k and ϕ. Therefore, each choice of m and n in (2.49) leads to a different model that may or may not work satisfactorily in the flow problem of interest.

2.5.2 Algebraic Reynolds Stress Modelling and Non-Linear Two-Equation Models

Differential Reynolds stress models can be simplified by modelling the transport terms by some means. Algebraic Reynolds stress models (ARSM) are derived this way. The most usual means to model the transport terms was first proposed by Rodi [33]. In this approach, the total transport of k is exploited in modelling of the stress tensor as follows

$$\mathfrak{D}\left(\overline{u_i'u_j'}\right) = k\mathfrak{D}\left(\frac{\overline{u_i'u_j'}}{k}\right) + \frac{\overline{u_i'u_j'}}{k}\mathfrak{D}(k) \tag{2.50}$$

where $\mathfrak{D}$ is a formal total transport operator including all the terms of the modelled Reynolds stress transport-equation that involve derivatives of $\overline{u_i'u_j'}$. These terms are the transport by mean flow, the turbulent transport (diffusion), and the molecular diffusion. Given that $\mathfrak{D}(k) = P - \varepsilon$ and writing (2.50) in terms of the anisotropy tensor results in

$$\mathfrak{D}\left(\overline{u_i'u_j'}\right) = k\mathfrak{D}\left(a_{ij}\right) + \left(a_{ij} + \frac{2}{3}\delta_{ij}\right)(P - \varepsilon) \tag{2.51}$$

The algebraic model for the transport terms is now obtained by ignoring the first term on the right-hand side

$$\mathfrak{D}\left(\overline{u_i'u_j'}\right) \approx \left(a_{ij} + \frac{2}{3}\delta_{ij}\right)(P - \varepsilon) \tag{2.52}$$

The algebraic approximation may be further improved by modelling also $\mathfrak{D}(a_{ij})$ partially by some algebraic expression. In particular, the sensitivity to the mean-flow curvature may be improved this way. Such techniques are one of the foci of this study and they are discussed and studied in detail in Chapter 5.

As a matter of fact, it is convenient to rewrite the RSM equation system in terms of the anisotropy tensor and then to ignore the transport terms of a_{ij}. This is obviously equivalent to applying (2.52) to the original form of the equation system expressed in terms of $\overline{u_i'u_j'}$. If the quasilinear model (2.39) is adopted for the redistribution tensor, the modelled equation system for a_{ij} can be written as

$$\begin{aligned}\tau\left(\frac{\mathrm{D}a_{ij}}{\mathrm{D}t} - \mathcal{D}_{ij}^{(a)}\right) = A_0\Bigg[&\left(A_3 + A_4\frac{P}{\varepsilon}\right)a_{ij} + A_1 S_{ij} - \left(a_{ik}\Omega_{kj} - \Omega_{ik}a_{kj}\right)\\ &+ A_2\left(a_{ik}S_{kj} + S_{ik}a_{kj} - \frac{2}{3}a_{kl}S_{lk}\delta_{ij}\right)\Bigg]\end{aligned} \tag{2.53}$$

where τ is the turbulent time-scale k/ε. Terms with different physical interpretation, such as production, dissipation, etc. are here lumped together and sorted according to their tensorial form. Coefficients $A_0, \ldots, A_4$ are functions of the original RSM coefficients only. Eq. (2.53) may be called a general quasilinear Reynolds stress model. Quasilinearity is a highly favourable feature when seeking the explicit solution for the ARSM. The tensor algebra becomes extremely complex in the case of higher-order models. In principle, however, there is an explicit solution for all ARS models. This fact is based on the reducibility of the higher-order tensors according to the Cayley-Hamilton theorem. Indeed, new explicit solutions for some higher-order ARSMs have been found very recently by Grundenstam *et al.* [34]. Such elaborate algebraic manipulation is needed in solving such ARSMs that it can only be accomplished using symbolic manipulation software.

The corresponding general quasilinear ARSM is now obtained in the weak equilibrium limit as

$$\begin{aligned} 0 = {} & \left(A_3 + A_4\frac{P}{\varepsilon}\right) a_{ij} + A_1 S_{ij} - \left(a_{ik}\Omega_{kj} - \Omega_{ik}a_{kj}\right) \\ & + A_2\left(a_{ik}S_{kj} + S_{ik}a_{kj} - \frac{2}{3}a_{kl}S_{lk}\delta_{ij}\right) \end{aligned} \tag{2.54}$$

This is an implicit algebraic tensor equation. It could, in principle, be solved iteratively. However, an iterative solution is found to be numerically troublesome in practical flow problems. Although (2.54) is tensorially linear, it contains a scalar nonlinearity. Therefore, multiple roots exist, and iteration may converge towards a non-physical root. Fortunately, an explicit solution can be found for (2.54) with the aid of tensor algebra.

In the weak-equilibrium limit, the anisotropy tensor can be assumed to only depend on the mean velocity-gradient tensor and the turbulent time scale k/ε. It is convenient to split the mean velocity gradient into the strain rate and vorticity tensors and to scale them using the turbulent time scale just as explained in Section 2.4.4. Thus, the anisotropy tensor can formally be expressed as

$$a_{ij} = f(S_{ij}, \Omega_{ij}) \tag{2.55}$$

where f is an isotropic second-order tensor-valued tensor function. The generalized Cayley-Hamilton theorem implies that the most general representation for a symmetric traceless second-order tensor, such as a_{ij}, which depends on two other second-order tensors is a tensor polynomial containing ten independent terms. Each term consists of a tensor group with a required tensorial form and a scalar coefficient that generally depends on the scalar invariants of the two tensors. This is known as the integrity basis of a_{ij} and it forms the most general representation basis for a_{ij}. The dimension of the integrity basis is higher than the number of the independent components in the represented tensor a_{ij} as it may have only five linearly independent components. The greater number of base-terms guarantees the minimum dimension of five in all possible situations when some of the groups may vanish. Thus the integrity basis is redundant in terms of linearly independent representation for each component of a_{ij}. For more details, see *e.g.* Refs. [17] and [18]. The integrity basis for a_{ij} is given by

$$\begin{aligned}
a_{ij} = {} & \beta_1 S_{ij} \\
& + \beta_2 \left(S_{ik}S_{kj} - II_S\delta_{ij}/3\right) + \beta_3 \left(\Omega_{ik}\Omega_{kj} - II_\Omega\delta_{ij}/3\right) + \beta_4 \left(S_{ik}\Omega_{kj} - \Omega_{ik}S_{kj}\right) \\
& + \beta_5 \left(S_{ik}S_{kl}\Omega_{lj} - \Omega_{ik}S_{kl}S_{lj}\right) + \beta_6 \left(S_{ik}\Omega_{kl}\Omega_{lj} + \Omega_{ik}\Omega_{kl}S_{lj} - IV\delta_{ij}/3\right) \\
& + \beta_7 \left(S_{ik}S_{kl}\Omega_{lp}\Omega_{pj} + \Omega_{ik}\Omega_{kl}S_{lp}S_{pj} - 2V\delta_{ij}/3\right) \\
& + \beta_8 \left(S_{ik}\Omega_{kl}S_{lp}S_{pj} - S_{ik}S_{kl}\Omega_{lp}S_{pj}\right) + \beta_9 \left(\Omega_{ik}S_{kl}\Omega_{lp}\Omega_{pj} - \Omega_{ik}\Omega_{kl}S_{lp}\Omega_{pj}\right) \\
& + \beta_{10} \left(\Omega_{ik}S_{kl}S_{lp}\Omega_{pq}\Omega_{qj} - \Omega_{ik}\Omega_{kl}S_{lp}S_{pq}\Omega_{qj}\right)
\end{aligned} \tag{2.56}$$

Also the number of independent scalar invariants is limited to five in the case of three-dimensional mean flow

$$\begin{array}{lll} II_S = S_{kl}S_{lk} & II_\Omega = \Omega_{kl}\Omega_{lk} & \\ III_S = S_{kl}S_{lm}S_{mk} & IV = S_{kl}\Omega_{lm}\Omega_{mk} & V = S_{kl}S_{lm}\Omega_{mn}\Omega_{nk} \end{array} \tag{2.57}$$

In two-dimensional mean flows, only two independent invariants II_S and II_Ω exist.

A linear system of equations for the β-coefficients is obtained by inserting (2.56) into (2.54) and applying (2.18) to reduce all the higher-order groups. The resulting linear system can be solved for the β-coefficients. But the solution is not yet complete, since there is still an unknown scalar parameter $P/\varepsilon = -a_{kl}S_{lk}$. Earlier models used a fixed equilibrium value for P/ε to close the solution, see *e.g.* Ref. [35]. This approach leads to a singular solution that needs further approximations to remove the singularities. This procedure is known as regularization. A complete solution features an explicit solution for P/ε. Such an approach provides a readily regular solution. Girimaji [36] and independently Wallin and Johansson [4] were the first to derive a complete EARSM.

An equation for P/ε must be derived in order to find a complete solution. Such an equation may be derived by expressing P/ε in terms of the determined solution of a_{ij}. This scalar polynomial equation is cubic in the case of two-dimensional mean flow and of the sixth order if the mean flow is three-dimensional, see Ref. [4] for details. The cubic equation can be solved explicitly, while the sixth-order equation cannot. In three-dimensional situations, the solution may in practice be approximated using the solution of the cubic equation. The explicit solution (EARSM) derived by Wallin and Johansson [4] is given in Section 6.6.2. As a_{ij} is known from the EARSM, the Reynolds stress tensor may finally be expressed as

$$\overline{u_i'u_j'} = k(\frac{2}{3}\delta_{ij} + a_{ij}) \tag{2.58}$$

EARSMs are formally nonlinear two-equation models. There are also such nonlinear two-equation models that are not derived as explicit solutions for ARSMs or as approximations of such solutions. Such models may be considered as nonlinear extensions of the ordinary eddy-viscosity two-equation models while EARSM may be considered as truncations of RSMs.

2.6 Other Models

So far, only the traditional Reynolds stress and two-equation modelling have been discussed. In fact, many more types of turbulence models exist. From the viewpoint of aerodynamics, perhaps the other most important model classes presently employed are the one-equation models and the algebraic mixing-length models. On the other hand, the traditional RANS Reynolds stress modelling has quite severe limitations in terms of its generality. These problems are also addressed in this study. Therefore, some scientists have been looking for some novel modelling approaches with a higher level of description. Structure-based modelling [12, 13] and two-point closure modelling, see *e.g.* [14] are worth mentioning as examples of proposed new concepts. To date, such concepts have not matured enough to be exploited with any engineering purposes. Therefore, these approaches are not discussed in this study, although they might become more important in the future.

The one-equation modelling has actually become rather popular in the field of aerodynamics after Baldwin and Barth [37] and later, Spalart and Allmaras published their models that are based on generic transport equations for the eddy viscosity (or turbulent Reynolds number) and tuned for aerodynamic flows. However, the Baldwin-Barth model never became as popular as its successor, the Spalart-Allmaras model, which has become some sort of standard model in aerodynamics in the USA. Earlier one-equation models were based on the transport equation for k with prescribed length-scale. The range of applicability of such models is more limited than that of two-equation models where the second scale variable is solved from a modelled transport equation. Obviously, the modern one-equation models, such as the Spalart-Allmaras model suffer from this incompleteness as well, although the second scale-variable does not appear explicitly in their formulation. These models are best suited for boundary-layer flows with no complex features.

Algebraic mixing-length models can be seen as the model class of the lowest level of description and of the most limited range of applicability and the least generality. This approach was first proposed by Prandtl in the 1920s. It is based on the analogy between the mixing by molecular motion and by turbulent eddies. In a broader sense, the concept of the eddy-viscosity is also based on this analogy. The mixing-length model by Balwin and Lomax [38] developed for boundary-layer flows has been very popular in aerodynamics up to the 1990s when more sophisticated one- and two-equation models started to become more popular also in boundary-layer dominated applications.

3 Requirements for Turbulence Modelling in High-Lift Problems

3.1 Overview

Modern jet-transport aircraft are typically designed for high subsonic cruise velocities such as $80 \ldots 85\%$ of the speed of sound. This unavoidably implies high wing loading. High wing loading, on the other hand, implies high stalling speed, which is unfavourable for landing and take-off. In order to keep the stalling speed within acceptable limits in landing and take-off situations, the wings are equipped with high-lift devices. These devices are usually extended from the leading and trailing edges of the wing for take off and landing, and they are retracted into the main wing for other phases of flight so that the wing retains its clean shape designed for cruise flight. Slotted trailing-edge flaps of one or more elements are typical examples of high-lift devices. Leading-edge devices are another important means of augmenting lift. The most typical examples of these are plain leading-edge flaps, Krüger flaps, and slotted slats. A combination of a slotted leading-edge slat and a slotted trailing edge flap of one or more elements is perhaps the most typical arrangement.

Multicomponent aerofoils are able to produce considerably higher maximum lift than single-component ones. Smith [39] provides quite a thorough discussion on this subject. Such a lengthy description is out of the scope of this study. Instead, only some brief remarks will be given. A three-component aerofoil in a typical take-off configuration is used as an example, see Fig. 3.1.

An aerofoil of two or more components can always be designed to give higher lift than a single-element aerofoil having the same chord. This is quite easy to understand with the aid of the following rough and highly simplified explanation. Each element set to an angle of attack deflect the flow past it, and thus its downstream element is exposed to a reduced effective angle of attack compared to that of an isolated element at the same geometric angle. Therefore, the downstream elements can be set to higher geometric angles than an isolated element without making them stall. Each element can be set to a higher geometric angle than the element just ahead of it. Of course, the situation is not that simple in reality, but this gives a rough overview of the physics involved. In reality, each element strongly interacts with the other and there are several mechanisms that increase the lift at a given angle as well as mechanisms that allow higher angles to be used without the risk of stall. Most of these mechanisms are interactions carried over by the pressure field, and

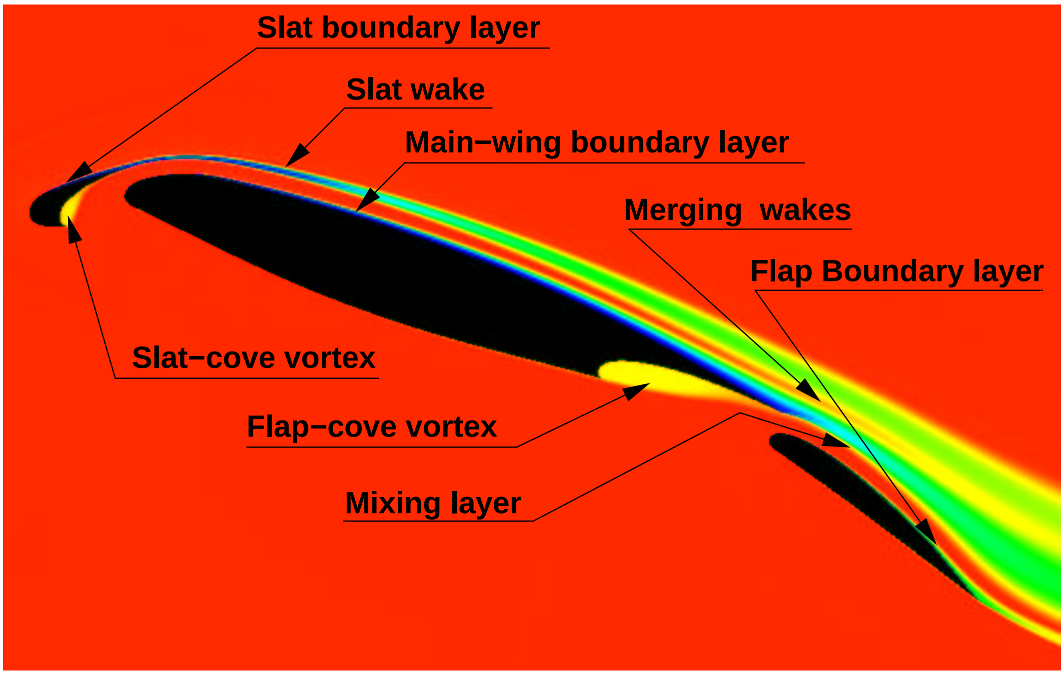

Figure 3.1: A three-element aerofoil in take-off configuration at an angle of attack of 20 degrees. The total pressure distribution shows flow regions where the losses occur. The most important flow details are identified. Note also the very thin boundary layers on the lower surfaces of the main wing and the flap.

thus do not directly depend on the viscosity. The vicinity of the trailing edge of an upstream element reduces the suction peak of a downstream element. Similarly, the leading edge of a downstream element induces lower pressure around the trailing edge of its upstream element. Both effects relieve the pressure rise in which the boundary layers are exposed, and therefore increase the margin of boundary-layer separation. It is, indeed, important to understand that the high-lift devices work primarily by means of manipulating the pressure field. There has been a lot of misunderstanding about how the slat influences the flow about the main element. It was long believed by many authors that a gap between a slat and a main wing functions by means of boundary-layer control, *i.e.* by imposing high-energy fluid into the retarded main-wing boundary layer. This misconception originates possibly from the work of Prandtl in the 1920s and 30s, and remained at least up to the early 1970s, if not even longer, see Smith [39]. For experimental and numerical studies of high-lift problems, see *e.g.* Refs. [40–45].

Fig. 3.1 shows that there are a number of turbulent flow details that are likely to have an important role in the whole problem. These are at least: boundary layers under adverse pressure gradient (APG), wakes under pressure gradient and curvature, merging wakes and possibly mergers of a boundary layer and a wake, mixing layer, and vortices. The importance of accurate modelling of the APG boundary layers is very well known, but also the importance of modelling the slat wake turbulence properly enough has been stressed by Rumsey *et al.* [46] and by Ying *et al.* [42]. It is thought that a successful numerical simulation of this complex flowfield can only be carried out if these individual flow features can be modelled with sufficient accuracy. Therefore, the focus in the turbulence model development in this study is largely put on the APG boundary layers, wakes, and also on mixing layers. The modelling of curvature-affected turbulence is dealt with as well. Some studies found in the literature concerning the above mentioned individual flow details are discussed in the next subsections.

It must be remembered that turbulence modelling is not the only source of error and uncertainty in high-lift flow situations. Transition locations are another important source of uncertainty. They should be known a priori, or estimated by some means, because the turbulence models cannot predict them reliably. The overall flow field is usually very sensitive to the transition locations. In CFD validation work the computed results are compared with experimental wind-tunnel data. The computations are typically made without simulating the wind-tunnel walls. Although wind-tunnel corrections are usually applied to the experimental data, there are still always uncertainties about the possible wall interference. These problems are, however, beyond the scope of this study. Only the turbulence modelling aspects are considered.

3.2 Boundary Layers under Adverse Pressure Gradients and Boundary-Layer Separation

3.2.1 Experimental Work and Suitable Test Cases

Sufficiently accurate modelling of turbulence in adverse pressure gradient (APG) boundary layers and separation is perhaps the most important requirement for the turbulence models employed in CFD analyses of high-lift problems. This is because separation of APG boundary layers on aerofoil upper surfaces often controls the maximum lift.

There are many experimental studies about APG boundary layers that can be exploited in assessment of turbulence modelling. These flow cases can be divided into equilibrium and non-equilibrium boundary layers. The latter class of flows may also involve separation. The former group of flows is especially suitable for basic development and initial validation of turbulence models, since equilibrium APG boundary layers at a limit of infinite Reynolds number can be considered as self-similar. Self-similarity is a very favourable feature, because the governing equations can be reduced to a system of ordinary differential equations, which allows easy and very fast numerical solution. By exploiting this, a large number of solutions can be computed within a short time frame. This is very important, especially in the model-calibration phase. Therefore, experimental studies about self-similar boundary layers will first be reviewed.

A loosely defined criterion for a boundary layer to be in equilibrium is that the nondimensional pressure-gradient parameter

$$\beta_T = \frac{\delta_1}{\tau_w}\frac{\mathrm{d}p}{\mathrm{d}x} \tag{3.1}$$

remains constant along the flow with sufficient accuracy. Here, τ_w is the wall shear-stress, and δ_1 is the displacement thickness of the boundary layer defined as

$$\delta_1 = \int_0^\delta \left(1 - \frac{U}{U_e}\right) \mathrm{d}y \tag{3.2}$$

where δ is the thickness of the boundary layer and U_e is the velocity on its outer edge. There are also stricter definitions for equilibrium boundary layers. In this study, however, it is believed that the self-similar equations approximate the flow with sufficient accuracy always if β_T can be kept constant.

The concept of self-similar boundary layers was first introduced by Clauser in the 1950s [47]. Clauser's experimental data will be used as one of the references also in this work, although its accuracy, especially in the sense of two-dimensionality [48], is perhaps not at the best possible level measured by modern standards. The first of Clauser's two experiments (designated as the FLOW-2200 in the 1968 AFOSR-IFP-Stanford Conference [48]) showed a region of nearly constant β_T varying between the values of 1.7 and 1.8. The boundary layer in Clauser's second experiment (FLOW-2300) includes two different regions with nearly constant β_T. The first one of these had $\beta_T \approx 5$, and the second one $\beta_T \approx 8$. The variation of β_T is somewhat more rapid than in the most of the more modern experiments. Despite this, there seems to be a common agreement that this flow can be considered as an equilibrium boundary layer. On the other hand, it is known that these flows are not purely two-dimensional, but it is not quite clear to the author how severe implications this fact may have on the quality of the data in this case. The highest β_T-case suffers from the three-dimensionality perhaps more than the other two, because the boundary-layer thickness achieved a value of about one half of the test-section width [48].

The proceedings of the 1968 AFOSR-IFP-Stanford Conference [48] includes also other useful sets of experimental data. One of them is a mild APG boundary layer of $\beta_T \approx 0.9$ by Bradshaw [49] (FLOW-2500). Bradshaw [49] contributed to the conference also another, stronger APG boundary layer with $\beta_T \approx 5$ (FLOW-2600). Unfortunately, the velocity profiles measured by Bradshaw and by Clauser disagree when $\beta_T \approx 5$. It is not known by the author whether this is owing to the mentioned three-dimensionality observed in Clauser's experiment. Owing to this uncertainty, the benefits of this case for calibration and validation remain modest. There is also a more recent experimental work on a strong APG equilibrium boundary layer by Skåre and Krogstad [50]. This flow has $\beta_T \approx 20$, and β_T remains constant with a better accuracy than is usually seen in the older work from the 1950s and 60s. This flow will be used for more detailed study and validation of the model developed in this study.

Non-equilibrium cases that are closer to real-life problems are of course needed for further validation. APG boundary layers that eventually separate from a smooth surface are suitable for this purpose. This is because the model's ability to predict separation location can be assessed. Perhaps the most often referred to non-equilibrium APG boundary-layer cases are the one by Samuel and Joubert [51], and the two cases by Driver [52]. Only one of these three cases, one case by Driver, involves separation. Therefore, this case will be used for validation of the model developed in this study.

Driver's flow features only a tiny recirculation region. Assessment for massive separation has to be undertaken with some other test case. Flow past a backward facing step is a common validation case for turbulence modelling, see *e.g.* Driver and Seegmiller [53]. It may be a less relevant problem to high-lift aerodynamics, however, because it involves a separation forced by the geometry, the step upper-corner, whereas in high-lift aerodynamics, the most influential separation typically takes place on a smooth surface owing to an action of adverse pressure gradient. On the other hand, also separations fixed by the geometry occur in the slat and flap coves. The step cases are perhaps more relevant to the problem of reattachment, which is not of such critical importance in high-lift aerodynamics as the problem of predicting the separation. In addition to the backward-facing step cases, a periodic flow past steep two-dimensional hill-shaped protuberances in a plane channel is worth mentioning. This configuration has been studied by means of a highly resolved large-eddy simulation by Mellen *et al.* [54], and by Temmerman and Leschziner [55]. Although this flow features separation from a smooth surface, the separation is still almost fixed by a fairly small local radius of curvature on the hill crest. This, among some other features of this flow, makes it less relevant to high-lift aerodynamics, although it is suitable for studying turbulence modelling in a separated recirculating flow. The planar asymmetric diffuser flow studied by Obi *et al.* [56] and by Buice and Eaton [57, 58] is perhaps a more suitable test case for this purpose. It features fully developed inflow from a plane channel, a ramp with an angle of ten degrees on one of its walls while the other wall is straight. The flow separates from the inclined wall and reattaches after a large region of recirculation. This flow has become quite a popular test case for turbulence models, although it has turned out to be a very challenging one. It is used in this study for testing the model in a massively separated flow.

3.2.2 Turbulence Modelling

It has been shown by several authors that most of the commonplace $k-\varepsilon$ models fail in predicting APG boundary layers and separation with sufficient accuracy for high-lift aerodynamics purposes [59–63]. Wilcox has shown that his $k-\omega$ model performs clearly better for APG boundary layers than the $k-\varepsilon$ models [60]. Moreover, the $k-\omega$ model can be solved down to the wall without any near-wall modifications. Menter showed later that Wilcox's model suffers from a severe anomaly which then became known as the free-stream sensitivity [64] — the solutions are highly sensitive to the specified free-stream boundary conditions for k and ω. Menter developed a zonal $k-\omega$ BSL model that inherited the favourable features of Wilcox's model but not the free-stream sensitivity [3, 65]. He then showed that the ability to correctly model APG boundary layers and separation largely depends on the constitutive model, and that the traditional linear Boussinesq model is not sufficient for this purpose. He then developed an extension of the Boussinesq model that prevents the shear-stress anisotropy from exceeding a certain limit. The resulting model is known as the $k - \omega$ SST model, and it quite soon became the state-of-the-art turbulence model in aerodynamics applications. The SST model is not a nonlinear model in the tensorial sense, *i.e.* it relies on a tensorially linear relation between the Reynolds stress and the strain-rate tensors. However, the coefficient of this relationship, C_μ, depends on a mean-strain (or vorticity) invariant. The correct sensitivity of C_μ upon the strain rate is more important in APG boundary layers and in separating flows than the tensorially nonlinear terms of the constitutive model. This has been confirmed by Apsley and Leschziner [66]. The higher-order terms are more important in predicting the normal-stress anisotropy (quadratic terms) and the effects of the mean-flow curvature, swirl, or other secondary-strain effects (cubic terms).

The role of the constitutive model and the scale-determining model in separating APG flows has been studied recently, *e.g.* by Rumsey and Gatski [62] and by Hellsten and Laine [63]. It has become quite clear that both parts of the model are critical in modelling turbulence of APG flows. Choosing a proper scale-determining model is especially important near the wall and in predicting the wall shear-stress in near-equilibrium conditions, while the constitutive model is critical, regardless of the chosen scale-determining model, in capturing non-equilibrium effects usually imposed by relatively rapid streamwise changes. Considering the scale-determining model in the light of the previous studies and validation efforts, it seems that the most straightforward way to achieve the goals of this work is to start from the $k - \omega$ framework and to recalibrate all the model coefficients in a systematic fashion. A more thorough and elaborate alternative would be to try to find a new scale variable, and to develop and calibrate a model equation for it. This route has been recently chosen by Bézard [67]. He developed a new $k - kl$ model for high-lift flows to be used with an EARSM as the constitutive model (l is a turbulent length scale). Bézard's work is a parallel effort with the present work within the HiAer project.

Some authors have developed linear and nonlinear $k - \varepsilon$ models that, comparably with the $k - \omega$ models, are able to predict APG boundary layers with better accuracy than the usual $k - \varepsilon$ models. This is usually achieved by adding a new term in the ε-equation. Yap [68] was probably the first to do so, and therefore these extra terms are often called Yap-terms or Yap-like terms. Yap introduced a term which tends to drive the turbulent length-scale towards its equilibrium value near the wall in APG boundary layers. The more recent proposals include cross-diffusion terms that have a similar influence as the Yap-term, see *e.g.* Rahman [69] and Merci [70]. Such a cross-diffusion term can be derived, *e.g.* by transforming Wilcox's $k - \omega$ model into the $k - \varepsilon$ form. As an example from the differential Reynolds stress modelling level, the work by Hanjalić and Jakirlić [71] and by Hanjalić *et al.* [72] should be mentioned. They attempted to avoid excessive near-wall length scales by incorporating a term that depends on the length-scale gradient in the ε-equation of their low-Reynolds-number Reynolds stress model.

Lien and Leschziner have compared a full differential Reynolds stress model, a nonlinear quadratic eddy-viscosity model, and a linear eddy-viscosity $k - \varepsilon$ model in a high-lift aerofoil case [73]. They found that none of the studied models performed well in respect of resolving separation, although the higher-order models performed better than the linear eddy-viscosity model. All the models predicted too high shear-stress values near the wall. Lien and Leschziner pointed out that this is owing to an overestimated near-wall anisotropy. Therefore, they dropped the wall term from the rapid part of the redistribution model to reduce the near-wall anisotropy level. As a result, they obtained a slight improvement in accuracy. Hanjalić *et al.* [72] have also studied the full differential Reynolds stress modelling in APG situations. As Lien and Leschziner, they concluded that it is important to model accurately the near-wall behaviour of each stress component, because the mean pressure-gradient partially influences the turbulence through the near-wall anisotropy. This requirement unavoidably leads to rather complex modelling approaches. Such approaches are not chosen for this work in order to avoid an impractically complicated model with reduced robustness. It is believed by the author that a reasonably good sensitivity to the pressure-gradient effects can be achieved by means of simpler modelling, which does not necessarily provide correct near-wall anisotropies. This belief is based on the experience with the $k-\omega$ models in APG flows. Near-wall modifications that lead to a fairly accurate near-wall anisotropy prediction were found to have only a negligibly small effect on the mean-velocity field [63, 66, 74].

Massively separated flows involve a mixing layer between the retarded recirculating fluid and the high-momentum fluid adjacent to it. This shear layer may feature coherent periodic oscillations. Experience has shown that the RANS turbulence models have serious difficulties in modelling the effects of this kind of motion [66]. This usually leads to a delayed reattachment, since the strong mixing effect of these oscillations may have been missed in the modelling. Furthermore, the computational results of massively separated flows often tend to remain time-dependent — perhaps another indication that turbulence models are not capable of modelling all the mixing of momentum needed to satisfy the momentum equation. Massively separated flows remain a big challenge for RANS turbulence modelling, while LES is in principle a very potential means of simulating them, but only in case of small Reynolds numbers to date. LES is far beyond being useful in high-lift aerodynamics, and thus the above discussed shortcoming of the present-day RANS modelling largely limits the accuracy and reliability of CFD in high-lift aerodynamics. Recently proposed hybrid RANS/LES concepts, such as detached eddy simulation (DES) [75, 76] have shown some potential to predict aerodynamic flows involving massive separation. However, the hybrid RANS/LES approaches are based more on intuition than rigorous physical and mathematical analysis. Fortunately, the prediction of the onset of separation is usually more critical in high-lift aerodynamics than the accurate simulation of massive separation. Therefore, the focus of this study is chiefly on the former phenomenon.

3.3 Wakes

3.3.1 Experimental Work and Suitable Test Cases

Just as the boundary layers can be broadly divided into the equilibrium and non-equilibrium ones, the plane wakes can be classified as fully developed far wakes and developing wakes. This classification is, of course, somewhat impractical being valid mainly for laboratory flows, since the wakes in real-life engineering problems are usually at least mildly three-dimensional and other phenomena, such as vortices, may be embedded in the wakes. In developing, calibrating, and validating turbulence models, however, simple planar wakes are useful as test cases. Wakes achieve an approximately self-similar state only quite far away from the wake-generating body. Again, the self-similar cases are very useful for the calibration and initial validation purposes. Developing wakes can then be used for further validation.

A self-similar planar far-wake has been studied already as early as in the 1930s by Fage and Falkner [77], and there are a number of studies carried out after those times. In most of the studies, the wake was generated using a circular cylinder perpendicular to the flow. Townsend pointed out in the late 1940s that the flow requires more than one thousand cylinder diameters to develop before the stress distributions become approximately self-similar, while the mean-velocity profile approximately reaches its self-similar form much closer to the cylinder, about one hundred diameters behind it [78]. In Townsend's first experiments [78], x/D ranged from 90 to 725, where D is the cylinder diameter. Later, he extended his measurements up to $x/D = 950$ [79], and this work resulted in a slightly different conclusion that the requirements for dynamical similarity are very nearly satisfied when $x/D > 500$. In light of Townsend's work, it is clear that the measurements have to be undertaken at least one hundred diameters downstream if not further away. This requirement invalidates the experiment by Fage and Falkner dating back to 1932, since they performed the measurements in a position with $x/D = 36$ only. Planar wakes behind circular cylinders have been studied later at least by Thomas 1973 [80], Fabris1979 [81], and by Antonia and Browne 1986 [82,83]. Thomas made his measurements at $x/D = 160$, Fabris used larger distances, $x/D = 200$ and 400, and Antonia and Browne had 420. The values $x/D = 160$ and 200 are quite low, but these can probably be kept as sufficient distances when the focus is on the mean-velocity profiles. The Reynolds stresses that will be used for comparison are measured at $x/D = 400$ (Fabris), and at $x/D = 420$ (Antonia and Browne). Also, the shear-stress distribution measured by Townsend beyond $x/D = 500$ will be used as a reference. In addition to the wakes generated by cylinders, one wake of a flat plate will be taken as a reference. This is from the work of Weygandt and Mehta [84]. Unfortunately, they did not report the mean-velocity profile in [84]. Instead, the data is taken from [28] readily in the similarity scaling. In this case, the wake seems to be slightly asymmetric for some reason. In principle, the far wake does not depend on the geometry of the object that created it, although the near wake strongly depends on it. The popularity of the circular cylinder as a wake generator is probably owing to the fact that wakes of blunt bodies reach self-similarity after a shorter distance of development than those of streamlined bodies.

Whereas the self-similar far wake is useful in the basic development, calibration, and initial validation of turbulence models, developing wakes are more practical cases for further validation. Ramaprian *et al.* have measured a wake behind a flat plate, but only up to $x/\delta_2 = 80$ [85]. Here δ_2 is the momentum thickness of the wake defined as

$$\delta_2 = \int_{-\delta/2}^{\delta/2} \frac{U}{U_e} \left(1 - \frac{U}{U_e}\right) \mathrm{d}y \tag{3.3}$$

They found that $x/\delta_2 = 80$ is far too small a value to reach the self-similar state. This became evident when they analysed the data by Pot [86] that became available just after their own experiments. Pot's measurements extended up to $x/\delta_2 = 960$. Before Pot's work, it was thought that a wake would reach the fully developed self-similar state after a distance of only about $x/\delta_2 = 25$. Owing to Pot's data, Ramaprian *et al.* came to the conclusion that self-similarity is reached only at about $x/\delta_2 = 350$, which is drastically further downstream than what was believed before. They pointed out that the wake has an intermediate phase $25 < x/\delta_2 < 350$, where the mean-velocity profile may be approximately self-similar, but the spreading rate differs from its final asymptotic value and depends on the details of the wake origin. Also, the ratio between the turbulent and mean kinetic energies has not yet become constant. Taking these observations into account, it seems reasonable to compute the wake of a flat plate at least somewhat past the location of $x/\delta_2 = 350$ and to compare the results with Pot's data. This will be done in Section 7.2.

The effects of curvature and pressure gradient on wakes have been experimentally studied at least by Nakayama [87] and by Ramjee *et al.* [88]. Nakayama studied the effect of weak curvature and pressure gradient on a fully developed plane wake. He found that even weak curvature and pressure gradient have significant effects on turbulence, especially on the shear stress, while the effect on the mean velocity remains small. Ramjee *et al.* [88] studied a wake of a symmetric aerofoil in a curved duct. This experiment is closer to the practical situation of the slat wake travelling above the curved upper surface of a main wing. Ramjee *et al.* studied two cases with different radii of curvature. In both cases, the radius scaled by the width of the wake is smaller than in Nakayama's experiment, and thus stronger curvature effects can be expected. Ramjee *et al.* had $R/\delta \approx 9$ and 18, while the minimum value of R/δ in Nakayama's experiments was 25. Unlike Nakayama, Ramjee *et al.* made no effort to separate the effects of curvature and pressure gradient. Ramjee *et al.* observed that the curved wake is significantly asymmetric, the inner side being thicker than the outer. The inner side is that one which is closer to the centre of curvature. This is consistent with the fact that the effect of curvature is to destabilize turbulence on the inner side and to stabilize on the outer side.

Liu *et al.* [89] have measured wake flows under zero, mild favourable, and adverse pressure gradient. Wakes exposed into sufficiently strong positive pressure gradient may show an increasing velocity defect relative to the surrounding fluid. This may ultimately lead to a flow reversal. Sometimes, the flow reversal in the slat wake may even initiate the stall of a multi-component aerofoil (off-surface separation). According to Smith [39], this is a relatively rare situation since the boundary layers are usually more prone to separate than wakes exposed to the same pressure field. Therefore, the boundary-layer separation is often responsible for the stall initiation. The flow reversal in wakes has, however, recently gained the attention of Driver and Mateer [90]. They studied wakes under three different adverse pressure gradients both experimentally and computationally. Two of these three cases involved flow reversal. The work by Driver and Mateer seems to form a good test case for turbulence modelling. The use of this case is not, however, included in this study, but it will very likely be exploited in future work.

3.3.2 Turbulence Modelling

Wilcox [28] compared the far-wake velocity profiles computed with his $k{-}\omega$ model, with the standard $k-\varepsilon$ model, and with the RNG $k-\varepsilon$ model [91, 92] to the experimental data by Fage and Falkner [77] and by Weygandt and Mehta [84]. Both the $k-\varepsilon$ models showed too slow a spreading rate and a very sharp outer edge. The $k-\omega$ results were in much better agreement with the experimental data. However, as will be discussed later in this work, the results obtained with this $k-\omega$ model are highly sensitive to the free-stream values of k and ω, and therefore much worse results can be obtained if slightly different free-stream values are chosen. Also, Menter shows that the standard $k-\varepsilon$ model predicts inhibited spreading and unphysically sharp edge for this flow [3]. Menter's $k-\omega$ models share this shortcoming — this is quite obvious since Menter's models are designed to behave like the standard $k-\varepsilon$ model in free turbulent flows in order to eliminate the free-stream sensitivity.

The curvature effects on wakes seem not to be much different from those on boundary layers. This is not very surprising since curvature mainly influences the outer part of boundary layers, which is often said to have a lot of similarities with wakes. Turbulence modelling for curvature-affected flows is quite deeply discussed in Section 5.2. The modelling technique is studied and validated for a boundary layer, for a flow in a U-duct with a small radius of curvature, and for a swirling flow in a combustion chamber, see Ref. [93]. The validation for curved wakes is not covered in this study because of the mentioned similarities of boundary layers and wakes.

Carlson *et al.* have computed plane wakes in zero, mild favourable, and mild adverse pressure gradients employing a linear EVM and an EARSM both based on a $k-\varepsilon$ model [94]. Both models predicted all the three wake flows in reasonably good agreement with the experimental data measured by Liu *et al.* [89]. According to this study, the higher-order constitutive modelling (EARSM) does not contribute to the accuracy in this case. This is quite reasonable, since the pressure gradients were rather mild and there are no curvature or other complicating secondary strains present. The practical problem of the slat wake exposed to strong and variable pressure gradient and curvature is more challenging, and the benefits of more advanced constitutive modelling probably become more important. Driver and Mateer computed wakes in heavily decelerated flows described above using the Spalart-Allmaras one-equation model and Menter's $k-\omega$ SST model [90]. They observed that these models failed to capture the flow reversal.

3.4 Interaction of Wakes and Boundary Layers

The slat wake runs in the close vicinity of the main-wing upper surface and its boundary layer such that these two turbulent layers may interact with each other and merge eventually. This is a consequence of the optimal slat positioning — the slat must be placed sufficiently near the main-wing leading edge to allow efficient interaction of the pressure fields of these two elements. On the other hand, excessively close slat setting leads to an early merger of the slat wake and the main-wing boundary layer. This would limit the maximum lift, because the merged layer is very thick and prone to separation. Naturally, the optimal flap setting is determined in a similar fashion as well. Roughly speaking, the two above described factors are the most important aerodynamic mechanisms contributing to the slat and flap positioning. The interaction and merging process is very sensitive to the details of the upstream wake and boundary layer. Thus, it is very important to predict them accurately, as pointed out by Rumsey *et al.* [46] and by Ying *et al.* [42].

The interaction of wakes and boundary layers is a rather complicated process. Squire [95] provides a comprehensive review on this subject. Squire [95] and Ying *et al.* [42] divide the interaction process into three phases: unmerged, merging, and fully merged phases. In the example shown in Fig. 3.1, the slat wake and the main-wing boundary layer are unmerged over a major portion of the main wing. The second phase begins only near the main-wing trailing edge.

In the first phase, there is a potential core between the layers. In spite of this core, the layers interact already in this phase. Savill and Zhou [96] have made a comprehensive study about the interaction process in the unmerged phase. This process depends on the wake structure. The near wakes of blunt bodies, such as circular cylinder, are characterized by organized large-scale structures, while the structures in the near wakes of aerofoils and other streamlined bodies as well as in all far wakes are much less organized. In the former case, rapid interaction takes place, while the interactions in the latter cases are slow according to Savill and Zhou. In high-lift problems, the interaction between the slat wake and the main-wing boundary layer is likely to appear more like the slow process. Savill and Zhou detected three different slow interaction mechanisms. The first is the interchange of so-called mushroom vortices. Vortices are occasionally drawn out from one layer into another. These vortices retain their structure and identity to some extent in the new environment. This way they change the turbulent structure of both layers. The second mechanism is that structures larger than the mushroom vortices develop from the outer boundary layer towards the wake inner edge and the edges may instantaneously meet each other. This happens less frequently than the interchange of the mushroom vortices. These two mechanisms share a common feature in that they function via instantaneous bridging of the irrotational potential core. As for the third mechanism, the pressure fluctuations induced by the large-scale motion in the wake may interfere with the boundary layer (interaction by the irrotational field).

The second phase corresponds to the initial merger of the layers. This phase is the most important and the most complicated according to Squire [95]. Although the outer wake and the inner boundary layer may remain almost unaffected, the overlap region differs strongly from the outer edge of an isolated boundary layer and from the inner edge of an isolated wake. Active interchange of turbulent structures between the wake-side and the boundary-layer side takes place. There may be a shift between the zero-points of the shear stress and strain, or in other words, counter-gradient transport of momentum. The eddy-viscosity models, even the nonlinear ones including EARSMs, cannot capture this. In principle, only full differential Reynolds stress models are capable of predicting such phenomena. The modelling strategy selected in this study is not, however, replaced by the differential Reynolds stress modelling, although the ARSM approach is in principle inappropriate for this flow feature. This shortcoming just has to be accepted, because the differential Reynolds stress modelling was initially defined to be out of the scope of this study as a too large development step for turbulence modelling to be utilized in the practical high-lift aerodynamics work within a short time-span. It must be remembered that this study aims at new modelling tools that can be implemented in industrial use within a very short time frame. Squire [95] and Agoropoulos and Squire [97] reviewed the ability of the $k-\varepsilon$, ARSMs, and even differential RSMs to predict the merging flow. The conclusion was that, for simulations of two-dimensional isolated merging-flow experiments, it is sufficient to use some kind of an algebraic Reynolds stress model, although these models cannot model the counter-gradient transport.

In the final phase of interaction, the layers are fully merged and form a new thicker boundary layer. The turbulence structure in such a new boundary layer differs from that of ordinary boundary layers developed alone. The shear-stress levels in the outer region are much lower than in ordinary boundary layers, see Squire [95]. This phase takes a long distance to develop. In practical high-lift problems, the layers usually pass the trailing edge well before the full merger is reached. Therefore, this final phase is of less interest in high-lift aerodynamics than the first two phases.

Several factors, such as pressure gradient, curvature, upstream conditions, and three-dimensionality may influence the interaction and the merging process. Squire points out that adverse pressure gradient accelerates the merger process via enhanced turbulent mixing [95]. Also the upstream history influences the interaction and the merging process. The slat wake tends to be significantly asymmetric, its inner side being thicker and more turbulent. This asymmetry accelerates the merging process. According to Squire, this is owing to the slat-cove separation and vortex. Also the curvature of the wake may influence the wake asymmetry. The EARSM technique for curved flows discussed in Section 5.2 may be beneficial here. Besides its ability to better capture the curvature effects on the wake, it has been observed to predict a higher turbulence level for the slat-cove vortex than the standard EARSM technique (unpublished work by the author).

Systematic turbulence model validation for this interaction problem has to be left for future work. The three-element aerofoil problem, which is used as a feasibility test in Section 7.5.4, will give a qualitative picture about the predictive realism of the new model for this problem. The velocity profiles through the boundary-layer/wake system are studied at four locations, giving some insight on the models' ability to predict the merging.

3.5 Mixing Layers

3.5.1 Experimental Work and Suitable Test Cases

Mixing-layer-like situations appear in high-lift aerodynamics in separated flows between the retarded recirculating flow and the high-speed fluid adjacent to it. Therefore, separated flows can be partially idealized using the simple planar self-similar mixing layer. A mixing-layer-like situation also occurs above the flap system, where irrotational high-energy fluid is injected from the flap slot alongside the very thick layer of retarded fluid formed by the merging wakes of the main wing and the slat, see Fig. 3.1. For these reasons, the planar self-similar mixing layer is selected as one of the elementary flows used in the model development and calibration.

Mixing layers differ from wakes most significantly owing to the fact that energy is constantly fed from the mean flow to the turbulent motion in mixing layers, while this energy transfer decays in wakes with the distance as the velocity difference decays. The fact that turbulence gets less and less energetic as the wake evolves downstream explains the observations that wakes "remember" the upstream disturbances over significantly longer distances and it takes a much longer distance for a wake to reach the self-similar state than mixing layers [84]. Mixing layers also differ from simple wakes owing to their apparent antisymmetry. Actually, spatially evolving mixing layers are always asymmetric — not antisymmetric but genuinely asymmetric. The low-speed side spreads more rapidly than the high-speed side [98]. Owing to at least these differences, it is difficult to model both wakes and mixing layers accurately with exactly the same model. It even seems to be difficult to predict both sides of a mixing layer accurately with the same model. Indeed, one kind of free shear flow is difficult to model correctly with a model calibrated for some other kind of free shear flow.

Free turbulent shear flows are strongly governed and characterized by coherent large-scale structures. These structures depend on the flow geometry and type. For instance, axisymmetric and planar wakes obviously feature very different large-scale structures. The well-known plane/round jet anomaly of turbulence models is one consequence of completely different dominant structures in those two elementary flows. The large-scale structures and intermittency are also closely related matters. Turbulence is said to be intermittent near the edges of shear layers because irrotational fluid is entrained between subsequent large structures. Intermittency is not directly accounted for in RANS turbulence modelling, since fully turbulent flow is assumed already in the derivation of the RANS equations. Turbulence models can be and are of course calibrated to take into account the effects of intermittency in one or more elementary flows for which it is calibrated. It is, however, difficult to calibrate a model for more than one sort of intermittent behaviour, and different patterns of large-scale motion in each flow mean also different intermittency. This is clearly seen also in this study. The planar mixing layers are strongly governed by highly organized coherent structures known as Brown-Roshko rollers and braids or ribs, see [8]. These very organized structures are nearly two-dimensional and similar structures exist also at very low Reynolds numbers similarly as the well known von Kármán vortices in flows behind cylinders. One could perhaps argue that such motion should be classified as unsteady mean flow instead of turbulent motion. One indication of the difficulties of turbulence models to capture this organized motion as part of the turbulence is that two-dimensional simulations are prone to turn time-dependent. A converged steady-state solution is very difficult to obtain. Exploitation of the self-similarity allows a one-dimensional solution in which such problems are obviously avoided. It was already mentioned earlier that similar difficulties often arise in simulations of massively separated flows.

In this study, only such a mixing layer is studied where the fluid is at rest on one of its sides. The similarity coordinate is simply $\eta = y/(x - x_0)$. There is an extensive work by Liepmann and Laufer dating back to 1947 [99]. Later, Wygnanski and Fiedler measured this flow, and their results are also used as reference data in this study [98]. Castro and Bradshaw studied a stably curved mixing layer but they also provide a velocity profile of a straight mixing layer in a form of a curve fitted to the measured data points [100]. The spreading rates measured by Liepmann and Laufer and by Wygnanski and Fiedler differ from each other to some extent. Wygnanski and Fiedler refer to some differences in the experimental setup, but the reason for this difference remains essentially unclear. This difference partially weakens the value of this case in the model development and calibration. However, it gives at least a qualitative reference. Wygnanski and Fiedler suggested two possible reasons. First, unlike Liepmann and Laufer, they used a trip wire in the nozzle to make the flow turbulent, while Liepmann and Laufer had an initially laminar mixing layer which turned turbulent at about 6 cm from the nozzle, and the measurements were taken from $x = 30 \ldots 90$ cm. It was attempted by the author to rescale the data using different values of x_0, but it turned out that values close to zero make the profiles to best collapse on each other. Thus, the uncertainty of x_0 is not the reason for the different spreading rate. Moreover, when a mixing layer has reached the fully developed self-similar state, it should not depend on the upstream conditions any more. Hence, it seems unlikely that the tripping is responsible for the different spreading rates. Another possible reason suggested by Wygnanski and Fiedler is the solid wall they had in the plane $x = 0$, while Liepmann and Laufer had no such plate. There might have also been some other differences in the experimental setup. For instance, the relative distance of the wall that confines the flow above the layer is not reported and it may influence the spreading rate especially if the wall is placed too close to the layer. Nevertheless, the results by Liepmann and Laufer and by Castro and Bradshaw support each other. Unfortunately, Castro and Bradshaw do not provide turbulent stresses for the straight mixing layer case. Moreover, extracting the stress data from the report by Liepmann and Laufer is difficult because some of the parameters needed for rescaling are not explicitly given. Their shear-stress data is included in Fig. 6.12, but it must be kept in mind that it might be inaccurate, since the scaling factors are approximated by comparing velocity profiles plotted over differently scaled y-coordinates found in their report [99].

3.5.2 Turbulence Modelling

Wilcox [28] compared the mixing layer velocity profiles computed with his $k-\omega$ model, with the standard $k-\varepsilon$ model, and with the RNG $k-\varepsilon$ model [91,92] to the experimental data by Liepmann and Laufer. As for the far-wake flow, both the $k-\varepsilon$ models showed too sharp edges on both sides of the layer. The $k-\omega$ result featured smooth edges, but it must be again stressed that this result is highly dependent on the free-stream values, and that some other choices of the free-stream values can lead to sharp-edged solutions. Excessive asymmetry is a common feature of all the numerical solutions shown by Wilcox as well as the solutions shown in Section 6.4.2 of this study. Moreover, this fault seems to be common to most standard turbulence models as it was detected already in the early days of Reynolds stress modelling [10, 11].

The excessive asymmetry of the computed results deserves some more attention. It is the mean-velocity convection that initially drives the turbulent-energy distribution towards the low-speed side. The convection terms are obviously larger on the high-speed side. However, there must be some balancing effect since the measurements indicate only very slight asymmetry. This balancing effect is not adequately modelled in the present turbulence models since they provide excessively asymmetric results. Wygnanski and Fiedler [98] provide a comparison of each term in the equation of k based on the their measurements. This data was investigated by the author, and it was observed that the pressure diffusion term

$$-\frac{\partial}{\partial x_j}(\overline{p'u'_j}) \tag{3.4}$$

might possibly be such a balancing term. Indeed, modelling of this term has been omitted completely, since there seems to be an almost common agreement that the pressure diffusion term is usually negligibly small, or that it can be absorbed into the model of the turbulent transport. These assumptions seem not to hold for the mixing layer according to Wygnanski and Fiedler. DNS data about a time-evolving mixing layer by Rogers and Moser reveal that the pressure diffusion is indeed not negligibly small [101]. The time-evolving mixing layer, however, differs from the present flow as it is antisymmetric about the midplane. Thus the DNS-data does not reveal if the pressure diffusion really is responsible for balancing the distorting influence of the mean-velocity convection.

There have been some attempts to model the pressure diffusion term [102–104]. Lumley [102] assumed that the pressure-velocity correlation $-\overline{p'u'_j}$ has a linear dependence on the triple velocity correlation $-\overline{u'_k u'_k u'_j}$ of the turbulent transport term, and thus his model essentially is merely a reduction of the model coefficient of the turbulent transport model by 20%. This model simply represents counter-gradient diffusion, and thus it does not transport turbulent energy from the low-speed side to the high-speed side. Kim and Chung [103] constructed a model in which the pressure-velocity correlation is split to a slow and rapid part just as the inter-component redistributive pressure-strain term is traditionally split. Also Demuren *et al.* split this term in a similar fashion [104]. The slow term is mainly counter-gradient diffusion and is modelled as a part of the turbulent flux model following Lumley's approach. The rapid term represents gradient diffusion and possibly other types of transport. If the latter is true, this term might have an opposing effect on the mean-velocity convection in the spatially evolving mixing layers. At least, Kim and Chung achieved some improvements in predicting the mixing layer and also other free shear-flows by using their approach that also involves a model for the rapid term [105]. Unfortunately, the asymmetry-balancing role of the pressure diffusion cannot be verified reliably since there are no DNS studies about spatially evolving planar mixing layers to the author's knowledge.

The above-mentioned improvements achieved by Kim and Chung [105] in predicting free shear-flows were, however, not purely owing to the pressure diffusion model. They also incorporated a model for the intermittency consisting of a generic transport equation for the intermittency factor γ. In fact, the asymmetrically distributed intermittency could be another possible reason for the excessive asymmetry of the computed results. Judging from the mixing-layer results by Kim and Chung [105], the intermittency modelling actually seems to be a more important factor than the pressure-diffusion modelling in this case. Such an additional complexity in modelling is not desirable from the viewpoint of the present work, and thus no attempts are made within this study to remedy the predicted excessive asymmetry in mixing layers. After all, the boundary layers and wakes are more important elementary flows to high-lift aerodynamics than the mixing layers.

3.6 Vortices

Trailing vortices are always present in flowfields around real three-dimensional lifting wings or any other lifting bodies. In two-dimensional idealized problems, there are obviously no trailing vortices present, but as seen in Fig. 3.1, vortices can well occur in two-dimensional flow fields owing to flow separation. The slat- and flap-cove vortices may be quite energetic and also quite influential on the downstream wake development.

Turbulence in vortices is usually strongly affected by the streamline curvature. Wallin and Girimaji have studied algebraic Reynolds stress modelling in an isolated vortex [106]. They found it is essential that the weak-equilibrium assumption to derive the algebraic stress model is invoked in a proper stream-following coordinate system. In that particular case, this means cylindrical coordinates. In more general flows, the curvature method for ARSM is needed. This is discussed in Section 5.2.

4 Numerical Methods

4.1 Self-Similar Flow Problems

4.1.1 Overall Description of the Solution Method

The calibration process of a turbulence model may require a large number of computations with different values for the model coefficients in different flows. This would mean a very elaborate and time consuming effort if all calibration computations are performed using a full Navier-Stokes solver. Fortunately, many simple flow situations may be idealized as one-dimensional self-similar approximations. In this study, plane channel flows, equilibrium boundary layers (less the viscous layer), planar far wake and mixing layer are studied.

A specific solver for self-similar turbulent flow problems was designed and set up to be employed in the model calibration process. The solver was designed in a generalizable and modular fashion. This means that the core of the solver is independent of the boundary conditions, integral constraints, and other flow-specific information. All flow-specific features are programmed in separate modules. The flow-specific modules are connected to the solver core using an interface module. When a new problem is to be set up, only a new flow-specific module must be programmed and installed into the interface. No changes are needed in the solver core. Also the details of turbulence modelling are isolated in a particular module outside the core. The modular structure turned out to be a good and flexible strategy. Furthermore, it reduces the amount of code verification and debugging when new cases are being set up. The code is written using the Fortran-90 programming language.

The system of equations consists of three ordinary differential equations in the present flow cases. These are the momentum equation, and the turbulence model equations for the turbulence kinetic energy k and the second scale variable ϕ. The second-scale equation is written in a generalized form where the second scale variable is expressed as $\phi \sim k^m \varepsilon^n$, see Appendix A. The system of equations may be expressed in the following general form

$$\frac{\mathrm{d}}{\mathrm{d}\eta}\left[\mathcal{V}\mathcal{X}_i - \sum_{j=1}^{p}(\delta_{ij}\nu + \sigma_{\mathcal{X}_i\mathcal{X}_j}\mathcal{N}_T)\frac{\mathcal{X}_i}{\mathcal{X}_j}\frac{\mathrm{d}\mathcal{X}_j}{\mathrm{d}\eta}\right] = Q_i + A_{\mathcal{X}_i}\mathcal{X}_i \tag{4.1}$$

where $i = 1 \dots p$ with p denoting the number of equations. The summation rule of repeated indices is not applied here over indices that appear as subscripts of another subscript, such as i in $\sigma_{\mathcal{X}_i}$. In the present cases, $p = 3$, and $\mathcal{X}^T = (\mathcal{U}, \mathcal{K}, \Phi)$. Here,

$\mathcal{U}$ is the nondimensional velocity variable, and $\mathcal{K}$ and Φ are the nondimensional turbulent scale variables. $\mathcal{N}_T$ is the nondimensional eddy viscosity, η is the nondimensional similarity coordinate, and $\mathcal{V}$ is the transverse convective velocity. The diffusive terms are here written in a generalized form involving also gradients of variables other than $\mathcal{X}_i$. The diffusivities $\sigma_{\mathcal{X}_i\mathcal{X}_j}$ associated with such gradient terms are usually zero, but the generalized second-scale equation includes a term proportional to the gradient of k, see Appendix A. This is why the diffusive term is here expressed as a general sum of gradient diffusions of all variables. The source term consists of two parts

$$\mathcal{Q}_i = Q_i + A_{\mathcal{X}_i}\mathcal{X}_i \tag{4.2}$$

where the former is the original source term of the equations expressed in the Cartesian coordinate system, and the latter appears as a result of the similarity transformation and it originates from the convective term. The coefficients $A_{\mathcal{X}_i}$ depend on the flow case. The details of the terms and factors of (4.1) and the boundary conditions as well as the integral constraints for each flow case are described in the next subsections.

The solver is based on the finite-difference method and implicit pseudo-time integration. Artificial time derivatives are added to the left-hand sides of the equations (4.1) in order to facilitate the pseudo-time integration. The diffusive terms are discretized using the standard central-differencing scheme. A second-order upwind scheme is used for the convective term in cases where it is nonzero. The upwind scheme was chosen to introduce some numerical dissipation that is necessary especially with such turbulence models which tend to predict sharp edges for turbulent layers, see Sections 6.2.4 and 6.3. The pseudo-time integration is formulated in the Δ-form similarly to the FINFLO solver [107, 108]. In the implicit phase, the convective term is discretized using the first-order upwind scheme. The source terms are integrated using either explicit or implicit Euler scheme depending on their sign. Negative terms are integrated implicitly. This is facilitated by means of approximating the source terms at the new pseudo-time level of $n+1$ using the following linearization

$$\mathcal{Q}_i^{(n+1)} \approx \mathcal{Q}_i^{(n)} + \left(\frac{\partial \mathcal{Q}_i}{\partial \mathcal{X}_j}\right)^{(n)} \Delta\mathcal{X}_j \tag{4.3}$$

where $\Delta\mathcal{X}_j$ is the quantity to be solved at each pseudo-time step, *i.e.* the change of the variable $\mathcal{X}_j$ over the pseudo-time step. Only the diagonal terms of the Jacobian $\partial\mathcal{Q}_i/\partial\mathcal{X}_j$ are kept in order to simplify the implicit method. A similar approximation is made also in the FINFLO solver. As the stability of the implicit Euler method is quite limited in case of positive source terms, they are integrated explicitly.

4.1.2 Plane Channel Flow

Fully developed Poiseuille flow between two parallel flat plates, *i.e.* the plane channel flow is one of the simplest turbulent flow problems. The fully developed flow can readily be described as a function of only the wall-normal coordinate y. Only one mean-velocity component is nonzero and there is no convection by the mean velocity.

The variables can be scaled either by the bulk velocity

$$U_b = \frac{1}{H} \int_0^H U(y) \mathrm{d}y \tag{4.4}$$

or by the friction velocity $u_\tau = \sqrt{\tau_w/\rho}$, where τ_w is the wall shear stress. The former scaling is relevant when the mass-flow rate is known and the latter one when the pressure gradient is known. In this case, the bulk velocity U_b is used as the velocity scale and the channel height H is the length scale, thus $\eta = y/H$ and $\mathcal{U} = U/U_b$. The turbulent variables are nondimensionalized as $\mathcal{K} = k/U_b^2$ and $\Phi = \phi H^n/(U_b^{2m+3n})$, where the latter is derived from the scaling of k and ε, which is $\mathcal{E} = \varepsilon H/U_b^3$. The eddy viscosity is, in this case, scaled as $\mathcal{N} = \nu_T/\nu$. The convection-related factors $\mathcal{V} = A_i = 0$ since the convective terms are zero. The viscous diffusion term is kept in this case since the flow is solved down to the wall through the viscous sublayer. The Reynolds number is defined by $Re = U_b H/\nu$. The system of equations reduces to

$$\frac{1}{Re} \frac{\mathrm{d}}{\mathrm{d}\eta} \left[(1 + \mathcal{N}_T) \frac{\mathrm{d}\mathcal{U}}{\mathrm{d}\eta} \right] = Q_1 \tag{4.5}$$

$$\frac{1}{Re} \frac{\mathrm{d}}{\mathrm{d}\eta} \left[(1 + \sigma_k \mathcal{N}_T) \frac{\mathrm{d}\mathcal{K}}{\mathrm{d}\eta} \right] = Q_2 \tag{4.6}$$

$$\frac{1}{Re} \frac{\mathrm{d}}{\mathrm{d}\eta} \left[(1 + \sigma_{\phi\phi} \mathcal{N}_T) \frac{\mathrm{d}\Phi}{\mathrm{d}\eta} + \sigma_{\phi k} \mathcal{N}_T \frac{\Phi}{\mathcal{K}} \frac{\mathrm{d}\mathcal{K}}{\mathrm{d}\eta} \right] = Q_3 \tag{4.7}$$

The streamwise mean-pressure gradient is the source term of the momentum equation, $Q_1 = -\mathrm{d}p/\mathrm{d}x$. The pressure gradient is computed from the wall shear stress as

$$\frac{\mathrm{d}p}{\mathrm{d}x} = -2\tau_w = -c_f \tag{4.8}$$

in the present case as the mass-flow rate is given. The source terms of the turbulence model equations Q_2 and Q_3, including the cross-diffusion terms, appear in their original form, see (6.74) for Q_3.

No-slip boundary conditions, $\mathcal{U} = \mathcal{K} = 0$, are given on the wall ($\eta = 0$). The wall-value of Φ obviously depends on the choice of the parameters m and n. In case of ω as the second scale variable, its wall value is approximated as explained in Section 6.4.7, see also Ref. [109]. Symmetry conditions are given on the mid plane of the channel. As no inflow boundary conditions can be specified in this case, the correct mass-flow rate must be maintained by requiring that the solution satisfies the integral constraint (4.4), which now becomes

$$\int_0^{1/2} \mathcal{U}(\eta) \, \mathrm{d}\eta - \frac{1}{2} = 0 \tag{4.9}$$

when U_b is used as the velocity scale. The integral constraint is implemented by multiplying the source term $-\mathrm{d}p/\mathrm{d}x$ by a factor $(1+c)$ where c depends on the value of the left-hand side of (4.9), and c becomes zero when (4.9) is exactly satisfied.

The code was initially validated by computing the simple laminar channel flow and comparing the numerical result with the analytical parabolic velocity profile. As the numerical and analytical solutions agreed perfectly in that case, the code with the turbulence model activated was next validated for turbulent cases. Menter's BSL $k-\omega$ model was employed in the validation phase. The velocity profiles at a number of different Reynolds numbers were compared with the logarithmic law. Also the skin-friction coefficient as a function of the Reynolds number was compared with a semi-empirical correlation by Dean [110], see Section 6.4.5.

4.1.3 Equilibrium Boundary Layers at the Limit $Re \to \infty$

This and the following free shear-layer cases differ from the channel flow quite remarkably, since these flows develop in the streamwise direction. This fact implies that also convection by the mean velocity takes place. The other difference is that the self-similar momentum equation is no more exact in these cases as it is in the channel case. Various minor simplifications must be made in order to arrive at self-similar equations, see Ref. [28].

The derivation is started by assuming that the boundary layer is in equilibrium in the sense that the nondimensional pressure-gradient parameter

$$\beta_T = \frac{\delta_1}{\tau_w}\frac{\mathrm{d}p}{\mathrm{d}x} \tag{4.10}$$

is constant along the layer. Furthermore, it is assumed that $Re_{\delta 1} = U_e\delta_1/\nu \to \infty$. The outer layer, also known as the defect layer, scales in a different way from the viscous wall layer. The proper length scale in the former must be proportional to the boundary-layer thickness while in the latter, the proper length scale is ν/u_τ. Therefore, similarity equations can only be derived separately for the viscous wall layer and for the defect layer. This problem is avoided by omitting the viscous wall layer and by placing the inner edge of the domain in the logarithmic layer where the logarithmic boundary conditions can be given. This means that the viscous diffusion terms may be ignored in the equations.

The original equations must be transformed into a new $\xi-\eta$ system. The streamwise coordinate is scaled as $\xi = x/L$ with L being a fictive plate length. The wall-normal coordinate is scaled as $\eta = y/\Delta$ where Δ is known as Clauser's delta defined by

$$\Delta = \int_0^\delta \frac{U_e - U}{u_\tau}\mathrm{d}y = \frac{U_e\delta_1}{u_\tau} \tag{4.11}$$

It should be noted that Δ is a function of x. This means that the $\xi - \eta$ system is a non-orthogonal curvilinear coordinate system as the constant-η curves are not straight. The scaling of the variables is as follows

$$\mathcal{U}(\eta) = [U_e(x) - U(x,y)]/u_\tau(x) \tag{4.12}$$

$$\mathcal{K}(\eta) = k(x,y)/u_\tau^2(x) \tag{4.13}$$

$$\Phi(\eta) = \phi(x,y)\frac{[U_e(x)\delta_1(x)]^n}{[u_\tau(x)]^{2(m+2n)}} \tag{4.14}$$

The last one of these is derived from the scaling of k and ε, which is

$$\mathcal{E}(\eta) = \varepsilon(x,y)\Delta(x)/u_\tau^3(x) \tag{4.15}$$

The original equations are transformed into the new system, and certain simplifying assumptions are made to arrive at a system of equations that are independent of ξ. The derivation involves lengthy algebra and therefore it is not presented here. Part of the derivation is given by Wilcox [28], and the complete derivation is given in two unpublished memoranda by the author (Helsinki University of Technology, Laboratory of Aerodynamics, MS-64, 2002 and MS-65, 2002, in Finnish). The resulting system of equations is

$$\frac{\mathrm{d}}{\mathrm{d}\eta}\left[-(1+2\beta_T)\eta\mathcal{U} - \mathcal{N}_T\frac{\mathrm{d}\mathcal{U}}{\mathrm{d}\eta}\right] = -\mathcal{U} \tag{4.16}$$

$$\frac{\mathrm{d}}{\mathrm{d}\eta}\left[-(1+2\beta_T)\eta\mathcal{K} - \sigma_k\mathcal{N}_T\frac{\mathrm{d}\mathcal{K}}{\mathrm{d}\eta}\right] = -\mathcal{K} + Q_2 \tag{4.17}$$

$$\begin{aligned}&\frac{\mathrm{d}}{\mathrm{d}\eta}\left[-(1+2\beta_T)\eta\Phi - \sigma_{\phi\phi}\mathcal{N}_T\frac{\mathrm{d}\Phi}{\mathrm{d}\eta} - \sigma_{\phi k}\mathcal{N}_T\frac{\Phi}{\mathcal{K}}\frac{\mathrm{d}\mathcal{K}}{\mathrm{d}\eta}\right]\\ &= [n-1+2(3n+m-1)\beta_T]\Phi + Q_3\end{aligned} \tag{4.18}$$

The corresponding equations for the $k-\omega$ and $k-\varepsilon$ models are also given by Wilcox [28] but in a slightly different form. The equations given above are, however, mathematically equivalent with those given by Wilcox when $m = -1$ and $n = 1$ ($k-\omega$ models), and when $m = 0$ and $n = 1$ ($k-\varepsilon$ models). By comparing Eqs. (4.16) – (4.18) with the general form (4.1), it is immediately seen that

$$\mathcal{V} = -(1+2\beta_T)\eta \tag{4.19}$$

$$A_{\mathcal{U}} = -1 \tag{4.20}$$

$$A_{\mathcal{K}} = -1 \tag{4.21}$$

$$A_\Phi = n-1+2(3n+m-1)\beta_T \tag{4.22}$$

Furthermore, $Q_1 = 0$, and the turbulence model source terms Q_2 and Q_3 have the same form as in the Cartesian system, see (6.74) for Q_3.

The solution domain begins from the logarithmic layer and extends beyond the outer edge of the boundary layer. Outside the boundary layer, $\mathcal{U}$ is set to zero and the turbulent variables are given small free-stream values. The logarithmic boundary conditions are given at the inner boundary. As the limit of infinite Reynolds number is assumed, the thickness of the viscous wall layer is approaching zero and thus the logarithmic conditions can be given arbitrarily close to the wall. This fact has no significance for the solution, but it makes comparisons with experimental data more straightforward, since the gap between the wall and the inner edge of the computational domain can be taken as negligibly small. The logarithmic boundary conditions at $\eta \to 0$ are given by

$$\mathcal{U}(\eta) = (-\ln\eta + \mathcal{U}_0)/\kappa \tag{4.23}$$

$$\mathcal{K}(\eta) = 1/\sqrt{\beta^*} \tag{4.24}$$

$$\Phi(\eta) = (\kappa^n\eta^n\beta^{*\,m/2})^{-1} \tag{4.25}$$

where β^* is a turbulence modelling parameter that usually is given a value of 0.09. Wilcox proposes to include also higher-order terms proportional to $\eta \ln \eta$ in the above formulas. Such terms, however, become negligibly small when $\eta \to 0$, and thus they are ignored in the present method. There is still one unknown parameter $\mathcal{U}_0$ that must be derived using the integral constraint

$$\int_0^\infty \mathcal{U}(\eta)\mathrm{d}\eta - 1 = 0 \tag{4.26}$$

which is obtained by substituting U solved from (4.12) into the definition of the displacement thickness (3.2). The integral constraint is implemented by updating $\mathcal{U}_0$ at each pseudo-time step by adding corrections that depend on the magnitude of the left-hand side of (4.26).

The implementation of this problem was validated by comparing the results with the measurements and with the results presented by Wilcox [28]. In the case of zero pressure gradient, the results were compared also with those obtained with the full Navier-Stokes solver FINFLO.

4.1.4 Far Wake

Planar wakes behind two-dimensional bodies become approximately self-similar far downstream from the body. The measured velocity profiles and other quantities, if measured sufficiently far downstream, collapse into single curves when properly scaled. Despite this, a self-similar momentum equation can only be derived by means of linearizing the streamwise convective term by assuming that

$$U\frac{\partial U}{\partial x} \approx U_e\frac{\partial U}{\partial x} \tag{4.27}$$

in order to eliminate all x-dependent terms in the equation. This linearization is based on the assumption that $U \to U_e$ as $x \to \infty$.

In this case, the variables are scaled as

$$\eta = \frac{y}{D}\sqrt{\frac{2D}{(x-x_0)c_d}} \tag{4.28}$$

$$\mathcal{U}(\eta) = \frac{U_e - U(x,y)}{U_e}\sqrt{\frac{2(x-x_0)}{Dc_d}} \tag{4.29}$$

$$\mathcal{K}(\eta) = \frac{2(x-x_0)}{Dc_d}\frac{k(x,y)}{U_e^2} \tag{4.30}$$

$$\Phi(\eta) = \frac{(x-x_0)^{m+2n}}{(Dc_d/2)^{m+n}U_e^{2m+3n}}\phi(x,y) \tag{4.31}$$

where x_0 is the location of a virtual origin of the self-similar far wake. D and c_d are the diameter of the wake generating cylinder (or reference length of some other wake generating body) and the drag coefficient, respectively.

The equations are formally similar to Eqs. (4.16) – (4.18), and the convection-related factors are given by

$$\begin{aligned} \mathcal{V} &= -\eta/2 && (4.32) \\ A_{\mathcal{U}} &= 0 && (4.33) \\ A_{\mathcal{K}} &= 1/2 && (4.34) \\ A_{\Phi} &= m + 2n - 1/2 && (4.35) \end{aligned}$$

The derivation is given in the unpublished memorandum by the author (Helsinki University of Technology, Laboratory of Aerodynamics, MS-65, 2002, in Finnish).

The solution domain begins from the wake midplane and extends beyond the outer edge of the wake. The boundary conditions are straightforward in this case. Symmetry conditions are specified on the midplane, and the free-stream conditions are specified on the outer edge just as in the boundary-layer problem. The integral constraint

$$\int_0^\infty \mathcal{U}(\eta)\mathrm{d}\eta - \frac{1}{2} = 0 \tag{4.36}$$

is implemented by adding an artificial control source term into the right-hand side of the momentum equation. This term depends on the error of the integral constraint, and it goes to zero when (4.36) is exactly satisfied.

The implementation of the far-wake equations was initially validated by comparing the velocity profile with the one presented by Wilcox [28]. In addition to this, a comparison with a full Navier-Stokes solution was made. A wake of a flat plate was computed with the FINFLO solver, see Section 7.2 for details. The velocity profiles computed with FINFLO were scaled according to Eqs. (4.28) and (4.29). This comparison is shown in Fig. 4.1. The computed velocity profile agreed very well with Wilcox's results when exactly the same turbulence model and free-stream boundary values were employed. However, there is some difference between the self-similar and full Navier-Stokes results in the outer part of the wake. This difference is of the order of the variation between measured profiles taken from different experiments. The linearization of the convective velocity is believed to be the primary reason behind this discrepancy. Although this discrepancy indicates that the self-similar wake solution is probably somewhat inaccurate, it does not mean that it would be useless in this study. It is still considered to be very useful since different turbulence models may give results that differ from each other clearly more than the self-similar and full Navier-Stokes solutions.

4.1.5 Mixing Layer

A planar mixing layer between a uniform stream with velocity U_1 and still fluid can be considered as self-similar. No such linearizations are needed in this case as in

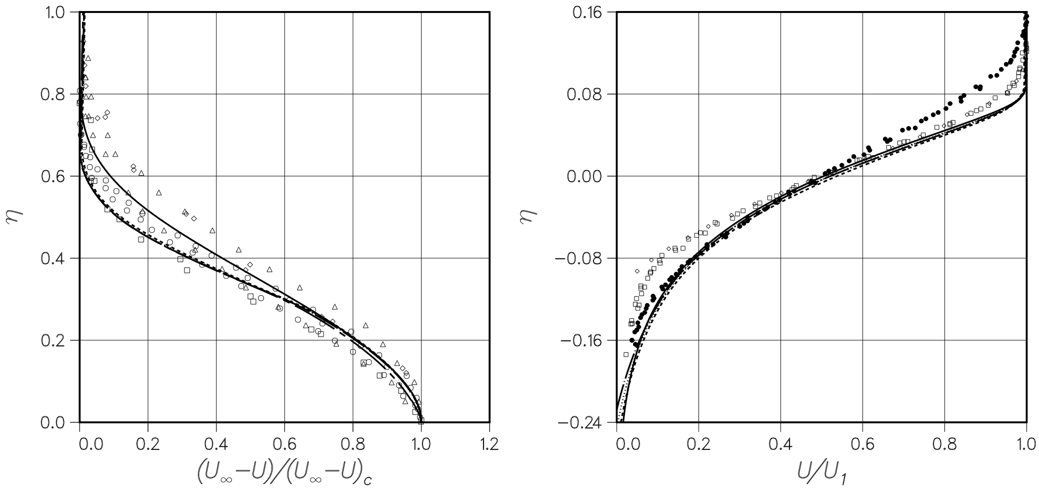

Figure 4.1: The far wake flow (left), and the mixing layer (right). Solid curves are the self-similar solutions and the other curves are from various x-stations of the full Navier-Stokes computations. Symbols represent various experimental measurements, see *e.g.* Fig. 6.11 for details.

the far-wake flow. The scaling is given by

$$\begin{aligned} \eta &= y/(x-x_0) &\quad (4.37)\\ \mathcal{U}(\eta) &= U(x,y)/U_1 &\quad (4.38)\\ \mathcal{K}(\eta) &= k(x,y)/U_1^2 &\quad (4.39)\\ \Phi(\eta) &= \frac{(x-x_0)^n}{U_1^{2m+3n}}\phi(x,y) &\quad (4.40) \end{aligned}$$

where x_0 is again the location of a virtual origin. The convection-related factors are as follows

$$\begin{aligned} \mathcal{V} &= -\int_0^\eta \mathcal{U}(\eta')\mathrm{d}\eta' &\quad (4.41)\\ A_\mathcal{U} &= \mathrm{d}\mathcal{V}/\mathrm{d}\eta &\quad (4.42)\\ A_\mathcal{K} &= \mathrm{d}\mathcal{V}/\mathrm{d}\eta &\quad (4.43)\\ A_\Phi &= n\mathcal{U}+\mathrm{d}\mathcal{V}/\mathrm{d}\eta &\quad (4.44) \end{aligned}$$

Also these equations are derived in the unpublished memorandum (Helsinki University of Technology, Laboratory of Aerodynamics, MS-65, 2002, in Finnish).

It is important to note that no symmetry or antisymmetry conditions can be exploited in this case since the turbulence field is not symmetric, and thus the mean-velocity field is not antisymmetric. The layer spreads more rapidly towards the still-fluid side. The domain ranges over the whole layer from the still fluid up to the undisturbed uniform flow. The boundary conditions for $\mathcal{U}$ are simply $\mathcal{U}=0$ at $\eta=0$ and $\mathcal{U}=1$ at $\eta=\eta_e$, *i.e.* at the high-speed edge. The free-stream conditions, similar to those in the wake and boundary-layer cases, are again given for the turbulent variables. The boundary conditions define this flow completely, and thus no other constraints are needed.

The solution is validated in the same fashion as in the wake case. Again, the solution agreed with that presented by Wilcox [28] when the same model and free-stream conditions were used. Now, the self-similar solution agrees also well with the full Navier-Stokes solution, see Fig. 4.1.

4.2 Two- and Three-Dimensional Mean Flows

4.2.1 General Remarks on the FINFLO Flow Solver

The new $k-\omega$ EARSM turbulence model proposed in this study, as well as Menter's models, have been implemented in the Navier-Stokes solver called FINFLO, see *e.g.* Refs. [107, 108]. More specifically, the version FINF2D for two-dimensional and axisymmetric flows with a two-componential mean-velocity field is utilized in all of the two-dimensional and axisymmetric computations of this study. Only the combustor case studied in Section 5.3.5 is computed using the FINFLO code for general three-dimensional flows. FINF2D is built by using the same methods and algorithms as the parent software FINFLO. For specific documentation of the FINF2D version, see *e.g.* [29, 111]. The FINFLO code, developed at Helsinki University of Technology, is based on the finite-volume approach and utilizes structured multi-block grids. The solution method is an implicit pseudo-time integration. A multigrid cycling is used to accelerate convergence. The inviscid fluxes are evaluated using Roe's flux-difference splitting with formally third-order upwind-biased MUSCL-type discretization, while the central-differencing scheme is used in the calculation of the viscous fluxes. No simplifications, such as the thin-layer approximation, are subjected to the diffusive terms.

The coupling of the EARSM constitutive model with the mean-flow equations differs formally from the ordinary technique of linear two-equation models only in the explicit phase. This is implemented by splitting the Reynolds-stress tensor into three parts as

$$\overline{\rho u_i' u_j'} = -\mu_T \left(\frac{\partial U_i}{\partial x_j} + \frac{\partial U_j}{\partial x_i} - \frac{2}{3} \frac{\partial U_k}{\partial x_k} \delta_{ij} \right) + \frac{2}{3} \rho k \delta_{ij} + \rho k a_{ij}^{(ex)} \tag{4.45}$$

where $\mu_T = \rho \nu_T$, and only the first two terms on the right-hand side of (4.45) are kept in the approximate implicit phase. The influence of the third term on the momentum and total-energy fluxes is taken into account in the explicit phase by adding appropriate corrective terms after the standard flux computation procedure. The tensor $a_{ij}^{(ex)}$ contains all terms of a_{ij} except the first-order term, *i.e.* the first term on the right-hand side of (4.45), see Section 6.6.2. For details of the implementation of the EARSM, see Ref. [112].

4.2.2 Far-Field Boundary Conditions

A particular circulation-correction method is applied at the far-field boundaries in high-lift aerofoil computations. This method is not reported in Refs. [29, 107, 108, 111], and thus it is explained here. The circulation correction means that the free-stream boundary conditions are corrected by applying the lifting line-vortex theorem. In incompressible two-dimensional flow, the lift may be expressed using a vortex line placed at the quarter-chord line of the aerofoil. The vortex strength is then

$$\Gamma = \frac{1}{2} V_\infty c\, c_l \tag{4.46}$$

where c is the chord of the aerofoil and c_l is the lift coefficient. V_∞ is the magnitude of the free-stream velocity. According to the potential-flow theory, the lifting vortex induces velocity disturbances at the far field given by

$$\delta U = \frac{\Gamma(y - y_v)}{2\pi[(x - x_v)^2 + (y - y_v)^2]} \tag{4.47}$$

$$\delta V = \frac{-\Gamma(x - x_v)}{2\pi[(x - x_v)^2 + (y - y_v)^2]} \tag{4.48}$$

where (x, y) are the coordinates of the far-field boundary point, and (x_v, y_v) is the location of the vortex line, *i.e.* the quarter-chord point of the aerofoil. The velocity field at the far-field boundary is corrected by adding the above-given corrections to the free-stream velocity components. This may have a remarkable effect on the results even in cases where the far-field boundary is set quite far from the aerofoil, say, at a distance of 30–50 chord lengths. It was shown in Ref. [113] that especially the drag coefficient is sensitive to the far-field conditions. This circulation correction is applied in all the high-lift aerofoil computations in this study.

5 Constitutive Model

5.1 Baseline ARSM

The EARSM developed by Wallin and Johansson [4] is selected as the baseline constitutive model. The motivation behind this choice is that this model is an exact solution for the underlying ARSM in two-dimensional mean flows. Although, the solution for the scalar P/ε is approximate in three-dimensional mean flows, the model can still be considered as a complete solution for the ARSM. Therefore, the model involves no singularities, and thus no approximate regularizations are needed. Moreover, this model is a quartic solution valid for three-dimensional mean flows unlike the model proposed by Girimaji [36]. The model coefficients in the underlying ARSM (2.54) are chosen so that one of its terms vanishes. This simplifies the explicit solution significantly, especially for three-dimensional mean flows. Constant values are assumed for the rapid model coefficients in (2.39). The coefficients A_1 to A_4 in (2.54) can be expressed as functions of the pressure-strain model coefficients, see Eqs. (2.30) and (2.39), as follows:

$$\begin{array}{ll} A_0 = C_4/2 - 1 & \\ A_1 = (3C_2 - 4)/(3A_0) & A_2 = (C_3 - 2)/(2A_0) \\ A_3 = -(C_1^{(0)} - 2)/(2A_0) & A_4 = -(C_1^{(1)} + 2)/(2A_0) \end{array} \tag{5.1}$$

The proposed values for C_3 are typically within the range between 1.2 and 2. For instance, Launder *et al.* proposed $C_3 \approx 1.75$ [11]. This means that the term with A_2 as coefficient may be of relatively little importance if C_3 is close to 2. Choosing $C_3 = 2$ exactly renders $A_2 = 0$, and the ARSM equation becomes

$$Na_{ij} = -A_1 S_{ij} + (a_{ik}\Omega_{kj} - \Omega_{ik}a_{kj}) \tag{5.2}$$

with

$$N = A_3 + A_4 \frac{P}{\varepsilon} \tag{5.3}$$

The other C-coefficient values are given in Table 5.1, and the corresponding A-values are given in Table 5.2. The simple linear Rotta model is assumed for the slow term, *i.e* $C_1^{(1)} = 0$. The given values follow from the LRR model with the exception that C_3 is set to 2, see Ref. [4]. The explicit solution is obtained as explained in Section 2.5.2, and it is given in Section 6.6.2. Note that the final model described in Section 6.6.2 also involves an attempt to model the ignored diffusion of the anisotropy, which is mostly turbulent transport. For further details of this

Table 5.1: The values of the redistribution model coefficients.

C_1^0	C_1^1	C_2	C_3	C_4
3.6	0	0.8	2	1.11

Table 5.2: The values of the A-coefficients.

A_0	A_1	A_2	A_3	A_4
-0.44	1.20	0	1.80	2.25

model, see Ref. [4]. The anisotropy-diffusion model prevents the coefficient of the linear term (C_μ) from obtaining unphysically high values in regions with vanishing shear. Also, the time-scale used for scaling the strain-rate and vorticity tensors is redefined to never drop below a certain viscous lower limit as

$$\tau = \max\left(\frac{1}{\beta^*\omega}; C_\tau\sqrt{\frac{\nu}{\beta^* k\omega}}\right) \tag{5.4}$$

with $C_\tau = 6.0$ and $\beta^* = 0.09$ if ω is defined as $\varepsilon/(0.09k)$ as usual, and $\beta^* = 1$ if ω is defined as ε/k.

5.2 ARSM for Strongly Curved Flows

5.2.1 Basic Formulation

Turbulent flows are known to be sensitive to streamline curvature. It is also clear that linear eddy-viscosity turbulence models are completely insensitive to the effects of streamline curvature. On the other hand, differential Reynolds stress models are able to capture these effects. EARSMs partially inherit the sensitivity to streamline curvature from the underlying RSMs. However, this sensitivity is partially lost through the weak-equilibrium assumption invoked in order to derive algebraic Reynolds stress models. It has been shown by several authors that, in principle, this deficiency can be removed by modelling the ignored convection of the anisotropy by some means. One approach is to seek a suitable curvilinear stream-following coordinate system, and to invoke the weak-equilibrium assumption in this system. Such an approach could be called a weak-equilibrium assumption consistent with curved mean flows. This can be formally carried out as shown by *e.g.* Wallin and Johansson [5, 114], and similarly by Gatski and Jongen [18]. As a result, the mean-velocity convection of the anisotropy can be written as

$$\frac{\mathrm{D}a_{ij}}{\mathrm{D}t} = T_{ip'}\frac{\mathrm{D}}{\mathrm{D}t}(T_{p'r}a_{rs}T_{sq'})T_{q'j} - \left(a_{ik}\Omega^{(r)}_{kj} - \Omega^{(r)}_{ik}a_{kj}\right) \tag{5.5}$$

where

$$\Omega^{(r)}_{ij} = \frac{\mathrm{D}T_{ip'}}{\mathrm{D}t}T_{p'j} = -T_{ip'}\frac{\mathrm{D}T_{p'j}}{\mathrm{D}t} \tag{5.6}$$

$T_{ip'}$ and $T_{q'j}$ are the transformation matrices between the Cartesian and curvilinear system, and vice versa. It is important to note that this transformation varies in space. The primed indices refer to the curvilinear system. In principle, the optimal ARSM for curved mean flows can be obtained by ignoring only the first term on the right-hand side of (5.5). The second term is algebraic, and it can be included in the ARSM — in fact, by just modifying the vorticity tensor, since the ARSM equation (5.2) already includes the tensor group $a_{ik}\Omega_{kj} - \Omega_{ik}a_{kj}$ and $\Omega_{ij}^{(r)}$ is of similar tensorial form as the vorticity tensor Ω_{ij} (skew-symmetry). Redefining the vorticity tensor as

$$\Omega_{ij}^{*} = \Omega_{ij} - \frac{\tau}{A_0}\Omega_{ij}^{(r)} \tag{5.7}$$

corresponds to formulating the ARSM in a given curvilinear coordinate system. The vorticity modification due to curvature $\Omega_{ij}^{(r)}$ is related to the rotation rate vector $\omega_k^{(r)}$ of the local basis of the curvilinear system by

$$\Omega_{ij}^{(r)} = -\epsilon_{ijk}\omega_k^{(r)} \tag{5.8}$$

where ϵ_{ijk} is the third-order permutation tensor. Its component has a value of 1 if the indices form a positive permutation of $(1, 2, 3)$ and -1 in case of a negative permutation. All components with repeated indices are zero.

The problem of formulating a suitable ARSM for flows with streamline curvature is now reduced to finding a suitable curvilinear system in which the weak-equilibrium assumption is best satisfied. In principle, the optimal system is such where the ignored differential term on the right-hand side of (5.5) is minimized. Such an optimal coordinate system that really minimizes the effect of the weak-equilibrium assumption cannot be found in closed form within the framework of ARS modelling. Instead, a suitable approximation for it must be found. The methods proposed in the literature are critically discussed by the author in Ref. [93], and this discussion is partially repeated below [1].

5.2.2 Streamline Coordinate System

Rodi and Scheuerer [115] used the streamline system in their curved boundary-layer computations. In computations of more general flowfields, this means equating $\omega_k^{(r)}$ with the rotation rate of a local basis attached to the velocity vector in the selected coordinate system. Galilean invariance, which is commonly required from rigorously derived turbulence models, is not satisfied. Therefore, other alternatives have been proposed by various authors to replace the streamline system.

5.2.3 Acceleration Coordinate Systems

Girimaji [116] proposed using a local frame that follows the acceleration vector $\dot{U}_k = \mathrm{D}U_k/\mathrm{D}t$. This is motivated by the acceleration being a Galilean invariant quantity.

---

[1] Note that Eq. (1) in that article is typed incorrectly; an extra $\boldsymbol{a}$ appears as a factor on the left-hand side.

Girimaji only discussed two-dimensional applications. More recently, Wallin and Johansson [114] proposed an approximate method for three-dimensional flows

$$\omega_k^{(r)} = \epsilon_{lmk} \frac{\dot{U}_l \ddot{U}_m}{\dot{U}_n \dot{U}_n} \tag{5.9}$$

where $\ddot{U}_m = \mathrm{D}\dot{U}_k/\mathrm{D}t$. Although not pointed out by Wallin and Johansson [114], Eq. (5.9) can easily be shown to be equal to the exact form in two-dimensional mean flows given by Girimaji [116]. Therefore, the behaviour of the acceleration basis is studied using Eq. (5.9) in this study.

In circular flows, the acceleration vector is orthogonal to the velocity vector. Therefore, the rate of change of the acceleration basis equals the rate of change of the streamline basis in a fixed background frame. Thus, ARSM derived in the acceleration frame is equal to the one derived in a streamline frame, provided that the velocity of the background coordinate system is chosen so that the flow is circular. Girimaji stated that every flow can be considered as locally circular because a suitable Galilean transformation can be made for the local frame in order to arrive at locally circular flow, that is, to make the velocity and acceleration vectors orthogonal. The central failure behind this reasoning is pointed out in this study. That is, although the flow may formally be seen as locally circular from a certain acceleration basis, it does not imply that such an acceleration system is suitable for the weak-equilibrium assumption. As a matter of fact, the acceleration basis may behave in a very wild manner and even become singular in certain circumstances. The velocity and the radius of curvature of locally circular flow correspond to the rotation rate of the local acceleration basis. Singularity formally corresponds to the limit of the infinite rotation rate of the acceleration system and, thus, the vanishing radius of curvature of the locally circular flow in that system.

As an example, let us consider a slightly curved flow that is first accelerating and then, at a certain point, begins to decelerate (or vice versa). If the radius of curvature of the streamlines is large enough, the velocity and the acceleration vectors are almost aligned with each other. This is a typical situation in flows over slightly curved surfaces, for example, on the upper surface of a wing. If the radius of curvature is roughly constant, the basis of the curvilinear system should also change at about a constant rate. The acceleration basis, however, singularly turns about $180°$ at the location where the streamwise acceleration changes its sign. In contrast, there is no reason for the anisotropy components to change rapidly in such a situation.

Starting and ending curvature are further examples of singularities of the acceleration base. At the very instant when a fluid particle enters or exits any curved part of a streamline, the acceleration vector immediately rotates to a new orientation, which may be almost orthogonal to its former orientation. Also, the anisotropy tensor may possibly change its orientation quite rapidly in this kind of situation, but hardly as fast as the acceleration vector.

5.2.4 Methods Based on the Strain-Rate Tensor

Spalart and Shur proposed using the rate of change of the strain-rate tensor $\dot{S}_{ij}$ as a measure of the rotation and curvature effects with the aim of correcting eddy-viscosity models [117]. The rationale, in two-dimensional flows, was to identify the rate of change of the direction of the principal axes of the strain-rate tensor, $\mathrm{D}\alpha/\mathrm{D}t$. This measure gives the rotation rate, $\omega_i^{(r)}$, in the direction normal to the plane of the flow as

$$\omega_3^{(r)} = \frac{S_{11}\dot{S}_{12} - S_{12}\dot{S}_{11}}{2(S_{11}^2 + S_{12}^2)} \tag{5.10}$$

This measure for two-dimensional mean flows was also derived by Gatski & Jongen [18]. It is expected to model the rotation rate of the optimal system quite well because the material derivatives of the strain-rate and anisotropy tensors are typically rather closely related to each other in the weak-equilibrium limit where $a_{ij} = f(S_{ij}, \Omega_{ij})$ and, furthermore, the leading term of anisotropy is directly proportional to S_{ij}. Based on this reasoning, Eq. (5.10) is expected to be the best available approximation for $\omega_3^{(r)}$ in two-dimensional mean flows. It is Galilean invariant, and, very recently, Wallin and Johansson derived a new, general strain-rate based method that reduces to Eq. (5.10) in two-dimensional mean flows [5]. They also showed that the original three-dimensional extension of Eq. (5.10) proposed by Spalart and Shur [117] is inconsistent with helical flows where the axial velocity component varies with the radial coordinate, see Refs. [5, 118].

The rationale behind the new, more general method derived by Wallin & Johansson [5] is to assume that the smallest error while ignoring the transport effects of the anisotropy tensor a_{ij} is obtained in a system where also the transport of the strain-rate tensor S_{ij} has a minimum. This is identical to finding the best solution for the $\Omega_{ij}^{(r)}$ tensor from the following relation

$$\dot{S}_{ij} \equiv \frac{\mathrm{D}\, S_{ij}}{\mathrm{D}t} \approx -\left(S_{ik}\Omega_{kj}^{(r)} - \Omega_{ik}^{(r)} S_{kj}\right) \tag{5.11}$$

This equation system is overdetermined since there are five (two in 2D) independent equations for $\dot{S}_{ij}$ and three (one in 2D) independent components of the system rotation rate tensor $\Omega_{ij}^{(r)}$, or $\omega_i^{(r)}$ through (5.8). Eq. (5.11) can, however, be solved in the least-square sense. For details, see Ref. [5]. The solution for $\omega_i^{(r)}$ reads

$$\omega_i^{(r)} = \frac{II_S^2\delta_{ij} + 12III_S S_{ij} + 6II_S S_{ik}S_{kj}}{2II_S^3 - 12III_S^2} S_{pl}\dot{S}_{lq}\epsilon_{pqj} \tag{5.12}$$

This relation, indeed, reduces to (5.10) in two-dimensional mean flows. The development of this method [5] was motivated by the singular behaviour of (5.9), and the acceleration-based methods in general, shown in Ref. [93].

5.2.5 Numerical Example

Flow in a 180° U-duct, see Monson et al. [119] and Monson and Seegmiller [120], is an illustrative example containing local flow situations where the acceleration basis

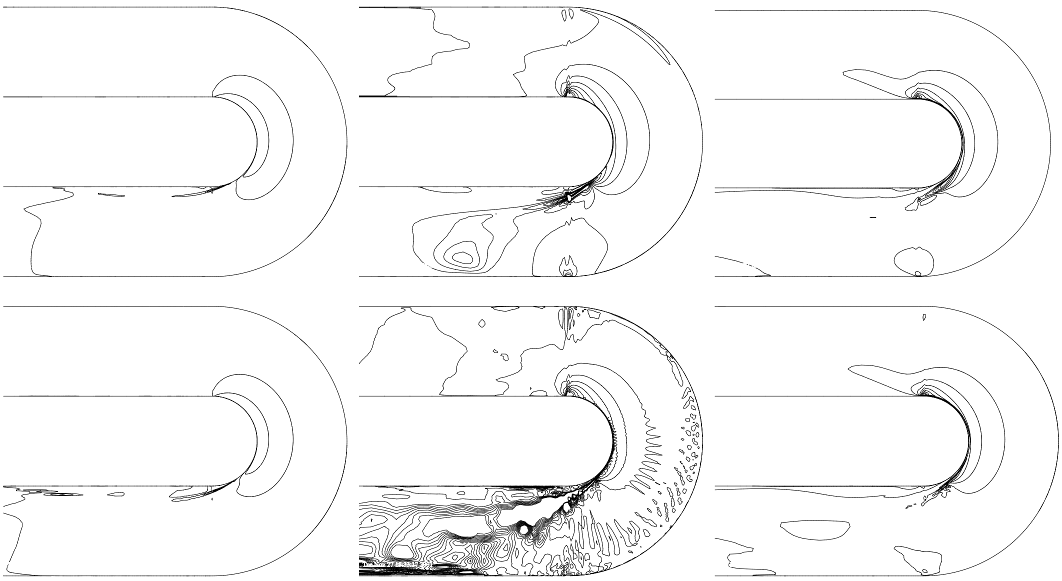

Figure 5.1: A-priori test (upper row) and actually predicted rotation rate $\omega_3^{(r)}$ (lower row) according to the stream-line method (left), the acceleration method (5.9) (middle), and the strain-rate method (5.10) (right). The flow direction is from up to down. (Figure taken from Ref. [93].)

behaves unfavourably and even goes singular. First, a priori test of Eqs. (5.9), (5.10), and the streamline method is performed. A priori means here that the rotation rate $\omega_3^{(r)}$ is evaluated from a frozen flowfield computed using the baseline EARSM. Menter's $k-\omega$ BSL model was used as the scale-determining model here [3].

The $\omega_3^{(r)}$ distributions are shown in Fig. 5.1. The plots reveal significant differences between each method. The angular velocity of the acceleration vector locally obtains of the order of 100 times higher values than Eq. (5.10) gives near the end of the curved duct. Furthermore, an unexpected area of relatively high negative (clockwise) rotation is observed downstream of the bend in an area with almost zero curvature. This is where the acceleration vector suddenly turns around. Surprisingly, the acceleration system behaves quite smoothly in the beginning of the curvature.

Next, the flowfield is really computed using the curvature corrections on the same EARSM. As expected, the acceleration method (5.9) overestimates the curvature effects so strongly that no steady-state solution can be obtained. Instead, the flow tends to oscillate owing to the strong laminarizing influence of high $\omega_3^{(r)}$. The strain-rate method (5.10) and the streamline method allowed the solution to converge, although the convergence rate slows down remarkably owing to the reduced damping effect of the turbulence model. The predicted $\omega_3^{(r)}$ distributions are also presented in Fig. 5.1. The exaggerated effect of the acceleration method amplifies itself, mostly near the end of the curved duct, resulting in much higher values of $\omega_3^{(r)}$ than are observed in the a priori test. Unlike Eq. (5.9), the strain-rate method (5.10) and the streamline method predicted quite similar $\omega_3^{(r)}$ distributions to those seen in the a priori tests. A detailed comparison of the computed results with experimental data is provided by Hellsten *et al.* [118]. This is also given in the next section.

Given these observations, no generalizability can be expected from any curvature corrections based on the coordinate system attached to the acceleration vector. On the other hand, the strain-rate based method (5.12) developed by Wallin and Johansson [5] seems to be a promising method, and therefore it has been validated for a few curvature-affected flows by Hellsten *et al.* [118] and by Wallin *et al.* [121]. Some of the validation results are also given in the next section.

5.3 Validation of the Curvature-Corrected EARSM

5.3.1 Final Form of the Curvature-Corrected EARSM

The new curvature-corrected EARSM (CC-WJ) by Wallin and Johansson [5] is obtained from the baseline EARSM simply by replacing Ω_{ij} with Ω^*_{ij} defined by Eqs. (5.7), (5.8), and (5.12). In addition, the coefficient A_0, see Table 5.2, is recalibrated. This coefficient has no influence on the baseline EARSM, but it enters the curvature-corrected model via (5.7). A_0 was derived by considering the point of neutral stability for the growth rate of k in rotating homogeneous shear flows, see Ref. [5]. Wallin and Johansson found a value of -0.72 for A_0. It is important to note that recalibration of A_0 influences all of the redistribution model coefficients except C_3 in this case, because $A_2 = 0$. The new values of the redistribution model-coefficients are seen in Table 5.3. Even C_1^1 now has a nonzero value, which implies that the underlying redistribution model is now quasi-linear while the baseline model was based on a purely linear redistribution model. The new value of C_2 actually disagrees with the rapid-distortion theory which implies $C_2 = 4/5$. Wallin and Johansson provide a more detailed discussion on this subject [5].

Table 5.3: The values of the redistribution model coefficients after recalibrating the A_0-coefficient.

C_1^0	C_1^1	C_2	C_3	C_4
4.6	1.24	0.47	2	0.56

5.3.2 Numerical Implementation

The strain-rate-based curvature correction methods involve numerical approximation of $\dot{S}_{ij} = \mathrm{D}S_{ij}/\mathrm{D}t$ in (5.12). In the present implementation, the velocity gradient components are computed onto each face of a control volume or cell using local staggered cells according to the finite-volume approach as

$$\frac{1}{V}\int_V \frac{\partial U_i}{\partial x_j}\mathrm{d}V = \frac{1}{V}\oint_{\mathcal{S}} U_i \mathrm{d}\mathcal{S}_j \approx \frac{1}{V}\sum_{m=1}^{6}(U_i\mathcal{S}_j)^{(m)} \tag{5.13}$$

where $\vec{\mathcal{S}}$ and V are the surface-area vector and volume of a staggered control volume, respectively. In the numerical algorithm, the control volumes are hexagonal cells (in three-dimensional flows) and m spans over the faces of a staggered cell. The necessary geometrical data of the staggered cells are approximated as averages of the surrounding actual cells. Next, the material derivatives of the strain-rate components are computed in the actual-cell centrepoints in a conservative form as

$$\begin{aligned}\frac{1}{\rho V}\int_V \rho U_k \frac{\partial S_{ij}}{\partial x_k}\mathrm{d}V &= \frac{1}{\rho V}\int_V \frac{\partial}{\partial x_k}\left(S_{ij}\rho U_k\right)\mathrm{d}V \\ &= \frac{1}{\rho V}\oint_{\mathcal{S}} S_{ij}\rho U_k \mathrm{d}\mathcal{S}_k \approx \frac{1}{\rho V}\sum_{m=1}^{6}(S_{ij}\rho U_k \mathcal{S}_k)^{(m)}\end{aligned} \tag{5.14}$$

where $\vec{\mathcal{S}}$ and V now refer to the geometry of the actual cell. This way the numerical error can, in principle, be kept small. However, a spatially oscillating distribution of $\dot{S}_{ij}$ may be obtained, especially when high-resolution grids are employed. Presently, this problem is handled by applying a spatial filter for the computed rotation vector field ${\omega_k}^{(r)}$. A top-hat filter of the width of three computational cells in each direction is employed. A filtered quantity $\widehat{q}$ is defined as

$$\widehat{q(\mathbf{x})} = \frac{\int_V G(\mathbf{x}')\, q(\mathbf{x}')\mathrm{d}V}{\int_V G(\mathbf{x}')\mathrm{d}V} \tag{5.15}$$

where the top-hat filter function $G(\mathbf{x}') = 1$ in the control volume at $\mathbf{x}_{i,j,k}$ and its 26 neighbouring control volumes (8 in 2-D cases) with indices $i \pm 1$,$j \pm 1$, and $k \pm 1$ and zero elsewhere. This kind of filtering turned out to be a sufficient remedy in the flows considered in this study. In practice, the singularity of (5.12) in non-strained regions must be removed by introducing a small lower limit for the denominator, 10^{-6} was used in this study. It is felt, however, that the numerical computation of $\dot{S}_{ij}$ still needs further attention.

Another point that needs further attention is the programming in structured multi-block solvers, such as the FINFLO-solver used in this study, see Chapter 4. Programming of the above-described method to numerically approximate $\dot{S}_{ij}$ is quite straightforward inside a grid block, but the block-corners may pose programming difficulties, especially when several grid blocks join in a single corner point. Such programming problems are not fully resolved within this study, and are left for future work. Thus, the present implementation of the curvature-corrected EARSM can be reliably used only in relatively simple geometries that can be handled using grids with no multiple block connections. In some more complex geometries, such as the NHLP-2D three-element aerofoil discussed in Section 7.5.4, the present programming may fail. In this particular case, the grid consists of 17 blocks connected together in a rather complex manner. Therefore, the curvature-corrected EARSM was not used in that case within this work.

The practical value of the curvature-correction method may remain smaller than expected if it significantly adds the implementation effort and problems in comparison with the baseline EARSM. Therefore, more attention should be paid to the numerical implementation issues to find sufficiently simple and robust algorithms for practical exploitation of this method. It must be remembered, however, that the computational workload of the curvature-corrected EARSM is by far smaller than that of a corresponding RSM. One possibility to approximate $\dot{S}_{ij}$ would be to approximate the strain-rate components on the actual-cell faces simply as averages of the surrounding centre-point values that are readily available. Programming of this algorithm is straightforward even at the block corners. On the one hand, it is a less accurate scheme than the one described above. On the other hand, as a result of the more accurate algorithm needing to be filtered, its accuracy is lost as well. Furthermore, the accuracy of the algorithm for approximating $\dot{S}_{ij}$ is probably not as an important matter as its robustness.

5.3.3 Two-Dimensional Boundary Layer on a Convex Wall

Rumsey *et al.* [122] have recently studied a curvature-corrected EARSM using the two-dimensional Spalart-Shur equation (5.10) for isolated curvature effects in a convex-curved boundary layer. This case has been experimentally studied by So and Mellor [123]. The curvature correction improved the accuracy of the results, especially for the shear stress and the skin-friction coefficient. The effect of curvature in this flow can be considered moderate. Ratio of the largest turbulent length-scale $k^{3/2}/\varepsilon$ in the boundary layer to the radius of wall curvature is about 0.05. This flow is used for basic validation of the curvature-corrected EARS-modelling. Menter's $k-\omega$ BSL model was used as the scale-determining model in these validation computations. The curvature-corrected EARSM (CC-WJ) will be tested using two different ways to obtain $\omega_3^{(r)}$: the strain-rate method (5.12), which reduces to Eq. (5.10) in two-dimensional mean flows, and the streamline method for comparison. As already pointed out, the latter method is not generalizable due to its lack of Galilean invariance. It can, however, be used as a reference here because the coordinate system can be attached to the apparatus. The results are compared with the experimental data, with the results computed using the parent RSM (see Ref. [29] for details), with the results obtained using the standard EARSM derived in the inertial coordinate system (iWJ), and also with the BSL $k-\omega$ eddy-viscosity model (EVM).

The computational domain consists of a straight duct, where the boundary layer initially develops, the curved section, and a straight outlet channel, see Fig. 5.2. In the computations, the length of the straight inlet duct has been chosen so that the displacement and momentum thicknesses of the boundary layer and the skin-friction coefficient match the experimental data at $s = 24$ in. The convex-wall geometry equals the shape of the experimental setup while the concave outer wall is contoured to obtain a pressure distribution as close to the measured one as possible. The computational grid consists of 320 control volumes in the streamwise direction and 128 volumes in the transverse direction. The thickness of the first volume adjacent to the convex wall is about 0.5 viscous units through the whole wall. Computations were performed also using a medium grid (160×64) and a coarse grid (80×32). It was found that the medium grid would have been sufficiently fine, actually. The shear-stress profiles computed using the fine and the medium grids were virtually identical, while those obtained with the coarse grid differed to some extent.

The skin-friction coefficient along the convex wall is shown in Fig. 5.2. The reference velocity used for nondimensionalizing the results, U_{pw}, is the local wall value of the corresponding potential flow. Clearly, both the CC-WJ EARSMs as well as the RSM agree well with the measurements, while the standard EARSM slightly overestimates the wall shear-stress, as expected. The eddy-viscosity model gives clearly wrong results as it is completely insensitive to the effects of curvature. The velocity and turbulent shear-stress distributions in the rear part of the curved wall ($s = 71$ in) are shown in Fig. 5.3. The velocity and shear stress are expressed in the curvilinear coordinate system following the tangential and normal directions of the inner wall. Comparisons at more upstream locations within the curved part $s = 59$ in and $s = 67$ in are shown in Ref. [118]. These are not repeated here because they are very similar to the results at $s = 71$ in. The differences in the velocity profiles are visible but quite small, while the shear-stress distributions reveal the differences very clearly. The turbulent shear stress $-\overline{u'v'}$ is damped by the curvature effect. This damping effect is most pronounced in the outer part of the boundary layer. The RSM and the CC-WJ EARSMs capture this damping effect quite accurately in this case, while the standard EARSM captures it only partially. This is clear, because the streamline curvature enters in the RSM mainly in two terms, the production and the convection. The standard EARSM only involves the former effect while the idea behind the curvature correction technique is to approximate the latter one. As a result, the CC-WJ EARSM gives a remarkable reduction in β_1 and consequently in μ_T in comparison with the standard EARSM. The choice of the method to approximate $\omega_3^{(r)}$ makes no difference in this case.

The curvature correction does not seem to significantly affect the stability and the convergence rate of the computations in this particular case. The CC-WJ EARSM needs only a few percent more computing time per iteration cycle than the standard EARSM and roughly 10–12% more than the EVM. In contrast to this, the RSM needs about 50% more computing time per iteration cycle than the EVM. Furthermore, the convergence rate of the RSM computations was significantly lower, so that the total computing time became several times larger than with all the other models studied here.

5.3.4 Plane U-Duct Flow

Next, a flow with stronger curvature effects will be studied. The plane U-duct flow experimentally studied by Monson *et al.* [119, 120] is such a flow, since the radius of curvature is of the same order as the integral length-scale of turbulence which can be estimated by the turbulent length-scale $k^{3/2}/\varepsilon$. Ratio of this length scale to the radius of wall curvature is about 0.7 in this case. Note, that this is more than ten times larger than in the So & Mellor flow. Rumsey *et al.* [124] have studied the curvature-corrected EARSM also in this particular flow. In this case, however, the curvature effect is not isolated as in the So & Mellor flow. In addition to the streamline curvature, there are strong pressure gradients, flow separation, and some three-dimensional phenomena. Therefore, excellent agreement with the experiments cannot be expected from the computed results.

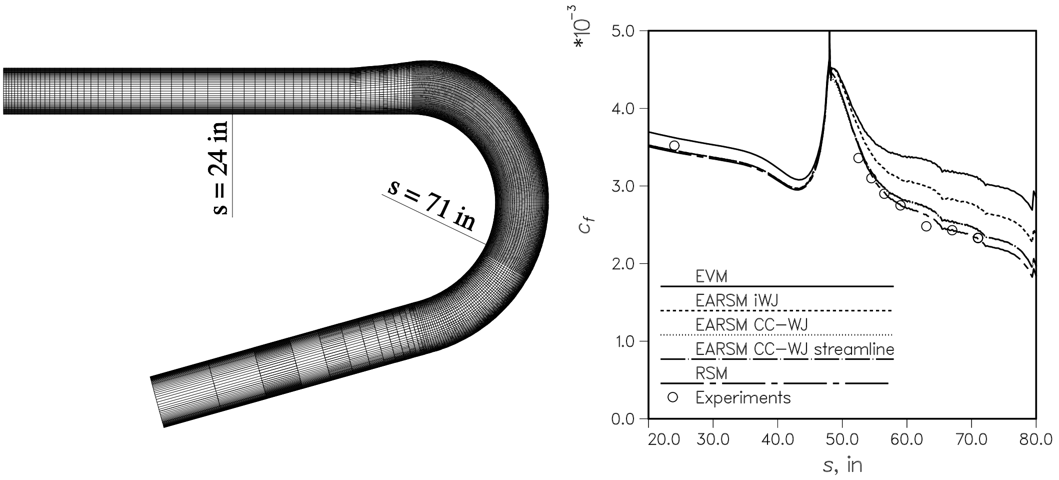

Figure 5.2: Computational grid for the convex-curved boundary layer case, and the skin-friction coefficient along the convex wall. The flow direction is downwards.

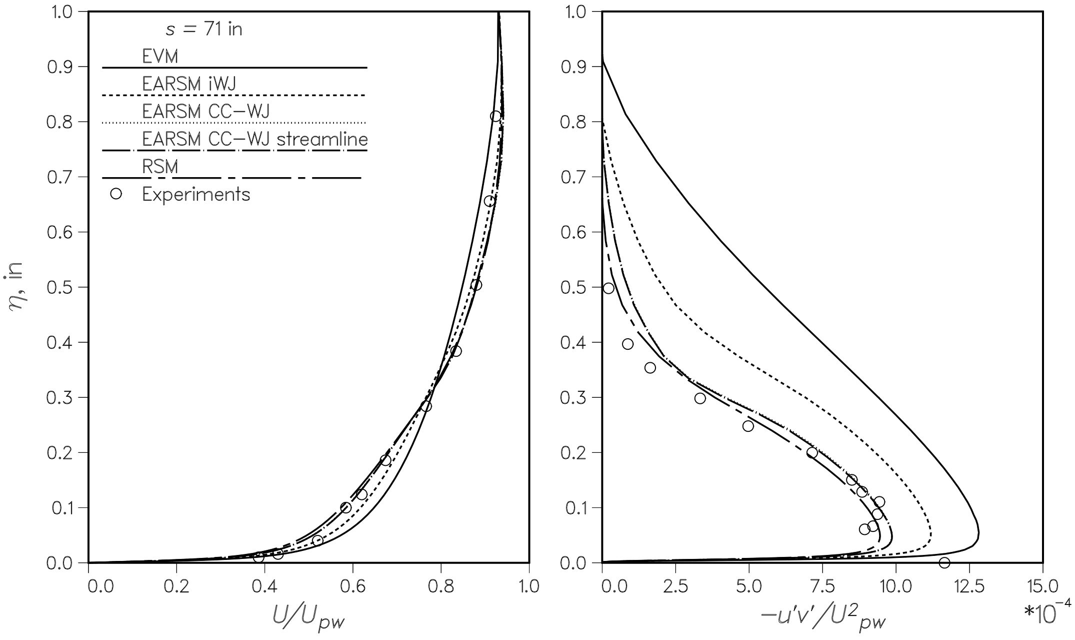

Figure 5.3: The convex-wall boundary layer. Velocity profiles (left) and turbulent shear stresses (right) in the section where $s = 71$ in. Note that the stresses are transformed into the local wall-tangential and -normal coordinate system.

The Reynolds number based on the channel height h and the bulk velocity is 10^6. The computational domain extends $4h$ upstream from the beginning of the curved part and $12h$ downstream from the end of the curved part. The inlet boundary conditions were approximated from the experimental data. The computational grid consists of 288×160 control volumes in the streamwise and transverse directions, respectively. The thicknesses of the first volumes adjacent to the walls vary from 0.2 to 1.2 viscous units. The computations were repeated also using a coarser grid (144×80). No significant differences were found in the results obtained with the fine and coarse grids.

The computations were performed using the same models as for the So & Mellor flow, except the EVM. The velocity and Reynolds shear-stress profiles (in the curvilinear wall-tangential and -normal system) are shown in Fig. 5.4 at two locations, at the beginning of the curved part ($\theta = 0$ deg), and in the middle of it ($\theta = 90$ deg). The Reynolds stress components $\overline{u_1'u_1'}$, $\overline{u_1'u_2'}$, and $\overline{u_2'u_2'}$ are also shown as colour plots in Fig. 5.5. Experimental results are available also at $\theta = 180$ deg and even further downstream. The flow separates near the location $\theta = 180$ deg and it is no more dominated by direct curvature effects. The separated flow is not very accurately captured by any of the present computations, see Ref. [118]. Only the locations $\theta = 0$ deg and $\theta = 90$ deg are studied here in order to focus on modelling of the direct curvature effects. Fig. 5.4 shows that the differences in the velocity profiles computed with different models are almost negligibly small. This is because the pressure gradient strongly dominates over the Reynolds-stress gradient in the mean-momentum equations.

There are large differences between the predicted shear stresses already in the beginning of the curved part. The strain-rate-based correction allows best agreement with the measurements near the convex wall. The streamline correction and the RSM also give shear-stress profiles close to the measured data and the results of Rumsey *et al.* [124]. The standard EARSM predicts a shear-stress profile that largely follows the strain rate and is therefore of opposite sign to the experimentally observed values, except in the immediate vicinity of the wall. The effect of the curvature correction here is primarily to reduce significantly the coefficient β_1 of the first-order term in the polynomial expression for a_{ij}, see Eqs. (2.56) and (6.112). Owing to this reduction, the second-order term,

$$\beta_4 \left(S_{1k}\Omega^*_{k2} - \Omega^*_{1k}S_{k2}\right) = \Omega^*_{12} \left(S_{11} - S_{22}\right) \tag{5.16}$$

which is of opposite sign, becomes dominant. As a result of this, the right sign and magnitude are predicted for the shear stress in this area. Near the outer wall, the CC-WJ variants seem to overestimate the shear stress to some extent in this station.

In the middle of the curved duct ($\theta = 90$ deg), the predicted shear stress is almost zero near the inner side of the duct, except in the near-wall region. This is also in quite a good agreement with the experiments, and in a very good agreement with the results of Rumsey *et al.* [124]. The RSM predicts a small amount of positive $\overline{u_1'u_2'}$ while the CC-WJ variants give practically zero shear stress in this region, see also Fig. 5.5. The colour plots also reveal that, according to the RSM, the reversal of the normal-stress anisotropies takes place in this region, that is, $\overline{u_2'u_2'} > \overline{u_1'u_1'}$.

This is also predicted with the CC-WJ models. This phenomenon is known to occur in shear flows subjected to rapid spanwise rotation, see for example, Bech and Anderson [125]. On the outer side of the duct, all models agree with each other reasonably well in this station. However, the predicted shear stresses are by far too low in comparison with the experiments. This difference is likely owing to streamwise Taylor-Görtler vortices typically found in concave-curved boundary layers, see Monson *et al.* [119]. Such vortices should probably be distinguished from the turbulent motion because they are quite deterministic in structure. The present two-dimensional computations naturally do not capture such vortices, and the turbulence models are not designed to model such non-turbulent instabilities. The effect of these vortices is, however, included in the measured stresses. The effect of this is also seen in the mean-velocity profile near the outer wall. Experiments indicate a fuller profile than the computations due to the enhanced mixing of the streamwise mean-momentum. It is assumed that the Taylor-Görtler vortices could be captured by a three-dimensional simulation. Averaged results from such a simulation should be in a better agreement with the measurements also near the outer wall. In this case, the use of the curvature correction seems to reduce the numerical stability and the convergence rate to some extent, but these were still clearly better than with the RSM.

5.3.5 Three-Dimensional Swirling Flow in a Model Combustor

Swirling flows involve additional strain components which may significantly influence the turbulence. The eddy-viscosity models are known to be unable to correctly capture these effects. The sensitivity of the algebraic Reynolds-stress models to the swirl effects is dependent on the coordinate system in which the weak-equilibrium assumption is made just like the sensitivity to planar curvature. Swirling flow is merely a more complex example of a curved flow. Therefore, the curvature-corrected EARSM is next validated using the model combustor flow experimentally studied by Roback and Johnson [126]. The geometry and the flow are axisymmetric and the swirl velocity is induced by the inflow boundary conditions, see Fig. 5.6.

The computational domain is a 2-degree sector beginning from the inlet plane and extending several tens of chamber diameters downstream of the interesting area. The domain is discretized using a grid consisting of 256 cells in the axial and 72 cells in the radial directions. Only one layer of cells is used in the circumferential direction, and the circumferential homogeneity is enforced using cyclic boundary conditions. The inflow boundary conditions are approximated by interpolating the experimental data. The high swirl rate tends to induce such a low pressure on the axis of revolution that flow reversal through the outflow boundary may take place if it is not brought sufficiently far away from the inflow plane. This is why the computational domain is made very long. The present results are not guaranteed to be completely grid independent. However, comparison with results obtained using still coarser 128×36 grid indicate that the grid dependence is small enough to make at least qualitative conclusions.

The CC-EARSM is tested using two different ways to obtain $\omega_i^{(r)}$: Eq. (5.12),

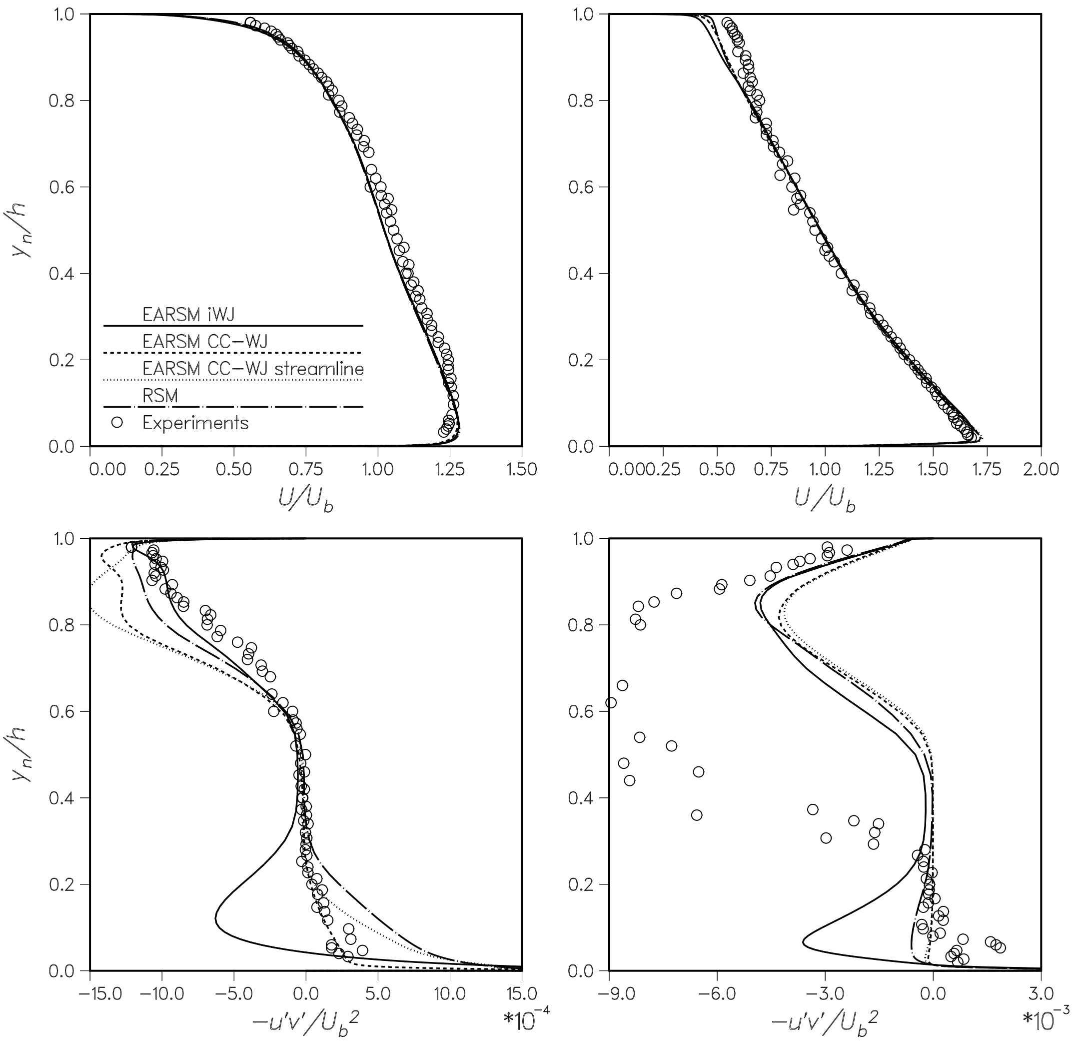

Figure 5.4: The U-duct flow. Velocity profiles (upper row) and turbulent shear stresses (lower row) in the beginning of the curved part, $\theta = 0$ deg (left), and in the middle of it, $\theta = 90$ deg (right). Note that the stresses are transformed into the local wall-tangential and -normal coordinate system. (Figure taken from Ref. [118].)

and a simplified streamline method that accounts for the azimuthal velocity component W only. Owing to the axisymmetry, this is simply

$$\omega_i^{(r)} = \delta_{i1}\frac{W}{r} \tag{5.17}$$

where r is the local radius from the axis of revolution. In the downstream part of the chamber, the radial velocity component and the axial derivatives are small, and the correction should then approach that of Eq. (5.17). Close to the inflow plane, (5.17) is expected to be in error, and the θ-component of the rotation rate becomes non-zero due to curvature in the $x - r$ plane. See Ref. [118] for more results. The CC-EARSM results are compared with the experimental data, with results computed using an RSM, with standard iWJ EARSM results, and with linear eddy-viscosity results. The RSM used in this case is not exactly the parent model of the EARSM.

This particular RSM is of general linear type and the model coefficients are reported by Rung *et al.* [127] in the context of another algebraic model derived from it. Also the linear eddy-viscosity model differs from the BSL $k - \omega$ model. In this case, the RSM- and the EVM-results are not computed by the author. Instead, they have been provided by T. Rung and M. Schatz from Hermann Föttinger Institut at Technical University of Berlin, see [121]. All other computational results presented in this study are produced by the author.

The axial and circumferential mean-velocity components as well as the shear-stress components $\overline{uv}$ and $\overline{vw}$ are shown in Fig. 5.7 at the station $x = 406$ mm, see Fig. 5.6. An excessive axial velocity defect on the axis of revolution predicted by the CC-EARSMs and by the RSM is a salient feature. The linear eddy-viscosity model (EVM) predicts a linear rise of the azimuthal velocity similar to a solid-body motion. The standard iWJ EARSM captures the curvature effect on the production term and this leads to a slightly better but still qualitatively wrong azimuthal velocity profile. The full differential Reynolds stress model is able to predict also the curvature effects entering in the convective term. Therefore, the RSM gives a rather good representation of the velocity profiles. The CC-EARSM using (5.12) as well as the a priori curvature correction according to (5.17) leads to results of almost the same quality as that of the RSM. The most important shear stress $\overline{vw}$ in the regions of low strain-rate downstream the of recirculation is in a very good agreement with that obtained by the RSM.

The outflow conditions that do not properly model the experimental setup are probably the origin of the axial velocity dip on the axis. The high swirl rate induces low pressure near the axis and this makes the flowfield very sensitive to the outflow conditions. The experimental setup featured an endplate at $x \approx 1000$ mm and an exhaust duct mounted at a 90° angle relative to the chamber axis. This was not known at the time of the computations. Attempts to better simulate the outflow will be left for the future work.

The convergence rates of all computations in this case were slow. This is partially owing to the stiffness introduced by the very long computational domain. The strain-rate based curvature corrections tend to inhibit the convergence rate even more. The streamline-based correction seems not to have such an unfavourable effect in this case.

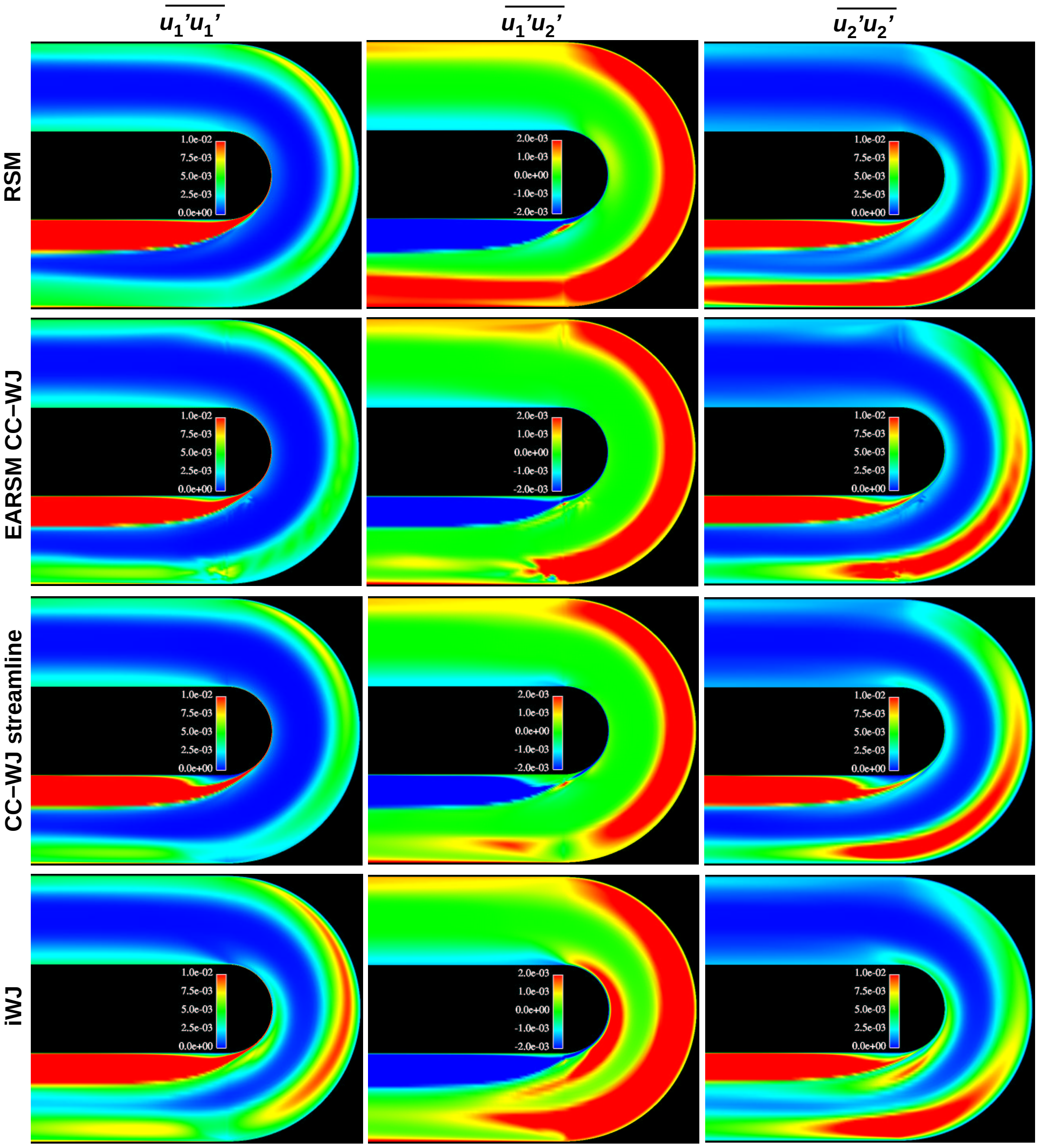

Figure 5.5: Reynolds stress components in a curvilinear coordinate system following the wall-tangential and -normal directions. From top to bottom: differential Reynolds stress model, curvature corrected EARSMs using Eq. (5.12), and the streamline method, and in the last line, the standard EARSM derived in an inertial coordinate system (iWJ). (Figure taken from Ref. [118].)

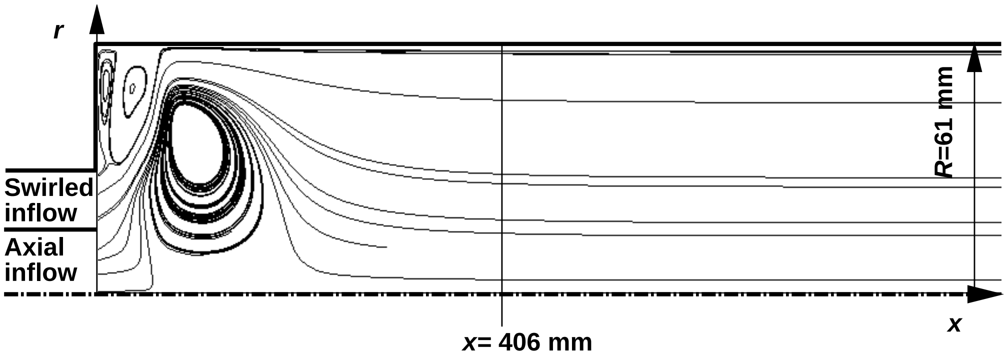

Figure 5.6: An illustration of the swirling combustor by Roback and Johnson (1983) with a typical streamline pattern (projected onto the plane). The vertical line indicates the location where the velocity profiles are studied. Note the horizontal shrinking of the image. (Figure taken from Ref. [118].)

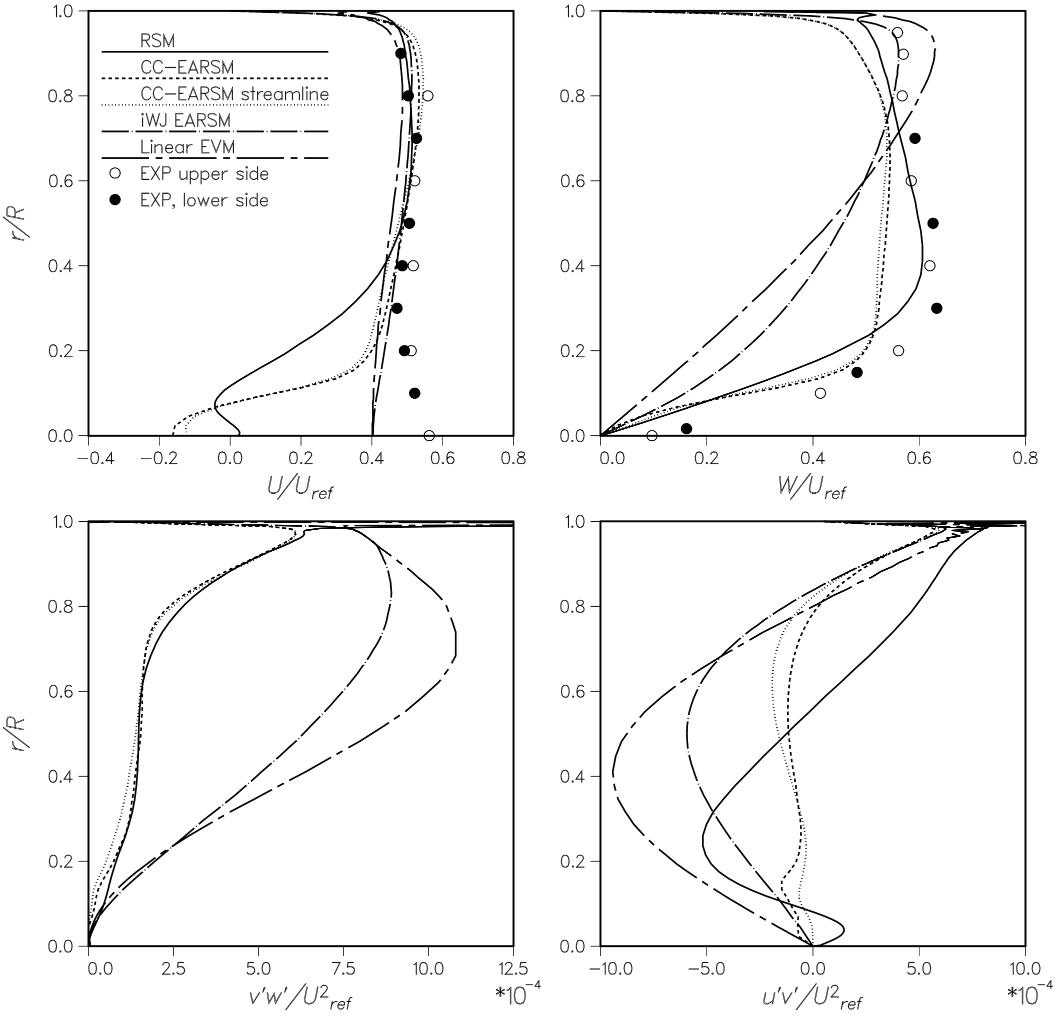

Figure 5.7: Velocity and shear-stress distributions in the model combustor at the station $x = 406$ mm. (Figure taken from Ref. [121].)

6 Scale-Determining Model

6.1 Starting Point

As was concluded in Chapter 3, the most promising two-equation models for aerodynamical applications, especially for high-lift aerodynamics, seem to belong to the category of the $k-\omega$ models. Thus, the $k-\omega$ models are selected for in-depth studies and for further development discussed in this chapter. The development aims at a new $k-\omega$ model that is suitable for high-lift aerodynamics problems. It is strictly designed to be used with the EARSM of Wallin & Johansson as the constitutive model.

The development work starts from theoretical studies of some idealized flow situations in Section 6.2. The analysis of the edge region between turbulent and laminar flow is the most important of these. Constraints for the model coefficients are derived as a result of the theoretical considerations. After this, existing $k-\omega$ models are reviewed in Section 6.3, and possibilities to extend them to the EASRM level are studied as well. The actual development of the new model then starts from Menter's $k-\omega$ BSL model [3]. The simple scalar-diffusivity gradient transport model for the turbulent transport and pressure diffusion terms (2.46) are kept, although the generalized gradient diffusion model of Daly and Harlow [30], or any other more complicated model, could have been chosen as for many other nonlinear two-equation models. It is, however, believed that the present choice makes the model more robust and numerically stable. Furthermore, it makes the model slightly simpler and easier to implement.

The existing $k-\omega$ models are not designed to be used with the EARSM or with any other higher-order constitutive model. Therefore, when combined with EARSM, some problems arise. Also, the original models that use the linear Boussinesq constitutive model have some weaknesses, which may have significant influence in high-lift aerodynamic problems. For instance, as will be shown in Section 6.3.2, Menter's model predicts the planar far wake and the mixing layer flows to spread clearly too slowly. Furthermore, its solutions for shear layers feature unphysically sharp edges. When combined with the EARSM, somewhat too low friction coefficient is predicted for a simple flat-plate boundary layer. Another fault of this model combination in the same elementary flow is that the velocity profile in the defect layer has a qualitatively wrong shape. There is a shallow pit in the profile, shown also in Sec. 6.3.2. These elementary flows play an important role in multi-element aerofoil problems. Such anomalies, among the observations made on the other $k - \omega$ models show that the constitutive model cannot be just replaced by another one without any recalibration of the scale-determining model.

After the new model is developed, calibrated, and validated for certain elementary flows, its sensitivity to the free-stream values is carefully studied. Finally, a systematic survey is made to look for possible other operational variables for which the model could be alternatively formulated to avoid some criticized features of the ω-formulation.

The new $k - \omega$ model proposed in this study is calibrated for such "building-block flows" that are relevant for high-lift aerodynamics. These are: fully developed plane channel flow, equilibrium boundary layers with zero, adverse, and favourable pressure gradients, planar far-wake flow, and a planar spatially evolving mixing layer. The calibration is assessed and fine-tuned using more complex two-dimensional flow problems such as flows around aerofoils, see Chapter 7.

The benefits of the new model over Menter's models are at least:

1. It predicts the wake and the mixing layer flows with clearly better accuracy.
2. It has a better behaviour on the edges of turbulent regions.
3. It is especially designed for the EARSM as the constitutive model.
4. As an EARSM-based model, it has more potential to predict complex flows.

The new model is, of course, designed to inherit the favourable features of Menter's models. One of these is that the model equations can be solved down to the wall with no *ad-hoc* near-wall damping or correction functions. Another important advantage, especially in high-lift aerodynamics, is that Menter's model, as well as Wilcox's model, gives the turbulent length-scale in the wall layer of APG boundary layers reasonably close to the experimentally observed values, while the $k - \varepsilon$ models typically predict far too high length-scale values. Owing to this fact, these models are able to predict adverse pressure-gradient boundary layers more accurately than most of the other models. Menter's idea was to transform the standard $k - \varepsilon$ model into the ω-form and to combine the favourable features of it and Wilcox's $k - \omega$ model. This approach is not followed in this work, although two sets of model coefficients are mixed in an almost similar fashion as in Menter's work. In this work, both sets of model coefficients are systematically calibrated without following any existing model.

For the development phase, the following definition for ω is used

$$\omega \equiv \frac{\varepsilon}{k} \tag{6.1}$$

and the model equations are formulated according to this definition. Finally, the model is rewritten also using the traditional definition $\omega \equiv \varepsilon/(\beta^* k)$. The starting point model equations can now be written as

$$\begin{aligned} \frac{\mathrm{D}k}{\mathrm{D}t} &= P - \varepsilon + \frac{\partial}{\partial x_j}\left[(\nu + \sigma_k \nu_T)\frac{\partial k}{\partial x_j}\right] && (6.2) \\ \frac{\mathrm{D}\omega}{\mathrm{D}t} &= \frac{\omega}{k}(C_{\omega 1}P - C_{\omega 2}\varepsilon) + \frac{\partial}{\partial x_j}\left[(\nu + \sigma_\omega \nu_T)\frac{\partial \omega}{\partial x_j}\right] + \frac{\sigma_d}{\omega}\frac{\partial k}{\partial x_j}\frac{\partial \omega}{\partial x_j} && (6.3) \end{aligned}$$

with all five model coefficients $C_{\omega 1}$, $C_{\omega 2}$, σ_k, σ_ω, and σ_d yet unspecified.

6.2 Constraints for the Model Coefficients

Some constraints for the model coefficients can be derived from analytical solutions to the model equations. Analytical solutions exist only in some of the most idealized flow situations. In this study, the following cases are exploited: decaying isotropic turbulence in homogeneous undistorted flow, turbulence in homogeneous shear flow, turbulence in the logarithmic layer of a ZPG boundary layer, and an idealized free-stream edge of a shear layer. These cases, except the last one, can be found in most of the turbulence modelling textbooks, see for instance [22]. The last one of these is considered the most important case in this study. The obtained constraints can be used as lower and upper limits for the calibration range of most of the coefficients.

6.2.1 Decaying Isotropic Turbulence in Homogeneous Undistorted Flow

The decay rate of approximately isotropic grid-generated turbulence in homogeneous undistorted mean flow can be measured in a wind tunnel. After the grid, there will be no mean-flow gradients and thus no production. The turbulence will start to slowly decay, and it also tends towards isotropy owing to the lack of mean strain or any other directional forcing. After the initial transient, the decay of the turbulent energy has been observed to approximately follow the law

$$k(x) = \frac{A k_0}{(x/h+1)^q} \tag{6.4}$$

where h is the wire spacing of the turbulence-generating grid and it acts as the length scale in this flow, and A is a coefficient that depends on the Reynolds number and on the details of the mesh geometry [23]. In these circumstances, the $k-\omega$ equations reduce to

$$U\frac{\mathrm{d}k}{\mathrm{d}x} = -\varepsilon = -k\omega \tag{6.5}$$

$$U\frac{\mathrm{d}\omega}{\mathrm{d}x} = -C_{\omega 2}\omega^2 \tag{6.6}$$

The diffusion terms have been dropped, because the decay process is slow, so that also the turbulence is almost homogeneous. The solution for ω is simply

$$\omega(x) = \frac{U}{C_{\omega 2} h}\frac{1}{(x/h+1)} \tag{6.7}$$

Substitution of ω from (6.7) and k from (6.4) into (6.5) yields

$$C_{\omega 2} = \frac{1}{q} \tag{6.8}$$

The decay rate has been measured in various experiments, but the results are quite scattered. Values of q between 1.1 and 1.5 are reported in the literature. This implies that

$$0.67 \leq C_{\omega 2} \leq 0.91 \tag{6.9}$$

This should not be taken as a strict constraint because of the high uncertainty in the experimental data. It gives, however, a hint of a suitable value for $C_{\omega 2}$. Wilcox's $k-\omega$ model has $C_{\omega 2} = \beta/\beta^* = 0.83$ which is close to the midpoint of this range. The standard $k-\varepsilon$ (transformed into ω-form) has $C_{\omega 2} = 0.92$ which is at the upper end of the recommended range.

6.2.2 Homogeneous Shear Flow

In a homogeneous shear flow, the equations for k and ω reduce to

$$\begin{aligned}
\frac{\mathrm{d}k}{\mathrm{d}t} &= P - k\omega && (6.10)\\
\frac{\mathrm{d}\omega}{\mathrm{d}t} &= C_{\omega 1}\frac{\omega}{k}P - C_{\omega 2}\omega^2 && (6.11)
\end{aligned}$$

and $P = -\overline{u'v'}\mathrm{d}U/\mathrm{d}y$. The turbulent shear stress can be expressed using the anisotropy as $\overline{u'v'} = a_{12}k$. By substituting these, the equations become

$$\begin{aligned}
\frac{\mathrm{d}k}{\mathrm{d}t} &= -a_{12}\frac{\mathrm{d}U}{\mathrm{d}y}k - k\omega && (6.12)\\
\frac{\mathrm{d}\omega}{\mathrm{d}t} &= -C_{\omega 1}a_{12}\frac{\mathrm{d}U}{\mathrm{d}y}\omega - C_{\omega 2}\omega^2 && (6.13)
\end{aligned}$$

It is known from the experiments that k grows exponentially while P/ε and a_{12} obtain constant values, when $\mathrm{d}U/\mathrm{d}y$ is kept constant. The fact that

$$\frac{P}{\varepsilon} = -a_{12}\frac{k}{\varepsilon}\frac{\mathrm{d}U}{\mathrm{d}y} \tag{6.14}$$

implies that also ε grows exponentially and thus ω remains constant. Constant $\omega = \omega_0$ really satisfies (6.13) and

$$\omega_0 = -a_{12}\frac{\mathrm{d}U}{\mathrm{d}y}\frac{C_{\omega 1}}{C_{\omega 2}} \tag{6.15}$$

Substitution of ω_0 from (6.15) and the trial $k(t) = k_0 e^{\lambda t}$ into (6.12) gives

$$\lambda = a_{12}\frac{\mathrm{d}U}{\mathrm{d}y}\left(\frac{C_{\omega 1}}{C_{\omega 2}} - 1\right) \tag{6.16}$$

and

$$\frac{P}{\varepsilon} = \frac{C_{\omega 2}}{C_{\omega 1}} \tag{6.17}$$

The measurements [128] have indicated that P/ε is between 1.4 and 1.8. Using this, the limits for $C_{\omega 1}$ as functions of $C_{\omega 2}$ are

$$\frac{C_{\omega 2}}{1.8} \leq C_{\omega 1} \leq \frac{C_{\omega 2}}{1.4} \tag{6.18}$$

The difference of $C_{\omega 2}$ and $C_{\omega 1}$ is very important, because it largely controls the spreading rate of free shear flows, such as wakes, which are considered important in this study.

6.2.3 Log-Layer

The logarithmic layer of a zero pressure-gradient (ZPG) boundary layer is the third special case where the equations can be simplified enough so that an analytical solution can be found. This is because the convection can be assumed to be negligible for all variables U, k, and ω, because k is constant in the log-layer, and third, because the mean velocity gradient is readily obtained from the logarithmic velocity profile as

$$\frac{\mathrm{d}U}{\mathrm{d}y} = \frac{u_\tau}{\kappa y} \tag{6.19}$$

The shear stress is also constant and known since $-\overline{u'v'} = u_\tau^2$. On the other hand, $-\overline{u'v'} = -a_{12}k$, thus $k = -u_\tau^2/a_{12}$. Using these, we obtain

$$-\overline{u'v'}\frac{\mathrm{d}U}{\mathrm{d}y} = P = \frac{u_\tau^3}{\kappa y} \tag{6.20}$$

The equation for k reduces to $P = \varepsilon$, thus ε is known, too. Therefore, $\omega = \varepsilon/k = -a_{12}u_\tau/(\kappa y)$. Finally, the eddy viscosity is defined as $\nu_T = C_\mu k/\omega$, where C_μ may have a constant value of β^* in case of linear constitutive modelling, or it may be variable if more general constitutive modelling is employed. The formula for σ_ω is obtained by inserting the above results into the ω-equation, which in these conditions reduces to

$$\sigma_\omega \frac{\mathrm{d}}{\mathrm{d}y}\left(\nu_T \frac{\mathrm{d}\omega}{\mathrm{d}y}\right) + \frac{\omega}{k}(C_{\omega 1}P - C_{\omega 2}\varepsilon) = 0 \tag{6.21}$$

This gives

$$\sigma_\omega = \frac{a_{12}^3}{\kappa^2 C_\mu}(C_{\omega 2} - C_{\omega 1}) \tag{6.22}$$

The anisotropy a_{12} is

$$a_{12} = -C_\mu \frac{1}{\omega}\frac{\mathrm{d}U}{\mathrm{d}y} = C_\mu \frac{u_\tau}{\kappa y}\frac{\kappa y}{a_{12}u_\tau} \tag{6.23}$$

yielding

$$a_{12} = -\sqrt{C_\mu} \tag{6.24}$$

and finally

$$\sigma_\omega = \frac{\sqrt{C_\mu}}{\kappa^2}(C_{\omega 2} - C_{\omega 1}) \tag{6.25}$$

This would imply that σ_ω should not be constant but a function of the variable C_μ. However, it happens that C_μ really is almost constant in a ZPG log-layer and the classical value of 0.09 can well be used in (6.25).

6.2.4 Edges of Shear Layers

The idealized edge problem

So far, no constraints for the coefficients σ_k and σ_d have been derived. The following analysis of the model behaviour near the edges of laminar and turbulent flow will provide constraints for the diffusion coefficients. Also σ_ω will have another constraint for the outer-edge region in addition to (6.25), which is active in the logarithmic layer.

The behaviour of two-equation turbulence models on the edge regions between turbulent and laminar flows can be understood with the aid of the analysis first deduced by Cazalbou *et al.* [129]. Furthermore, this approach provides constraints for the diffusion coefficients. A model that satisfies these constraints behaves properly near the free-stream edges of turbulent regions, and it should show no anomalous sensitivity to the free-stream values. This is confirmed by numerical tests, see Section 6.4.6.

Cazalbou *et al.* assumed that the turbulent transport (modelled as turbulent diffusion) balances the transport by mean flow, while the production and destruction terms and also the molecular viscosity are negligible on the outer edges of turbulent shear layers. This means that the model equations reduce to a nonlinear convection-diffusion problem locally in such regions. Moreover, one-dimensionality must be assumed in order to be able to find an analytical solution. The practical problems are multi-dimensional, of course, even locally in the edge zone. However, the velocity gradient as well as the gradients of the turbulent scales are often quite well aligned with the edge-normal direction especially in thin shear flows that are in an equilibrium state, *e.g.* equilibrium boundary layers, far wakes, etc. The simplified one-dimensional problem is considered to be physically relevant with such situations. The exact conditions for the physical validity of the one-dimensional problem are as follows. The molecular viscosity is negligibly small ($Re \to \infty$). This is thought to be a reasonably realistic assumption also at large finite Reynolds numbers since ν_T is comparable with ν only in a narrow zone around the edge as ν_T goes to zero linearly according to the solutions that are to be derived. Both the mean-flow transport and turbulent transport are assumed to be aligned with the edge-normal direction, and the entrainment velocity

$$U_e \sin\left(\frac{\mathrm{d}\delta}{\mathrm{d}x}\right) - V_e \cos\left(\frac{\mathrm{d}\delta}{\mathrm{d}x}\right) \approx U_e \frac{\mathrm{d}\delta}{\mathrm{d}x} - V_e \tag{6.26}$$

is constant along the edge. U_e and V_e are the mean-velocity components at the edge. In (6.26), $\mathrm{d}\delta/\mathrm{d}x$ denotes the streamwise rate at which the turbulent layer penetrates into the surrounding flow, or which is equivalent, the angle between the edge and the velocity of the free flow. This angle is usually quite small, and hence the simplified form of (6.26) is often adequate. In practice, the entrainment velocity is seldom constant along the edge, but it often varies relatively slowly. Finally, the convective velocity is assumed to be constant near the edge. This is a rather realistic assumption since we are only interested in a relatively narrow zone near the edge where changes in the convective velocity are typically small. After all, it is assumed that the behaviour of the original equation system can be understood by studying a simplified one-dimensional nonlinear convection-diffusion problem. The dominance of the transport terms over the production and dissipation will be checked after the solution is found.

Near the edge, the mean-momentum equation and $k-\omega$ model equations reduce to

$$\begin{aligned} \mathcal{V}\frac{\mathrm{d}U}{\mathrm{d}y} &= \frac{\mathrm{d}}{\mathrm{d}y}\left(\nu_T\frac{\mathrm{d}U}{\mathrm{d}y}\right) \\ \mathcal{V}\frac{\mathrm{d}k}{\mathrm{d}y} &= \frac{\mathrm{d}}{\mathrm{d}y}\left(\sigma_k\nu_T\frac{\mathrm{d}k}{\mathrm{d}y}\right) \\ \mathcal{V}\frac{\mathrm{d}\omega}{\mathrm{d}y} &= \frac{\mathrm{d}}{\mathrm{d}y}\left(\sigma_\omega\nu_T\frac{\mathrm{d}\omega}{\mathrm{d}y}\right) + \sigma_d\frac{\nu_T}{k}\frac{\mathrm{d}k}{\mathrm{d}y}\frac{\mathrm{d}\omega}{\mathrm{d}y} \end{aligned} \tag{6.27}$$

Note, that the factor $1/\omega$ in the cross-diffusion term must here be replaced by ν_T/k in order to find a solution also in case of variable C_μ. The convective velocity $\mathcal{V}$ may be associated with the entrainment velocity (6.26) of some real problem, and, as stated above, it must be assumed to be constant. In this problem, all the variables U, k, and ω are defined as positive quantities that go to zero on the edge. Thus U can be considered either as a velocity defect of a wake-like flow or a velocity excess of a jet-like flow. Cazalbou *et al.* presented a solution to a corresponding problem for the $k-\varepsilon$ models, and later Kok [130] carried out a similar analysis for the $k-\omega$ models of the form of (6.2) and (6.3). Cazalbou *et al.* and Kok formulated the problem in a moving coordinate frame to make $\mathcal{V}$ zero. In such a frame, the problem takes the form of an unsteady nonlinear diffusion problem. The present system of equations (6.27), which is written in a stationary frame, is obtained from Kok's equations, or vice versa, by a simple Galilean transformation.

Solution of linear models with constant C_μ

Kok found that the following power functions form at least a weak solution to (6.27) if σ_k, σ_ω, and σ_d are suitably selected [130]:

$$U(y) = U_0 f^{\sigma_k\sigma_\omega/(\sigma_\omega-\sigma_k+\sigma_d)} \tag{6.28}$$

$$k(y) = k_0 f^{\sigma_\omega/(\sigma_\omega-\sigma_k+\sigma_d)} \tag{6.29}$$

$$\omega(y) = \omega_0 f^{(\sigma_k-\sigma_d)/(\sigma_\omega-\sigma_k+\sigma_d)} \tag{6.30}$$

where

$$f(y) = \max\left(\frac{\delta_0 - y}{\delta_0}; 0\right) \tag{6.31}$$

Here, U_0, k_0, ω_0, and δ_0 are the characteristic scales of the problem, and the convective velocity becomes

$$\mathcal{V} = -\frac{\sigma_k \sigma_\omega}{\sigma_\omega - \sigma_k + \sigma_d} \frac{C_\mu k_o}{\omega_0 \delta_0} \tag{6.32}$$

Note that here C_μ is not absorbed into the definition of ω as in Ref. [130]. Depending on the values of the diffusion coefficients, it may happen that (6.28) – (6.30) are not differentiable enough at $y = \delta_0$ to form a rigorous solution of (6.27). In such a case, Eqs. (6.28) – (6.30) can be considered a weak solution. For proof, see Ref. [129].

Now, constraints can be derived from the requirements that (6.28) – (6.30) must be non-singular to form at least a weak solution to the problem, and that the slope of the velocity remains bounded at the edge. The resulting conditions are

$$\sigma_\omega - \sigma_k + \sigma_d > 0 \tag{6.33}$$

$$\sigma_k - \sigma_d > 0 \tag{6.34}$$

$$\sigma_\omega - \sigma_k + \sigma_d \leq \sigma_k \sigma_\omega \tag{6.35}$$

If a smooth edge is required from the solution, then "$\leq$" must be replaced by "$<$" in (6.35). To ensure that diffusion really dominates over production and dissipation, we have to require the exponent of f in the production and dissipation terms to be larger than that in the diffusion term. If C_μ is assumed constant, these terms of the k-equation can be written as

$$\frac{\mathrm{d}}{\mathrm{d}y}\left(\sigma_k \nu_T \frac{\mathrm{d}k}{\mathrm{d}y}\right) \sim f^{(\sigma_k - \sigma_d)/(\sigma_\omega - \sigma_k + \sigma_d)} \tag{6.36}$$

$$P = \nu_T \left(\frac{\mathrm{d}U}{\mathrm{d}y}\right)^2 \sim f^{[(2\sigma_k - 1)\sigma_\omega + \sigma_k - \sigma_d]/(\sigma_\omega - \sigma_k + \sigma_d)} \tag{6.37}$$

$$\varepsilon = k\omega \sim f^{(\sigma_\omega + \sigma_k - \sigma_d)/(\sigma_\omega - \sigma_k + \sigma_d)} \tag{6.38}$$

Thus, the above requirement is satisfied when

$$\sigma_k > 0.5 \quad \text{and} \quad \sigma_\omega > 0 \tag{6.39}$$

Also the source and sink terms of the ω-equation must go to zero more rapidly than its diffusion and cross terms. It is straightforward to show that this is also ensured by satisfying (6.39).

A new solution of a variable C_μ case idealizing nonlinear models

The validity of the above analysis and the applicability of the constraints (6.33) – (6.35) and (6.39) to models utilizing nonlinear constitutive relations, such as EARSMs, is not obvious. This is because the solution (6.28) – (6.30) is only valid for models based on the Boussinesq approximation with constant C_μ. Fortunately, the contribution of the higher-order terms to the principal shear stress in the momentum equation is negligible near the outer edges of shear layers. The present modelling

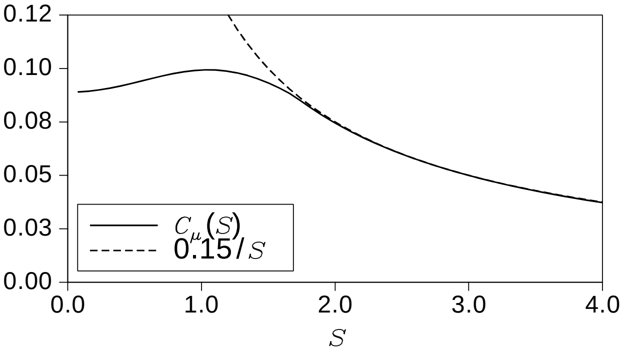

Figure 6.1: C_μ as a function of S according to Wallin-Johansson EARSM in simple parallel flows with $\partial U/\partial y$ being the only nonzero velocity-gradient component.

of the diffusive terms of k and ω is also independent of the higher-order terms. Thus, the only difference that actually must be considered is the fact that C_μ is variable in nonlinear constitutive modelling.

In the following, the analysis is extended for variable C_μ assuming that C_μ is of a similar power form as the solutions of U, k, and ω. A condition that solutions of power form exist is that $\nu_T \sim f$. Since $\nu_T = C_\mu k/\omega$, k/ω must be proportional to f^{1-m} if $C_\mu \sim f^m$. With these assumptions, it is straightforward to show that

$$\begin{aligned}
U(y) &= U_0 f^{\sigma_k\sigma_\omega(1-m)/(\sigma_\omega-\sigma_k+\sigma_d)} = U_0 f^{n_u} \\
k(y) &= k_0 f^{\sigma_\omega(1-m)/(\sigma_\omega-\sigma_k+\sigma_d)} = k_0 f^{n_k} \\
\omega(y) &= \omega_0 f^{(\sigma_k-\sigma_d)(1-m)/(\sigma_\omega-\sigma_k+\sigma_d)} = \omega_0 f^{n_\omega}
\end{aligned} \tag{6.40}$$

satisfy the system (6.27) if $m < 1$. It is immediately seen that if C_μ decreases towards the edge as with $m > 0$, the edges in the solutions become sharper. This may well lead to a situation where the velocity exponent n_u, originally larger than one with constant C_μ, now becomes less than one. The edge will be perfectly sharp with $\mathrm{d}U/\mathrm{d}y$ being indefinite always when $n_u \leq 1$. This is an unphysical situation and may also cause numerical troubles. In practice, the numerical dissipation and the molecular viscosity may alleviate the situation to some extent, but also the numerical solutions will be qualitatively wrong at least when $n_u < 1$. If C_μ increases towards the edge as with $m < 0$, the exponents increase and the solution around the edge just becomes smoother. This has no severe consequences since the Reynolds-averaged distributions around the shear-layer edges are smooth in reality. Now, knowing that C_μ distributions decreasing towards the edge may spoil the solution even qualitatively, this kind of situation must be avoided. Therefore, the question is: in which circumstances could C_μ decrease towards the edge? In the nonlinear constitutive models, C_μ is typically approximately inversely proportional to the nondimensional strain parameter $S = \sqrt{2S_{ij}S_{ji}}$ when S is not small. The actual expression of C_μ in the Wallin-Johansson EARSM is quite complex, see Section 6.6.2, and it is not easily seen that $C_\mu \sim S^{-1}$ at high S-values. Plotting C_μ as a function of S shows that it approximately is, see Fig. 6.1. Therefore, S increasing towards the edge may be an unfavourable situation. Now, S is given by

$$S = \frac{1}{\omega}\frac{\mathrm{d}U}{\mathrm{d}y} \sim f^{[\sigma_k\sigma_\omega(1-m)+(\sigma_k-\sigma_d)m-\ \sigma_\omega]/(\sigma_\omega-\sigma_k+\sigma_d)} \tag{6.41}$$

A situation where S remains constant or decreases when the edge is approached would be favourable. This is achieved when $\mathrm{d}U/\mathrm{d}y$ decreases at least as rapidly as ω. This is the case only if the exponent in (6.41) is non-negative. Hence, a new condition

$$\sigma_k \geq \frac{\sigma_\omega + m\sigma_d}{\sigma_\omega + m(1-\sigma_\omega)} \tag{6.42}$$

is obtained. Now m is an unknown parameter and different values have to be considered. Cases with $m > 0$ are not of interest as it was already seen that positive values of m representing decreasing C_μ are potentially unfavourable, and the aim here is to derive a constraint to avoid solutions with decreasing C_μ. In the case of $m = 0$, this constraint reduces to $\sigma_k \geq 1$. In practice, it may be safer to require

$$\sigma_k > 1 \tag{6.43}$$

This constraint was actually first derived by Bézard [131] very recently when he studied the ratio of production to dissipation based on the solution (6.28) – (6.30) valid for constant C_μ. In the case of $m < 0$, constraint (6.42) becomes less restrictive if $\sigma_d > 1 - \sigma_\omega$. This, in turn, happens always to be the case if (6.33) is satisfied and if $\sigma_k > 1$. Hence, it is sufficient simply to apply (6.43), and thus the former constraint in (6.39) must be replaced by (6.43). The constraints (6.33) and (6.34) remain unchanged, but the constraint (6.35) becomes passive if (6.34) and (6.43) are satisfied. In other words, (6.43) guarantees the edge-smoothness without (6.35). The latter constraint in (6.39) now becomes

$$\sigma_\omega > m(\sigma_k - \sigma_d) \tag{6.44}$$

This constraint is of little importance when m is zero or negative as desired. Finally, all the active diffusion-coefficient constraints, relevant in the nonlinear level of $k-\omega$ modelling, are collected together as follows:

$$\begin{aligned} \sigma_\omega - \sigma_k + \sigma_d &> 0 && (6.45)\\ \sigma_k - \sigma_d &> 0 && (6.46)\\ \sigma_k &> 1 && (6.47) \end{aligned}$$

These constraints are illustrated in Fig. 6.2 for the case $\sigma_k = 1.1$.

It was assumed above that C_μ follows a power function f^m near the edge. Whether this is the case in reality or not depends, of course, on the details of the constitutive model. In the case of the Wallin-Johansson EARSM [4] used here, the dependency between C_μ and S is not that simple. However, at smaller values of S, say, when $S < 1.5$, C_μ is almost constant according to Fig. 6.1. At larger values of S, C_μ is approximately proportional to S^{-p} with $p \approx 1$. If $p = 1$ exactly, then also $m = 1$ and the exponents of U, k, and ω would become zero. However,

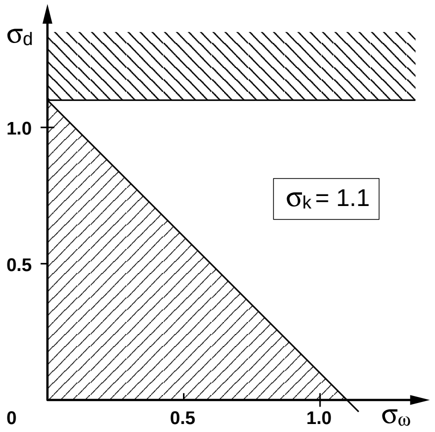

Figure 6.2: Constrained $(\sigma_\omega, \sigma_d)$-space when $\sigma_k = 1.1$, see Eqs. (6.45) – (6.47).

the numerical experiment in the anomalous case, which will be discussed below, show behaviour similar to the case when the exponents are nonzero but the velocity exponent is smaller than one. This is what may happen if $0 < m < 1$ as already discussed. Values of p slightly different from unity may lead to this kind of situation depending on the diffusion-coefficient values. In reality, C_μ of the present EARSM does not exactly follow any power function, but the power function seems to be a sufficiently good approximation for this kind of qualitative analysis.

To learn more about the edge behaviour, numerical studies of a zero pressure-gradient boundary layer are made with three different models: Kok's original linear $k - \omega$ TNT model [130], Kok's model combined with the EARSM, and a generic model (EARSM) having diffusion coefficients $\sigma_k = 1.1$, $\sigma_\omega = 0.8$, and $\sigma_d = 0.74$, which produce $n_u = 2(1 - m)$. Kok's model is designed to satisfy the constraints (6.33) – (6.35) and (6.39), but not the constraint (6.47) as it is a linear Boussinesq model. More specifically, it features $\sigma_k = 2/3$, and $\sigma_\omega = \sigma_d = 1/2$, and thus $n_u = 1 - m$. As seen in Fig. 6.3, it produces an anomalous hook-shaped solution for U on the edge when combined with the EARSM. This is because it predicts S to rapidly increase and thus C_μ to drop near the edge as if $m > 0$. Kok's original linear model gives a sharp edged solution as its $n_u = 1$. The generic model gives a healthy solution with $n_u = 2(1 - m)$ and $m \approx 0$. It turns out that the hook-like solution follows fairly well a power solution with $n_u = 0.7$ or, which is equivalent, $m = 0.3$, although C_μ seems not to follow the 0.3-power function, according to the numerical result. It even does not go to zero on the edge as the assumed power-form. It must be kept in mind that the numerical solution for C_μ is, of course, extremely sensitive to the numerical details, since S has a singularity on the edge. However, the point here is that C_μ makes a sudden dive near the edge because ω vanishes more rapidly than the velocity gradient, and thus S becomes very high.

It can be concluded that the above theory based on the solution (6.40) is at least qualitatively valid, although C_μ does not necessarily follow any power function according to the present EARSM. The present theory is valid when a simple scalar-diffusivity gradient model is used for the diffusive terms. Possibilities to extend

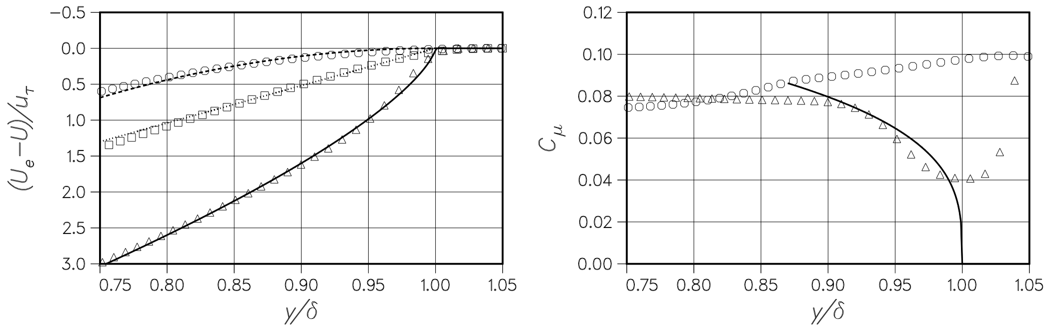

Figure 6.3: Left: numerical solutions of a boundary layer (symbols), and analytical solutions (6.40) of the idealized edge problem (curves) using different models: Kok's original model with constant C_μ where $n_u = 1$ (squares and dotted curve), Kok's model combined with the EARSM where $n_u = 1 - m$ and $m \approx 0.3$ (triangles and solid curve), and a generic model with the EARSM where $n_u = 2(1 - m)$ and $m \approx 0$ (circles and dashed curve). Right: computed C_μ distributions and a $3/10$-power curve.

the analysis for higher-order modelling of diffusive terms will be studied in future work.

The numerical solutions shown in Fig. 6.3 are obtained by solving the self-similar equilibrium outer boundary-layer equations, see Section 4.1. The results have been verified by computing also full Navier-Stokes solutions which feature the same phenomena. This verifies also the analysis based on the simplified system of ordinary differential equations (6.27).

6.3 Review of the Existing $k - \omega$ Models

Some existing $k - \omega$ models of the form (6.2) – (6.3) are reviewed in this section, and possibilities to extend them to the EASRM level are studied as well. The coefficients of the models to be discussed are summarized in Table 6.1.

6.3.1 Wilcox's Models and the Free-Stream Sensitivity

Wilcox's $k - \omega$ model from 1988 [60] is widely known with its pros and cons. Wilcox showed that this model can be solved down to the wall without any near-wall modifications. This model also performs quite well in boundary layers retarded by adverse pressure gradient. On the other hand, it suffers from anomalous solutions near the edges of turbulent regions, which is discussed below in detail. It should be remembered, however, that this model is an important step in the evolution of the $k - \omega$ models because the later models developed, *e.g.* by Menter, Abid *et al.*, and by Kok are based on Wilcox's work. Wilcox has developed also a new version of this model [28], but its edge-behaviour is not significantly different from its predecessor. This new version (1998 model) includes a new function f_{β^*} which controls the dissipation of k. This function depends on the product of the gradients

Table 6.1: The coefficients of some $k-\omega$ models, see Eqs. (6.2) – (6.3).

	$C_{\omega 1}$	$C_{\omega 2}$	σ_k	σ_ω	σ_d
Wilcox 1988	0.556	0.833	0.5	0.5	0.0
Wilcox 1998	0.52	0.8	0.5	0.5	0.0
Menter BSL Set 1 (inner)	0.553	0.833	0.5	0.5	0.0
Menter BSL Set 2 (outer)	0.44	0.92	1.0	0.856	1.712
Menter SST Set 1 (inner)	0.553	0.833	0.85	0.5	0.0
Menter SST Set 2 (outer)	0.44	0.92	1.0	0.856	1.712
Abid *et al.*	0.547	0.83	0.714	0.5	0.0
Abid *et al.* mod. by Gatski	0.561	0.83	0.714	0.454	0.0
Kok	0.556	0.833	0.667	0.5	0.5
Peng (high-Re asymptote)	0.42	0.833	1.25	0.741	0.75

of k and ω as follows

$$f_{\beta^*} = \frac{1+680\chi^2}{1+400\chi^2} \qquad \text{where} \qquad \chi = \max\left(\frac{1}{\omega^3}\frac{\partial k}{\partial x_k}\frac{\partial \omega}{\partial x_k}; 0\right) \tag{6.48}$$

Neither of Wilcox's model versions is suitable to be combined with the EARSM, except if only fully turbulent internal flows are to be computed. This is because they both have $\sigma_k = 0.5$. As was shown in the previous section, σ_k must be larger than one if the EARSM is employed as a constitutive model. Although the analysis is not valid for Wilcox's models, numerical tests have shown that the velocity profile gets a similar hook shape, as seen in Fig. 6.3, and Fig. 6.10.

As mentioned above, Wilcox's 1988 model is known to suffer from anomalous sensitivity to the free-stream boundary value of ω. This will hereafter be referred to simply as free-stream sensitivity. In non-disturbed laminar flow, ω tends to decrease, because its transport equation essentially reduces to a convection-destruction equation in such situations. This is because the productive term becomes negligibly small owing to the lack of mean-velocity gradient. Also diffusion is negligible if Re is not small. Thus, in external flow problems, ω will not keep its given far-field value. Instead, it may typically be orders of magnitude lower than desired near the turbulent parts of the flowfield. However, this model is designed to give proper solutions for boundary-layers as well as for free shear-layers when ω is relatively large at the edge of the turbulent layer. Smaller values lead to excessive eddy viscosity that extends far outside the turbulent layer. This, in turn, leads to overestimation of the boundary-layer thickness and the friction drag, and the spreading rate of free shear-layers. The free shear-layers are even more sensitive than the boundary layers to the free-stream value ω_f. This anomaly was first observed by Menter [64]. Owing to this free-stream sensitivity, the use of this model should be limited to fully turbulent internal flow problems. Wilcox's new model version [28] is designed to give the desired solutions at the limit $\omega_f \rightarrow 0$, thus it is better suited to external flow problems. However, otherwise it shares the edge behaviour with the 1988 model featuring high ν_T across the edge. In practice, this implies that its solutions are as sensitive to ω_f as those of the 1988 model if too high values of ω_f are specified. Therefore, it must be ensured that ω_f is really sufficiently small through all the edges of turbulent parts of the flowfield.

To understand the free-stream sensitivity, it is instructive to look again at the simplified edge problem (6.27). The special features are now that the cross term is not present, and that the diffusion coefficients $\sigma_k = \sigma_\omega = \sigma$. In this particular situation, the power solutions (6.28) – (6.30) are not valid, since the convective speed (6.32) would increase unboundedly. No general analytical solution has been found in this case. However, there is a simple analytical solution to a special case where the ratio of the external boundary values k_f/ω_f equals the ratio of the values on the turbulent side k_0/ω_0, thus producing the same eddy viscosity on both sides. In this particular case, the eddy viscosity will be constant through the problem domain and hence the problem becomes linear. The solution for k and ω is simply

$$\begin{aligned} k(y) &= k_0 e^{\mathcal{V} y/(\sigma \nu_T)} + k_f && (6.49) \\ \omega(y) &= \omega_0 e^{\mathcal{V} y/(\sigma \nu_T)} + \omega_f && (6.50) \\ \nu_T &= k_0/\omega_0 = k_f/\omega_f && (6.51) \end{aligned}$$

The higher values are given for k_f and ω_f, the deeper the free-stream influence penetrates, but in this case, it has no effect in ν_T since it remains constant anyway. Fig. 6.4 illustrates this situation by showing the analytical solutions (6.49) – (6.51) with an arbitrarily chosen convective velocity $\mathcal{V}$. In practical problems, ν_T will not be constant, of course. When $\nu_{Tf} \neq \nu_{T0}$ is specified for this model problem, the eddy viscosity still tends to be constant near the edges of the domain. There will somewhere be a relatively narrow zone where ν_T changes from its inner value to the outer one, see numerical solutions plotted in Fig. 6.5. In such a zone, the problem is locally nonlinear and no analytical solution was found in that region. Now, the location of the zone where the eddy viscosity changes is highly dependent on the free-stream boundary values of ω and k, as seen in Fig. 6.5. Hence, for large free-stream values, the eddy viscosity drops down close to the source of turbulence ($\eta = 0$) and for small values, typical in external flow problems, the high eddy-viscosity values extend far into the laminar region. Fig. 6.6 shows for comparison the analytical and numerical solutions for a model with $\sigma_k = 0.6$ and $\sigma_\omega = 0.9$, which allow the power solutions (6.29) – (6.30).

6.3.2 Menter's Models

Menter's $k-\omega$ SST model [3] is nowadays one of the most popular turbulence models in aeronautical CFD-work as well as in other areas of aerodynamics. It is capable of predicting adverse pressure-gradient boundary layers and flow separation fairly accurately in comparison with most of the other two-equation models. Furthermore, it is reasonably simple in formulation and, similarly to Wilcox's model, it does not involve any near-wall modifications. Menter eliminated the poor edge behaviour of

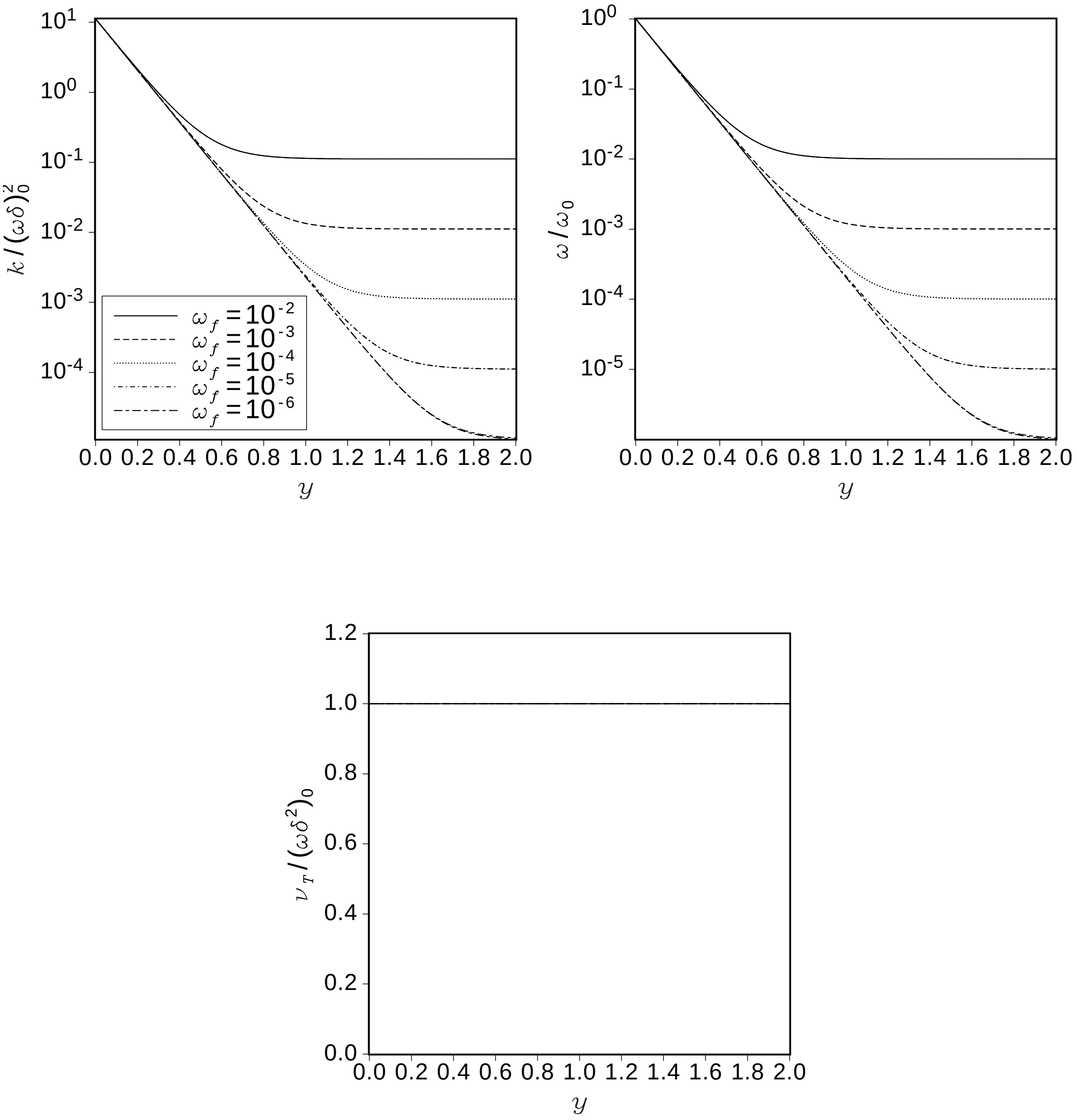

Figure 6.4: Analytical solutions (6.49) – (6.51) for the idealized edge problem (6.27) when $\sigma_k = \sigma_\omega = 0.5$ in the special case of constant eddy viscosity. Different curves correspond to different k_f and ω_f values.

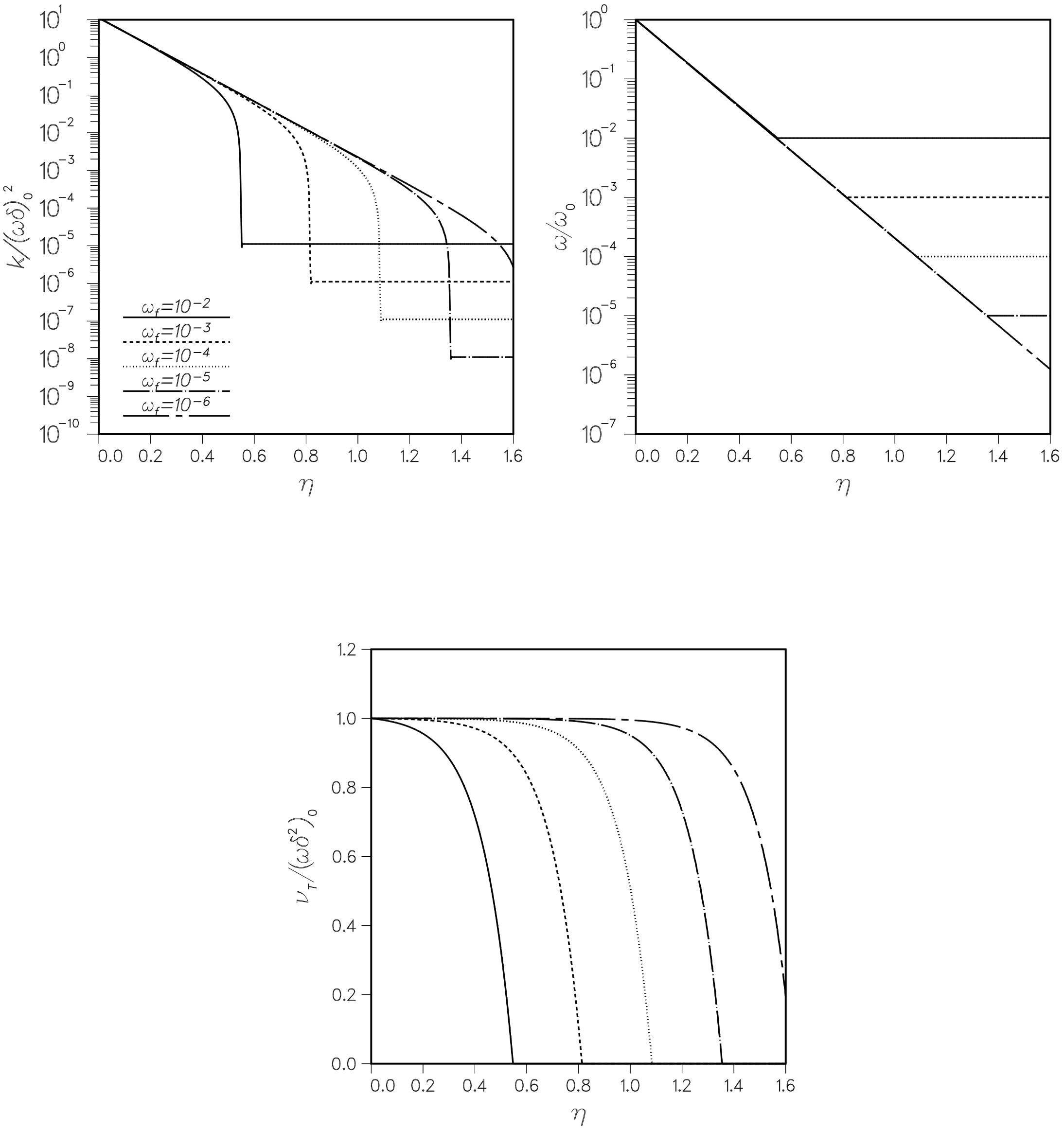

Figure 6.5: Numerical solutions for the idealized edge problem (6.27) when $\sigma_k = \sigma_\omega = 0.5$ with $\nu_{Tf} = 10^{-4}\nu_{T0}$. Different curves correspond to different k_f and ω_f values and $\eta = y/\delta_0$.

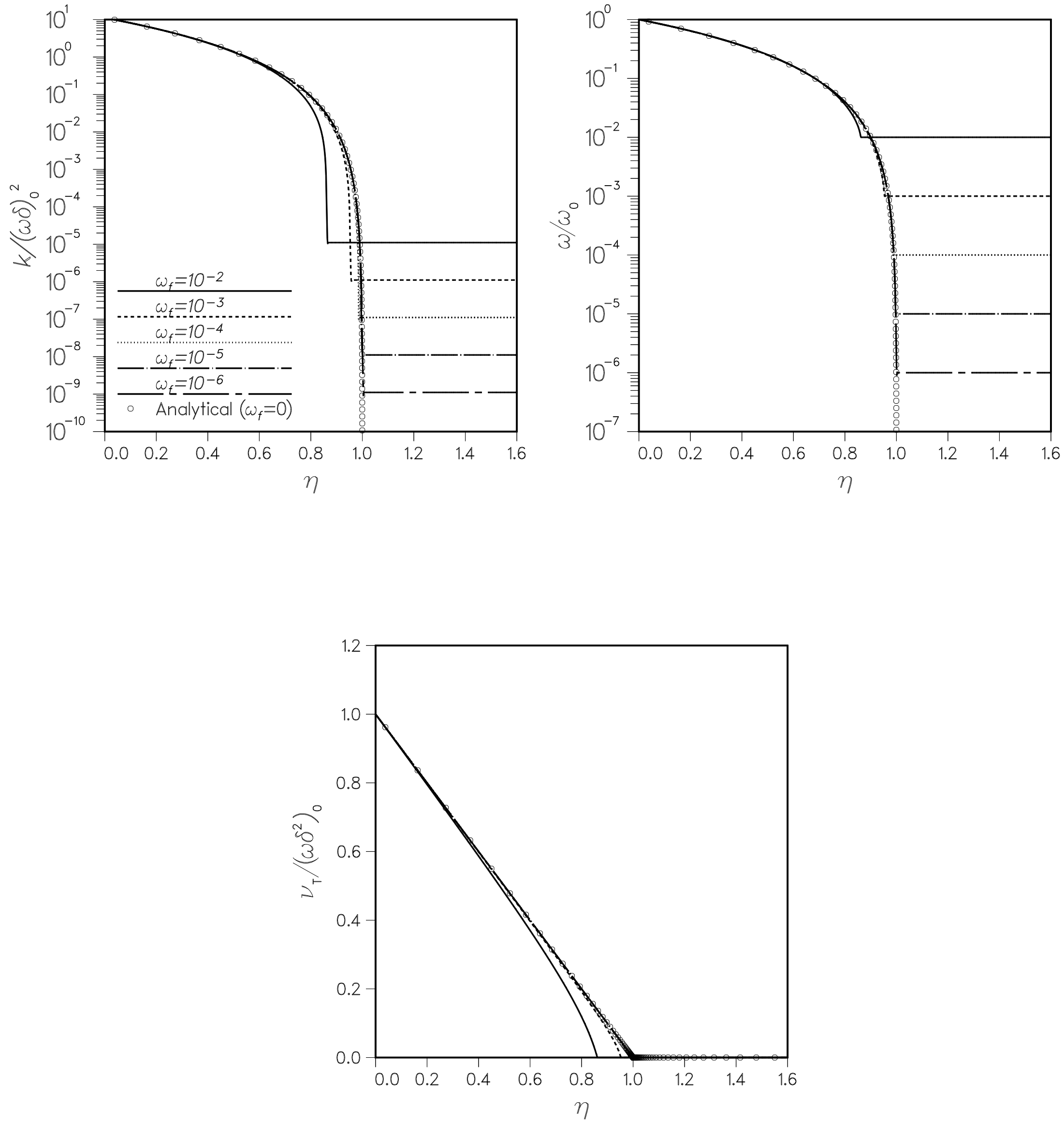

Figure 6.6: Numerical solutions for the idealized edge problem (6.27) when $\sigma_k = 0.6$ and $\sigma_\omega = 0.9$ and $\nu_{Tf} = 10^{-4}\nu_{T0}$. Different curves correspond to different k_f and ω_f values and $\eta = y/\delta_0$. The analytical solution is shown as circles.

Wilcox's model by combining it (the 1988 version) with the Jones-Launder $k - \varepsilon$ model [132] in such a way that the latter is effective around the edges of boundary layers and also in free turbulent flows. This is achieved by transforming the $k - \varepsilon$ model into the $k - \omega$ form and switching between the two models using a specific blending function. The resulting model version that employs constant C_μ is known as the BSL $k - \omega$ model. The final version, known as the $k - \omega$ SST model, is actually a step forward from the classical Boussinesq modelling, because the coefficient C_μ is not constant but depends on the second strain-rate invariant $II_S = S_{ik}S_{kj}$, as

$$C_\mu = \frac{\beta^* a_1}{\max\left(a_1; \beta^* \sqrt{2II_S}\right)} \tag{6.52}$$

To be exact, the original form of the SST model uses $II_\Omega = \Omega_{ik}\Omega_{kj}$ instead of II_S, but these two are almost identical in simple shear flows.

The scale-determining model is of the form of Eqs. (6.2) – (6.3). Two different sets of model coefficients are combined by means of a mixing function F_1 so that set-1 values are used in the inner part of boundary layers and set-2 values elsewhere. The coefficients change smoothly in the outer boundary layer. The mixing is formally written as

$$\begin{pmatrix} C_{\omega 1} \\ C_{\omega 2} \\ \sigma_k \\ \sigma_\omega \\ \sigma_d \end{pmatrix} = F_1 \begin{pmatrix} C_{\omega 11} \\ C_{\omega 21} \\ \sigma_{k1} \\ \sigma_{\omega 1} \\ \sigma_{d1} \end{pmatrix} + (1 - F_1) \begin{pmatrix} C_{\omega 12} \\ C_{\omega 22} \\ \sigma_{k2} \\ \sigma_{\omega 2} \\ \sigma_{d2} \end{pmatrix} \tag{6.53}$$

where F_1 is the mixing function described below. The coefficient values are given in Table 6.1. These values apply if ω is defined as $\omega \equiv \varepsilon/k$. Note that Menter defined ω as $\omega \equiv \varepsilon/(\beta^* k)$ similarly as Wilcox, and $\beta^* = 0.09$. This influences only $C_{\omega 2}$ which is denoted by β in Wilcox's and Menter's formulations, and $\beta = \beta^* C_{\omega 2}$. The mixing function F_1 is defined as

$$F_1 = \tanh\left(\Gamma^4\right) \qquad \text{with} \qquad \Gamma = \min\left[\max\left(\Gamma_1; \Gamma_2\right);\ \Gamma_3\right] \tag{6.54}$$

where

$$\Gamma_1 = \frac{\sqrt{k}}{\omega d} \tag{6.55}$$

$$\Gamma_2 = \frac{500\beta^* \nu}{\omega d^2} \tag{6.56}$$

$$\Gamma_3 = \frac{2k}{d^2 \max\left[(\nabla k \cdot \nabla \omega)/\omega;\ 10^{-20}\right]} \tag{6.57}$$

It is quite an obvious idea to furnish the BSL $k - \omega$ model with the EARSM as a constitutive model instead of Eq. (6.52). This has been done, see *e.g.* Refs. [44, 63, 74, 133], and the resulting model behaves much like the SST, but there are also some differences. One salient difference is that a somewhat too low friction coefficient is predicted for a simple flat-plate boundary layer. This is illustrated in

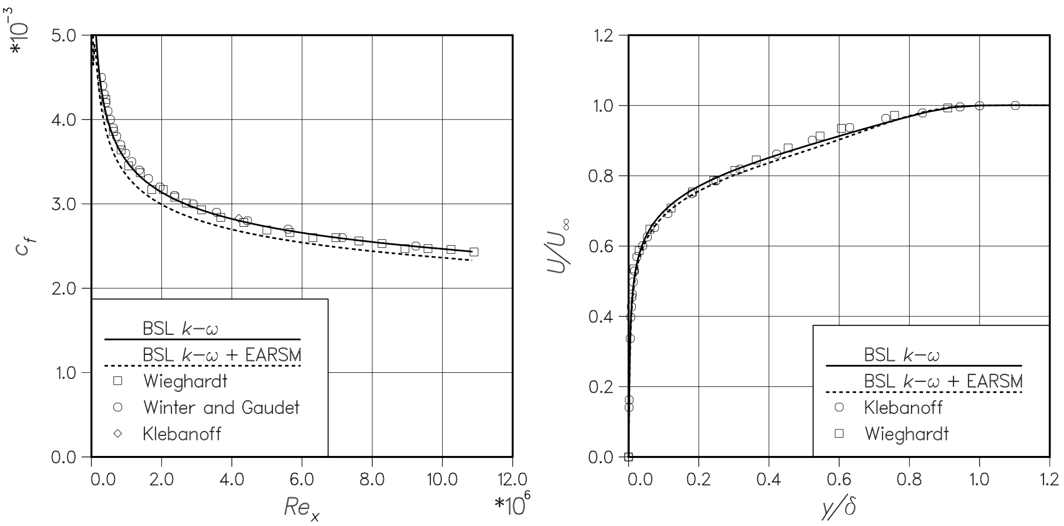

Figure 6.7: Left: skin friction distribution over a flat-plate boundary layer up to $Re_{\delta_2} \approx 15,000$. Right: velocity profiles at $Re_{\delta_2} \approx 7,300$. Computations with the standard BSL $k-\omega$ model and the same model with EARSM as the constitutive model.

Fig. 6.7 (left), where the friction coefficients computed using the BSL $k-\omega$ model as such and equipped with the EARSM as the constitutive model are compared with the experimental data by Wieghardt [134] (taken from the proceedings of the 1968 AFOSR-IFP-Stanford Conference [48]), Winter and Gaudet [135], and Klebanoff [136]. Another fault of the BSL-EARSM combination in the same elementary flow is that the velocity profile in the defect layer has a qualitatively wrong shape. There is a shallow pit in the profile, visible in Fig. 6.7, the second derivative of U with respect to y having a locally wrong sign.

Menter's original $k-\omega$ models have some weaknesses as well, which may have significant influence in high-lift aerodynamic problems. The EARSM version has shown to have inherited these weaknesses. One of these is that the outer edges of turbulent regions are predicted as unphysically sharp. In practical simulations, the grid resolution is typically not quite good near the edges and thus, the numerical damping smoothens the edge (as is the case in Fig. 6.7). This fact, however, makes it very difficult to obtain grid-converged results, and also numerical problems are likely to take place on the limit of grid convergence. This anomaly is at least partially associated with the fact that these models predict clearly too low spreading rates for planar far-wake and mixing layer flows. This is shown in Fig. 6.8, where a computed wake velocity profile is compared with the measurements of Thomas [80], Fabris [81], Antonia and Browne [82, 83] and Weygandt and Mehta [84]. Also a mixing layer profile is compared with the data measured by Liepmann and Laufer [99], Castro and Bradshaw [100], and by Wygnanski and Fiedler [98], in Fig. 6.8. These elementary flows play an important role in multi-element aerofoil problems.

The BSL model does not satisfy the constraint (6.46), and hence (6.28) – (6.30) do not satisfy the BSL-model equations on the edge regions. This may be somewhat surprising because it can be easily shown that the Jones-Launder $k-\varepsilon$ model [132]

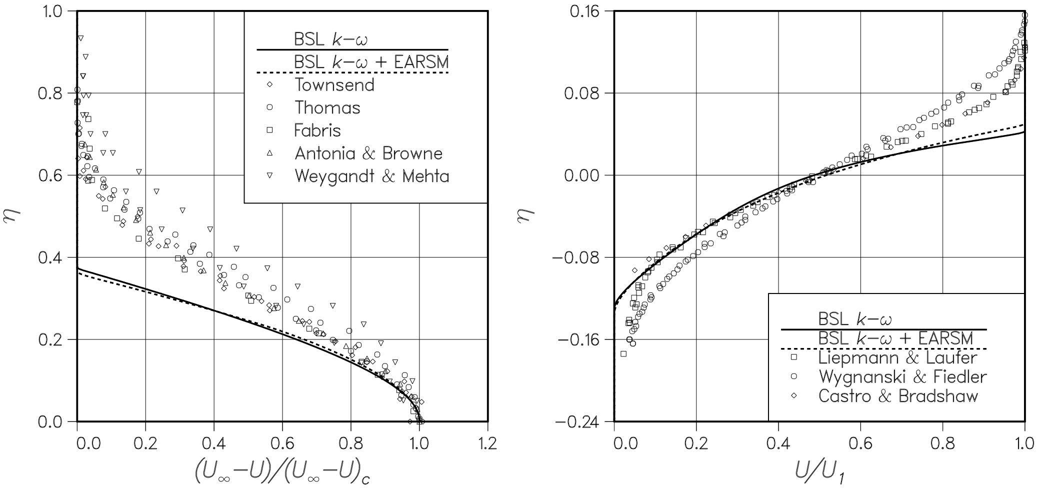

Figure 6.8: Velocity profiles of plane far wake (left) and plane mixing layer according to the standard BSL $k-\omega$ model as such and equipped with EARSM as the constitutive model.

satisfies Cazalbou's constraints, and the outer form of the BSL model (active when $F_1 = 0$) is derived by transforming this $k-\varepsilon$ model into the $k-\omega$ formulation. So, why does the BSL model not satisfy the corresponding constraints derived for the $k-\omega$ models? The reason for this difference is that Menter dropped one term from the ω-equation. This term arises from the exact transformation from the $k-\varepsilon$ form to the $k-\omega$, and it reads

$$\frac{\omega}{k}\frac{\partial}{\partial x_j}\left[(\sigma_\varepsilon - \sigma_k)\nu_T \frac{\partial k}{\partial x_j}\right] \tag{6.58}$$

Fig. 6.9 shows the velocity-defect distributions near the outer edge of a flat-plate boundary layer solved using Menter's original BSL $k-\omega$ model, and a variant with the outer coefficients employed down to the logarithmic layer, and the Jones-Launder $k-\varepsilon$ model. The only mathematical difference between the last two models is that the last one includes the term (6.58) when transformed into the $k-\omega$ form. Thus, Fig. 6.9 demonstrates the influence of the ignored term (6.58). The inclusion of this term makes the edge somewhat smoother, but it is still nearly sharp. As shown in Section 6.2.4, the analytical solutions will feature smooth edges if the exponent of the analytical velocity solution is larger than one. The edge solution for velocity in the case of the $k-\varepsilon$ models is

$$U(y) = U_o f^{\sigma_k \sigma_\varepsilon/(2\sigma_\varepsilon - \sigma_k)} \tag{6.59}$$

see Cazalbou *et al.* [129]. For the Jones-Launder model the exponent is only 1.2, which explains why it predicts an almost sharp edge profile. When the term (6.58) is dropped from this model (after transforming it into the $k-\omega$ form) the edge becomes almost like a junction of two straight lines.

In the case of the $k-\omega$ models, the formation of unphysically sharp edges is associated with the high value of σ_{d2} (in Menter's models $\sigma_{d2} = 2\sigma_{\omega 2} = 1.712$, and

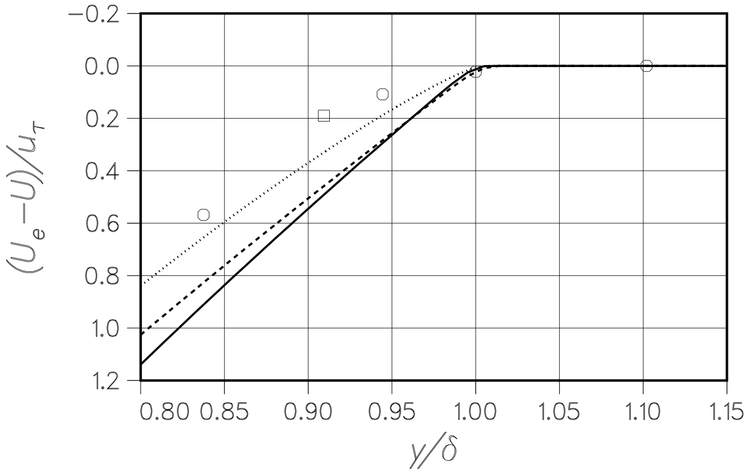

Figure 6.9: Velocity-defect profiles through the outermost part of a ZPG boundary layer according to Menter's original $k-\omega$ BSL model (solid line), a variant with the outer coefficients employed throughout the boundary layer (dashed line), and the Jones-Launder $k-\varepsilon$ model (dotted line). Symbols represent experimental data by Wieghardt (squares) and by Klebanoff (circles).

$\sigma_{k2}=1$). Now, the condition for the edge not to be sharp is

$$\sigma_k\sigma_\omega > \sigma_\omega - \sigma_k + \sigma_d \tag{6.60}$$

This is seriously violated in this case since the left-hand side equals to 0.856 and the right-hand side is 1.568. Thus, it is clear that σ_d must be reduced quite a lot from Menter's value.

6.3.3 Abid-Rumsey-Gatski Model

Abid, Rumsey, and Gatski [137] combined the Gatski-Speziale EARSM [35] with a $k-\omega$ model that is essentially the Wilcox 1988 model [60]. In comparison with Wilcox's original model, they elevated the value of σ_k from 0.5 to 0.714, see Table 6.1. This model was later slightly modified by Gatski [46, 138], see Table 6.1. The value of σ_k is still too low to satisfy the constraint (6.47). Note that these models employ a so-called equilibrium eddy viscosity in the model for turbulent transport (diffusion). In other words, a constant $C_\mu=0.088$ is used in those terms. The hook-shaped edge profile is avoided this way. If the C_μ given by the EARSM is used in these terms, the hook anomaly will arise. This has been verified by numerical computations where the Wallin-Johansson EARSM was used instead of the Gatski-Speziale EARSM, see Fig. 6.10. It is felt that using the variable C_μ in modelling all the diffusive terms is generally a better choice. This is also recommended by Wallin and Johansson [4]. Therefore, the model by Abid *et al.* will not be adopted for further studies in this work.

More recently, Rumsey and Gatski [45] again modified the model by changing σ_k back to 0.5 and by multiplying the dissipation term of the k-equation by a function f_{β^*}, see (6.48), adopted from Wilcox's 1998 model [28]. These modifications make the model essentially similar to Wilcox's 1998 model.

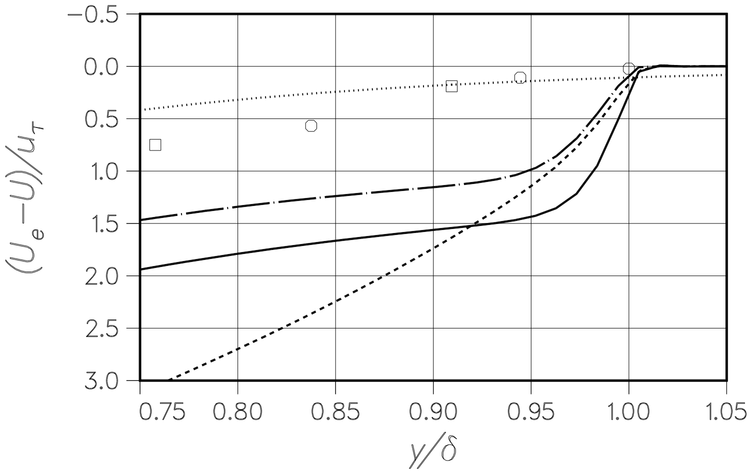

Figure 6.10: Velocity-defect profiles through the outer part of a ZPG boundary layer computed with different $k-\omega$ models combined with the EARSM. The models are: Wilcox 1988 (solid line), Kok (dashed line), and Abid *et al.* with constant (dotted line) and variable (dash-dotted line) C_μ employed in the diffusivity of k and ω. Symbols represent experimental data by Wieghardt (squares) and by Klebanoff (circles).

6.3.4 Kok's Model

Kok [130] designed a $k-\omega$ model that satisfies the constraints (6.33) – (6.33) discussed in Section 6.2 and shares the near-wall behaviour of Wilcox's and Menter's models using only one set of model coefficients. It should be mentioned that σ_d is nonzero only when $\nabla k \cdot \nabla \omega \geq 0$. Kok selected the diffusion coefficients, for some reason, such that the mean-velocity exponent in (6.28) becomes equal to one, which leads to solutions with unphysically sharp edges. This is seen in Fig. 6.3. As also shown in Fig. 6.3, this model cannot be combined with the EARSM because of the emergence of anomalous hook-shaped edge solutions, see Fig. 6.10.

6.3.5 Peng's Low-Reynolds-Number $k-\omega$ Model

The models with low-Reynolds-number modifications are not of primary interest in this study. However, the high-Reynolds-number asymptote of Peng's model [139] differs from all other $k-\omega$ models. Therefore, it will be briefly discussed, too. The diffusion coefficients of this model have values quite different from Wilcox's models. Most importantly, $\sigma_k = 1.25$, which satisfies the constraint (6.47). It satisfies also the other constraints (6.45) and (6.46). Thus, its edge behaviour should be good also when combined with the EARSM. Peng's model coefficients cannot be used near the walls without the near-wall modifications, but they could possibly be suitable as outer coefficients employed near the outer edges of boundary layers and in free turbulent flows. However, since this model is not designed for typical aerodynamical problems, it is not considered as such.

6.4 Recalibration of the Model Coefficients and the Mixing Function

6.4.1 Calibration Strategy

Calibration of the model coefficients and the mixing function is described step by step in this Section. The final form of the model resulting from these development steps is summarized in Section 6.6.

The shortcomings of the BSL $k - \omega$ model and its extension that uses EARSM as the constitutive model (BSL-EARSM) have been discussed and demonstrated in Section 6.3.2. These are largely related to the behaviour of the BSL model near the edges of turbulent regions. Therefore, this problem will be tackled first.

It was concluded in Section 6.3.2 that σ_{d2} must be given a much smaller value than 1.712. Unfortunately, lowering σ_{d2}, without changing any other coefficients, makes the boundary layers spread too rapidly. A value as low as 0.4 is needed to predict the far-wake flow properly. With this value, the boundary-layer thickness would become seriously overpredicted. One way to overcome this contradiction is to change the mixing function in such a way that the change of the model coefficients from the inner (set 1) to the outer (set 2) values takes place further away from the wall. It is probably the best practice to design the mixing function in such a way that the change of the coefficients occurs closer to the boundary-layer edge than in the BSL model, and to calibrate both coefficient sets to obey the constraints (6.45) – (6.47). The inner coefficients should also provide acceptably good edge behaviour because in some circumstances, the mixing function might behave unexpectedly and activate the inner coefficients on the edge. Added robustness is achieved this way. Choosing this approach means that a value of about 0.4 should be assigned to σ_{d2}, and σ_{d1} should be about 1.0 according to preliminary numerical tests. The outer coefficients will be first looked for, and the modifications to the mixing function will be considered after that in Section 6.4.3.

6.4.2 Free Shear Layers

Background

Before proceeding with the boundary-layer problem, the outer coefficients must be calibrated so that the selected elementary free shear flows, the far wake and the mixing layer, will be predicted with sufficient accuracy. These coefficients also become active on the edges of the boundary layers, hence they must be calibrated before attempting to optimize the inner coefficients for the boundary layer. It is already anticipated that σ_{k2} and σ_{d2} should be about 1.1 and 0.4, respectively. On the other hand, $C_{\omega 12}$ should be selected from the lower end of its permitted range (6.18), and $C_{\omega 22}$ from near the upper extreme of (6.9) in order to keep ω relatively small, and thus to allow rapid spreading of free turbulent layers owing to a sufficiently high rate of turbulent mixing of momentum. Numerical experiments showed that the values of the BSL model, 0.44 and 0.92 for $C_{\omega 12}$ and $C_{\omega 22}$, respectively, are suitable.

These values correspond to the most commonly used $k - \varepsilon$ values $C_{\varepsilon 1} = 1.44$ and $C_{\varepsilon 1} = 1.92$. Further numerical tests suggest that 1.0 is a suitable value for $\sigma_{\omega 2}$ when the focus is in the planar far wake and mixing layer flows.

Far wake

Mean-velocity and Reynolds-stress profiles of the far-wake flow are shown in Fig. 6.11 as functions of the similarity coordinate

$$\eta = \frac{y}{D}\sqrt{\frac{2D}{c_d(x - x_0)}} \tag{6.61}$$

where D is the diameter of the wake-generating cylinder, c_d is its drag coefficient, x is the distance between the cylinder and the measurement station, and x_0 is the location of a virtual origin of the self-similar system. The results computed with the new coefficients are compared with the BSL-EARSM results and with experimental data. The new outer coefficients provide a velocity profile that fares well through the somewhat scattered measurement data. Five sets of measured mean-velocity data are shown: Townsend 1949 [79], Thomas 1973 [80], Fabris 1979 [81], Antonia and Browne 1986 [82, 83], and Weygandt and Mehta 1995 [84]. The drag coefficients are estimated on the basis of the reported cylinder Reynolds number UD/ν and are of the order of one. One source of uncertainty is the virtual origin x_0. The smaller x/D is, the more significant this uncertainty becomes. Thomas made his measurements at $x/D = 160$, Fabris used larger distances, $x/D = 200$ and 400, and Townsend had even larger x/D ranging from 500 up to 950. Townsend used $x_0/D = 90$, while Fabris selected for both his own and for Thomas' measurements quite a different value of -40. Unlike the other cases, Weygandt and Mehta have studied the wake of a flat plate. Unfortunately, they did not report the velocity profile in [84]. Instead, the data is taken from [28].

The Reynolds shear-stress comparisons are based on the measurement by Townsend [79] measured at stations ranging from $x/D = 500$ to 800, and by Fabris [81] measured at $x/D = 400$. The normal stresses are compared with the data by Fabris and by Antonia and Browne. The shear stress must naturally be rather well predicted because the mean velocity is. A comparison with the measurements, indeed, shows fair agreement, although the model predicts somewhat higher values in the outer part of the flow. Also the experimental results of Townsend and Fabris disagree with each other near the region of the maximum shear stress. The computed normal stresses and thus the turbulent energy are, however, significantly higher than measured. Although not shown here, the measurements by Townsend support the normal-stress data by Fabris and by Antonia and Browne, except that Townsend measured even lower $\overline{u'u'}$-values than Fabris. The differences in computed and measured normal stresses, and the fact that the model-predicted C_μ is close to 0.09 throughout the flow, reveal a flaw in the model — it predicts too high k and ω but still roughly correct $\nu_T \sim k/\omega$ in this case. Nevertheless, the mean velocity and the shear stress are much better modelled with the new outer coefficients than with the BSL values.

It was studied whether the above-observed discrepancy could be cured by introducing a small addition to β^* in the dissipation term of the k-equation when $f_{mix} = 0$. This was done without changing β^* in the definition of turbulent time scale. The idea behind this is to make both k and ω smaller for free flows without changing much the eddy viscosity and consequently the shear stress. The latest version of Wilcox's $k - \omega$ model [28] includes the same kind of feature. Now, it was found that β^* could be increased by only about 10% without spoiling the boundary-layer predictions in this case, while in Wilcox's model it is increased by as much as 70%. In connection with this modification, $C_{\omega 12}$ had then to be lowered to a value of 0.4 in order to maintain sufficient level of eddy viscosity in the wake and mixing layer flows. Still, with this modification the improvement was less than modest. While the shear stress dropped only a tiny amount as desired, the turbulent energy did not decrease more than about 10% in this case — roughly the same percentage as β^* was increased. This idea was abandoned as it gave no significant benefit despite adding one more coefficient to the calibration process.

After all, it must be remembered that the self-similar wake solution is somewhat inaccurate probably owing to the linearization of the convective terms in the derivation of the self-similar equations. Therefore, it is not sensible to stubbornly require that the self-similar solution must accurately match with the measurements.

Mixing layer

Fig. 6.12 compares the computed velocity and stress profiles of the self-similar planar mixing layer with experimental data. This particular mixing layer is a shear layer between a still fluid and a uniform stream of velocity U_1. The similarity coordinate is simply $\eta = y/(x - x_0)$. Measurements are by Liepmann and Laufer 1947 [99], by Wygnanski and Fiedler 1970 [98], and by Castro and Bradshaw 1976 [100]. The velocity profile measured by Wygnanski and Fiedler shows a clearly higher spreading rate than the other two profiles. The reason for this is not completely clear. See Section 3.5 for more discussion on this topic.

The different spreading rate of the measured mixing layers means that the experimental reference data is not as reliable as desired. This has been pointed out by other authors as well, *e.g.* [10, 11]. Nevertheless, the new model calibration yielded a velocity profile that agrees clearly better with all experiments than the BSL-EARSM on the high-speed side, although it still is somewhat too sharp-edged there. However, on the low-speed side, the new model agrees better with the data by Wygnanski and Fiedler while the BSL-EARSM results are supported by the other measurements there. The stress profiles show even more clearly than the mean-velocity profile that the models give significantly too asymmetric results. Excessive asymmetry seems to be a common shortcoming of the majority of turbulence models that is not easily avoided, see Section 3.5. Also, the new model gives somewhat too high shear stress in the middle and on the low-speed side, and excessive anisotropy of the normal components. The BSL model gives too little turbulent energy throughout the flow, although it happens to predict the stress components reasonably well on the low-speed side. The above-discussed trial to use an elevated dissipation rate did not remove the observed discrepancies of the new model. In addition to this, some other attempts were made to find such a calibration that would give less asymmetric results without spoiling the wake-flow results. However, no such values were found.

6.4.3 Mixing Function

As proposed in Section 6.4.1, Menter's mixing function F_1 is modified to push the mixing towards the boundary-layer edge. This can be achieved by using the same kind of parameters Γ_1, Γ_2, and Γ_3 as in the BSL model. Only some coefficients have to be changed. Most importantly, Γ_3 has to be multiplied by a factor of, say ten to allow the hyperbolic tangent function to remain at unity almost up to the edge. Now, Γ_3 reads

$$\Gamma_3 = \frac{20k}{\max\left[d^2(\nabla k \cdot \nabla \omega)/\omega;\ 200k_\infty\right]} \tag{6.62}$$

where d is the distance to the nearest wall point. The lower limit of the denominator is made proportional to the free-stream value of k. In fully turbulent internal flows, this limiter is of no significance, and any small value may be used. The other parameters, Γ_1 and Γ_2 are adopted from the BSL model as such. However, the final value

$$\Gamma = \min\left[\max\left(\Gamma_1; \Gamma_2\right);\ \Gamma_3\right] \tag{6.63}$$

is multiplied by a factor of 1.5 to obtain the desired behaviour, see Fig. 6.13. Hence, the final form of the mixing function is given by

$$f_{mix} = \tanh\left(1.5\Gamma^4\right) \tag{6.64}$$

The use of $\max$- and $\min$-functions may produce locally non-smooth behaviour. In Fig. 6.13, this is more salient with the new form, but Menter's form has been observed to give similar non-smoothnesses in many situations. According to the experience with Menter's models, these non-smoothnesses of the mixing function have no harmful effects on the physical quantities. Although not shown here, it was checked that the mixing function behaves properly also in cases with a nonzero pressure gradient.

6.4.4 Zero Pressure-Gradient Boundary Layer

Given a mixing function with the desired behaviour, we now look for suitable values for the inner coefficients that fulfil the edge constraints (6.45) – (6.47) and give accurate prediction for the ZPG boundary layer. First, it must be remembered that the cross term must not be included in the near-wall region. Therefore, σ_{d1} will be nonzero only when $\nabla k \cdot \nabla \omega > 0$. The diffusion coefficient σ_{k1} must be increased to, say 1.1 in order to satisfy the constraint (6.47). It was also observed that this change removed the unphysical pit from the velocity profile in the defect layer, see Figs. 6.7 and 6.14. At this point, it was checked that the $k - \omega$ model's ability to fairly accurately model the APG boundary layers is still maintained with the

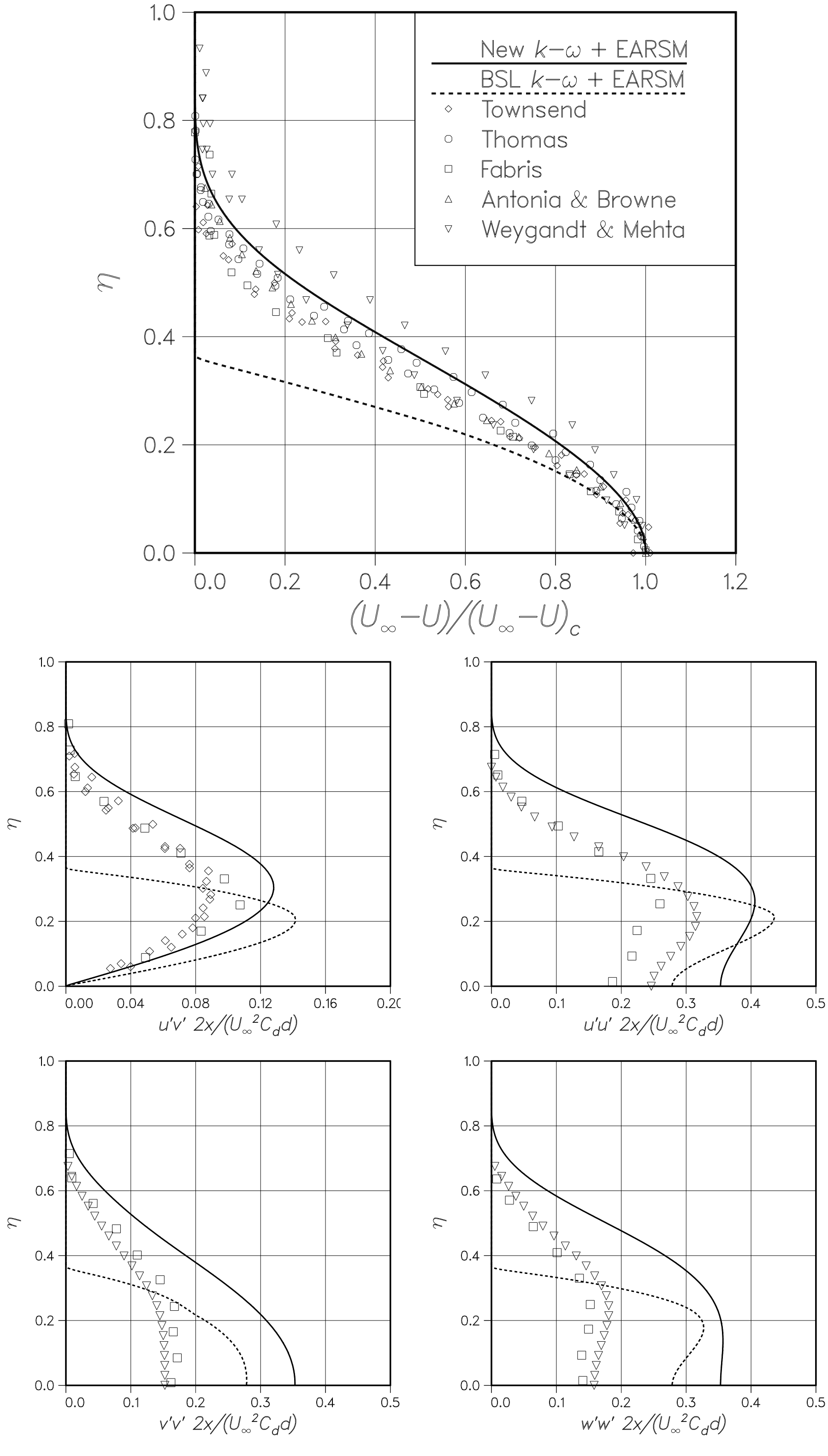

Figure 6.11: Velocity and Reynolds stress profiles of the planar far wake according to the $k-\omega$ EARSM model with the new outer coefficients compared with the BSL $k-\omega$ EARSM model and experimental data.

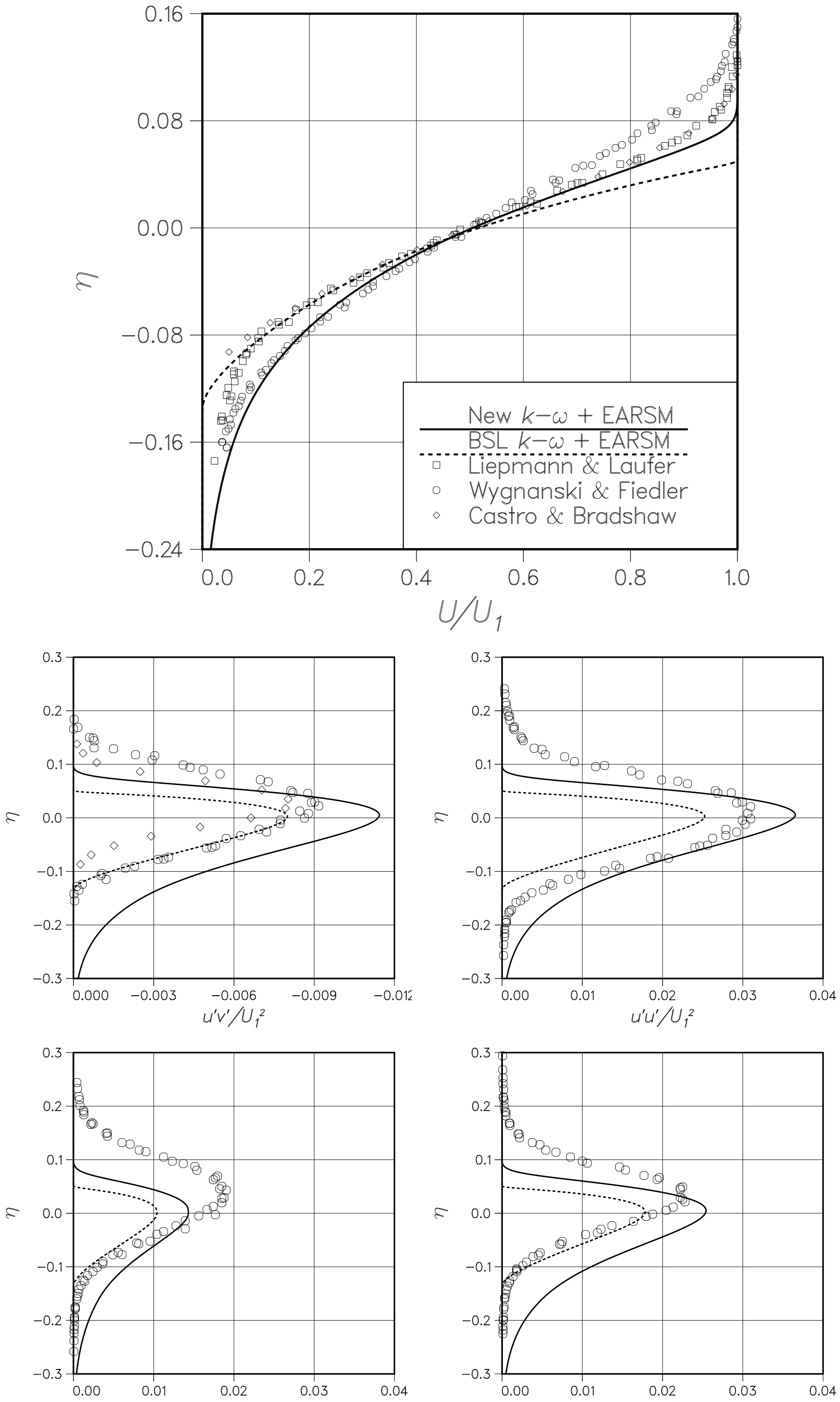

Figure 6.12: Velocity and Reynolds stress profiles of plane mixing layer according to the $k - \omega$ EARSM model with the new outer coefficients compared with the BSL $k - \omega$ EARSM model and experimental data.

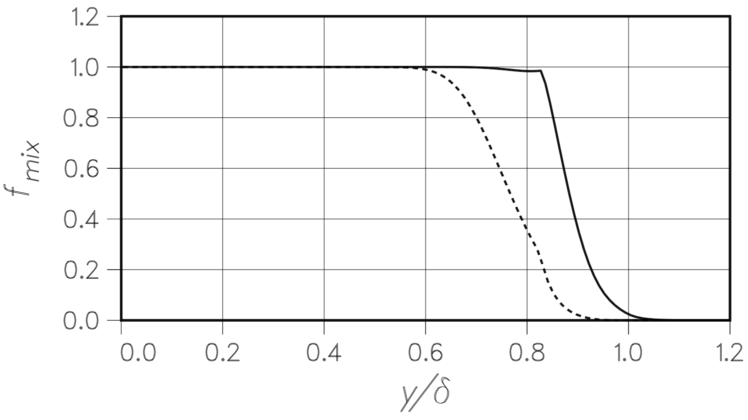

Figure 6.13: Behaviour of the mixing functions through a ZPG boundary layer. The solid line represents the new mixing function (6.64), and the dashed line is Menter's F_1.

elevated value of σ_{k1}. It was seen that equilibrium boundary layers with strong adverse pressure gradients, $\beta_T = 8$ and $\beta_T = 20$ can be predicted with the new coefficients at about the same accuracy as with the BSL-EARSM, except near the outer boundary, where the new model provides a significant improvement. This will be discussed in more detail in Section 6.4.8.

The other diffusion coefficient σ_ω has to be kept close to 0.5 in order to maintain the favourable feature of the $k - \omega$ models that they can be solved down to the wall without any near-wall modifications. Extensive numerical experimenting with the ZPG boundary layer and with the fully developed channel flow, discussed in the next section, showed that the following values are close to optimum:

$$\sigma_{k1} = 1.1 \quad \sigma_{\omega 1} = 0.53 \quad C_{\omega 21} = 0.83$$

and

$$\sigma_{d1} = \begin{cases} 1.0 & \text{if } \nabla k \cdot \nabla \omega > 0 \\ 0 & \text{else} \end{cases} \tag{6.65}$$

while $C_{\omega 11}$ is solved from (6.25) using $\kappa = 0.42$ and constant $C_\mu = 0.09$. This gives $C_{\omega 11} = 0.518$. The selected inner diffusion coefficients satisfy the constraints (6.45) – (6.47) as well as the outer values.

Experiments were also conducted in which the variable C_μ was used in (6.25) to determine the value of $C_{\omega 11}$. Furthermore, the factor σ_d/ω of the cross term was replaced by the form $\sigma_d \nu_T/k$ which includes the variable C_μ. Numerous tests with both self-similar and two-dimensional flows showed no consistent improvement owing to these modifications. Therefore, it was decided to retain the simpler form with no additional C_μ dependencies.

The results for the ZPG boundary layer are shown in Figs. 6.14 and 6.15. The new model gives clearly a smoother edge for the boundary layer and removes the pit anomaly from the velocity profile. However, the new model seems to give even a slightly too diffuse outer edge according to the left-hand plot where the y-coordinate is scaled by Clauser's delta $\Delta = \delta_1 U_e/u_\tau$. Moreover, this is seen as a somewhat too full velocity profile, when y is scaled by the boundary-layer thickness. These

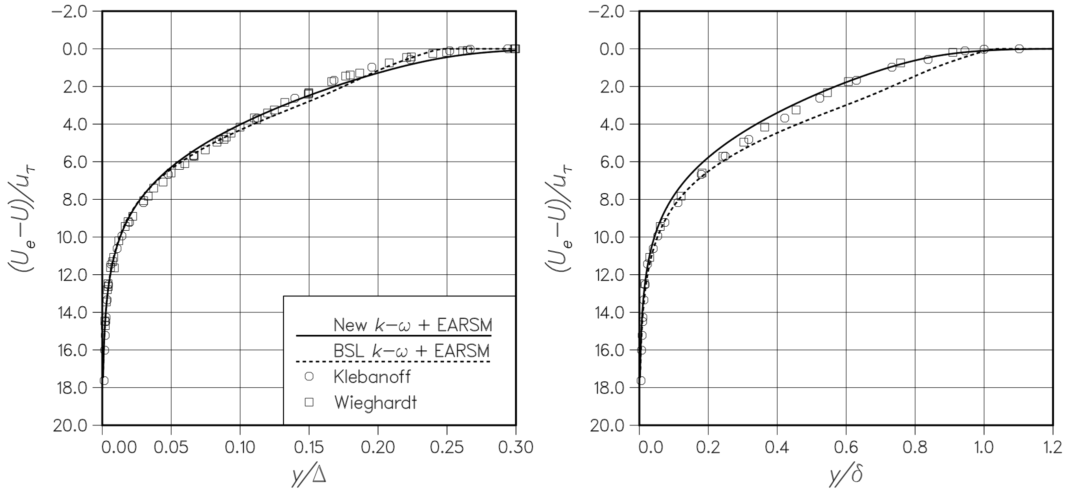

Figure 6.14: Velocity-defect profiles through a ZPG boundary layer according to the new $k-\omega$ EARSM model, and with the BSL model furnished with the EARSM. On the left-hand side, the y-coordinate is scaled by Clauser's delta $\Delta = U_e\delta_1/u_\tau$, and on the right-hand side by the boundary-layer thickness. The symbols represent experimental data by Klebanoff (circles) and by Wieghardt (squares).

results are from one-dimensional computation on the limit $Re \to \infty$ in which self-similarity is assumed. The results are verified in Section 7.1 by a two-dimensional computation which does not show such a discrepancy. It is, thus, likely that this difference is connected to the simplifications made in the derivation of the self-similar equations.

6.4.5 Fully-Developed Channel Flow

The fully-developed channel flow was computed at several Reynolds numbers to ensure that the logarithmic velocity profile and the skin-friction coefficient are computed with sufficient accuracy. This could not be checked from the self-similar boundary-layer results because both the wall- and the defect layers cannot be solved mutually on the self-similar limit owing to the different scaling of these regions. The logarithmic law is used as a boundary condition in the defect-layer computations.

Fig. 6.16 compares the computed velocity profiles with the log-law

$$U^+ = \frac{1}{\kappa}\ln y^+ + B \tag{6.66}$$

at Reynolds numbers: 10^4, 10^5, 10^6, and 10^7. The coefficient values $\kappa = 0.41$ and $B = 5.0$ are adopted. Especially the new model is in very good agreement with (6.66), but also the BSL-EARSM gives velocity profiles that are well within the uncertainty of the log-law coefficients. Noticeably, the new model predicts a somewhat stronger wake with Coles' wake-strength parameter $\Pi \approx 0.1$ than the BSL-EARSM, which predicts $\Pi \approx 0.0$. Dean [110] suggests a value of 0.14 for Π, but this is based on very scattered data.

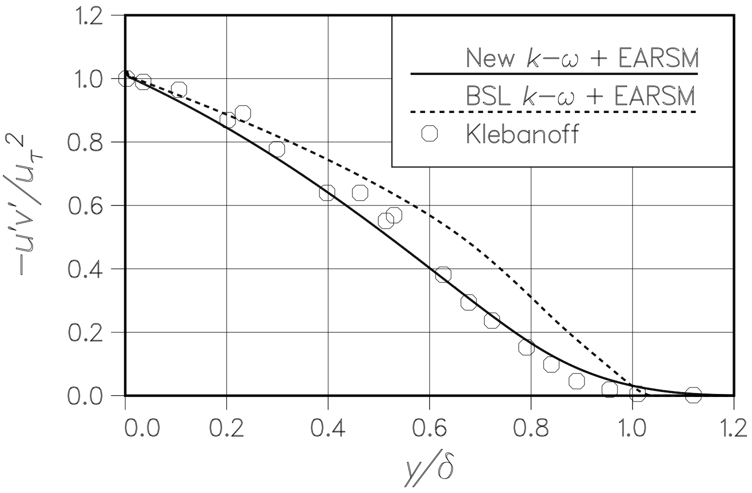

Figure 6.15: Shear-stress profiles through a ZPG boundary layer according to the new $k-\omega$ EARSM model, and with the BSL model furnished with the EARSM. The circles represent experimental data by Klebanoff.

The skin-friction coefficient is shown in Fig. 6.17 as a function of the bulk Reynolds number $U_b h/\nu$ ranging from 10^4 to 10^7. The computed values are in good agreement with Dean's implicit friction formula [110]

$$\sqrt{\frac{2}{c_f}} = \frac{1}{\kappa} \ln \left(\frac{Re_b}{2\sqrt{2/c_f}} \right) + 3.2 \tag{6.67}$$

Fig. 6.17 also shows good agreement between the new model and the BSL-EARSM, although they predict a remarkably different friction coefficient for the flat-plate boundary layer, which will be shown in Section 7.1. This means that the reason why the BSL-EARSM underpredicts the boundary-layer skin friction is not in the wall layer but in the defect layer. This flaw is probably connected to the "pit anomaly" that was removed by increasing the value of σ_{k1}.

6.4.6 Free-Stream Sensitivity

The influence of the free-stream values of k and ω on the solution is studied in the case of the far-wake flow. Menter has shown that Wilcox's $k - \omega$ model suffers from anomalous sensitivity to the free-stream value of ω [64]. This was discussed in Section 6.3.1. Fig. 6.18 demonstrates this for the present wake problem. If a small value is specified for ω_e, then ν_T will not decrease towards the edge but maintain a high value of the order of its maximum value inside the wake far up to the laminar flow. On the other hand, if too large a value is given to ω_e, it will affect ν_T throughout the turbulent zone. The low end of the ω-range approaches an asymptotic solution. In principle, the sensitivity can be avoided by always using a sufficiently small boundary value for ω to obtain the asymptotic solution. The asymptotic solution of this model, however, does not agree with the measurements,

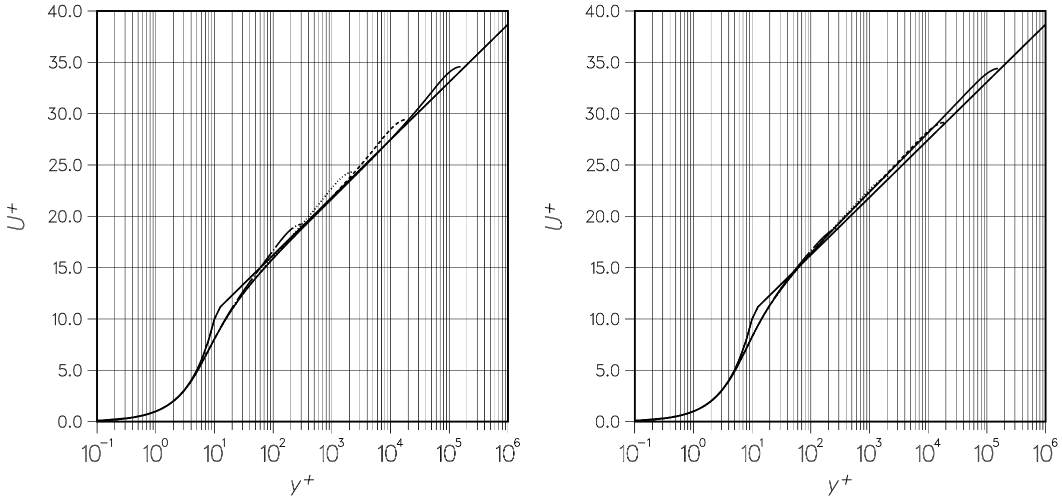

Figure 6.16: Fully developed channel flow. The velocity profiles at four Reynolds numbers 10^4, 10^5, 10^6, and 10^7 computed with the new model (left) and with the BSL-EARSM (right) compared with the log law with $\kappa = 0.41$ and $B = 5.0$.

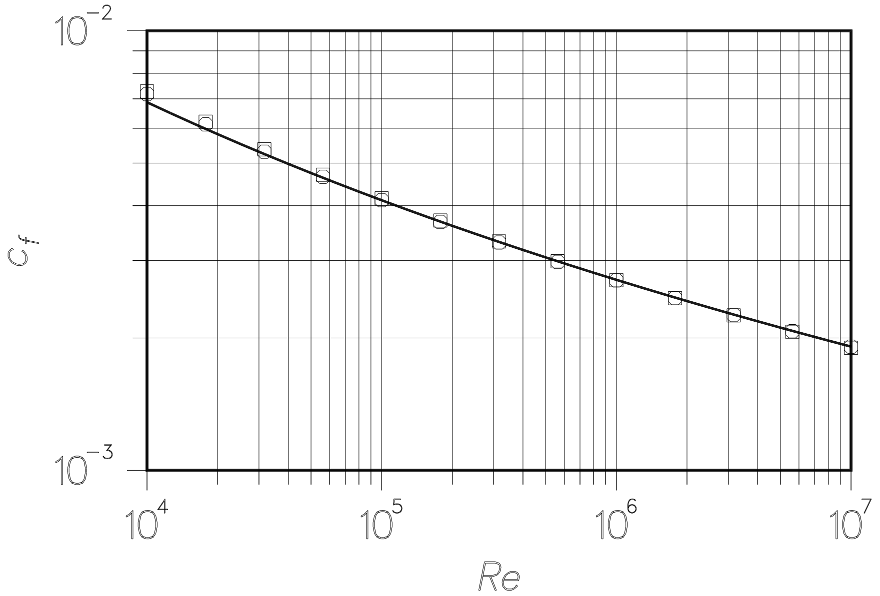

Figure 6.17: Fully developed channel flow. The computed skin-friction coefficient compared with Dean's formula (6.67). Circles stand for the new model and squares for the BSL-EARSM.

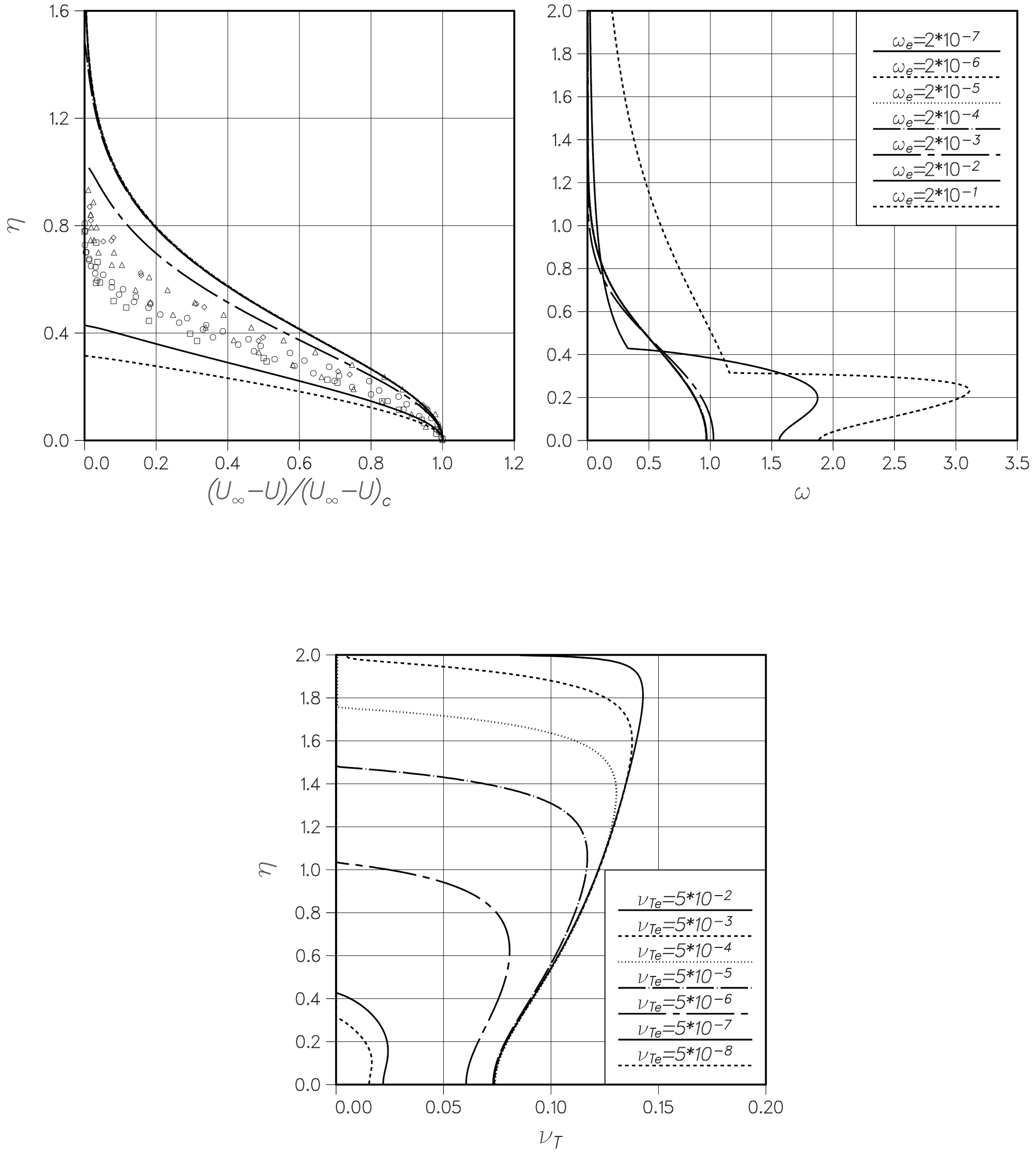

Figure 6.18: Free-stream sensitivity of Wilcox's 1988 $k - \omega$ model. Influence of the free-stream value of ω on the wake flow. Nondimensional k_e is kept at a constant value of 1.11×10^{-7} and ω_e is varied from 2×10^{-7} to 2×10^{-1}.

neither in the wake flow, as seen in Fig. 6.18, nor in the boundary layers. The asymptotic solutions are also very different from those shown in Refs. [28, 60, 140]. As discussed in Section 6.3.1, the behaviour of the eddy viscosity, seen in Fig. 6.18, can be traced back to the fact that the diffusion coefficients σ_k and σ_ω have values equal to each other. This choice, when $\sigma_d = 0$, makes k and ω decrease at the same rate when the edge is approached. Therefore, ν_T will be large on the edge, unless a very high value, related to k_e, is given for ω_e. It is much more convenient to have ν_T go to zero towards the edge. This can be achieved by choosing the diffusion coefficients so that they satisfy the constraints (6.45) – (6.47).

The plots in Figs. 6.19 – 6.21 show how the wake solutions of the new model depend on the free-stream values. Fig. 6.19 shows k, ω, and ν_T distributions computed by varying ω_e from 10^{-7} up to 0.1 and keeping k_e at a constant value of 1.11×10^{-7}. The highest value of ω_e is about 10% of its maximum value inside the wake. This seems to be too high a boundary value in this case as the boundary is placed at $\eta = 1$, just next to the wake edge. The next smaller value, 0.01, makes only a small difference compared with the rest of the results with still smaller values of ω_e. When ω_e is made very small, the eddy viscosity jumps up outside the wake. This, however, has no influence on the solution inside the turbulent region. Thus, the solution is insensitive to the choice of ω_e provided that it is small enough, say a couple of decades smaller than ω inside the turbulent region. The velocity profiles, although not shown here, are equal to each other except for the highest values of ω_e in a way quite similar to k and ω. Fig. 6.20 shows that the same applies to the free-stream value of k. Here, ω_e is kept as constant 10^{-3}, and k_e is varied from 1.11×10^{-7} to 0.111. Again, the choice of k_e does not affect the solution if it is kept as 10^{-4} or smaller. With values higher than this, k_e starts affecting the solution like ω_e. Now, however, the eddy viscosity becomes extremely high outside the edge and this probably first begins to influence the solution inside the wake. Fig. 6.21 shows a third survey in which ν_T is kept as 10^{-5} and ω_e is again varied from 10^{-7} to 0.1. No further observations are made, and this just supports the conclusion that the only requirement for the free-stream values is that too high values should not be given. It may also be convenient to set a smaller value for k_e than for ω_e in order to keep ν_T small in the surrounding laminar flow. The theory of Section 6.2.4 assumes exactly zero values outside the edge and thus it makes sense that we must not use too high free-stream values if we wish to obtain a solution that approximately follows the theory near the edge. The numerical solutions with small k_e and ω_e, indeed, seem to behave much like the theory predicts.

In the self-similar wake flow, the external boundary condition was specified very near the edge of the wake. In this situation, the values at the edge of the wake are, indeed, approximately the same as those given at the external boundary. This is seldom the case in practical aerodynamics. It is a common practice, especially in high-lift aerodynamics, to extend the computational domain far away from the interesting parts of the flowfield. In such a domain, the values of k and ω may have much smaller values on the edges of turbulent regions than on the edge of the domain. This is because their transport equations reduce to convection-destruction equations in undisturbed laminar flow. Hence, k and ω are likely to have relatively

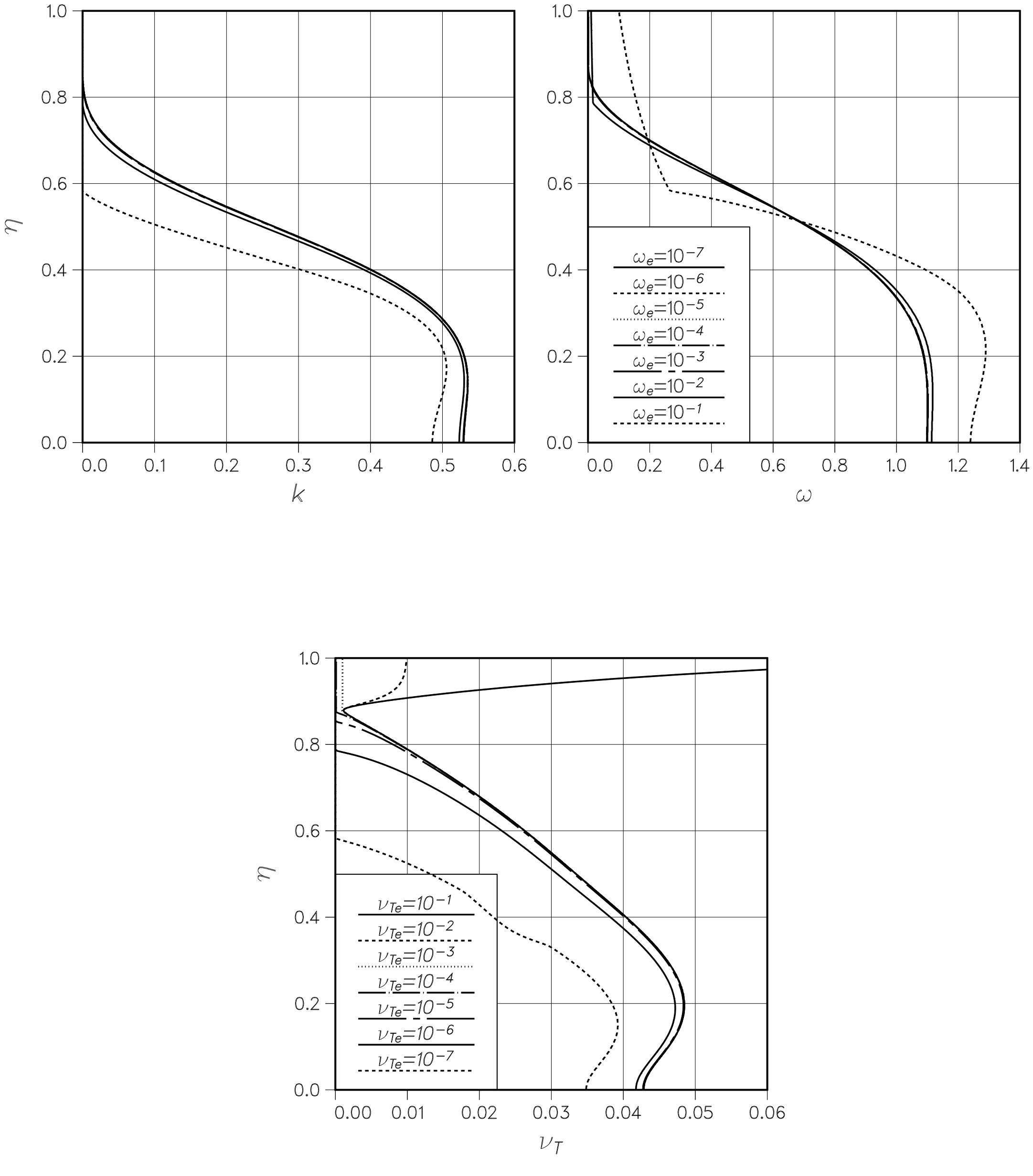

Figure 6.19: Influence of the free-stream values of k and ω on the wake-flow solution using the new model. Nondimensional k_e is kept at a constant value of 1.11×10^{-7} and ω_e is varied from 10^{-7} to 10^{-1}.

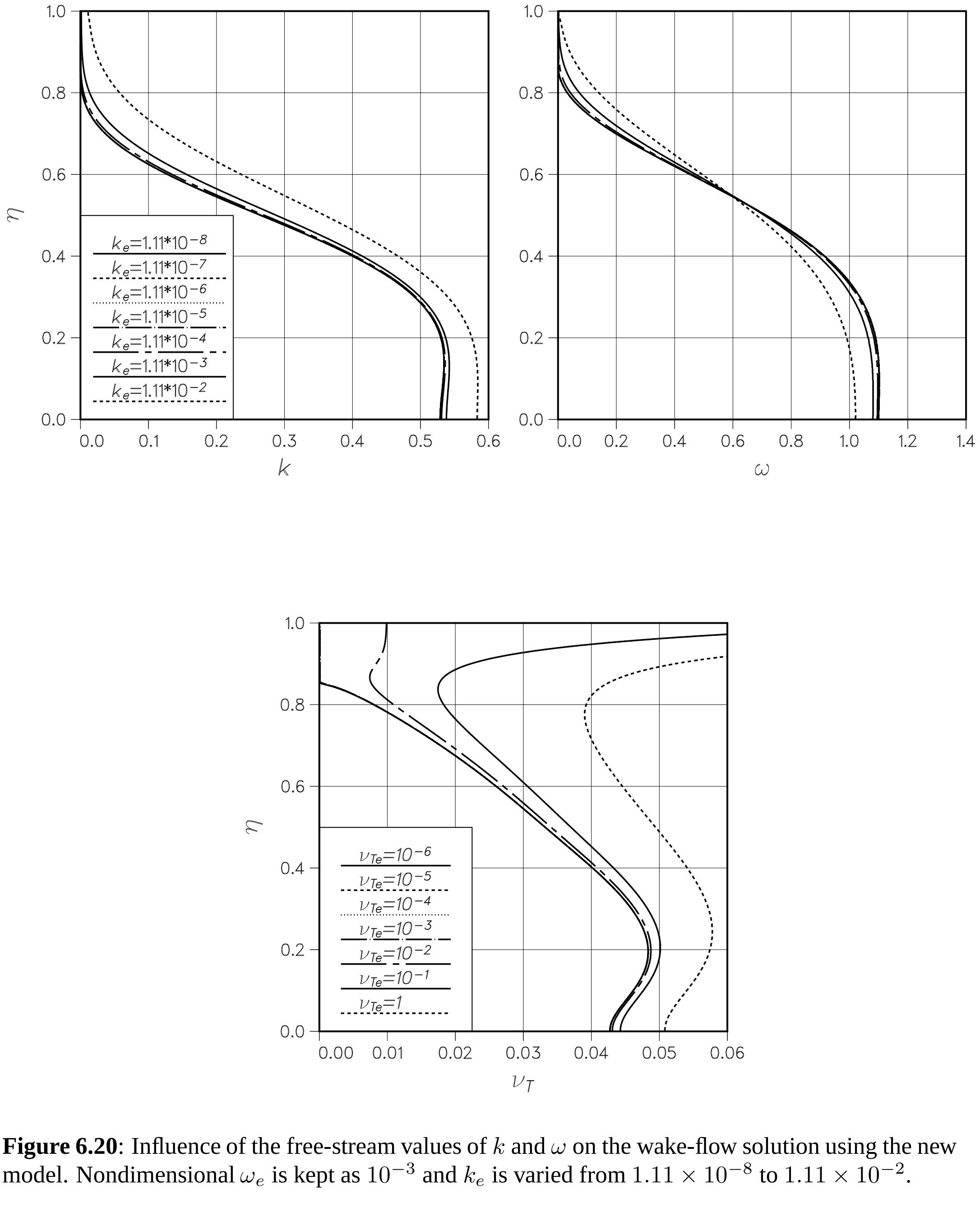

Figure 6.20: Influence of the free-stream values of k and ω on the wake-flow solution using the new model. Nondimensional ω_e is kept as 10^{-3} and k_e is varied from 1.11×10^{-8} to 1.11×10^{-2}.

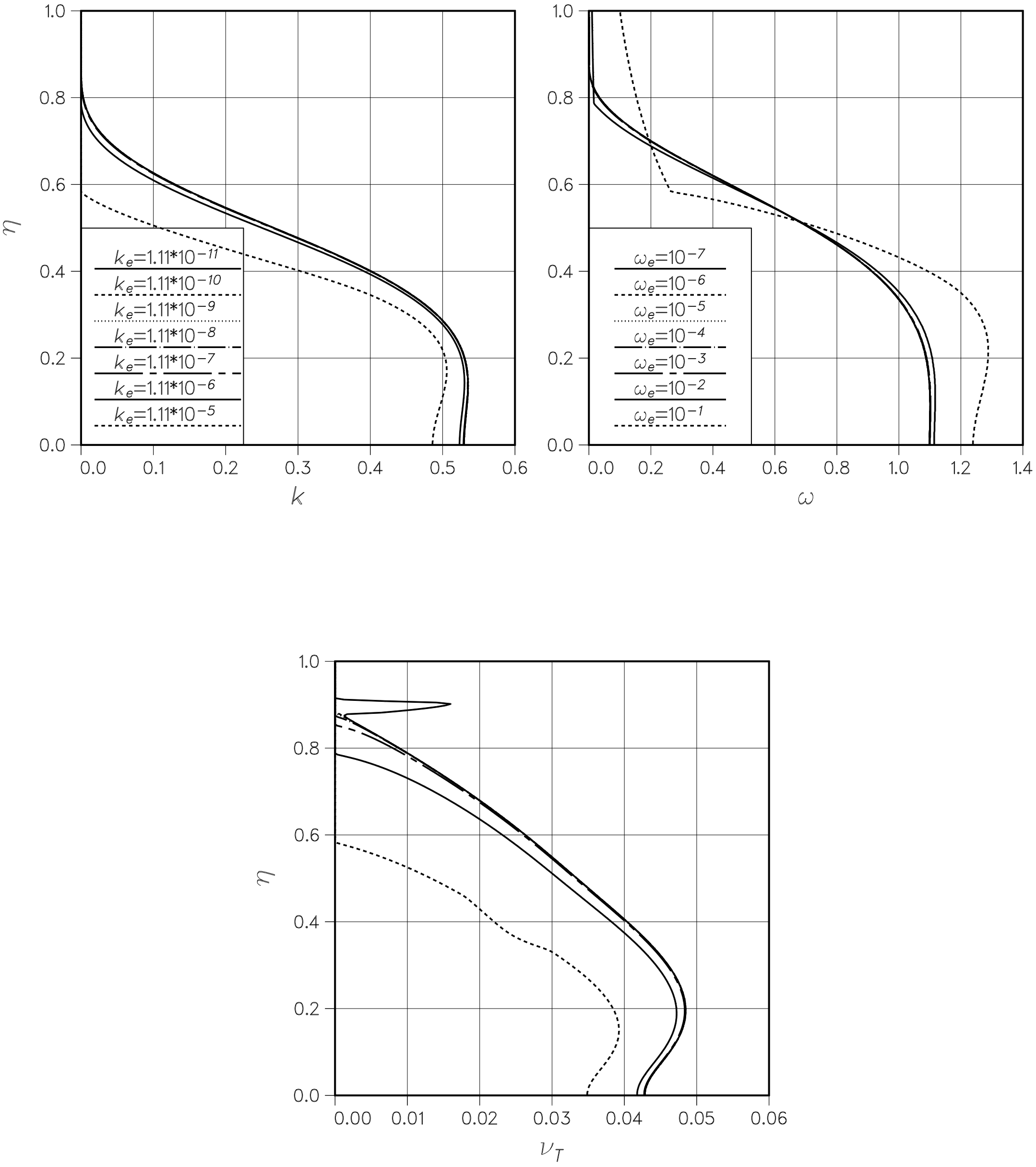

Figure 6.21: Influence of the free-stream values of k and ω on the wake-flow solution using the new model. Nondimensional ν_T is kept as 10^{-5} and ω_e is varied from 10^{-7} to 10^{-1}.

low values on the edges of turbulent regions compared to their values specified at the far-field boundaries.

To ensure that the inner coefficients provide similar behaviour on the free-stream edges, the wake flow is computed using them, too. Fig. 6.22 shows the case where k_e is kept constant corresponding to Fig. 6.19. Now, the wake spreads much more slowly, because the inner coefficients are not calibrated for this kind of flow. Nevertheless, the edge behaviour is seen to remain similar, or even less sensitive, as with the outer coefficients.

The role of the variable C_μ in the edge behaviour was discussed in Section 6.2.4. It was concluded that a nearly constant or slightly increasing trend over the edge is desirable. At this point, it was checked whether this is really achieved with the new model. All the numerical computations of the wake, mixing layer, and all self-similar boundary layers with different pressure gradients show either slightly increasing or constant C_μ on the edge. As expected, healthy smooth edges were predicted in all cases.

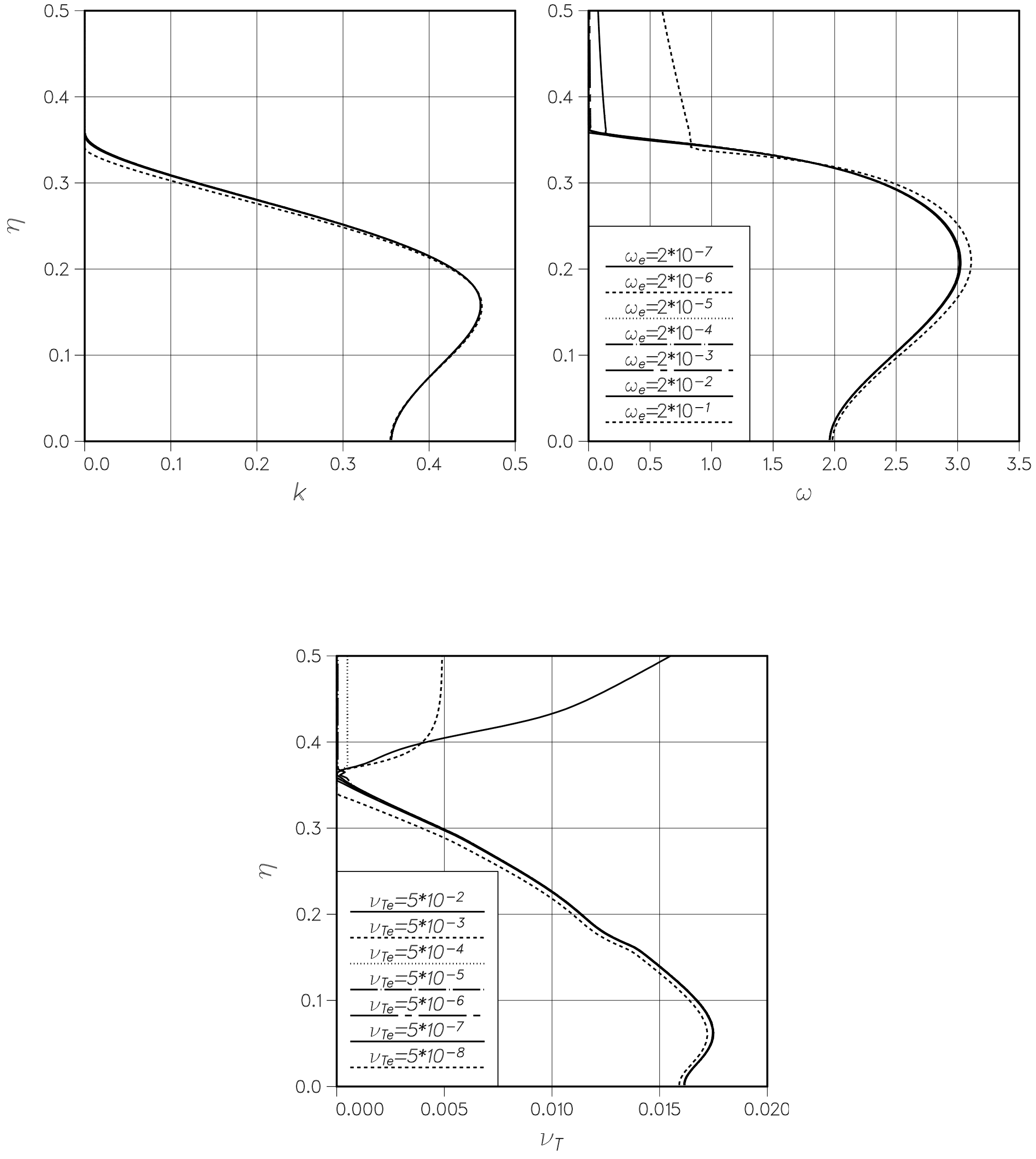

Figure 6.22: Influence of the free-stream value of ω in the wake-flow solution when the inner model coefficients of the new model are used. Nondimensional k_e is kept at a constant value of 1.11×10^{-7} and ω_e is varied from 2×10^{-7} to 2×10^{-1}.

6.4.7 Wall-Boundary Conditions

The usual no-slip condition ($k = 0$ on the wall) should be given for k on wall boundaries. The wall-boundary condition for ω is not that obvious because theoretically ω has a singularity on a solid wall. As very recently suggested by Gullman-Strand [141], ω can be split into two as

$$\omega = \tilde{\omega} + \omega_w = \tilde{\omega} + \frac{6\nu}{\beta y^2} \tag{6.68}$$

where ω_w is the general near-wall analytical solution valid in the viscous sublayer. Substitution of this into the ω-model equation yields a new form in which $\tilde{\omega}$ is the variable to be solved. A zero value is given for $\tilde{\omega}$ as a wall-boundary condition. This is an interesting technique and it certainly deserves more attention. However, studies of this method will be left for future work. At this stage, the method developed in Ref. [109] is employed. This is based on Wilcox's rough-wall boundary condition method [28, 60, 140]

$$\omega_w = \frac{u_\tau^2}{\nu} S_R \tag{6.69}$$

where S_R is a nondimensional function defined as

$$S_R = \begin{cases} [50/\max(k_s^+; k_{s\,min}^+)]^2 & \text{for } k_s^+ < 25 \\ 100/k_s^+ & \text{for } k_s^+ \geq 25 \end{cases} \tag{6.70}$$

and k_s^+ is the inner-scaled sand-roughness height $k_s u_\tau/\nu$, so that rough walls can be simulated if the equivalent sand roughness can be estimated. For smooth walls, $k_{s\,min}^+$ becomes active. It is known from experiments that the surface roughness does not influence the flow if k_s^+ is less than, say 4. The computed wall shear stress is, however, quite sensitive to the choice of $k_{s\,min}^+$ [109, 142]. The optimal value is a function of the grid spacing next to the wall. It has been found in Ref. [109] that the grid sensitivity can be largely eliminated if $k_{s\,min}^+$ is defined as the following function of y_1^+, the inner-scaled thickness of the first control volume

$$k_{s\,min}^+ = \min\left[2.4(y_1^+)^{0.85}; 8\right] \tag{6.71}$$

The upper limit is to avoid excessive values in the case of flow separation. Eq. (6.71) was optimized for the $k - \omega$ SST model, but it turned out that it works as well with the new model. This is shown in Fig. 6.23, which displays the variation in the skin-friction coefficient as a function of y_1^+ in fully developed channel flows at two Reynolds numbers: 10^6 and 2×10^4. The variation remains reasonably small up to y_1^+ as high as 4 or 5, especially at the higher Reynolds number.

A wall-function approach is an alternative to solving the equations through the viscous wall layer. Although the wall-function approach is not considered in this study, except in the self-similar boundary-layer computations, it is worth mentioning that this kind of wall treatment seems to have gained some fresh attention during the last few years. The traditional simple logarithmic wall-function approach is

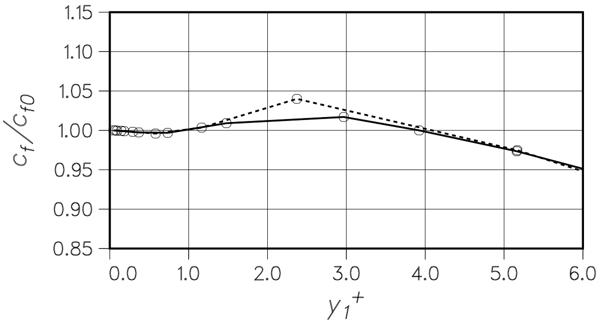

Figure 6.23: Influence of the near-wall grid spacing on the computed skin-friction coefficient of fully developed channel flows at $Re = 10^6$ (solid line), and at $Re = 2 \times 10^4$ (dashed line).

known to suffer from severe limitations since the logarithmic law is valid only over a limited range of situations. New, more flexible wall-function approaches have been proposed by Grotjans and Menter [143], by Rautaheimo and Siikonen [144], at least. Schatz and Thiele are currently working on further improvements and extensions of such techniques [131]. These methods attempt to combine the two traditional methods, *i.e.* the use of the log-law wall functions and the solution down to the wall, in a flexible and user-friendly way.

6.4.8 Equilibrium Boundary Layers under Pressure Gradients

So far, boundary-layer results have been shown only for the ZPG case. Next, the performance of the new model is investigated in equilibrium boundary layers with different non-zero pressure gradients. First, the mean-velocity profiles of six cases with β_T ranging from -0.35 to about 20 are shown together with experimental data. The $k-\omega$ results are compared also with the results computed using the standard $k-\varepsilon$ model [145]. The significantly different behaviour of the $k-\varepsilon$ and $k-\omega$ models is investigated. After this, the strongest adverse pressure-gradient case ($\beta_T = 20$) is studied in more detail. The first case is a favourable pressure-gradient boundary layer measured by Herring and Norbury with $\beta_T \approx -0.35$ [146]. Next, two mild adverse pressure-gradient

boundary layers are computed: $\beta_T \approx 0.9$ by Bradshaw [49], and $\beta_T \approx 1.8$ by Clauser [47]. Three boundary layers subjected to pressure gradients ranging from moderate to strong are finally computed. These are: $\beta_T \approx 5$ by Bradshaw and Ferris [147] (white symbols) and by Clauser [47] (black symbols), $\beta_T \approx 8$ by Clauser [47], and $\beta_T \approx 20$ by Skåre and Krogstad [50]. All this data, except that of Skåre and Krogstad, is taken from the proceedings of the 1968 AFOSR-IFP-Stanford Conference [48].

All the predicted velocity profiles involving $k-\omega$ modelling agree fairly well with the measured data in all cases except when $\beta_T \approx 5$. In this case, there is a disagreement also between the experimental profiles measured by Bradshaw [147] and by Clauser [47]. The role of the constitutive model is not as important here as in the non-equilibrium situations usually occurring in practical flow problems.

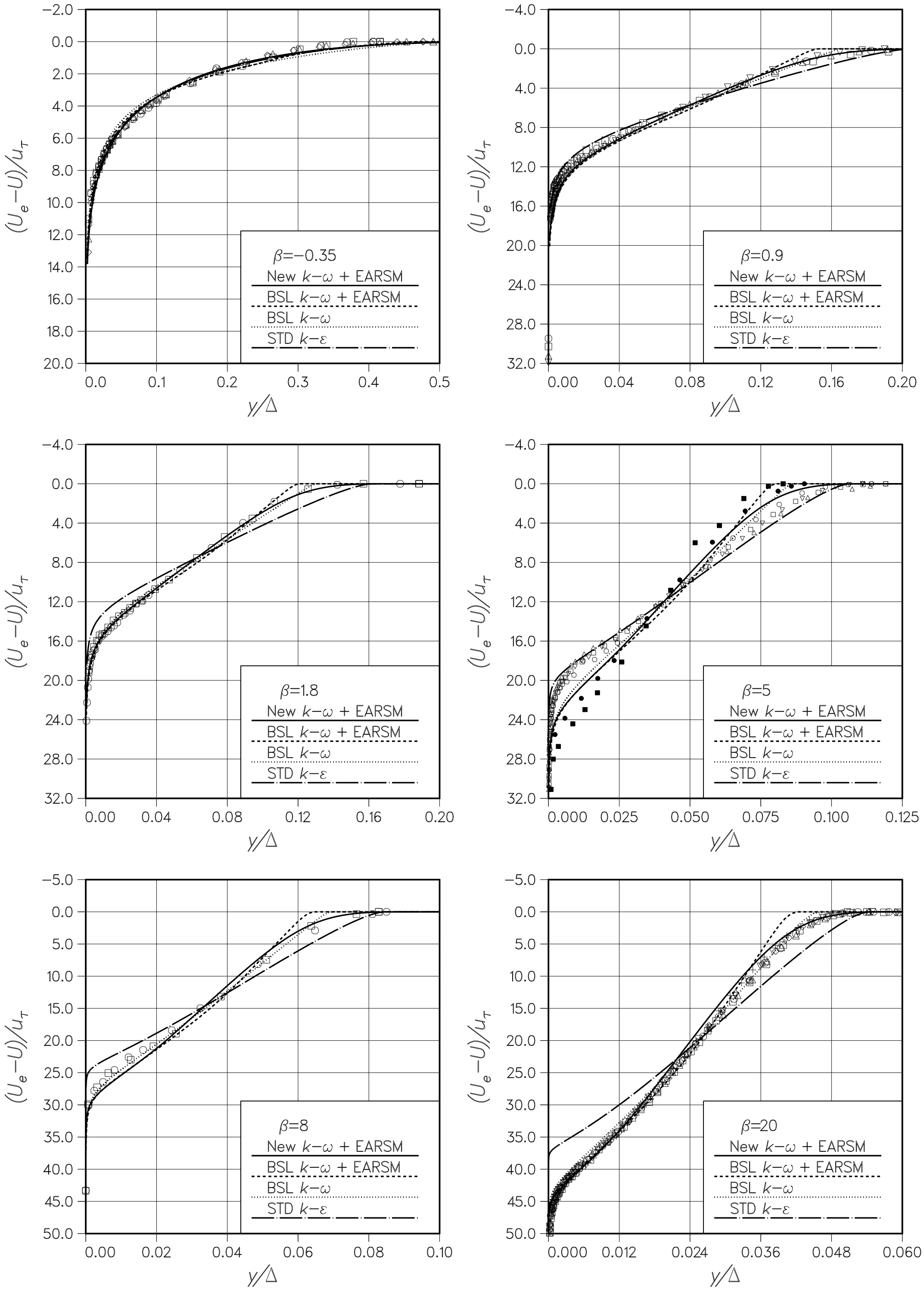

Figure 6.24: Velocity-defect profiles of six equilibrium boundary layers with different pressure gradients. Different symbols are used to separate measurements at different locations in the same experiment. In the case with $\beta_T \approx 5$, white symbols represent experimental data by Bradshaw and Ferris [147], and black symbols represent Clauser's measurements [47].

Therefore, the original linear BSL model is no worse in this case than the BSL-EARSM version. The velocity profiles computed using the new model and the BSL-EARSM are relatively similar to each other except near the edges. As expected, the velocity profiles computed employing the new model are in clearly better agreement with the measurement data on the edge regions. The differences between the results would become much larger in favour of the new model if the y-coordinate were scaled by the boundary layer thickness δ instead of Δ.

In contrast to all the $k-\omega$ results, the standard $k-\varepsilon$ model is in strong disagreement with the experimental data, especially at higher values of β_T. It gives too low a velocity defect near the wall. The velocity profiles are not only excessively full, but the overpredicted scaling velocity u_τ further increases the error. This is typically seen as overestimated skin friction and delayed separation in practical flow simulations. This shortcoming of the $k-\varepsilon$ models has been known for quite a long time. Wilcox critisized the $k-\varepsilon$ models for this reason in 1988 [60], and Rodi and Scheuerer [59] proposed already in 1986 that this problem is associated with the overestimation of the turbulent length-scale in the wall layer. This, indeed, is the reason. It is known from the experiments [50, 148] that the mixing length

$$l_{mix} = \sqrt{\frac{\nu_T}{|\mathrm{d}U/\mathrm{d}y|}} \tag{6.72}$$

shows linear growth $l_{mix}/\delta = \kappa_l y/\delta$ in the wall layer. The experiments show that the slope κ_l increases rapidly with β_T from 0.41 in ZPG boundary layer at least up to 0.78 in the APG case of Skåre and Krogstad with $\beta_T = 20$. It should be noted that the von Kármán constant of the logarithmic velocity profile, however, does not depend on the pressure gradient as first observed by Perry *et al.* [149]. Rodi and Scheuerer stated that “the length-scale gradient is virtually independent of the pressure gradient over a wide range”. This is in contrast with the experimental findings by Glowacki and Chi, and by Skåre and Krogstad. However, this does not invalidate the finding of Rodi and Scheuerer that the $k-\varepsilon$ model overestimates the length-scale slope in the wall layer. The usual length scale defined as $l_T = k^{3/2}/\varepsilon$ differs from the classical definition of the mixing length (6.72), but these two are linearly proportional to each other in the logarithmic layer. The mixing-length slope in the wall layer is plotted in Fig. 6.25 as a function of β_T.

Fig. 6.25 shows that the $k-\varepsilon$ model strongly overestimates the mixing-length slope in the wall layer while the $k-\omega$ models are engaged with much less severe overestimation. The experimental data is based on the measurements by Bradshaw [150], East and Sawyer [151], and Skåre and Krogstad [50], and it is taken from [50]. Menter’s BSL and SST models are also included in the comparison. The BSL model is in the best agreement with the experimental data. The new model as well as the SST model are slightly more in error in this sense. It was studied whether this difference comes from the constitutive model or from the coefficient σ_{k1} that takes the values 0.5, 0.85, and 1.1 in the BSL, SST, and the new models, respectively. It turned out that σ_{k1} is purely responsible of this difference while the constitutive model has virtually no effect in this case as the boundary layers are in equilibrium. One could now conclude that the value 1.1 selected for σ_{k1} is too large.

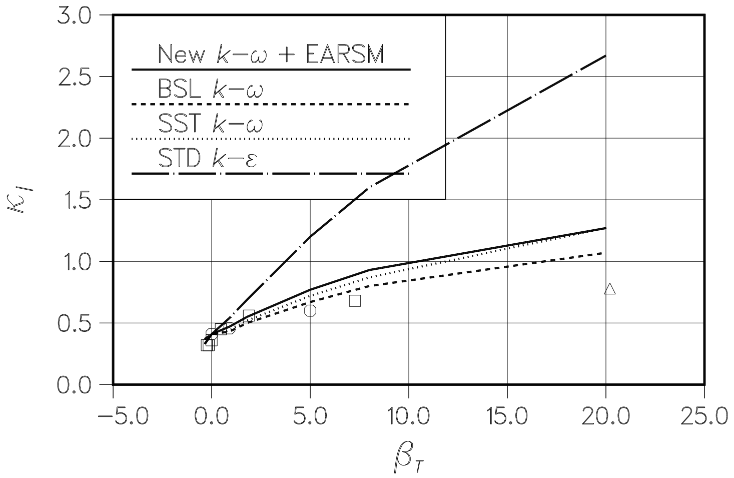

Figure 6.25: The log-layer slope of the turbulent length-scale or the mixing-length as a function of the nondimensional pressure-gradient parameter β_T. Measurements by Bradshaw (circles), East and Sawyer (squares), and Skåre and Krogstad (triangle). All measurement data is taken from [50].

However, the velocity profiles computed with the new model are in good agreement with the experiments. In addition, the SST model, which has quite a high σ_{k1}, has a good record of reasonably accurate predictions of retarding and separating boundary layers over the years. Furthermore, some two-dimensional computations with the new model showed that there is no need to reduce σ_{k1}, see Chapter 7. It must also be remembered that the ZPG boundary-layer profile will become concave in the defect layer as with the BSL-EARSM combination if σ_{k1} is reduced much below 1. This concave shape is somewhat similar to typical velocity profiles of APG boundary layers. Thus, it may be that a model that follows the experimental values of the mixing-length slope very well will show some features typical for the APG boundary layers already in the ZPG case. In this regard, it would be better to accept somewhat overestimated mixing-lenght slopes, especially as this overestimation is several times smaller than that of the $k - \varepsilon$ model.

The overestimation of the length scale obviously leads to excessive shear stress in the wall layer and this, in turn, leads to overestimated skin friction and too full a velocity profile. It is interesting to see that this difference in the $k - \varepsilon$ and the $k - \omega$ models is restricted to the wall layer. Somewhat surprisingly, both the models overestimate the shear stress in the defect layer. This is shown by Fig. 6.26, which illustrates the maximum shear stress as a function of β_T. This maximum occurs in the defect layer. Experiments show a linear increase with β_T, *i.e.*

$$-\frac{\overline{u'v'}_{max}}{u_\tau^2} - 1 \approx 0.75\beta_T \tag{6.73}$$

In contrast to this, both the $k - \varepsilon$ and the $k - \omega$ models predict similar growth that has a slope of about 1. This is also seen in the shear-stress plot of Fig. 6.27 where $\beta_T = 20$.

The consistently overestimated maximum shear stresses raise a question whether the simplifying assumptions invoked in the derivation of the self-similar equations

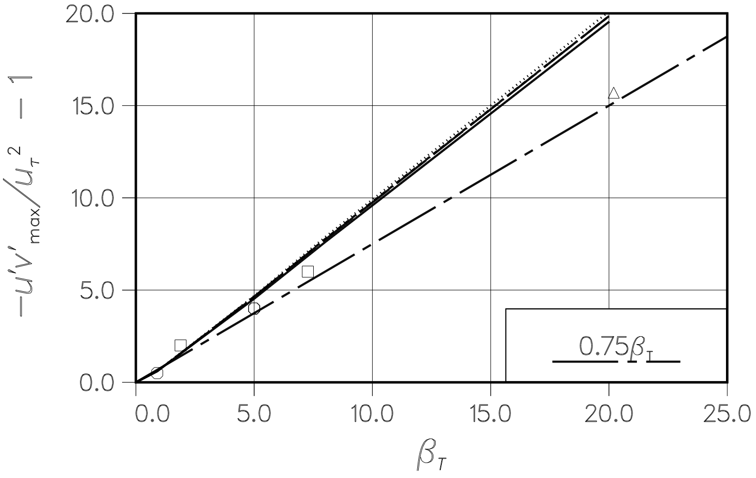

Figure 6.26: The maximum shear stress as a function of the nondimensional pressure-gradient parameter β_T. The dash-dotted line is a line fitted to the measured data as $-\overline{u'v'}_{max}/u_\tau^2 - 1 = 0.75\beta_T$. Measurements by Bradshaw (circles), East and Sawyer (squares), and Skåre and Krogstad (triangle). All measurement data is taken from [50]. Legends as in Fig. 6.25.

employed here could be responsible for this discrepancy. It must be kept in mind that the results shown here are numerical solutions to a simplified set of equations derived by applying certain equilibrium assumptions, see Section 4.1.3. Therefore, it may be necessary to verify that the simplifications of the equations do not cause errors comparable with the modelling errors. In this particular case, it is considered that the most significant simplification is that the rate of streamwise change of the normal-stress component $\partial\overline{u'u'}/\partial x$ has been omitted from the momentum equation. The influence of this is not studied in this work but, according to Skåre and Krogstad, the contribution of this term to the shear-stress profile is only of the order of 3% of the peak value. Thus, it can be assumed that this simplification is not responsible for the difference between the computed and measured shear-stress profiles. Instead, the reasons are very likely in the turbulence models.

The $k - \varepsilon$ model used for comparisons above is a standard linear Boussinesq model. Using higher-order constitutive models, like EARSMs, or models with only a scalar nonlinearity, like the SST, does not resolve the overestimation of the wall-layer length-scale. Such constitutive models typically give some improvements in predicting non-equilibrium flows, but a $k - \varepsilon$ model furnished with a higher-order constitutive model will still suffer from overestimated turbulent mixing near the wall. This has been shown by Hellsten in Ref. [63], where separating APG flows were computed using linear $k-\varepsilon$ and $k-\omega$ models, SST $k-\omega$, and EARSM based on the $k - \varepsilon$ and $k - \omega$ models. The linear models failed completely while the SST and the EARSM $k - \omega$ models gave satisfactory results. The $k - \varepsilon$ EARSM model was much better than the linear one, but very importantly, near the wall it failed almost similarly to the linear $k-\varepsilon$ model. In one of the cases, it completely refused to predict separation.

The strongest pressure-gradient case by Skåre and Krogstad is studied next in more detail. Fig. 6.27 shows the velocity profile in the logarithmic scale to study the wall layer (top left). The difference between the experiments and all the computations when $y/\delta \to 0$ is owing to the fact that the viscous sublayer is not included in the computations. The logarithmic boundary conditions are given at a very small value of y/δ. This is possible, because $Re \to \infty$ is assumed, which implies vanishing thickness of the viscous sublayer. The velocity profiles plotted in log-scale reveal that the $k-\omega$ models underestimate the slope of the logarithmic profile $1/\kappa$. According to the BSL $k-\omega$ model $\kappa = 0.66$ and the new model gives $\kappa = 0.8$ while the measurements follow the slope of $\kappa = 0.41$ familiar from the ZPG boundary layers. The $k-\varepsilon$ model shows an even much higher value of $\kappa = 1.9$. This shows that neither the existing $k-\omega$ models nor the new one is ideal for APG boundary layers, although they are by far superior to the $k-\varepsilon$ models. It is probably difficult to improve further the accuracy of the $k-\omega$ modelling for APG boundary layers without deteriorating the accuracy in other kinds of flow situations. Further improvements might require a completely different approach, such as starting the development from some other scale variable than ω. Such efforts are beyond the scope of this study, but research on this is currently active at ONERA [131].

Fig. 6.27 (top right) shows the mixing-length distributions through the layer. Although the new model overpredicts the slope in the wall layer as well as the other $k-\omega$ models, its agreement with the measurements is overwhelming in comparison with the other models in the outer parts. In this regard, it is somewhat surprising that it overestimates the shear stress as well as the normal stresses, also shown in Fig. 6.27. Nevertheless, the new model predicts also the stress components somewhat more accurately than the other models in the comparison, especially near the outer edge. The linear models, the BSL $k-\omega$ and the standard $k-\varepsilon$, are of course incapable of predicting the normal stresses properly, because they just assume an isotropic distribution of energy on the normal stresses $\overline{u_i'u_j'} = 2k/3$ when $i = j$. It is also interesting to see that, unlike the other models in the comparison, the new model gives the mixing length with at least a qualitatively correct trend when the outer edge is approached. The experimental data [50, 152] suggests that the mixing length increases towards the edge, when the shear goes to zero. The new model does the same as the length scale $l_T = \sqrt{k}/\omega \sim f^{-2/3}$ if C_μ is assumed to be constant around the edge. The other models predict a decreasing mixing length when the edge is approached. This is still other evidence that exploitation of the edge analysis of Section 6.2.4 in the development has been beneficial.

6.5 Alternative Operational Scale Variables

6.5.1 Generalized Formulation for the Scale-Determining Model

As discussed in Section 2.5, the choice of the second scale variable $\phi = k^m\varepsilon^n$ strongly affects the resulting model. New terms proportional to products of gradients of ϕ and k will appear, when a given model of the form (2.49) written for some variable, say ϕ_1, is transformed for another variable ϕ_2 with different values of m and n. If the equation (2.49) is extended by adding new terms of such form, the

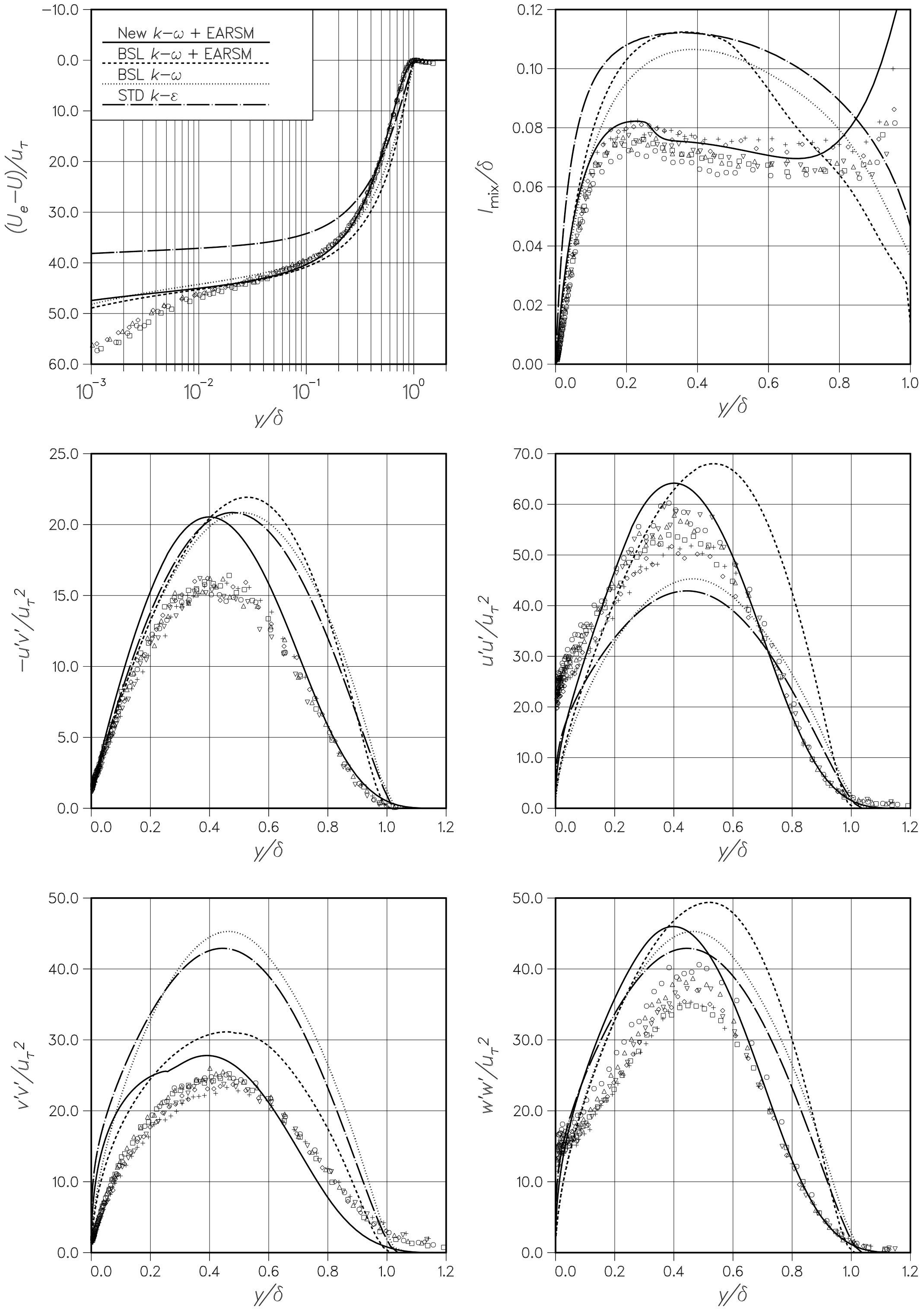

Figure 6.27: The APG boundary layer with $\beta_T = 20$ studied experimentally by Skåre and Krogstad. Velocity-defect profiles in logarithmic scale (top left), the mixing-length distributions (top right), and the turbulent stresses $-\overline{u'v'}$, $\overline{u'u'}$, $\overline{v'v'}$, and $\overline{w'w'}$.

model will then allow different choices of ϕ. Transformations from one variable to another will merely change the values of the model coefficients rather than bring in new terms.

It might be useful to set up the newly developed $k-\omega$ model in a generalized form so that arbitrary operational variables can be studied. Usually a turbulence model is operated in the form it has been developed, but sometimes it may be useful to transform the model for some other operational variable. For instance Kok developed his model in the $k-\omega$ form [130], but the model is operated in the $k-\tau$-form [153] ($\tau \sim 1/\omega$). Using a generalized formulation, the given model can be transformed for any new operational variable in principle. Therefore, this method could be exploited in studying the choice of an alternative operational variable for an existing model. This will be systematically attempted in Section 6.5.3. Furthermore, it might be possible to study the effect of the choice of the original second scale variable, *i.e.* ω in this case, in a systematic way. This is because the generalized model coefficients can be derived as functions of the operational variable parameters m, n, the model coefficients, and the m, n-parameters of the original variable. In principle, this makes it possible to perturb the definition of the original variable by small increments around its m and n values. It would be interesting to see if the choice of the original second scale variable could be optimized this way. For example, most of the $k-\omega$ models predict the wall shear-stress and the logarithmic velocity profile better than the other scale-determining models without any near-wall corrections. The question arises: could this be made even better by changing m and n slightly from their ω-values and recalibrating the obtained model? Such studies are, however, beyond the limits of this study and are left for the future.

The generalized second-scale determining model can be derived by first expressing the selected original variable as $\tilde{\omega} = k^{\tilde{m}}\varepsilon^{\tilde{n}}$ and transforming it for arbitrary operational variable $\phi = k^m\varepsilon^n$. The tilde-notation is used in order to emphasize that the $\tilde{\omega}$ is not necessarily the usual ω, but for instance a new variable obtained by perturbing the definition of $\tilde{\omega} = k^{\tilde{m}}\varepsilon^{\tilde{n}}$ around the ω-exponents $m=-1$ and $n=1$ as proposed above. It must be noted that non-integer values can well be applied because the final m and n of the operational variable can be chosen as integers. In this study, the new model, or more generally, any $k-\omega$ model of the form given by Eqs. (6.2) – (6.3) is selected as the baseline model. The necessary algebra is carried out in Appendix A, and the resulting equation is

$$
\begin{aligned}
\frac{\mathrm{D}\phi}{\mathrm{D}t} &= \frac{\phi}{k}\left(C_{\phi 1}P - C_{\phi 2}\varepsilon\right) + \frac{\partial}{\partial x_j}\left(\nu_{\phi\phi}\frac{\partial \phi}{\partial x_j} + \nu_{\phi k}\frac{\phi}{k}\frac{\partial k}{\partial x_j}\right) \\
&+ \left(C_{\phi 3}^{(V)}\nu + C_{\phi 3}^{(T)}\nu_T\right)\frac{1}{k}\frac{\partial k}{\partial x_j}\frac{\partial \phi}{\partial x_j} + \left(C_{\phi 4}^{(V)}\nu + C_{\phi 4}^{(T)}\nu_T\right)\frac{\phi}{k^2}\frac{\partial k}{\partial x_j}\frac{\partial k}{\partial x_j} \\
&+ \left(C_{\phi 5}^{(V)}\nu + C_{\phi 5}^{(T)}\nu_T\right)\frac{1}{\phi}\frac{\partial \phi}{\partial x_j}\frac{\partial \phi}{\partial x_j}
\end{aligned}
\tag{6.74}
$$

where

$$\begin{array}{ll} \nu_{\phi\phi} = \nu_{\tilde{\omega}} & \nu_{\phi k} = m'(\nu_{\tilde{\omega}} - \nu_k)/n' \\ C_{\phi 1} = (C_{\tilde{\omega}_1} - m')/n' & C_{\phi 2} = (C_{\tilde{\omega}_2} - m')/n' \\ C_{\phi 3}^{(V)} = 2m' & C_{\phi 4}^{(V)} = m'(m'-1)/n' \\ C_{\phi 5}^{(V)} = n' - 1 & C_{\phi 3}^{(T)} = 2m'\sigma_{\tilde{\omega}} + m'(\sigma_k - \sigma_{\tilde{\omega}})/n' + \sigma_d \\ C_{\phi 4}^{(T)} = m'(m'\sigma_{\tilde{\omega}} - \sigma_k + \sigma_d)/n' & C_{\phi 5}^{(T)} = (n'-1)\sigma_{\tilde{\omega}} \end{array} \tag{6.75}$$

The auxiliary parameters m' and n' are defined as

$$m' = (\tilde{m}n - m\tilde{n})/n \qquad \text{and} \qquad n' = \tilde{n}/n \qquad \text{where} \qquad n \neq 0 \tag{6.76}$$

The scalar-diffusivity gradient diffusion model is employed in (6.74). The diffusivities are given by

$$\nu_k = \nu + \sigma_k \nu_T \tag{6.77}$$

$$\nu_{\tilde{\omega}} = \nu + \sigma_{\tilde{\omega}} \nu_T \tag{6.78}$$

where the molecular diffusion is included. The molecular viscosity is also kept in the additional gradient terms for the sake of completeness.

6.5.2 Some Numerical Aspects

The mathematical properties of the source terms should be understood in order to avoid numerically troublesome formulations. The mathematical nature of each term must also be known when the numerical algorithms are to be selected. This can be studied by analysing the generalized model formulation (6.74). It can be simplified by omitting the viscosity in the gradient terms. Furthermore, the production of k can be approximated as

$$P = -\overline{u_k' u_l'} \frac{\partial U_k}{\partial x_l} \approx \nu_T \left(\frac{\partial U_k}{\partial x_l} + \frac{\partial U_l}{\partial x_k} \right) \frac{\partial U_k}{\partial x_l} = 2\nu_T \mathbf{S} : \nabla \mathbf{U} \tag{6.79}$$

Note that $\mathbf{S}$ is here the dimensional strain-rate tensor

$$\mathbf{S} = \frac{1}{2} \left(\frac{\partial U_k}{\partial x_l} + \frac{\partial U_l}{\partial x_k} \right) \tag{6.80}$$

After these simplifications Eq. 6.74 can be formally written as

$$\frac{\mathrm{D}\phi}{\mathrm{D}t} - \frac{\partial}{\partial x_j} \left(\nu_{\phi\phi} \frac{\partial \phi}{\partial x_j} + \nu_{\phi k} \frac{\phi}{k} \frac{\partial k}{\partial x_j} \right) = \sum_{l=1}^{5} C_{\phi l} \phi^{\alpha_l} k^{\beta_l} T_l \tag{6.81}$$

Here, each source term is expressed as a product of a coefficient $C_{\phi l}$, powers of ϕ and k, and an inner product of gradients of either mean velocity or ϕ or k (note, that $T_2 = 1$). Expressions of these factors are given in Table 6.2 as functions of the background model coefficients, and the exponents $\tilde{m}$, $\tilde{n}$, m, and n.

Table 6.2: Source term factors in Eq. (6.81). Note that $m' = (\tilde{m}n - m\tilde{n})/n$ and $n' = \tilde{n}/n$.

l	α_l	β_l	T_l	$C_{\phi l}$
1	$1 - 1/n$	$1 + m/n$	$\mathbf{S} : \nabla\mathbf{U}$	$2C_\mu(C_{\tilde{\omega}1} - m')/n'$
2	$1 + 1/n$	$-1 - m/n$	1	$-(C_{\tilde{\omega}2} - m')/n'$
3	$-1/n$	$1 + m/n$	$\nabla k \cdot \nabla\phi$	$C_\mu \{m'[(2 - 1/n')\sigma_{\tilde{\omega}} + \sigma_k/n'] + \sigma_d\}$
4	$-1 + 1/n$	m/n	$\nabla k \cdot \nabla k$	$C_\mu m'(m'\sigma_{\tilde{\omega}} - \sigma_k + \sigma_d)/n'$
5	$1 + 1/n$	$2 + m/n$	$\nabla\phi \cdot \nabla\phi$	$C_\mu(n' - 1)\sigma_{\tilde{\omega}}$

To make it easier to study the behaviour of the source terms, the gradient terms must be considered frozen. With this assumption, the behaviour of each term depends on the sign of the product $C_{\phi l}T_l$ and on the signs of α_l and β_l and also on their relative magnitude. If $C_{\phi l}T_l < 0$, the term is dissipative, but for positive values of the factor $C_{\phi l}T_l$ it becomes productive. Terms with both α_l and the coefficient $C_{\phi l}$ having a negative value may potentially behave in an unfavourable manner depending somewhat on the value of β_l and also on the behaviour of the gradient factor.

The above can be understood by studying a simple model equation

$$\frac{\mathrm{d}\phi}{\mathrm{d}t} = \lambda\phi^\alpha \tag{6.82}$$

If $\alpha = 1$, the equation is linear and its solution is simply $\phi(t) = Ce^{\lambda t}$, *i.e.* exponential growth or decay depending on the sign of λ. C is a constant determined by the initial condition. For all other values of α, the equation is nonlinear and at least a following solution exists that does not satisfy an arbitrary initial condition

$$\phi(t) = [(1 - \alpha)\lambda t]^{1/(1-\alpha)} \quad \text{with} \quad \alpha \neq 1 \tag{6.83}$$

representing either algebraic growth or decay as long as ϕ is real-valued. For instance if $\alpha = 2$, the solution is simply $\phi(t) = -1/(\lambda t)$. On the other hand, if $\alpha = -1$ the solution will be complex-valued if $\lambda < 0$ (negative exponent and negative coefficient). The source terms of Eq. (6.81) can be studied similarly, although it must be remembered that, of course, the real problem is much more complicated than (6.82) including, *e.g.* diffusion and variable factors k^{β_l} and the gradient products.

By inspecting the values of α and the sign of $C_{\phi l}T_l$ of Eq. (6.81) we can check that none of the terms involve both negative exponent and negative coefficient. If the third or the fifth term of (6.81) are of this form, the negative exponent can be eliminated by transforming the partial derivative $\partial\phi/\partial x_j$ for another variable $\psi = k^p\phi^q$ using the formula

$$\frac{\partial\phi}{\partial x_j} = \frac{1}{qk^p\phi^{q-1}}\frac{\partial\psi}{\partial x_j} - \frac{p\phi}{qk}\frac{\partial k}{\partial x_j} \tag{6.84}$$

It will also be found whether a term is dissipative or productive. This is useful information not only in selecting the operational variable but also when the numerical solution procedure is designed. This is because of the broadly known fact that implicit treatment is best suited for dissipative terms and explicit methods for terms that make the solution to grow exponentially. This becomes clear when (6.82) with $\alpha = 1$ is discretized using the explicit Euler scheme as

$$\phi^{n+1} = (1 + \lambda\Delta t)\phi^n \tag{6.85}$$

and the implicit Euler scheme as

$$\phi^{n+1} = \frac{\phi^n}{1 - \lambda\Delta t} \tag{6.86}$$

The former has a severe stability limit in dissipative cases ($\lambda < 0$) while the latter has a similar limit in the productive cases, but is unconditionally stable in dissipative cases.

Let us study the case of $\alpha = -1$ and $\lambda > 0$ as an example of a situation when the solution grows algebraically. Now the explicit Euler scheme gives

$$\phi^{n+1} = \phi^n + \frac{\lambda\Delta t}{\phi^n} \tag{6.87}$$

which has no stability limit but is singular when $\phi \rightarrow 0$. The implicit scheme provides

$$\phi^{n+1} = \frac{1}{2}\left(\phi^n \pm \sqrt{(\phi^n)^2 + 4\lambda\Delta t}\right) \tag{6.88}$$

This is also unconditionally stable and non-singular for all values of ϕ. These kinds of terms are probably acceptable in the real problem provided that $\beta_l > -\alpha_l$ to ensure that the term vanishes at the limit when both k and ϕ approach zero. It is assumed that the implicit treatment is a better choice for these kinds of terms. For the real problem, the implicit method cannot be derived similarly as (6.86) or (6.88). Instead, it is derived by means of approximating the source term at the time level of $n + 1$ using a linearized Taylor polynomial expansion.

As an example, the ω model equation (6.3) is analysed. The production term is approximated to the leading order as $2C_{\omega 1}C_\mu \mathbf{S} : \nabla\mathbf{U}$. This does not depend on ω itself at all. See also Table 6.2. This kind of source term makes the solution grow only algebraically if the other variables are thought to be frozen. An algebraically growing solution is probably easier to manage with any numerical solution method than the exponential growth. The cross term also supports algebraic growth (provided that its gradient factor does not grow very rapidly). This is because it is proportional to the inverse of ω and it is always non-negative. The sink term in turn is $-C_{\omega 2}\omega^2$ which supports algebraic decay. Hence, there are no ill-behaving source terms or even any terms supporting exponential growth. This may partially explain why $k-\omega$ models are usually reported to be numerically better behaving than some alternative models, for instance the low-Reynolds-number $k - \varepsilon$ models.

6.5.3 Constraints in the Operational Scale-Variable Space

The newly calibrated second-scale model has not necessarily to be formulated using ω as an operational variable, although ω has been one of the most popular choices in aerodynamics following the work of Wilcox [60] and Menter [3]. The use of ω has some advantages. For example, the source term of the usual ω model equation has a form favourable for numerical solution. It also easily allows the modelling of sand-roughness on walls [60, 154]. On the other hand, the use of ω has been criticized, mainly because of its singular near-wall behaviour. Theoretically, $\omega \sim 1/y^2$ when $y \to 0$ and thus the wall-boundary condition, in principle, should approach infinity and the gradient of ω is very high near the wall. This anomaly can be overcome by means of careful numerical implementation of the wall-boundary condition, see *e.g.* Ref. [109]. On the other hand, splitting ω into two parts has been recently proposed by Gullman-Strand [141], see Section 6.4.7. This way, the ω variable to be solved will go to zero on the wall. However, it may be interesting to look for some other operational variable with a zero value at the wall as an alternative to ω.

The possibilities to find a good alternative for ω with a zero wall-value are studied in this section. Such an operational variable should have a decaying solution in laminar free stream so that the free-stream boundary condition approaches zero. Otherwise, it would be very difficult to specify the free-stream boundary value since the solution would grow along the free flow. A number of other requirements can be posed concerning the form of source terms appearing in the model equation transformed for the new variable. There should be no singular source terms or terms supporting ill-behaved solutions. Such terms may cause instabilities in the numerical solution procedure.

The choice of the operational variable is here studied with the aid of the generalized scale variable $\phi = k^m \varepsilon^n$ and its model equation (6.74). This way, the selection of m and n can be studied systematically. The above-mentioned requirements can be expressed as constraints in the m, n-space.

It is proposed that an ideal operational form of a scale-determining model should fulfil the following requirements:

1. Non-growing solution in free stream *i.e.* boundary condition $\phi_\infty \to 0$ allowed
2. Wall-boundary condition $\to 0$ is desirable
3. All source terms non-singular on walls and in free-stream conditions
4. Source terms with a negative exponent of ϕ should never have a negative coefficient
5. Growth rate from the wall preferably not steeper than that of k ($k \sim y^2$ when $y \to 0$)

These requirements can be expressed as formal constraints in the m, n-space. These constraints are derived in the following.

The first requirement will be satisfied if $C_{\phi 2} \geq 0$. This is the case when

$$\frac{C_{\tilde{\omega}2} - m'}{n'} \geq 0 \tag{6.89}$$

Table 6.3: Exponents γ_l of (6.91) and their non-negativity conditions for each term.

Term	γ_l	$\gamma_l \geq 0$ when
Extra diffusion	$m-1$	$m \geq 1$
1	$m+1$	$m \geq -1$
2	$m-1$	$m \geq 1$
3	1	Always non-singular
4	$2-m$	$m \geq 0$
5	$m-1$	$m \leq 2$ and $n \neq 1$
All		$m \geq 1$ and $m \leq 2$ if $n \neq 1$

which, after substituting m' and n', yields the constraint

$$m \geq \frac{\tilde{m} - C_{\tilde{\omega}2}}{\tilde{n}} n \tag{6.90}$$

The second requirement implies that $m > 0$. Note, that ω and ε do not satisfy this requirement.

In order to find the limits of singularities in the m, n-space, we have to transform all the source terms into the form

$$C_{\phi l} k^{\gamma_l} \varepsilon^{\delta_l} T_l \tag{6.91}$$

The exponent of k must be non-negative for all terms in order to avoid singularities at no-slip walls, where $k \rightarrow 0$ and ε remains non-zero. Also the extra diffusion term may go singular. The exponents of k and their non-negativity conditions are given for each term in Table 6.3. It is concluded that m must be at least 1 and it may not exceed the value of 2 except if $n = 1$.

The fourth requirement is probably not critical for the production term even when the exponent of ϕ is negative, *i.e.* when $0 < n < 1$. This is because the production term is typically non-negative and may get negative values only locally in some circumstances. This requirement can always be satisfied for the gradient terms 3, 4, and 5 by means of yet another transformation of ϕ using the formula (6.84). Thus, this condition needs to be satisfied only for the sink term (term 2). Its coefficient is required always to be negative (requirement 1), thus the exponent of ϕ, which is $1 + 1/n$, must be positive. This is the case when $n > 0$ or $n \leq -1$.

The last requirement is to prevent the second derivative of ϕ from becoming too high next to the wall. This is because the grid convergence may slow down in the near-wall region if the second derivative of ϕ gets considerably larger values than that of k. It is known that $k \sim y^2$ when the wall is approached. Therefore, the corresponding exponent of ϕ should not be much larger than 2. This, however, is not a strict constraint but merely a hint of not choosing m much higher than one.

The above-derived constraints deny certain regions of the m, n-space. This is illustrated in Fig. 6.28. Most of the suggested scale-determining variables found

Table 6.4: A few possible operational variables suggested in the literature.

Variable ϕ	m	n	notes
ε	0	1	$\varepsilon_w \neq 0$
ω	-1	1	$\omega_w \neq 0$, very steep gradient when $y \to 0$
φ	$-1/2$	1	$\varphi_w \neq 0$, steep gradient when $y \to 0$
ω^2 (or ζ)	-2	2	$\omega_w^2 \neq 0$, very steep gradient when $y \to 0$
τ	1	-1	$\tau_\infty \to 0$ not allowed
g	$1/2$	$-1/2$	$g_\infty \to 0$ not allowed
σ	$1/2$	-1	$g_\infty \to 0$ not allowed
l	$3/2$	-1	$l_\infty \to 0$ not allowed
R	2	-1	high 2nd derivative when $y \to 0$
kl	$5/2$	-1	high 2nd derivative when $y \to 0$

in the literature are also shown in Fig. 6.28 a. These variables are also given and commented on in Table 6.4. All of them are found to violate some of the constraints suggested here. For instance, singularities appear in many proposed models, even in the most popular $k-\varepsilon$ models. These singularities are usually removed by means of wall-damping functions that go to zero when the wall is approached. In this work, however, it is one of the principal requirements that no wall-damping functions are included in the model. On the other hand, some models *e.g.* $k-\tau$ and $k-l$ formulations give growing solutions in a free stream. This makes it difficult to specify free-stream boundary conditions. For instance, in order to avoid the growing free-stream solution, Kok and Spekreijse [153] redefined τ as $\tau = 1/(\omega+\omega_0)$ with ω_0 being a fixed finite free-stream value. In this work, the variables with growing free-stream solutions are not accepted so that such tricks can be avoided.

It must be remembered that the constraints derived here are only for the transformations of the $k-\omega$ models of the form of (6.2) – (6.3) considered in this study. Moreover, the requirements set for the ideal operational form are really stringent ones, indeed, and not absolute requirements that any model must obey. In other words, the observation that most of the proposed second scale variables do not satisfy the given constraints, should not be understood as criticism towards the numerous proposed models employing such variables.

Because most of the displayed variables are not suitable for this study, a new candidate as an alternative operational variable is suggested here. This is $k\varepsilon$ called here α. Also $R = k^2\varepsilon^{-1}$ appears promising, because it also fulfils the given conditions, except the last of them; its second derivative gets higher values than that of k near the wall, because it is proportional to k^2. R has been chosen as a scale variable in some proposed models, *e.g.* [155]. These two variables are displayed in Fig. 6.28 b.

Numerical experiments, however, showed that the generalized form (6.74) with an arbitrary choice of m and n cannot be easily solved numerically. Unresolvable

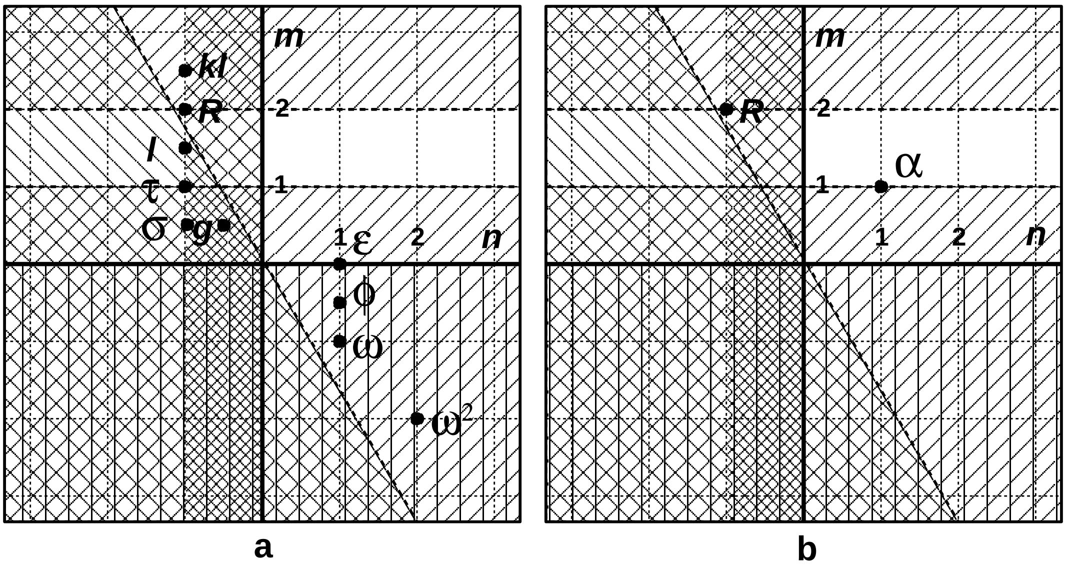

Figure 6.28: Constrained m, n-space with: a) most of the scale-determining variables suggested in the literature, and b) proposed candidates to be studied: $\alpha = k\varepsilon$, and $R = k^2/\varepsilon$. The lines bordering the allowed regions also belong to these regions except the line $n = 0$. For example, $1 \leq m \leq 2$ is allowed when $n > 0$.

troubles arose even with the selected variables $\alpha = k\varepsilon$ and $R = k^2/\varepsilon$ which were anticipated to be numerically well-behaving. The reason for these numerical difficulties is not known at present. The extra diffusion term was considered as one possible reason, but the elimination of it by trying equal values for σ_k and σ_ω did not solve the problem. Perhaps the gradient products in some of the cross terms trigger numerical instabilities near the walls. Attention was also paid to the numerical treatment of these terms, but without much success. Finally, the attempts to find an alternative operational variable were stopped after considerable efforts. An important reason for this was that Gullman-Strand proposed at the same time to replace the traditional ω by a wall-vanishing variable $\tilde{\omega}$ (6.68) [141]. The use of this decomposition of ω removes the wall singularity and leads to a much simpler equation than (6.74). Because the ω-formulation has practically no other weaknesses than the wall-singularity, it is considered that there is probably no need to continue the efforts to find alternative operational forms. Within this study, the final operational form of the new model will be its original $k - \omega$ form. If it is considered important in the future to remove the wall-singularity, the model can be transformed as proposed by Gullman-Strand [141].

6.6 Summary of the Model

6.6.1 The Scale-Determining Model

The transport equations for k and ω of the new $k-\omega$ model are written as

$$\begin{aligned}\frac{\mathrm{D}k}{\mathrm{D}t} &= P-\varepsilon+\frac{\partial}{\partial x_j}\left[(\nu+\sigma_k\nu_T)\frac{\partial k}{\partial x_j}\right] && (6.92)\\ \frac{\mathrm{D}\omega}{\mathrm{D}t} &= \frac{\omega}{k}(C_{\omega1}P-C_{\omega2}\varepsilon)+\frac{\partial}{\partial x_j}\left[(\nu+\sigma_\omega\nu_T)\frac{\partial\omega}{\partial x_j}\right] && (6.93)\\ &+ \frac{\sigma_d}{\omega}\max\left(\frac{\partial k}{\partial x_j}\frac{\partial\omega}{\partial x_j};0\right)\end{aligned}$$

Note, that the cross term is only included when the inner product of the gradients of k and ω is positive. The model coefficients vary in space as

$$\begin{pmatrix}C_{\omega1}\\ C_{\omega2}\\ \sigma_k\\ \sigma_\omega\\ \sigma_d\end{pmatrix}=f_{mix}\begin{pmatrix}C_{\omega11}\\ C_{\omega21}\\ \sigma_{k1}\\ \sigma_{\omega1}\\ \sigma_{d1}\end{pmatrix}+(1-f_{mix})\begin{pmatrix}C_{\omega12}\\ C_{\omega22}\\ \sigma_{k2}\\ \sigma_{\omega2}\\ \sigma_{d2}\end{pmatrix} \tag{6.94}$$

where f_{mix} is a new mixing function (replacing Menter's F_1) and is described below. The coefficient values of the new model are as follows:

	$C_{\omega1}$	$C_{\omega2}$	σ_k	σ_ω	σ_d
Set 1	0.518	0.83	1.1	0.53	1.0
Set 2	0.44	0.92	1.1	1.0	0.4

The values of $C_{\omega11}$, $C_{\omega21}$, and $\sigma_{\omega1}$ are related through the log-layer relation

$$C_{\omega11}=C_{\omega21}-\frac{\kappa^2\sigma_{\omega_1}}{\sqrt{\beta^*}} \tag{6.95}$$

with $\beta^*=0.09$ and $\kappa=0.42$. Note that the BSL model uses $\kappa=0.41$ here.

The mixing function f_{mix} is slightly modified from Menter's corresponding function F_1 but is based on the same ideas. The mixing function is equal to one almost up to the edge of boundary layers and is zero in the free turbulent flows and in laminar regions. Wall distance is needed also in this model. The ratio of turbulent length-scale and wall distance d is used as the first measure just as in the BSL model

$$\Gamma_1=\frac{\sqrt{k}}{\omega d} \tag{6.96}$$

as well as the viscous measure

$$\Gamma_2=\frac{500\beta^*\nu}{\omega d^2} \tag{6.97}$$

and maximum of Γ_1 and Γ_2 is again taken. Following Menter, even a third measure is exploited. This is based on the length-scale of the cross term $\nabla k \cdot \nabla \omega / \omega$ and the wall distance, and it is used as an upper bound for the maximum of Γ_1 and Γ_2. In the present model, the mixing is designed to occur clearly closer to the boundary-layer edge than in Menter's model. This is achieved by multiplying Menter's Γ_3 by a factor of ten. Also a different lower limit for the cross term is introduced. Hence, the redefinition for Γ_3 now reads

$$\Gamma_3 = \frac{20k}{\max\left[d^2(\nabla k \cdot \nabla \omega)/\omega;\ 200k_\infty\right]} \tag{6.98}$$

with k_∞ being the user-specified free-stream value of k. In fully turbulent internal flows this limiter is of no significance, thus any small value may be used. Finally, the mixing function is defined as

$$f_{mix} = \tanh\left(C_{mix}\Gamma^4\right) \qquad \text{with} \qquad \Gamma = \min\left[\max\left(\Gamma_1; \Gamma_2\right);\ \Gamma_3\right] \tag{6.99}$$

where for the new model, $C_{mix} = 1.5$ is selected while Menter's model has $C_{mix} = 1.0$. The larger coefficient is chosen to maintain $f_{mix} = 1$ almost up to the outer edge.

As concluded in Section 6.4.6, the far-field boundary conditions can be quite arbitrarily chosen as long as not too large values are given for either k_e or ω_e. It is recommendable, although not absolutely necessary, to specify k_e and ω_e such that ν_{Te} is small in comparison with the ν_T values inside the turbulent regions.

The wall-boundary condition for k is the usual no-slip condition ($k = 0$ on the wall), and the following equations define the recommended wall value for ω:

$$\omega_w = \beta^* \frac{u_\tau^2}{\nu} S_R \tag{6.100}$$

where S_R is defined as

$$S_R = \begin{cases} \left[50/\max\left(k_s^+; k_{s\,min}^+\right)\right]^2 & \text{for } k_s^+ < 25 \\ 100/k_s^+ & \text{for } k_s^+ \geq 25 \end{cases} \tag{6.101}$$

with k_s specified for rough walls, and for smooth walls

$$k_{s\,min}^+ = \min\left[2.4(y_1^+)^{0.85}; 8\right] \tag{6.102}$$

becomes active.

The new model rewritten for the traditionally defined ω

The new model can as well be rewritten using the traditionally defined ω-variable that is $\omega \equiv \varepsilon/(\beta^* k)$. This makes it more convenient to implement the model into CFD software where Menter's model, or any other $k - \omega$ model based on this definition, is already available. In fact, the implementation task is very straightforward if Menter's model is used as a starting point. Now, the transport equations take the form familiar from Menter's BSL model (6.92)

$$\frac{\mathrm{D}k}{\mathrm{D}t} = P - \beta^* k\omega + \frac{\partial}{\partial x_j}\left[(\nu + \sigma_k \nu_T)\frac{\partial k}{\partial x_j}\right] \tag{6.103}$$

$$\frac{\mathrm{D}\omega}{\mathrm{D}t} = \gamma\frac{\omega}{k}P - \beta\omega^2 + \frac{\partial}{\partial x_j}\left[(\nu + \sigma_\omega \nu_T)\frac{\partial \omega}{\partial x_j}\right] + \frac{\sigma_d}{\omega}\max\left(\frac{\partial k}{\partial x_j}\frac{\partial \omega}{\partial x_j}; 0\right) \tag{6.104}$$

The constant β^* has the standard value 0.09. Again, the cross term is only included when the inner product of the gradients of k and ω is positive. The model coefficients vary in space according to (6.94), where $C_{\omega 1}$ and $C_{\omega 2}$ must be replaced by γ and β, respectively. The coefficient values are the following:

	γ	β	σ_k	σ_ω	σ_d
Set 1	0.518	0.0747	1.1	0.53	1.0
Set 2	0.44	0.0828	1.1	1.0	0.4

Eq. (6.95) becomes

$$\gamma_1 = \frac{\beta_1}{\beta^*} - \frac{\kappa^2 \sigma_{\omega_1}}{\sqrt{\beta^*}} \tag{6.105}$$

with $\beta^* = 0.09$ and $\kappa = 0.42$. The arguments of the mixing function f_{mix} are

$$\Gamma_1 = \frac{\sqrt{k}}{\beta^* \omega d} \tag{6.106}$$

as well as the viscous measure

$$\Gamma_2 = \frac{500\nu}{\omega d^2} \tag{6.107}$$

and

$$\Gamma_3 = \frac{20k}{\max\left[d^2(\nabla k \cdot \nabla\omega)/\omega;\ 200k_\infty\right]} \tag{6.108}$$

Finally, the mixing function is defined as

$$f_{mix} = \tanh\left(C_{mix}\Gamma^4\right) \qquad \text{with} \qquad \Gamma = \min\left[\max\left(\Gamma_1; \Gamma_2\right);\ \Gamma_3\right] \tag{6.109}$$

with $C_{mix} = 1.5$. The wall-boundary value becomes

$$\omega_w = \frac{u_\tau^2}{\nu} S_R \tag{6.110}$$

and the definition of S_R remains unchanged, see Eqs. (6.101) and (6.71).

6.6.2 The Constitutive Model

The proposed $k - \omega$ model is designed to be used with the EARSM developed by Wallin and Johansson [4] as the constitutive model. The model is written for the Reynolds-stress anisotropy tensor defined as

$$a_{ij} = \frac{\overline{u_i u_j} - 2/3\, k\delta_{ij}}{k} \tag{6.111}$$

The formulation of the algebraic Reynolds stress model is not repeated here, only its explicit solution is given. The anisotropy tensor is expressed using the following tensor polynomial:

$$\begin{aligned} a_{ij} &= \beta_1 S_{ij} \\ &+ \beta_3 \left(\Omega^*_{ik}\Omega^*_{kj} - \frac{1}{3} II_\Omega \delta_{ij} \right) + \beta_4 \left(S_{ik}\Omega^*_{kj} - \Omega^*_{ik} S_{kj} \right) \\ &+ \beta_6 \left(S_{ik}\Omega^*_{kl}\Omega^*_{lj} + \Omega^*_{ik}\Omega^*_{kl} S_{lj} - \frac{2}{3} IV \delta_{ij} \right) \\ &+ \beta_9 \left(\Omega^*_{ik} S_{kl} \Omega^*_{lm} \Omega^*_{mj} - \Omega^*_{ik}\Omega^*_{kl} S_{lm} \Omega^*_{mj} \right) \end{aligned} \tag{6.112}$$

The nondimensional strain-rate and vorticity tensors are defined by

$$S_{ij} = \frac{1}{2}\tau \left(\frac{\partial U_i}{\partial x_j} + \frac{\partial U_j}{\partial x_i} \right) \tag{6.113}$$

$$\Omega^*_{ij} = \frac{1}{2}\tau \left(\frac{\partial U_i}{\partial x_j} - \frac{\partial U_j}{\partial x_i} \right) - \frac{\tau}{A_0} \Omega^{(r)}_{ij} \tag{6.114}$$

The last term, which depends on $\Omega^{(r)}_{ij}$, is an optional part which may be beneficial if the streamline-curvature effects on turbulence are considered important. The model can, however, be operated also without adding this so-called vorticity modification due to curvature. This quantity is calculated from

$$\Omega^{(r)}_{ij} = -\epsilon_{ijk} \frac{II_S^2 \delta_{km} + 12 III_S S_{km} + 6 II_S S_{kl} S_{lm}}{2 II_S^3 - 12 III_S^2} S_{pr} \dot{S}_{rq} \epsilon_{pqm} \tag{6.115}$$

The reader is advised to consult Ref. [5] to understand this method. The time-scale τ is taken as the maximum of turbulent and viscous time-scales as follows:

$$\tau = \max \left(\frac{1}{\beta^* \omega}; C_\tau \sqrt{\frac{\nu}{\beta^* k \omega}} \right) \tag{6.116}$$

with $C_\tau = 6.0$ and $\beta^* = 0.09$. The β coefficients in (6.112) are functions of the invariants $II_S = S_{kl}S_{lk}$, $II_\Omega = \Omega^*_{kl}\Omega^*_{lk}$, $III_S = S_{kl}S_{lm}S_{mk}$, and $IV = S_{kl}\Omega^*_{lm}\Omega^*_{mk}$ as follows:

$$\begin{array}{lll} \beta_1 = -N(2N^2 - 7 II_\Omega)/Q & \beta_3 = -12 IV/(NQ) & \\ \beta_4 = -2(N^2 - 2 II_\Omega)/Q & \beta_6 = -6N/Q & \beta_9 = 6/Q \end{array} \tag{6.117}$$

where the denominator Q reads

$$Q = \frac{5}{6}(N^2 - 2II_\Omega)(2N^2 - II_\Omega) \tag{6.118}$$

In two-dimensional mean flows, only two independent invariants, II_S and II_Ω, exist and only the first and third terms remain in (6.112):

$$\beta_1 = -\frac{6}{5}\frac{N}{N^2 - 2II_\Omega} \qquad \text{and} \qquad \beta_4 = -\frac{6}{5}\frac{1}{N^2 - 2II_\Omega} \tag{6.119}$$

The function N is solved from a cubic equation in two-dimensional mean flows (see Ref. [4]). In three-dimensional cases, the corresponding equation is of the sixth order and no explicit solution can be found for it. The solution of the cubic equation N_c can be used also for three-dimensional cases as the first approximation. It is given by

$$N_c = \begin{cases} A'_3/3 + (P_1 + \sqrt{P_2})^{1/3} + \operatorname{sign}(P_1 - \sqrt{P_2})|P_1 - \sqrt{P_2}|^{1/3} & \text{for } P_2 \geq 0 \\ A'_3/3 + 2(P_1^2 - P_2)^{1/6}\cos\left(\frac{1}{3}\arccos\left(\frac{P_1}{\sqrt{P_1^2 - P_2}}\right)\right) & \text{for } P_2 < 0 \end{cases} \tag{6.120}$$

where

$$P_1 = \left(\frac{A'^2_3}{27} + \frac{9}{20}II_S - \frac{2}{3}II_\Omega\right)A'_3 \tag{6.121}$$

$$P_2 = P_1^2 - \left(\frac{A'^2_3}{9} + \frac{9}{10}II_S + \frac{2}{3}II_\Omega\right)^3 \tag{6.122}$$

Even better approximation for N in three-dimensional mean flows is obtained by perturbing the invariants IV and V around the two-dimensional solution as proposed by Wallin and Johansson [4]. This results in the following formula for N

$$N \approx N_c + \frac{162\left[IV^2 + \left(V - \frac{1}{2}II_S II_\Omega\right)N_c^2\right]}{20N_c^4\left(N_c - \frac{1}{2}A'_3\right) - II_\Omega(10N_c^3 + 15A'_3N_c^2) + 10A'_3 II_\Omega^2} \tag{6.123}$$

which is employed in the FINFLO solver for three-dimensional mean flows. In two-dimensional mean flows $IV = 0$ and $V = II_S II_\Omega/2$ hence the second term is zero and $N = N_c$. Finally A'_3 is defined by

$$A'_3 = \frac{9}{5} + \frac{9}{4}C_{\text{Diff}}\max\left(1 + \beta_1^{(eq)}II_S; 0)\right) \tag{6.124}$$

here $9/5$ is the original value of A_3, see Table 5.2. The purpose of the additive term in A'_3 is to model the ignored diffusion of the anisotropy, see Ref. [4]. The new parameter $\beta_1^{(eq)}$ is defined as

$$\beta_1^{(eq)} = -\frac{6}{5}\frac{N^{(eq)}}{(N^{(eq)})^2 - 2II_\Omega} \tag{6.125}$$

where

$$N^{(eq)} = A_3 + A_4 = \frac{81}{20} \qquad \text{and} \qquad C_{\text{Diff}} = 2.2 \tag{6.126}$$

To facilitate practical implementation in general CFD solvers, the Reynolds-stress tensor is expressed using an effective eddy viscosity formulation including a corrective extra-anisotropy tensor

$$\overline{u_i' u_j'} = -\nu_T \left(\frac{\partial U_i}{\partial x_j} + \frac{\partial U_j}{\partial x_i} \right) + \frac{2}{3} k \delta_{ij} + a_{ij}^{(ex)} k \tag{6.127}$$

in which the effective eddy viscosity is defined as

$$\nu_T = C_\mu k \tau \qquad \text{and} \qquad C_\mu = -\frac{1}{2}(\beta_1 + II_\Omega \beta_6) \tag{6.128}$$

and

$$\begin{aligned} a_{ij}^{(ex)} &= a_{ij} - (\beta_1 + II_\Omega \beta_6) S_{ij} \\ &= \beta_3 \left(\Omega^*_{ik} \Omega^*_{kj} - \frac{1}{3} II_\Omega \delta_{ij} \right) + \beta_4 \left(S_{ik} \Omega^*_{kj} - \Omega^*_{ik} S_{kj} \right) \\ &+ \beta_6 \left(S_{ik} \Omega^*_{kl} \Omega^*_{lj} + \Omega^*_{ik} \Omega^*_{kl} S_{lj} - II_\Omega S_{ij} - \frac{2}{3} IV \delta_{ij} \right) \\ &+ \beta_9 \left(\Omega^*_{ik} S_{kl} \Omega^*_{lm} \Omega^*_{mj} - \Omega^*_{ik} \Omega^*_{kl} S_{lm} \Omega^*_{mj} \right) \end{aligned} \tag{6.129}$$

7 Validation for Two-Dimensional Flows

7.1 Full Navier-Stokes Computation of Flat Plate Boundary Layer

The ZPG boundary layer of a flat plate was studied in Section 6.4.4 at the self-similar limit. It is verified in this section that a real developing ZPG boundary layer can be computed accurately enough using the new model. The boundary layer is computed up to $Re_x = 1.1 \times 10^7$ or $Re_{\delta_2} \approx 1.5 \times 10^4$. All the $k - \omega$ models tested in this study predict the transition to occur almost immediately after the leading edge. The computational grid over the plate consists of 128×96 control volumes in the streamwise and transverse directions, respectively. The inner-scaled thickness of the first cells above the wall (y_1^+) is typically about 0.8. The grid resolution is found to be sufficient, except that in case of the BSL models, the sharp edge is smeared out to some extent due to the numerical damping. This is why the BSL models seem to give a smoother edge than in the self-similar computations where much better resolution was used on the edge region.

Fig. 7.1 shows the computed skin-friction distributions as functions of Re_x. The new model is shown to give a higher friction coefficient than the BSL-EARSM — about equal to that obtained by the original linear BSL model. These curves agree well with the experimental data by Wieghardt [134] (taken from [48]), and by Winter and Gaudet [135]. At small Reynolds numbers, the computed friction is a bit lower than measured. Fig. 7.1 shows also the velocity profiles at $Re_x = 4.2 \times 10^6$. The agreement with the measurements is now better than according to the self-similar computations shown in Fig. 6.14. This is probably owing to the simplifications made in the derivation of the self-similar equations, such as the log-law boundary condition, or because the Reynolds number in the measurement, $Re_x = 4.2 \times 10^6$, may be insufficient to properly reach the limit of self-similarity. It should be remembered that in the derivation of the self-similar equations, $Re_{\delta_2} \to \infty$ is assumed. Nevertheless, the new model gives significantly better results than the BSL-EARSM. Also the momentum thicknesses δ_2 and the shape parameter $H_{12} = \delta_1/\delta_2$, where δ_1 is the displacement thickness, agree well with the measurements and with the original linear BSL model.

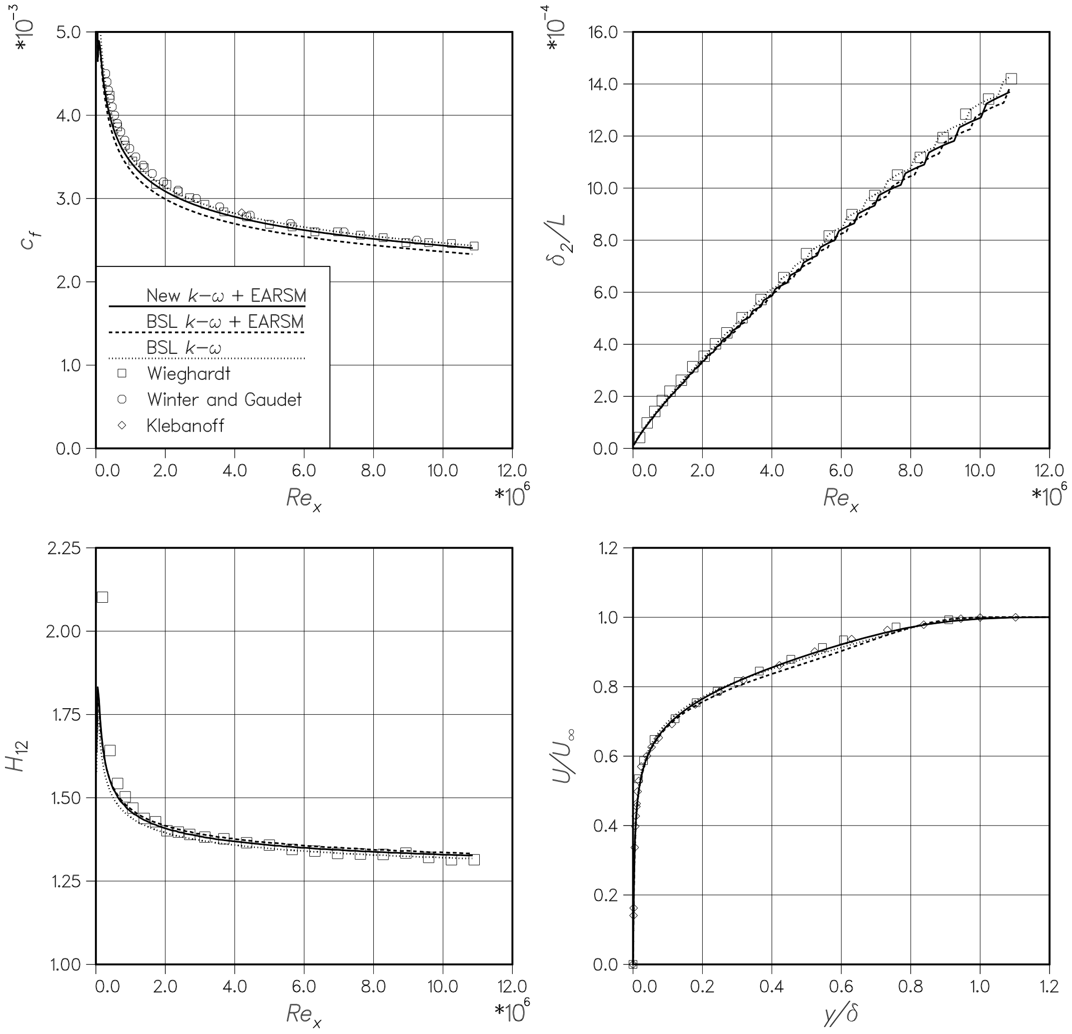

Figure 7.1: Skin friction c_f (upper left), momentum thickness δ_2 (upper right), and shape parameter H_{12} (lower left) distributions over a flat-plate boundary layer up to $Re_{\delta_2} \approx 15,000$ ($Re_x = 10.9 \times 10^6$). Lower right: velocity profiles at $Re_{\delta_2} \approx 7,300$ ($Re_x = 4.2 \times 10^6$). Computations with the new $k - \omega$ EARSM, with the BSL-EARSM, and with the standard BSL model.

7.2 Developing Wake behind a Flat Plate

The self-similar far wake was used as one of the building-block flows in the model development process. In practical aerodynamics, the far wake is seldom as important as different developing wakes. Wakes of streamlined objects reach the self-similar state usually quite far away from the trailing edge. Furthermore, in practical problems, such as the interaction problem of the slat wake and the main-wing boundary layer, the wake interacts with a curved flowfield of varying pressure. The effects of such more complex phenomena are beyond the scope of this study. Instead, the models' abilities to predict a developing wake of a thin flat plate at zero angle will be assessed from the trailing edge up to the far wake clearly beyond the point where the self-similarity is reached. The experimental results of Pot [86] indicated that in this case, the wake reaches self-similarity as far away from the trailing edge as $x/\delta_2 \approx 350$. Here, δ_2 is the momentum thickness of the wake defined as

$$\delta_2 = \int_{-\infty}^{\infty} \frac{U}{U_\infty} \left(1 - \frac{U}{U_\infty}\right) dy \tag{7.1}$$

This is constant in the wake, and equals the trailing-edge momentum thickness obtained by adding the momentum thicknesses of the boundary layers on both plate surfaces at the trailing edge. In this case, the wake is computed up to $x/\delta_2 \approx 600$. The computed maximum velocity defect and the half-width are compared with the experimental values in Fig. 7.2. The maximum velocity defect is plotted as its squared inverse $[U_\infty/(U_\infty - U)]^2$. This quantity increases linearly in the self-similar region, hence, this way the self-similar region is easier to detect from the curves. Similarly, the half width b is plotted as $(b/\delta_2)^2$, because it also shows a linear growth in the self-similar region. The half width b is defined as such a value of the y-coordinate where the mean velocity-defect equals half of its maximum value that occurs in the symmetry plane.

The wake is generated by a flat plate on which the boundary layer develops up to $Re_x = 3 \times 10^6$ which equals $Re_{\delta_2} \approx 5000$. The plate-length is set to unity and the whole domain is 3 units long and 0.4 units in height. The computational grid consists of 256×256 control volumes in the streamwise and plate normal directions, respectively. The subvolume over the plate consists of 96×256 control volumes whereas 160×256 volumes are left for the wake behind the trailing edge. Symmetry about the x-axis is exploited by placing a symmetry boundary condition on the symmetry plane, and only computing the flow above it. The grid convergence study was performed by comparing the new model results obtained with the finest 256×256 grid and grids of 128×128 and 64×64 control volumes. Although not shown here, the results obtained with the two finest grid levels are practically identical, thus the results are believed to be grid-independent — at least those obtained with the new model.

Fig. 7.2 shows that the new model follows the measurements clearly better than the BSL models. This was expected because the self-similar computations indicated that the BSL models predict by far too low a spreading rate for the far wake. Now, this is seen as too high a maximum velocity defect and as wrong slopes of the half-width curves in the self-similar region. In the intermediate region, $25 < x/\delta_2 < 350$, the wake spreads more slowly than in the final self-similar far wake where $x/\delta_2 > 350$, see Ramaprian *et al.* [85]. In this region, all the tested models overestimate the spreading rate to some extent. It is interesting to observe that unlike the new model, the BSL models seem to predict almost the same rate of spreading in both the intermediate and the far-wake regions. This is in contrast with the experiments. The new model also predicts the wake to reach the far-wake phase at roughly the correct distance from the trailing edge. These observations are encouraging, since they indicate that the new model predicts the wake development more correctly than the BSL models, at least in a qualitative sense.

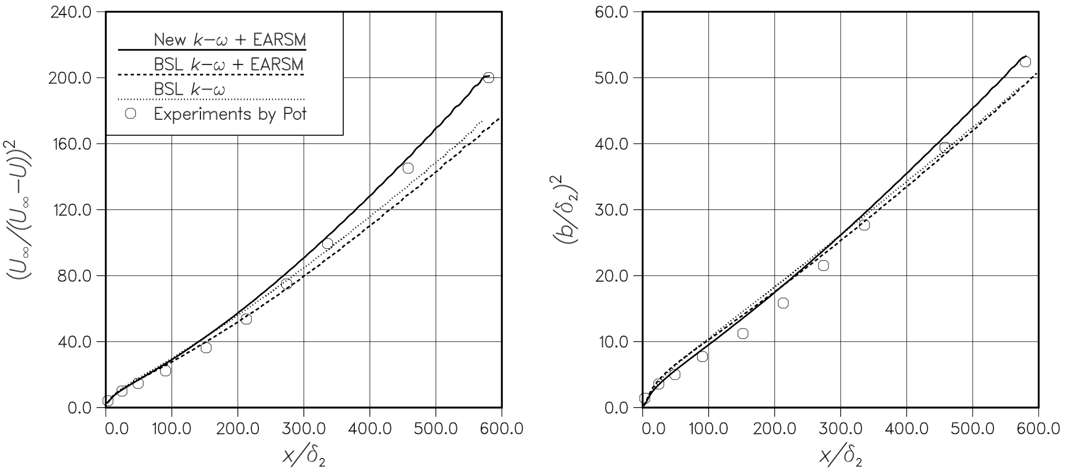

Figure 7.2: The squared inverse of the maximum velocity defect (left) and the squared half-width of the wake behind the flat plate as functions of the distance x/δ_2 from the trailing edge. Circles represent the experimental values measured by Pot [86].

7.3 Separating Adverse Pressure-Gradient Boundary Layer on an Axisymmetric Body

Equilibrium APG boundary layers were studied in Section 6.4.8. Such equilibrium boundary layers can be set up in a laboratory, and the equilibrium is a very beneficial state of affairs in research work. In practical engineering problems, however, the APG boundary layers are extremely seldom in equilibrium. The boundary layers on the upper surfaces of wing elements are typically subjected to pressure gradients that produce increasing β_T values. These kinds of situations often lead to separation. Since the physics involved in the high-lift aerofoil problems is quite complex — even in single-element cases — the studies of separating APG boundary layers are started from a simpler, more idealized flow problem. The decelerating boundary-layer flow past a cylinder is a suitable case for this purpose. Driver studied this flow experimentally [52], and it has been frequently used in turbulence-model validation, see *e.g.* [3, 65, 156, 157]. This case was also used as one of the flows in Ref. [63] to study the effect of the constitutive and the scale-determining models in separating APG boundary-layer problems. The results computed with the $k - \varepsilon$ models and with the $k - \omega$ SST model in [63] are not repeated here. Only the results computed with the new model, with the BSL-EARSM, and with the original linear BSL model are shown.

The cylinder axis is oriented in the streamwise direction, and the test-section walls are diverged in order to decelerate the flow. Driver considered two cases, one without separation (B) and another with separation (C). Only case C is studied here. The inflow Reynolds number based on the cylinder diameter D is 2.8×10^5, and about $4{,}000$ based on the inlet momentum thickness δ_2. The inflow boundary conditions have been obtained from the result of a separate computation of a zero pressure-gradient boundary layer on the same cylinder. The outer edge is modelled as an inviscid slip-wall contoured according to the streamlines plotted by Driver.

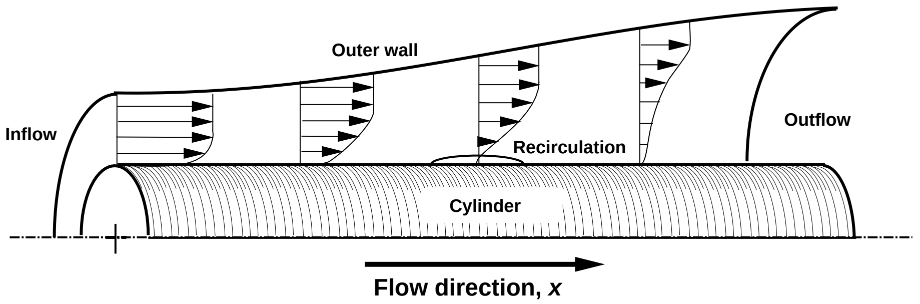

Figure 7.3: A schematic illustration of Driver's decelerating boundary layer.

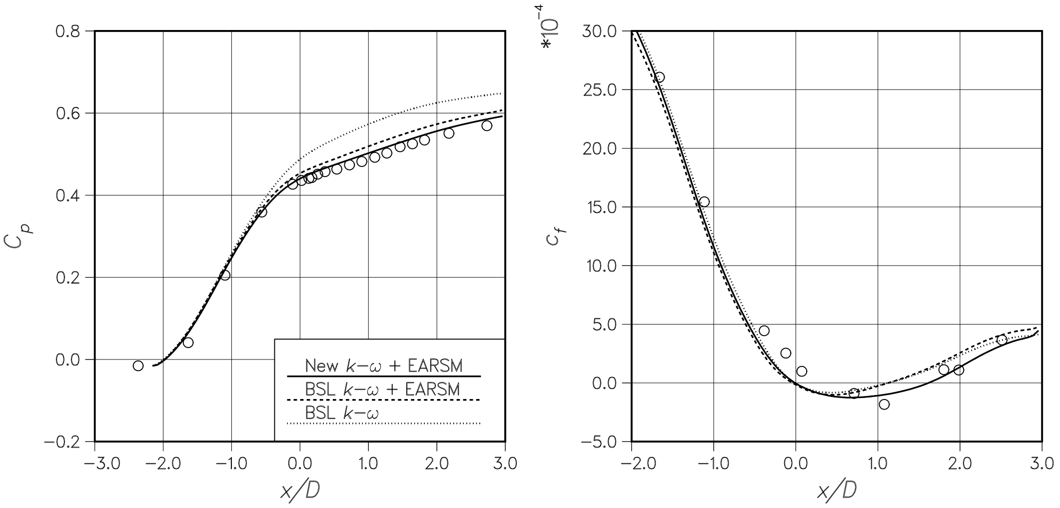

Figure 7.4: Pressure coefficient C_p (left), and skin-friction coefficient $10^4 \times c_f$ (right) along the cylinder surface in Driver's decelerating boundary layer.

This slip wall had to be placed quite close to the outer edge of the boundary layer because no streamline information was available further away. The influence of this fact could not be studied, unfortunately. The computational grid consisted of 160×96 control volumes in the axial and radial directions, respectively. The grid independency was studied in [63] by repeating the SST computation using a 320×192 grid (not shown here). Virtually unchanged results were obtained, except that the edge of the boundary layer became slightly sharper. This seemed to have only local influence on the solution. It should be noted here that it was not properly understood by the author at the time when Ref. 63 was published that this model tends to predict sharp edges and therefore the grid convergence is slow. Nevertheless, at least the results of the new model are believed to be sufficiently grid-independent.

The pressure and skin-friction distributions are plotted in Fig. 7.4. One can immediately observe that the original BSL model underestimates the pressure loss more significantly than the EARSM-based models. Hence, it can be assumed that the role of the constitutive model is important in this flow. This has been shown by Menter in the case of the SST-model [3], and later by Hellsten in [63] using also EARSM-based models. All the $k - \omega$ models predict the flow separation at almost the same location, which is only slightly upstream from the measured sep-

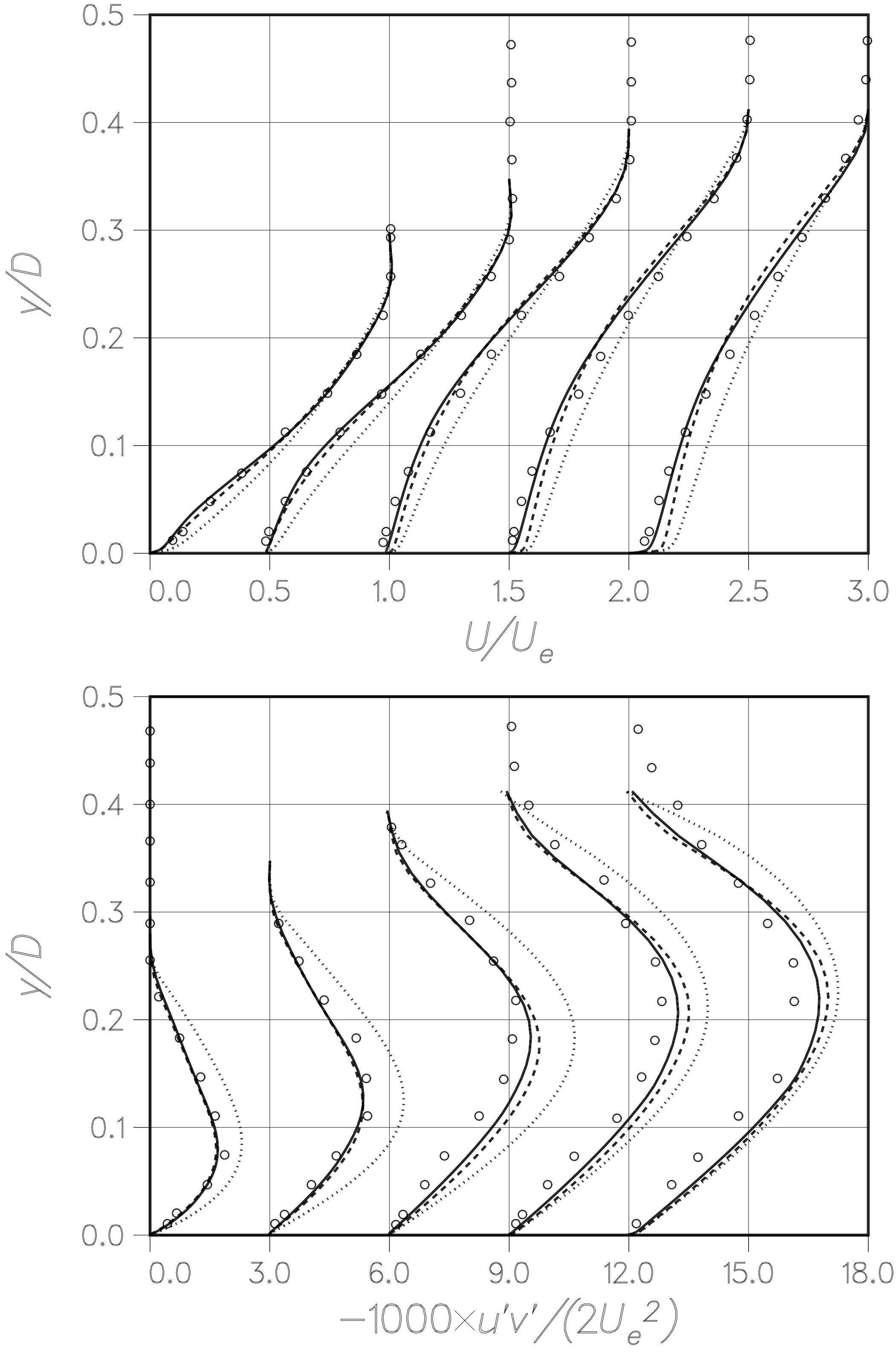

Figure 7.5: Velocity U/U_e (upper) and Reynolds shear-stress $-\overline{u'v'}/(2U_e^2)$ (lower) profiles in Driver's decelerating axisymmetric boundary layer at five stations: x/D = -0.091, 0.363, 1.088, 1.633, and 2.177. Note the shifted origin of each station. Legends as in Fig. 7.4.

aration line. The new model predicts a slightly longer separation bubble than the BSL models, and is thus in slightly better agreement with the measurements. This is seen in the pressure distribution as well, which is closer to the measurements than that of the BSL-EARSM. It was shown in [63] that the $k-\varepsilon$ models do not predict separation at all, regardless of the employed constitutive model, Boussinesq or EARSM. Nevertheless, the EARSM-based $k-\varepsilon$ predicted a significantly larger pressure loss than the linear Boussinesq $k-\varepsilon$ model. This is yet further evidence that the most significant difference between the $k-\varepsilon$ and $k-\omega$ models in APG flows takes place near the wall.

The velocity and Reynolds shear-stress profiles around the separation bubble are plotted in Fig. 7.5 at five stations: $x/D =$ -0.091, 0.363, 1.088, 1.633, and 2.177. The velocity profiles show that the BSL model underestimates the extent of separation. The reversed flow is restricted into an extremely thin region near the wall. The BSL-EARSM also underestimates the extent of separation, and it predicts the flow to reattach and to recover somewhat too early. This was observed already in Ref. [63]. The new model is seen to perform somewhat better in this regard, although it still slightly underpredicts the backflow and the flow retardation over the bubble. The accuracy of the new model in this particular case is very similar to that of the SST model, see [3, 63]. The shear-stress curves in Fig. 7.5 just show how the linear BSL model overestimates the shear stress indicating the importance of the advanced constitutive modelling in this kind of flow.

7.4 Asymmetric Plane Diffuser Flow

The asymmetric plane diffuser flow experimentally studied by Buice and Eaton [57, 58, 158], and also by Obi *et al.* [56], is considered next to assess the model in a challenging flow with massive separation. The situation is schematically illustrated in Fig. 7.6. The Reynolds number, based on the inflow centre line velocity U_{cl} and the inlet channel height H, is 20,000. The expansion ratio is 4.7. The inlet plane-channel flow is turbulent and fully developed. The x-coordinate initiates from the beginning of the ramp, and the ramp ends at $x/H = 21$. The flow separates from the ramp at roughly $x/H \approx 7$ and reattaches at about $x/H \approx 29$. After the reattachment, a new boundary layer develops, and eventually, the flow recovers from the separation and distortion caused by the diffuser ramp. This flow was one of the test cases in the 8th ERCOFTAC/IAHR/COST Workshop on Refined Turbulence Modelling [74]. For this workshop, several contributors computed the diffuser flow with many different types of turbulence models.

The present computations were performed employing a grid with 240×96 control volumes in the streamwise and cross-channel directions, respectively. The sufficient grid-independency was confirmed by repeating some of the computations using a double-resolution grid with 480×192 control volumes. The results obtained with the double-resolution grid were almost identical to those obtained with the basic grid.

Fig. 7.7 shows the distributions of the pressure coefficient C_p and the skin-friction coefficient c_f along the inclined wall. In this case, the scaling factor of C_p and c_f is $\rho U_b^2/2$, where U_b is the bulk velocity, *i.e.* the mass-flow rate divided by the density and the cross-sectional area of the upstream channel. The velocity profiles at x/H-locations 5.98, 13.56, 20.32, and 30.42 are plotted in Fig. 7.8. The results computed with the new model, with the BSL-EARSM, and with the original linear BSL model are shown. The pressure distributions indicate that the new model predicts higher pressure loss than the BSL-EARSM combination, while the linear BSL predicts the lowest pressure loss. The pressure distribution indicates that the new model would be in best agreement with the measurements, but the other results reveal that this is not the case. The higher pressure loss is owing to the larger recirculation region with stronger backflow. It turns out, however, that the new model predicts a too large and strong recirculation. In fact, the BSL-EARSM is in better agreement with the measurements in this case. An inspection of the c_f-distribution reveals that the new model as well as the BSL-EARSM predict a too early separation, and the new model predicts also delayed reattachment and a too high reversed wall shear stress. This is seen also in the velocity profiles, which also show somewhat too strong backflow and excessive asymmetry according to the new model. Both EARSM-based models give, however, more realistic velocity profiles than the linear BSL model. It should be mentioned here that the $k - \omega$ SST variant gives rather similar results to the BSL-EARSM in this case, see Refs. [63, 74].

Predicting the correct separation location is very difficult in this case. Failure to do so easily spoils the results downstream. The new model and the BSL-EARSM, as well as the SST model, although not shown here, all predict far too early separation in this case but none of these models show such behaviour in Driver's flow. This has been discussed by Apsley and Leschziner in the case of the SST model [66]. They suggest as one possible reason that there might be a tiny separation bubble just around the ramp upper-corner. Such a small bubble would produce coherent structures which appear as a periodic flapping motion. Such motion, in turn, greatly increases the shear stress levels behind the bubble, and consequently the flow may remain attached much further downstream. Such a separation bubble is not predicted by the models studied here. On the other hand, Apsley and Leschziner show that the nonlinear low-Reynolds-number model developed by Craft, Launder and Suga [159] predicts such a bubble and also the correct location of the massive separation. LES further enforces this assumption [160], but unfortunately no measurements have been made close enough to the beginning of the ramp. It may be questionable to further assess the accuracy of the results downstream of the separation as the EARSM-based models (as well as the SST) fail in predicting the correct separation location.

It has already been shown that the linear eddy-viscosity models perform badly in this case [63, 66, 74]. Thus, probably the only new conclusion that can be made here is that the new model predicts larger and stronger recirculation than the BSL-EARSM. On the other hand, flow past the NACA-4412 aerofoil at a high angle of attack involves a relatively large separation region, and as will be shown in Section 7.5.3, the new model predicts the velocity profiles with a better accuracy than the BSL-EARSM (but the results are probably grid-dependent in that case). One

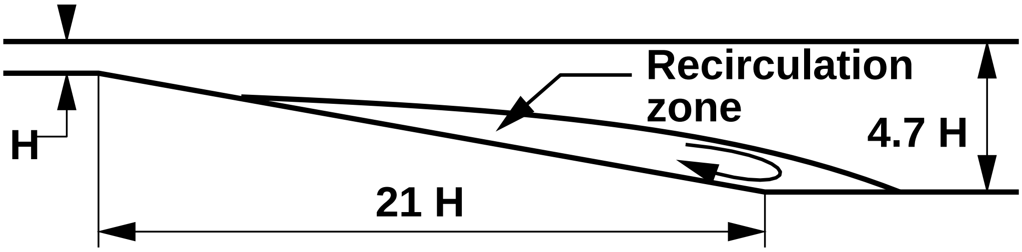

Figure 7.6: A schematic illustration of the asymmetric plane diffuser. Flow enters from the left.

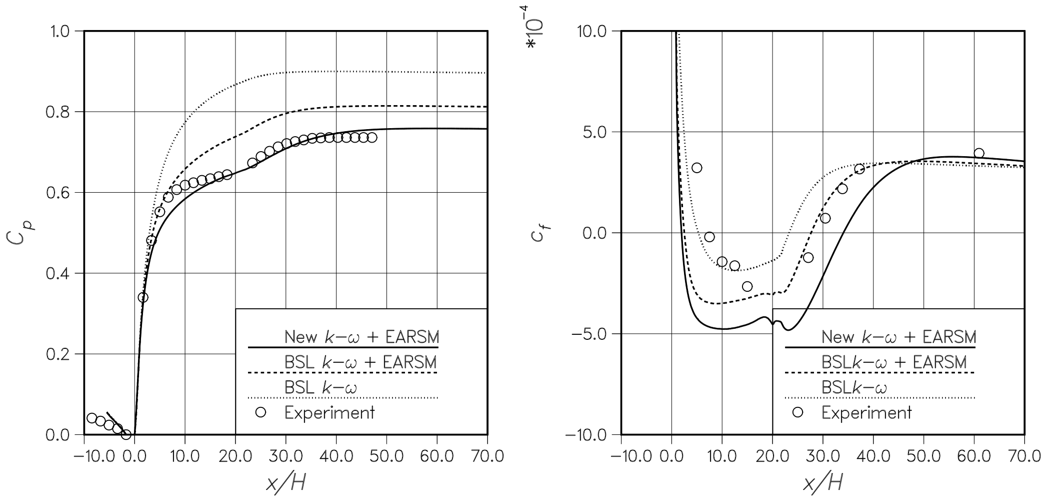

Figure 7.7: Pressure coefficient C_p (left) and skin-friction coefficient $10^4 \times c_f$ (right) along the inclined wall of the asymmetric plane diffuser.

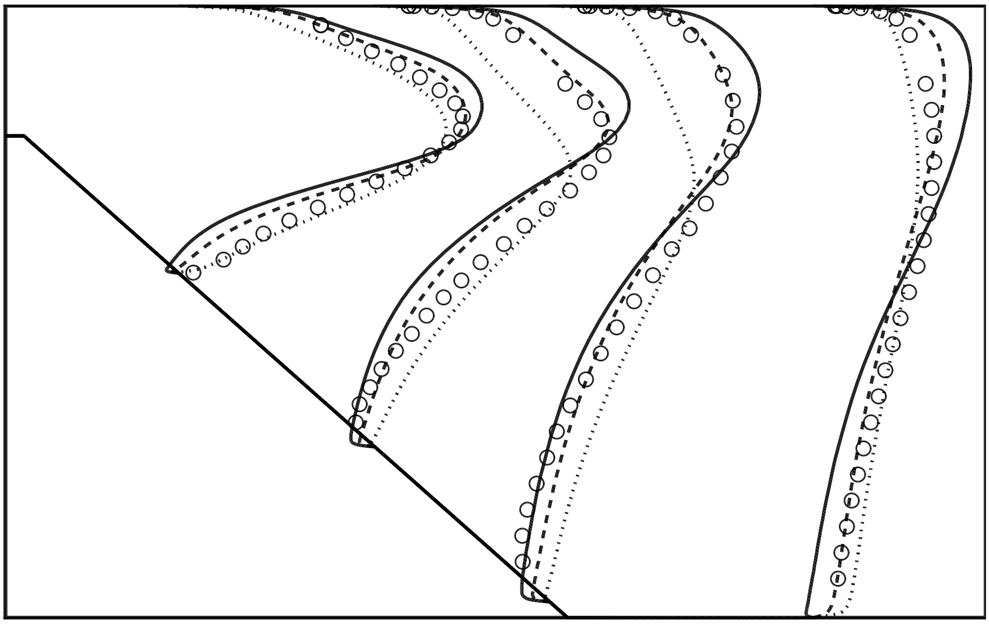

Figure 7.8: Velocity profiles U/U_b in the asymmetric plane diffuser. Inflow channel on the left. Streamwise stations x/H =5.98, 13.56, 20.32, and 30.42, and the diffuser ramp begins at $x/H = 0$. Legends as in Fig. 7.7.

difference between these cases is that the aerofoil case involves separation from a surface with almost constant radius of curvature, while in this case, the ramp wall begins with an almost sharp bend. However, a proper validation for flows with massive separation would require investigation of several suitable flow problems. It is considered that it is more important in high-lift aerodynamics to be able to predict the onset of separation more accurately than massively separated flows. Driver's flow, discussed in Section 7.3, indicated that the new model seems to have potential to predict the onset of separation with quite good accuracy. The Aerospatiale A aerofoil flow that will be discussed in Section 7.5.2 also supports this conclusion. However, flows with massive separation are of great technical interest in general, and will be given more attention in future work.

7.5 High-Lift Aerofoil Flows

7.5.1 General Remarks

Finally, attention is turned towards high-lift aerofoil flows, the main purpose for which the model is designed. Only three aerofoils are studied and each of them at only one angle of attack. This can by no means be considered a proper validation campaign, but more comprehensive validation is beyond the scope of this study. This preliminary validation should merely be considered as a feasibility study of the new model.

The three cases are selected to reflect somewhat different flows past two-dimensional aerofoil sections near maximum lift. The first case is the single-element Aerospatiale A aerofoil at an angle of attack of 13.3° [161]. In this case, the flow on the upper surface separates near the trailing edge. The recirculation region is small, and the separation can be classified as mild. The second case is also a single-element aerofoil NACA-4412 at 13.87°. This situation differs from the first one in the extent of separation. Now, there is a substantial region of backflow with a rather strong displacement effect. This is computationally a very hard case, since the models tend to predict time-dependent results as the grid is refined. Unfortunately, the grid convergence was not achieved in this case. The final case is the NHLP 2D three-element aerofoil at 20.18°. This is a take-off configuration with a moderate flap deflection of 20°. No flow separation occurs in this case. The main focus is in the prediction of the confluent wakes and boundary layers.

7.5.2 Single-Element Aerospatiale A Aerofoil near Maximum Lift

The first high-lift flow to be studied is flow past the Aerospatiale A aerofoil at $\alpha = 13.3^\circ$. The chord Reynolds number is 2×10^6. This flow has been used previously for validating CFD methods and turbulence models in European projects EUROVAL [162] and ECARP [163]. The experiments were performed in two different wind tunnels at ONERA, F1 [164] and F2 [165]. The lift and drag coefficients and

Table 7.1: Computed and measured lift and drag coefficients of the Aerospatiale A aerofoil at $\alpha = 13.3°$.

Turbulence model	c_l	c_d
New $k - \omega$ EARSM	1.55	0.0201
BSL $k - \omega$ EARSM	1.57	0.0196
$k - \omega$ BSL	1.64	0.0190
$k - \omega$ SST	1.60	0.0191
Experiment	1.56	0.0210

distributions of the surface-pressure and skin-friction coefficients were measured in the F1-experiments. These were measured also in the F2-experiments in addition to the velocity and Reynolds-stress profiles through the upper-surface boundary layer at certain locations. Unfortunately, the flow situations in these two experiments were significantly different, although the measurements were performed in nominally similar conditions. The lift and drag forces measured in F1 and F2 differ from each other clearly. In F1, $c_l = 1.55 - 1.575$ and $c_d = 0.0208 - 0.0212$ while in F2, $c_l = 1.49 - 1.515$ and $c_d = 0.0308$ [161], see also [113]. Furthermore, a comparison of the friction-coefficient distributions measured in these two experiments reveals that the upper-surface boundary layer separated clearly earlier in the F2 than in the F1 experiment. It is also stated by Gendre that the mean flow turns three-dimensional in the F2 wind tunnel at around $\alpha = 13°$ [161]. It seems likely that this indeed occurred in the F2 experiment making the flow separate earlier and rendering the recirculation stronger in the spanwise position where the measurements were taken. This is unfortunate, since the velocity and the Reynolds-stress profiles were not measured in the F1 experiment, which much better simulates a two-dimensional aerofoil flow in a free stream just as the computations.

A C-grid of 512×128 control volumes in the streamwise and near-normal directions was used. The computations with the BSL-EARSM, BSL and the SST models were repeated with a coarser grid of 256×64 control volumes. The results showed that the effect of the truncation error in the lift coefficient is only about 1% already with the 256×64 grid. However, the drag coefficients predicted using these two grids differed about 10%. This is the reason why the finer grid results are used for comparisons. The boundary layers were tripped in the computations at $x/c = 0.12$ on the upper surface and $x/c = 0.3$ on the lower surface, just as in the experiments [161].

The above-discussed differences between the experimental flow situations in the F1 and F2 wind tunnels mean that the computed results should be compared only with the F1 data. However, a rough comparison of the velocity and shear-stress profiles with the F2 data is shown at two stations, $x/c = 0.90$ and $x/c = 0.99$, in Fig. 7.9. It is, however, very important to keep in mind that this comparison gives no real indication of the predictive realism of the models since the flow in

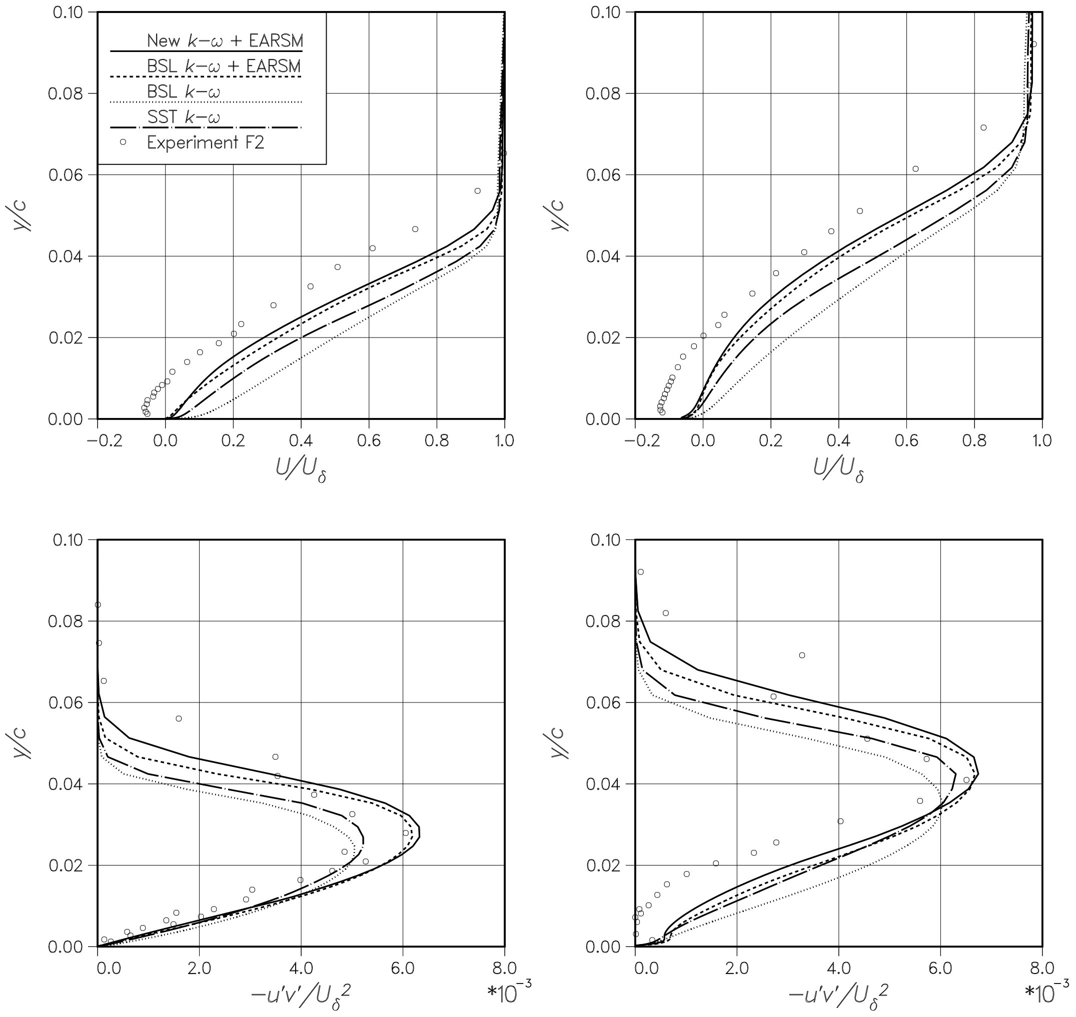

Figure 7.9: Velocity profiles (top) and shear-stress profiles (bottom) on the upper surface of the Aerospatiale A aerofoil at two locations $x/c = 0.90$ (left) and $x/c = 0.99$ (right).

the F2 experiment significantly differs from that being simulated computationally. The models can be assessed by comparing the computed lift and drag coefficients with those measured in the F1 wind tunnel. Also the pressure and skin-friction coefficient distributions can be compared with the F1 measurements.

The integrated force coefficients are given in Table 7.1. Both EARSM-based models give the lift coefficient within the experimental uncertainty. The SST-predicted lift is also quite close to the measured value, while the original linear BSL model gives about a 5% too high lift coefficient. All the studied models seem to give a slightly too low drag coefficient, and as the effect of the truncation error is to increase the computed drag, the ideal grid-independent drag predictions would probably be a few percent lower than the values presented in Table 7.1.

The pressure-coefficient curves are shown in Fig. 7.10. Also a close-up view near the trailing edge is shown in order to clearly see the pressure plateau originating from the flow separation. The pressure plateau near the trailing edge is strongly coupled with the suction peak near the leading edge. None of the computed pressure

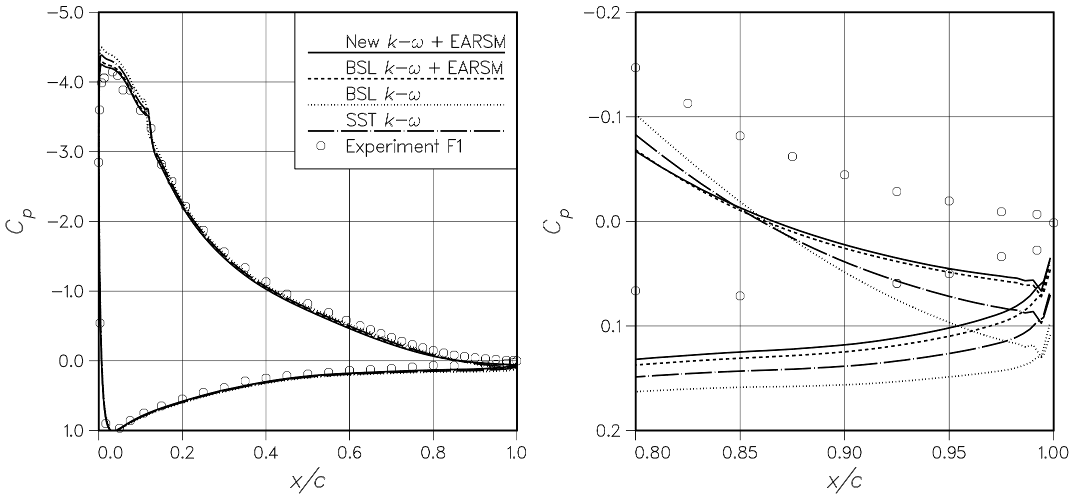

Figure 7.10: Surface-pressure distribution on the Aerospatiale A aerofoil. A close-up view of the trailing-edge region is shown on the right-hand side.

curves follow the measured distribution perfectly near the trailing edge, but the EARSM-based models show the closest agreement with the measurements. This is also true around the suction peak near the leading edge. Finally, the skin-friction coefficient on the upper surface is shown in Fig. 7.11, which shows that all the models predict the flow separation to occur at approximately the correct location. It should be mentioned here that this is not the case with many other models. It has been shown in, *e.g.* [163] that most of the widely-used engineering turbulence models, such as most of the different $k - \varepsilon$ model variants, are inadequate for this kind of flow problems.

An a-priori estimation of the curvature effects on turbulence was made by evaluating $\omega_3^{(r)}$ using (5.10) from the flowfield computed with the standard EARSM and the new $k - \omega$ model. The obtained values of $|\tau\omega_3^{(r)}/A_0|$ were negligibly small, typically about 1% of the actual vorticity $|\Omega_{12}|$ throughout the boundary layers. Thus, it was concluded that the curvature-correction method discussed in Chapter 5 is not necessary in this case.

7.5.3 Single-Element Aerofoil NACA 4412 near Maximum Lift

The NACA 4412 aerofoil is considered next as an example of a two-dimensional single-element high-lift aerofoil flow with a larger extent of flow separation than the Aerospatiale A case. The experiments were performed by Coles and Wadcock [166]. This flow case was also used for the basic validation of the original $k - \omega$ BSL and SST models by Menter [3, 65]. Later, Rudnik assessed several models in this case [167]. Only the SST model and Wilcox's $k - \omega$ model gave accurate results in Rudnik's work. He used a 480×128 C-grid, and his results agreed well with the measurements and with Menter's results. Also, the BSL-EARSM among some other models have already been studied earlier using this flow [63].

The lift and drag coefficients are next studied, and the velocity profiles are com-

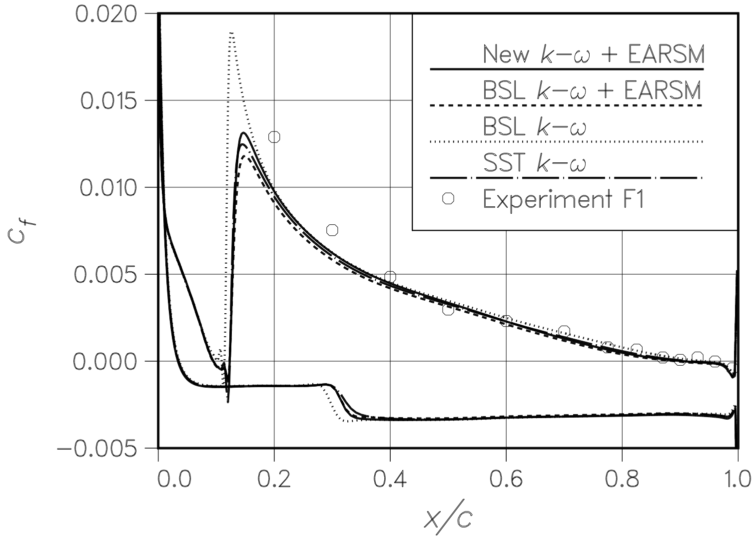

Figure 7.11: Surface-friction coefficient distribution on the Aerospatiale A aerofoil.

pared with measurements at five sections on the upper surface. These sections are located at x/c = 0.675, 0.786, 0.842, 0.897, and 0.953 and the velocity profiles are shown in Fig. 7.12. The angle of attack is $\alpha = 13.87°$, and the chord-Reynolds number is 1.52×10^6. The transition was not specified, and all the tested models generated the transition very near the leading edge stagnation point. In the experiments, the boundary layer was tripped at $x/c = 0.023$ and 0.1 on the upper and lower surfaces, respectively. However, computations with these transition locations tended to predict a laminar separation bubble before the upper trip, see also Refs. [3, 65]. This fact indicates that, in the experiments, a natural transition probably occurred before the trip. Some uncertainty is always involved in high-lift aerofoil test cases. This comes not only from the possibly uncertain transition location, but also the wind-tunnel wall effects are error sources for the angle of attack and the measured force coefficients. The experimentalists usually attempt to eliminate these errors using certain wind-tunnel corrections, but some uncertainty always remains.

The computations refused to converge to a steady-state solution using the pseudo-time integration. Approximately steady solutions could only be obtained using very time-consuming time-accurate simulations. Three different grids were used for computations with the new model as an attempt to eliminate the grid-dependency from the results. The grids were of O-type and had 160×48, 320×96, and 640×192 control volumes around the airfoil and in the near-normal direction, respectively. Unfortunately, the grid-dependency could not be eliminated, and this must be remembered when the results are studied. The aerodynamic force coefficients obtained using all three grids and the new model are shown in Table 7.2. Usually, the grid-dependency of the drag coefficient is clearly stronger than that of the lift coefficient. In this case, however, just the opposite seems to happen. The drag coefficient changes by about 5% when the grid is refined from the standard 320×96 level up to the fine 640×192 level, whereas the lift increases by 7%. The reason for

Table 7.2: Grid-dependency of the lift and drag coefficients of the NACA 4412 aerofoil at $\alpha = 13.87°$ computed with the new model.

Grid	c_l	c_d
Coarse 160×48	1.41	0.047
Standard 320×96	1.56	0.037
Fine 640×192	1.67	0.039
Experiment	1.67	–

Table 7.3: Lift and drag coefficients of the NACA 4412 aerofoil at $\alpha = 13.87°$. Computations are performed using the finest grid.

Turbulence model	c_l	c_d
New $k - \omega$ EARSM	1.67	0.039
BSL $k - \omega$ EARSM	1.58	0.036
$k - \omega$ BSL	1.71	0.031
$k - \omega$ SST	1.61	0.035
Experiment	1.67	–

this unusual behaviour is not really known, but possibly the relatively large extent of separation influences the grid convergence. When the grid is refined, more and more time-dependent motion is resolved. This motion increases the mixing of momentum and part of the shear stress might become both resolved and modelled in the recirculation region. If this happens, the extent of recirculation may be reduced and thus the lift might increase. However, neither a comprehensive grid-refinement study nor an in-depth analysis on the role of the resolved time-dependent motion have been made. Thus, these comments are merely speculative thoughts.

The separated flow is dominated by coherent structures very different from those appearing in the attached boundary layers, and the turbulence models designed for boundary layers often have serious difficulties in modelling the effects of such motion correctly. This has already been discussed in Section 3.2.2. In practice, this is seen as unsteady solutions, since the turbulence model cannot produce sufficiently high shear stress in the separated flow.

The lift and drag coefficients computed with the fine grid and the measured lift coefficient are given in Table 7.3. The lift coefficient predicted by the new model is very close to the experimentally measured value, but it is really not known how close this is to an ideal grid-independent result. Rudnik obtained a lift coefficient of 1.67 using the $k - \omega$ SST model [167]. This contrasts with the present SST results but the reason for this difference is unknown. Rudnik used a C-grid of 480×128 cells. In this case, the BSL-EARSM gave somewhat too low lift. As ex-

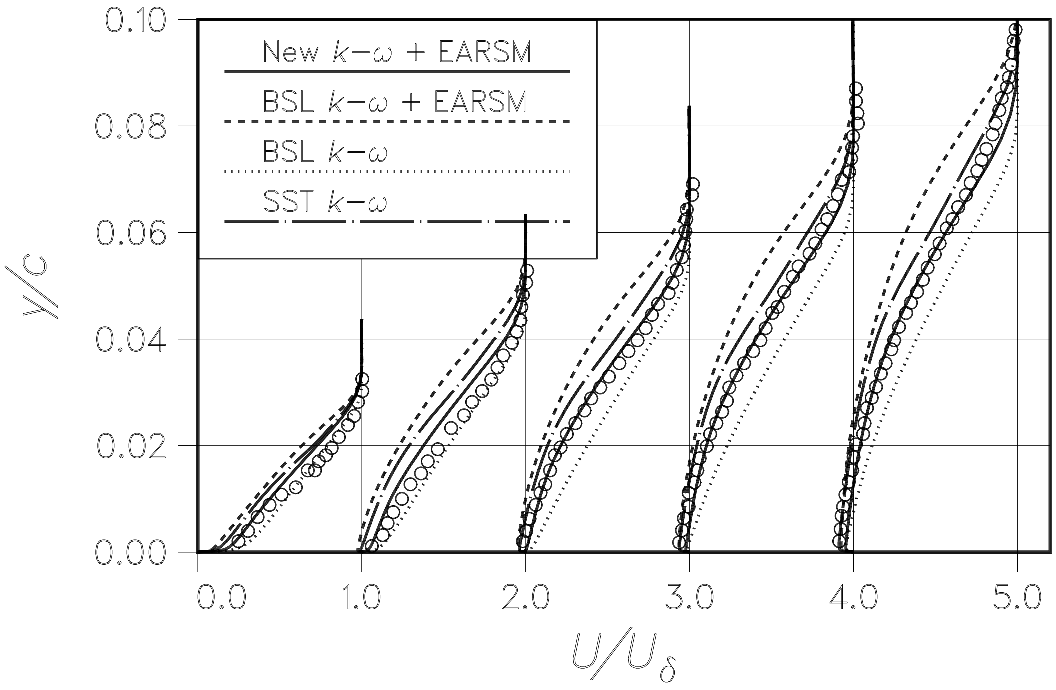

Figure 7.12: Velocity profiles U/U_δ on the upper surface of the NACA 4412 aerofoil at 13.87° angle of attack. Streamwise stations x/c =0.675, 0.786, 0.842, 0.897, 0.953.

pected, the standard linear BSL gave the highest lift coefficient. Figure 7.12 shows how the BSL-EARSM predicted too retarded velocity profiles. The new model and also the SST model gave velocity profiles that agree quite well with the measurements. Menter has published results obtained with the SST model in slightly closer agreement with the experiments than the present results. He utilized a 241×61 grid that was much coarser than the one used in this study [3] — this might be a possible explanation for this slight difference.

7.5.4 Three-Element Aerofoil NHLP 2D

Most of the real-life high-lift aerodynamics deals with multi-element wing sections. This means added complexity in comparison with the single-element problems. Not only are the geometry and the grid generation more complex in multi-element cases, but they also involve more complex flow details. The confluent and possibly merging boundary layers, wakes, and mixing layers become important. The main goal in this study is to develop a turbulence model that is more suitable for these kinds of problems than the existing models. Therefore, such a flow problem is selected as the final test case, although the focus of this study is in the basic development. The computations presented in this section are not claimed to form a complete validation for multi-element aerofoil problems. Instead, this is merely a feasibility test for the new model in order to make sure that it can generally be applied to these kinds of problems, as desired. A more complete validation is beyond the scope of this study, but such validation will be carried out as part of the HiAer project task 3 by the other project partners.

The NHLP 2D three-element take-off configuration has been selected for this purpose, see Fig. 3.1 in Chapter 3. The reason for this choice was simply that, as far as the author knows, this case is the only multi-element aerofoil test case with proper measurement data that is freely available. As this is a take-off configuration with the slat angle of 25° and flap angle of only 20°, there is no substantial flow separation, and this makes it somewhat easier for the turbulence model to yield accurate results. The focus is kept on the wake/boundary-layer interaction process, pressure distributions, and on the integrated lift and drag coefficients. The model's ability to predict the separation of boundary layers without wake-interaction has already been assessed using the single-element cases. The angle of attack is 20.18° in this case, and the chord-Reynolds number and the free-stream Mach number are 3.52×10^6 and 0.197, respectively.

The measurements were performed in the early 1970s by the former British Aerospace Company (BAC). The results are reported by Moir [41]. The experimental results include the lift and drag coefficients, pressure distributions along the surfaces of each element, and total-pressure coefficient distributions through the boundary layer and confluent wakes at four stations on the main wing and flap upper surfaces. This flow case has been previously studied computationally at least by Rumsey *et al.* [168], by Rudnik [167], and recently Wild studied CFD-based aerofoil optimization using, *e.g.* this case [169].

Rumsey *et al.* computed this flow using the Spalart-Allmaras one-equation model, Menter's $k - \omega$ SST, and $k - \omega$ EARSM models. This particular $k - \omega$ EARSM model is discussed in Section 6.3.3. They obtained quite similar results with all three models. The lift and drag coefficients as well as the pressure distributions agreed well with the measurements up to the angle of attack of the maximum lift. Beyond this angle, all the models kept on predicting still increasing lift and quite low drag. In other words, all the models predicted a too high stall angle and maximum lift coefficient. They also failed in predicting the stall mechanism correctly. The computations showed reasonably soft stall while the experiments indicated a more abrupt leading-edge stall. The interactions between the wakes and boundary layers were not very accurately captured at the high angle of attack, $\alpha = 20.18$ deg. As Rumsey *et al.* discussed, it is not clear whether the discrepancies come from the turbulence modelling or from the fact that the computations simulate the aerofoil in a free flow while the experiments are obviously conducted in a confined wind tunnel. Moreover, it is known that the boundary-layer transition from laminar to turbulent flow plays a very important role in these kinds of flow situations. There is only very limited information about the transition locations in the experiments.

Rudnik studied the performance of three linear two-equation models for a few single-element aerofoil cases and completed his study by computing the present three-element case at $\alpha = 20.18^\circ$ using a slightly modified version of Wilcox's 1988 $k-\omega$ model [167]. This modification is merely that the value of the coefficient β was lowered from 0.075 to 0.071. Rudnik's grid consisted of 177,000 control volumes, thus it has quite a high resolution covering most of the important regions.

Table 7.4: Grid-dependency of the lift and drag coefficients of the NHLP-2D aerofoil computed with the new model.

	c_l	c_d
Fine grid	4.06	0.057
Medium grid	4.03	0.061
Coarse grid	3.94	0.083

However, the high-resolution region did not extend sufficiently far away from the upper surfaces of the main wing and the flap to fully cover the region occupied by the slat wake. Therefore, the numerical error spoiled the outer slat wake results in the rear part of the aerofoil. It should be mentioned that the grid used by Rumsey *et al.* does not suffer from such a discrepancy.

Wild recently studied the aerofoil design optimization problem using, *e.g.* this case [169]. He utilized a grid of only 77,000 control volumes, but this grid was more efficiently organized than Rudnik's grid. Despite this, it probably also suffers from the same problem as Rudnik's grid, and thus the total-pressure profiles are probably contaminated by numerical error, especially around the slat wake in the rearmost sections. Wild used and reported transition locations for each element obtained by means of a boundary-layer stability calculations using the e^n method in DLR. This information, although its reliability is not fully known, is highly useful for all current and future CFD studies of this case. These transition locations were also used in this study. Wild showed a comparison of the lift and drag polars computed with free transitions and with the transitions specified according to the e^n-prediction. This comparison indicated that the results obtained with the e^n-predicted transition locations are in clearly better agreement with the measurements. Especially, the angle of stall was reduced to an almost correct value while it was overestimated by more than two degrees by the free-transition computations. Wild used the Spalart-Allmaras one-equation model and Wilcox's 1988 $k - \omega$ model just as Rudnik.

The present computations were made using a relatively fine grid that consists of 364,608 cells in 17 blocks. The grid convergence is studied by comparing the aerodynamic force coefficients computed with the fine grid and with medium and coarse grids, see Table 7.4. The medium grid was obtained from the fine grid by omitting every second grid line in both directions. The coarse grid, in turn, was obtained similarly from the medium grid. Also, the total-pressure profiles computed using these three grids are compared. These profiles are shown in Fig. 7.13. The grid convergence study was made using the new model only. Both comparisons indicate that the fine-grid results are not fully grid-independent but, nevertheless, reasonably grid-converged. Only the fine-grid results are used for turbulence model comparisons. All the fine-grid computations refused to converge to a stationary result using the pseudo-time integration. Stationary solutions were obtained by means of time-accurate simulations.

The computed and measured lift and drag coefficients are shown in Table 7.5,

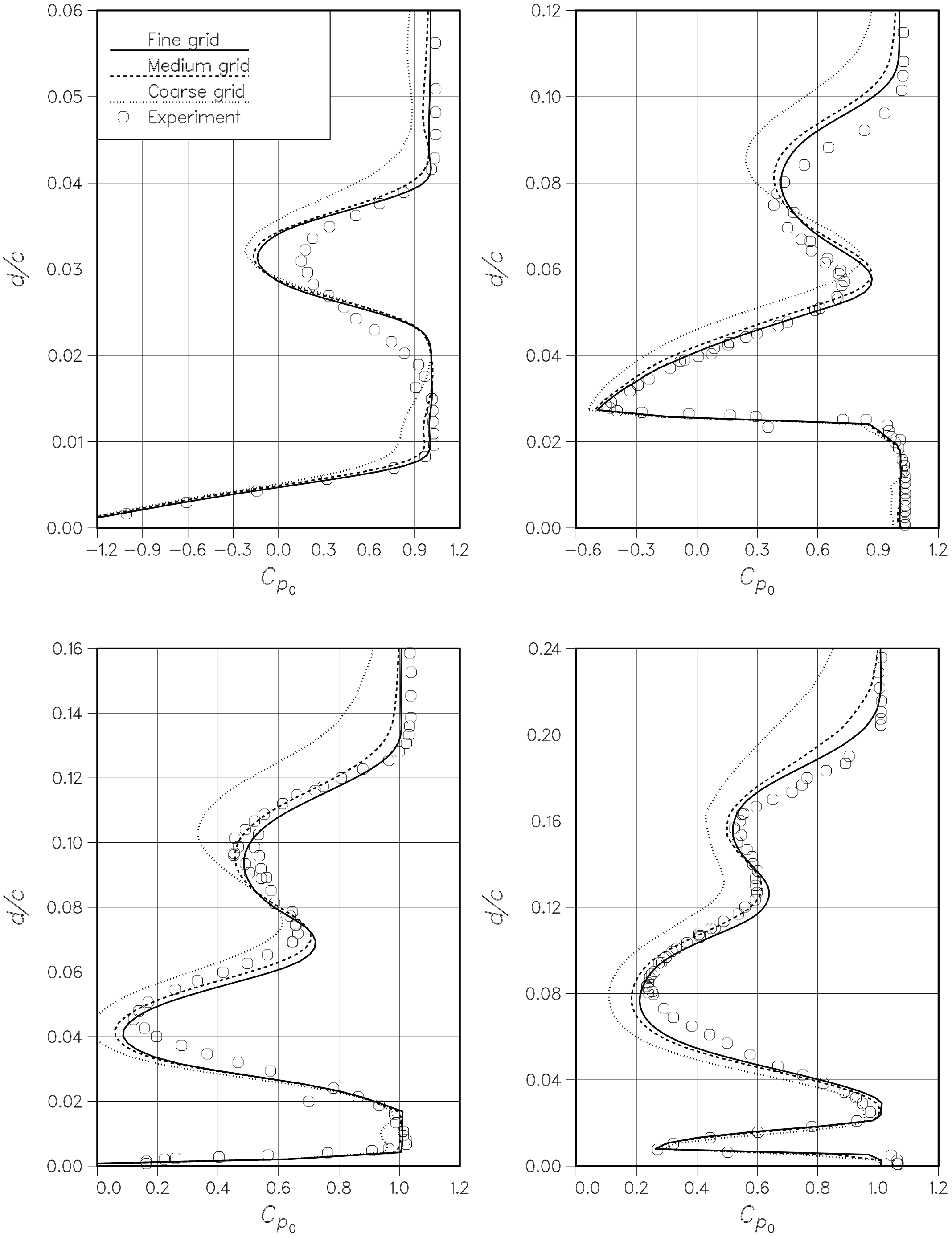

Figure 7.13: Grid-convergence study using the new $k - \omega$ EARSM model. Distributions of the total-pressure coefficient through the upper surface boundary layers of the main wing and the flap and the confluent wakes at four stations: main wing at 35% of the stowed chord c (upper left), just behind the main-wing trailing-edge starting from the flap upper surface (upper right), flap mid-chord (lower left), and just behind the flap trailing edge (lower right).

Table 7.5: Comparison of the lift and drag coefficients of the NHLP-2D aerofoil computed with different turbulence models.

	c_l	c_d
New $k-\omega$ EARSM	4.06	0.057
BSL $k-\omega$ EARSM	4.05	0.056
SST $k-\omega$	4.09	0.055
Rumsey [168] ($k-\omega$ EARSM)	4.08	0.068
Rudnik [167] ($k-\omega$)	4.01	0.071
Experiment, uncorr.	4.11	0.055
Experiment, corr.	4.11	0.068

which also includes the $k-\omega$ EARSM results by Rumsey *et al.* and Rudnik's results. The lift coefficients were predicted within the experimental uncertainty with all three models. In general, the differences between the models are insignificant. This can also be seen in Fig. 7.14, which shows the surface-pressure coefficient distributions. The curves are practically indistinguishable. The predicted drag coefficients are quite clearly lower than the experimental wind-tunnel corrected value. Incidentally, the predicted values agree very well with the measured uncorrected drag coefficient. Rudnik's computation provided a slightly lower lift coefficient and a clearly higher drag that agrees with the measurement. It is reasonable to assume that the grid used by Rudnik caused more numerical dissipation than the present grid. If this is true, it means that an asymptotic numerical result in which the numerical errors approach zero would predict an even lower drag coefficient than the present computations. However, even this does not mean that the models are fully responsible of the underpredicted drag. Uncertain transition locations and the fact that the computations simulate a free-stream situation instead of the confined experimental situation are, indeed, significant factors causing differences between the computed and measured drag. As stated earlier, predicting the drag of a high-lift configuration is an extremely difficult task. The sensitivity of the predicted drag coefficient to the circulation correction on the free-stream boundaries, described in Section 4.2.2, is a good example of the difficulties involved [113].

The total-pressure coefficient profiles through the upper surface boundary layers of the main wing and the flap and through the confluent wakes are shown in Fig. 7.15. Also the $k-\omega$ EARMS results by Rumsey *et al.* and linear $k-\omega$ results by Rudnik are included for comparison. In this case, the interactions between the wakes and boundary layers are weak and do not influence the aerodynamic forces. At a slightly higher angle of attack, the interactions probably become more important. The present results give, however, some impression about the ability of the new model to predict the merger of the wakes and boundary layers. The first plot in Fig. 7.15 is over the main wing at a location of 35% of the stowed chord. Here, the predicted wake is too symmetric in comparison with the experiment, which means that the turbulence is underestimated on the inner side of the wake. This is probably

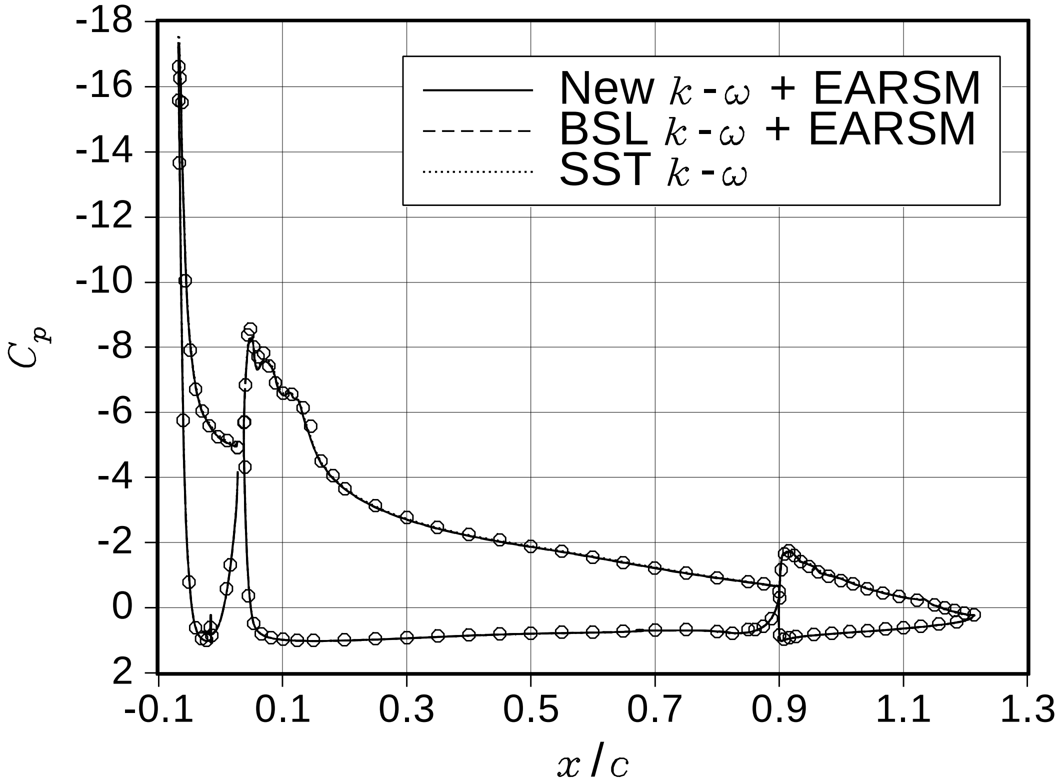

Figure 7.14: Computed and measured pressure-coefficient distributions along the aerofoil surfaces.

owing to two reasons. First, the turbulent stresses generated in the slat cove are probably not correctly convected downstream in the computations. This is a consequence of the weak equilibrium assumption and could only be avoided by using differential RSM. The second possible reason is the effect of the wake curvature, which is destabilizing on the inner side of the wake. The use of the curvature-corrected EARSM (CC-EARSM) discussed in Chapter 5 could probably be a partial remedy to this problem. However, computations employing the CC-EARSM are left for the future owing to some implementation problems encountered in complex geometries, see Section 5.3.2. Also RSM computations will be tried in the future. At the main-wing trailing edge, the wake is predicted to be slightly further away from the wing surface in comparison with the measurement data. This may be owing to the above-discussed underestimated turbulence on the inner side of the wake. The fact that the new model predicts a more rapidly spreading wake than the BSL-EARSM or the SST model can be seen at this station. The merger of the wake and the boundary layer has already begun at this station according to the measurements. The new model predicts this better than the BSL-EARSM and the SST models. This is even more clearly seen at the next stations, *i.e.* at the flap midchord and at the trailing edge of the flap.

In general, the computed results are in a better agreement with the measurements than the earlier computations [167–169]. The new model seems to predict the evolution of the wakes and the merger processes quite accurately, except that

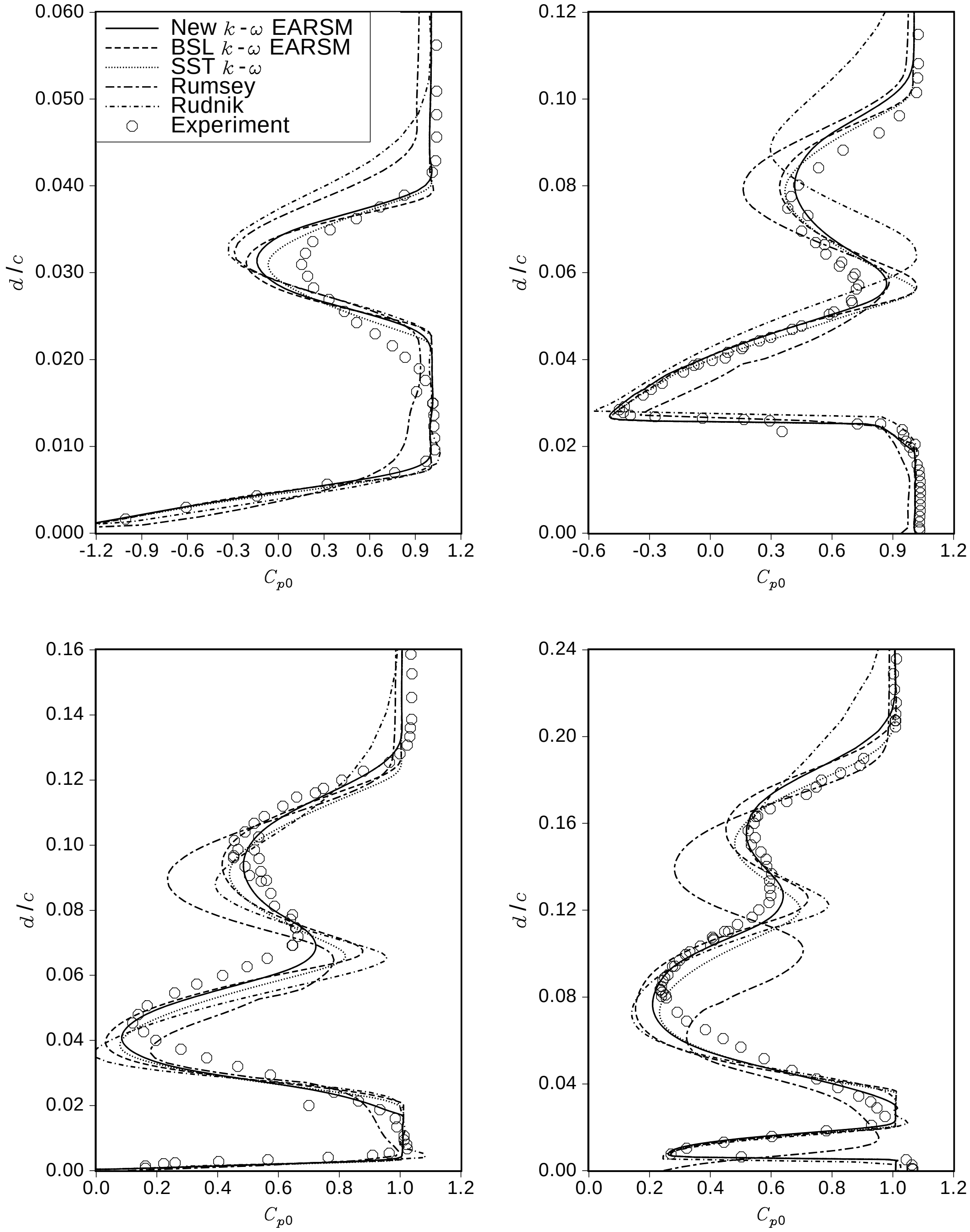

Figure 7.15: Turbulence model comparison. Also Rumsey's $k - \omega$ EARSM results as well as Rudnik's $k - \omega$ results are shown. Distributions of the total-pressure coefficient at the same stations as in Fig. 7.13.

the slat wake asymmetry is not correctly captured. This issue will be studied by means of RSM and CC-EARSM computations in the future. Computing this aerofoil at a number of angles of attack up to the stall angle would be a more stringent test for the new model. Such a test would indicate whether the model can predict the stall angle and the corresponding aerodynamic forces correctly. Unfortunately, such results are very sensitive to the transition locations, and it would be very difficult to distinguish the influences of the turbulence model and the transition settings. The further validation process of the new model to be performed within the HiAer project will probably involve such computations.

8 Conclusions

In this study, a new two-equation turbulence model was developed for computational aerodynamics purposes, especially for high-lift aerodynamics applications. The new model employs the explicit algebraic Reynolds stress model (EARSM) developed by Wallin and Johansson [4] as the constitutive relation between the turbulent stress tensor and the mean-velocity gradient. The new scale-determining model is based on the $k-\omega$ formulation. The model equations are of similar form to Menter's $k-\omega$ models [3], but the model is completely recalibrated.

The development of constitutive modelling was also contributed by this study. The proposed techniques to extend the EARSM method for significantly curved flows were critically discussed and assessed. One of the proposed methods, which is based on a curvilinear coordinate system following the acceleration vector, was shown to behave singularly even in very simple curved flows. Methods based on the strain-rate tensor were shown to behave much better.

The main focus of this study was on the development of the new scale-determining model to be used with the EARSM as the constitutive model. This new $k-\omega$ model was especially designed for the requirements typical in high-lift aerodynamics. In the model development, particular attention was paid to the model's sensitivity to pressure gradients, to the behaviour near the edges between turbulent and laminar flow, and to the calibration of the model coefficients for flow phenomena relevant to high-lift aerodynamics. The model development was based on both theoretical studies and numerical experimenting. New values for the model coefficients were found leading to significant improvements in comparison with Menter's models and other previously proposed $k-\omega$ models.

A theoretical analysis concerning the model behaviour near the edges of turbulent regions valid for linear two-equation models [129, 130] was extended for nonlinear models such as EARSMs. This analysis is a very useful theoretical tool providing understanding of anomalies occurring with many $k-\omega$ models near the edges of turbulent flows. Many existing $k-\omega$ models produce unphysically sharp or even hook-shaped velocity profiles around the edges when combined with a nonlinear constitutive model. The proposed theory explains these anomalies and it provides constraints for the diffusion coefficients to avoid such unphysical solutions. These constraints were very useful in the calibration process. In general, the theoretical analysis provided new information about the conditions under which the $k-\omega$ scale-determining models and nonlinear constitutive models can be successfully combined. Existing $k-\omega$ models were reviewed in the light of this information, and it was shown that most of the existing models are not suitable to be combined with any nonlinear constitutive model.

The final model calibration was carried out by means of a large number of numerical computations of selected elementary flows. These were equilibrium boundary layers under zero, adverse, and also favourable pressure gradients, plane channel flow, and planar far wake and mixing layer. The elementary flow problems were formulated in a self-similar form in order to facilitate quick numerical solution and thus a large number of computations needed in the calibration process. Also, more realistic two-dimensional flows were computed already during the calibration process. The proposed new model is believed to be applicable to a wider range of flows than most of the other $k - \omega$ models. This is owing to two reasons. Firstly, the EARSM constitutive model has a wider range of applicability than the linear Boussinesq relation, which is used in most of the other $k - \omega$ models. Secondly, a relatively wide base of different flows was used in the calibration.

After the calibration was finished, it was systematically studied if a more suitable operational second scale variable could be found for the new model. For this purpose, the model was transformed into a general ϕ-form, where $\phi \sim k^m \varepsilon^n$. According to this study, two candidate variables were selected for numerical experiments. However, ω itself was chosen owing to the numerical problems associated with the proposed alternative operational variables. Although this survey did not lead to a new formulation for the present model, it, however, provided tools for future work. For instance, the definition of the second scale variable could possibly be optimized by introducing small perturbations to some existing scale variable.

Finally, the new model was preliminarily assessed and validated using a set of realistic flow problems, including high-lift aerofoil flows. The new model showed relatively good behaviour in the considered test cases. Improvements over the reference models [3] were achieved especially near the edges of turbulent regions and also in predicting flows with mild separation. Computation of an asymmetric diffuser flow with massive separation indicated that the model may be less reliable in massively separated flows as in the other test flows. A three-element aerofoil at a high angle of attack was studied as the final validation case. The new model predicted the evolution of the wakes and the merger process of the wakes and boundary layers somewhat more accurately than the reference models. However, the model as well as the reference models predicted a too symmetric slat wake.

The proposed new $k - \omega$ EARSM model is a promising model to be employed in practical CFD work in aerodynamic design and analysis. It is easy to implement, particularly in the CFD packages already equipped with Menter's $k - \omega$ model.

Bibliography

[1] D. Reckzeh. Aerodynamic design of the high-lift-wing for a megaliner aircraft. *Aerospace Science and Technology*, 7:107–119, 2003.

[2] B.N. Nield. An overview of the boeing 777 high-lift aerodynamic design. *The Aeronautical Journal*, 99, November 1995.

[3] F.R. Menter. Two-equation eddy-viscosity turbulence models for engineering applications. *AIAA Journal*, 32(8):1598–1605, 1994.

[4] S. Wallin and A. Johansson. A complete explicit algebraic Reynolds stress model for incompressible and compressible turbulent flows. *Journal of Fluid Mechanics*, 403:89–132, 2000.

[5] S. Wallin and A.V. Johansson. Modelling streamline curvature effects in explicit algebraic Reynolds stress turbulence models. *International Journal of Heat and Fluid Flow*, 23(5):721–730, 2002.

[6] H. Tennekes and J.L. Lumley. *A first course in turbulence*. The MIT Press, 8. edition, 1982.

[7] P. Bradshaw. *An Introduction to Turbulence and its Measurements*. Pergamon Press, Oxford, 1st edition, 1971. ISBN 08–016621–0.

[8] G.L. Brown and A. Roshko. On density effects and large structures in turbulent mixing layers. *Journal of Fluid Mechanics*, 64:775–814, 1974.

[9] J. Mathieu and J. Scott. *An introduction to turbulent flow*. Cambridge University Press, Cambridge, United Kingdom, 2000. ISBN 0–521–77538–8.

[10] K. Hanjalic and B. E. Launder. A Reynolds stress model of turbulence and its application to thin shear flows. *Journal of Fluid Mechanics*, 52(4):609–638, 1972.

[11] B. E. Launder, G. J. Reece, and W. Rodi. Progress in the development of a Reynolds-stress turbulence closure. *Journal of Fluid Mechanics*, 68:537–566, 1975.

[12] W.C. Reynolds and S.C. Kassinos. A one-point modeling of rapidly deformed homogeneous turbulence. *Proceedings of Royal Society of London A*, 451:87–104, 1995.

[13] S.C. Kassinos, C.A. Langer, S. Haire, and W.C. Reynolds. Structure-based modeling for wall-bounded flows. *International Journal Heat and Fluid Flow*, 21(5):599–605, Sep. 2000.

[14] J.-P. Bertoglio. Two-point closures and turbulence modeling. In N. Kasagi, J.K. Eaton, R. Friedrich, J.A.C. Humphrey, M.A. Leschziner, and T. Miyauchi, editors, *Third International Symposium on Turbulence and Shear Flow Phenomena*, pages 857–862, June 2003.

[15] P.Y. Chou. On the velocity correlations and the solution of the equations of turbulent fluctuation. *Quart. Appl. Math.*, 3:38, 1945.

[16] J.C. Rotta. Statistische Theorie nichthomogener Turbulenz. *Zeitschrift für Physik*, 129:547–572, 1951.

[17] A. J. M. Spencer and R. S. Rivlin. The theory of matrix polynomials and its application to the mechanics of isotropic continua. *Arch. Rational Mech. Anal.*, 2:309–336, 1959.

[18] T.B. Gatski and T. Jongen. Nonlinear eddy viscosity and algebraic stress models for solving complex turbulent flows. *Progress in Aerospace Sciences*, 36(8):655–682, 2000.

[19] C.G. Speziale, R. Abid, and E.C. Anderson. A critical evaluation of two-equation models for near wall turbulence. *AIAA Paper*, 90-1481, 1990.

[20] M. Hallbäck, J. Groth, and A.V. Johansson. An algebraic model for non-isotropic turbulent dissipation rate term in Reynolds stress closures. *Physics of Fluids*, A2(10):1859–1866, 1990.

[21] T. Sjögren and A.V. Johansson. Development and calibration of algebraic nonlinear models for terms in the Reynolds stress transport equations. *Physics of Fluids*, 12(6):1554–1572, 2000.

[22] P.A. Durbin and B.A. Pettersson Reif. *Statistical theory and modeling for turbulent flows*. John Wiley & Sons, England, 2001. ISBN 0–471–49744–4.

[23] S.B. Pope. *Turbulent flows*. Cambridge University Press, Cambridge, United Kingdom, 2000. ISBN 0–521–59886–9.

[24] C.G. Speziale, S. Sarkar, and T.B. Gatski. Modelling the pressure-strain correlation of turbulence: an invariant dynamical systems approach. *Journal of Fluid Mechanics*, 227:245–272, 1991.

[25] A.V. Johansson and M. Hallbäck. Modelling of rapid pressure-strain in Reynolds-stress closures. *Journal of Fluid Mechanics*, 269:143–168, 1994. See also J. Fluid Mech. 290: 405, 1995.

[26] W.C. Reynolds. Fundamentals of turbulence for turbulence modelling and simulation. Lecture notes for Von Karman Institute, AGARD-CP-93, NATO, 1987.

[27] W.C. Reynolds. Computation of turbulent flows. *Ann. Rev. Fluid Mech.*, 8:183–208, 1976.

[28] D.C. Wilcox. *Turbulence modeling for CFD*. DCW Industries Inc., La Cañada, California, second edition, 1998.

[29] K. Salo. Implementing a Reynolds stress turbulence model in the FINFLO flow solver. Report B-55, HUT, Laboratory of Aerodynamics, 2003. ISBN 951–22–6391–2.

[30] B.J. Daly and F.H. Harlow. Transport equations of turbulence. *Physics of Fluids*, 13:2634–2649, 1970.

[31] W.P. Jones and B.E Launder. The prediction of laminarization with a two-equation model of turbulence. *International Journal of Heat and Mass Transfer*, 15:301–314, 1972.

[32] W. Rodi and N.N. Mansour. Low Reynolds number $k - \epsilon$ modelling with the aid of direct simulation data. *Journal of Fluid Mechanics*, 250:509–529, 1993.

[33] W. Rodi. A new algebraic relation for calculating the Reynolds stresses. *Z. angew. Math. Mech.*, 56:219–221, 1976.

[34] O. Grundenstam, S. Wallin, and A.V. Johansson. A generalized EARSM based on a nonlinear pressure strain rate model. In *Third International Symposium on Turbulence and Shear Flow Phenomena*, Sendai, Japan, June 2003.

[35] T.B. Gatski and C.G. Speziale. On explicit algebraic stress models for complex turbulent flows. *Journal of Fluid Mechanics*, 254:59–78, 1993.

[36] S.S. Girimaji. Fully explicit and self-consistent algebraic Reynolds stress model. *Theoretical and Computational Fluid Dynamics*, 8:387–402, 1996.

[37] B.S. Baldwin and T.J. Barth. A one-equation turbulence transport model for high-reynolds number wall-bounded flows, 1991. AIAA Paper 91–0610.

[38] B.S. Baldwin and H. Lomax. Thin layer approximation and algebraic model for separated turbulent flows, January 1978. AIAA Paper 78–257.

[39] A.M.O. Smith. High-lift aerodynamics. *Journal of Aircraft*, 12(6):501–530, 1975.

[40] A. Nakayama, H.-P. Kreplin, and H.L. Morgan. Experimental investigation of flowfield about a multielement airfoil. *AIAA Journal*, 28(1):14–21, 1990.

[41] I.R.M. Moir. Measurements on a two-dimensional aerofoil with high-lift devices. In *AGARD-AR-303*, volume 2, pages A2.1–A2.12, 1994.

[42] S.X. Ying, F.W. Spaid, C.B. McGinley, and C.L. Rumsey. Investigation of confluent boundary layers in high-lift flows. *Journal of Aircraft*, 36(3):550–562, 1999.

[43] I.A.A. Lindblad and K.M.J. de Cock. CFD prediction of maximum lift of a 2D high lift configuration. In *17th AIAA Applied Aerodynamics Conference*. AIAA, 1999. AIAA Paper 99–3180.

[44] L. Lorentzen and I.A.A. Lindblad. Application of two-equation and EARSM turbulence models to high-lift aerodynamics. In *17th AIAA Applied Aerodynamics Conference*. AIAA, 1999. AIAA paper 99–3181.

[45] C. L. Rumsey and T.B. Gatski. Recent turbulence model advances applied to multielement airfoil computations. *Journal of Aircraft*, 38(5):904–910, 2001.

[46] C.L. Rumsey, T.B. Gatski, S.X. Ying, and A. Bertelrud. Prediction of high-lift flows using turbulent closure models. *AIAA Journal*, 36(5):765–774, 1998.

[47] F. Clauser. Turbulent boundary layers in adverse pressure gradients. *Journal of Aeronautical Sciences*, 21:91–108, 1954.

[48] D.E. Coles and E.A. Hirst, editors. *Computation of turbulent boundary layers–1968 AFOSR-IFP-Stanford conference*, volume II, Stanford University, California, 1969.

[49] P. Bradshaw. The turbulence structure of equilibrium boundary layers. Technical Report 1184, NPL Aero, 1966.

[50] P.E. Skåre and P. Krogstad. A turbulent equilibrium boundary layer near separation. *Journal of Fluid Mechanics*, 272:319–347, 1994.

[51] A.E. Samuel and P.N. Joubert. A boundary layer developing in an increasingly adverse pressure gradient. *Journal of Fluid Mechanics*, 66:481–505, 1974.

[52] D.M. Driver. Reynolds shear stress measurements in a separated boundary layer flow. In *22nd fluid dynamics, plasma dynamics, and lasers conference*. AIAA, 1991. AIAA paper 91–1787.

[53] D.M. Driver and H.L. Seegmiller. Features of reattaching turbulent shear layer in divergent channel flow. *AIAA Journal*, 23(2):163–171, 1985.

[54] C.P. Mellen, J. Fröhlich, and W. Rodi. Large eddy simulation of the flow over periodic hills. In *Proceedings of IMACS World Congress 2000*, 2000.

[55] L. Temmerman and M.A. Leschziner. Large eddy simulation of separated flow in a streamwise periodic channel constriction. In 2^{nd} *Symp. on Turbulence and Shear-Flow Phenomena*, Stockholm, June 2001.

[56] S. Obi, K. Aoki, and S. Masuda. Experimental and computational study of separating flow in an asymmetric plane diffuser. In *9th Symposium on Turbulent Shear Flows*, pages P305.1–P305.4, Kyoto, Japan, August 1993.

[57] C.U. Buice and J.K. Eaton. Experimental investigation of flow through an asymmetric plane diffuser. In *CTR Annual Research Briefs*, pages 243–248. Centre for Turbulence Research, NASA Ames Research Centre and Stanford University, 1996.

[58] C.U. Buice and J.K. Eaton. Experimental investigation of flow through an asymmetric plane diffuser. Technical Report Report No. TSD-107, Centre for Turbulence Research, Stanford University, Stanford, California 94305-3030, 1997.

[59] W. Rodi and G. Scheuerer. Scrutinizing the $k-\epsilon$ Turbulence Model Under Adverse Pressure Gradient Conditions. *Journal of Fluid Engineering*, 108:174–179, 1986.

[60] D.C. Wilcox. Reassessment of the scale-determining equation for advanced turbulence models. *AIAA Journal*, 26(11):1299–1310, 1988.

[61] F.R. Menter. A comparison of some recent eddy-viscosity turbulence models. *Journal of Fluids Engineering*, 118:514–519, 1996.

[62] C.L. Rumsey and T.B. Gatski. Recent turbulence model advances applied to multielement airfoil computations. In *18th AIAA applied aerodynamics meeting*. AIAA, 2000. AIAA Paper 2000–4323.

[63] A. Hellsten and S. Laine. Explicit algebraic Reynolds-stress modelling in decelerating and separating flows. In *AIAA Fluids 2000*. AIAA, 2000. AIAA paper 2000–2313.

[64] F.R. Menter. Influence of freestream values on $k-\omega$ turbulence model predictions. *AIAA Journal*, 30(6):1657–1659, 1992.

[65] F.R. Menter. Zonal two equation $k-\omega$ turbulence models for aerodynamic flows. In *24th AIAA Fluid Dynamics Conference*. AIAA, 1993. AIAA Paper 93–2906.

[66] D.D. Apsley and M.A. Leschziner. Advanced turbulence modelling of separated flow in a diffuser. *Flow, Turbulence and Combustion*, 63:81–112, 2000.

[67] H. Bézard. A new $k-kl$ turbulence model for explicit algebraic Reynolds stress constitutive relation. HiAer project report D2.2-3, ONERA, DMAE, 2003. Unpublished.

[68] C. Yap. *Turbulent heat and momentum transfer in recirculating and impinging flows*. PhD thesis, University of Manchester, Manchester, UK, 1987.

[69] M.M. Rahman and T. Siikonen. Improved low-Reynolds number $k-\tilde{\varepsilon}$ model. *AIAA Journal*, 38(7):1298–1299, 2000.

[70] B. Merci, C. De Langhe, J. Vierendeels, and E. Dick. A quasi-realizable cubic low-Reynolds eddy-viscosity turbulence model with a new dissipation rate equation. *Flow, Turbulence and Combustion*, 66:133–157, 2001.

[71] K. Hanjalic and S. Jakirlic. Contribution towards the second-moment closure modelling of separating turbulent flows. *Computers and Fluids*, 27(2):437–456, 1998.

[72] K. Hanjalic, I. Hadzic, and S. Jakirlic. Modelling turbulent wall flows subjected to strong pressure variations. *Journal of Fluids Engineering,*, 121(1):57–64, March 1999.

[73] F.S. Lien and M.A. Leschziner. Modelling 2D separation from a high-lift aerofoil with a non-linear eddy-viscosity model and second-moment closure. *The Aeronautical Journal*, pages 125–144, April 1995.

[74] A. Hellsten and P. Rautaheimo, editors. *8th ERCOFTAC/IAHR/COST workshop on refined turbulence modelling,* Laboratory of Applied Thermodynamics, Report 127, Espoo, Finland, 1999. ISBN 951–22–4772–0.

[75] P.R. Spalart, W.-H. Jou, M. Strelets, and S.R. Allmaras. Comments on the feasibility of LES for wings, and on a hybrid RANS/LES approach. In C. Liu and Z. Liu, editors, *First AFOSR International Conference on DNS/LES*, Advances in DNS/LES. Greyden Press, Columbus, OH, 1997.

[76] M. Shur, P.R. Spalart, M. Strelets, and A. Travin. Detached-eddy simulation of an airfoil at high angle of attack. In *Engineering Turbulence Modelling and Experiments 4*, pages 669–678, 24-26 May 1999.

[77] A. Fage and V.M. Falkner. Note on experiments on the temperature and velocity in the wake of a heated cylindrical obstacle. In *Proceedings of the Royal Society*, volume A135, pages 702–705. Royal Society, 1932.

[78] A.A. Townsend. Measurements in the turbulent wake of a cylinder. In *Proceedings of the Royal Society*, volume A190, pages 551–561. Royal Society, 1947.

[79] A.A. Townsend. The fully developed turbulent wake of a circular cylinder. *Australian Journal of Scientific Research*, 2:451–468, 1949.

[80] R.M. Thomas. Conditional sampling and other measurements in a plane turbulent wake. *Journal of Fluid Mechanics*, 57(3):549–582, 1973.

[81] G. Fabris. Conditional sampling study of the turbulent wake of a cylinder. part 1. *Journal of Fluid Mechanics*, 94(4):673–710, 1979.

[82] R.A. Antonia and L.W.B. Browne. Anisotropy of temperature dissipation in a turbulent wake. *Journal of Fluid Mechanics*, 163:393–403, 1986.

[83] L.W.B. Browne, R.A. Antonia, and D.A. Shah. Turbulent energy dissipation in a wake. *Journal of Fluid Mechanics*, 179:307–326, 1987.

[84] J.H. Weygandt and R.D. Mehta. Three-dimensional structure of straight and curved plane wakes. *Journal of Fluid Mechanics*, 282:279–312, 1995.

[85] B.R. Ramaprian, V.C. Patel, and M.S. Sastry. The symmetric turbulent wake of a flat plate. *AIAA Journal*, 20(9):1228–1235, 1982.

[86] P.J. Pot. Measurements in a 2-D wake and in a 2-D wake merging into a boundary layer. Technical report TR 79063 U, National Aerospace Laboratory NLR, The Netherlands, 1979.

[87] A. Nakayama. Curvature and pressure-gradient effects on a small-defect wake. *Journal of Fluid Mechanics*, 175:215–246, 1987.

[88] V. Ramjee, E.G. Tulapurkara, and R. Rajasekar. Development of airfoil wake in a longitudinally curved stream. *AIAA Journal*, 26(8):948–953, 1988.

[89] X. Liu, F.O. Thomas, and R.C. Nelson. An experimental investigation of wake development in arbitrary pressure gradient, 1999. AIAA Paper 99–0677.

[90] D.M. Driver and G.G. Mateer. Wake flow in adverse pressure gradient. *International Journal of Heat and Fluid Flow*, 23:564–571, 2002.

[91] V. Yakhot and S.A. Orszag. Renormalization group analysis of turbulence: 1. basic theory. *Journal of Scientific Computing*, 1:3–51, 1986.

[92] V. Yakhot, S.A. Orszag, S. Thangam, T.B. Gatski, and C.G. Speziale. Development of turbulence models for shear flows by a double expansion technique. *Physics of Fluids A*, 4:1510–1520, 1992.

[93] A. Hellsten. Curvature corrections for algebraic Reynolds stress modeling: a discussion. *AIAA Journal*, 40(9):1909–1911, 2002.

[94] J.R. Carlson, N. Duquesne, C.L. Rumsey, and T.B. Gatski. Computation of turbulent wake flows in variable pressure gradient. *Computers & Fluids*, 30(2):161–187, 2001.

[95] L.C. Squire. Interactions between wakes and boundary-layers. *Progress in Aerospace Sciences*, 26:261–288, 1989.

[96] A.M. Savill and M.D. Zhou. Wake/boundary layer and wake/wake interactions — smoke flow visualization and modelling. In *Proceedings of Second Asian Congress of Fluid Mechanics*, pages 743–754. Science Press, 1983.

[97] D. Agoropoulos and L.C. Squire. Interactions between turbulent wakes and boundary layers. *AIAA Journal*, 26(10):1194–1200, 1988.

[98] I. Wygnanski and H.E. Fiedler. The two-dimensional mixing region. *Journal of Fluid Mechanics*, 41(2):327–362, 1970.

[99] H.W. Liepmann and J. Laufer. Investigations of free turbulent mixing. Technical note TN 1257, NACA, 1947.

[100] I.P. Castro and P. Bradshaw. The turbulence structure of a highly curved mixing layer. *Journal of Fluid Mechanics*, 73(2):265–304, 1976.

[101] M.M. Rogers and R.D. Moser. Direct simulation of a self-similar turbulent mixing layer. *Physics of Fluids*, 6(2), Feb. 1994.

[102] J.L. Lumley. Computational modeling of turbulent flows. In *Advances in Applied Mechanics*, volume 18, pages 123–176. Academic Press, 1978. ISBN 0–12–002018–1.

[103] S.K. Kim and M.K. Chung. Spatial transport of reynolds stresses by pressure fluctuations. *Physics of Fluids*, 6(11):194–201, Nov. 1994.

[104] A.O. Demuren, M.M. Rogers, P. Durbin, and S.K. Lele. On modeling pressure diffusion in non-homogeneous shear flows. In *Center for Turbulence Research: Proceedings of the Summer Program 1996*, 1996.

[105] S.K. Kim and M.K. Chung. Roles of pressure transport and intermittency for computation of turbulent free shear flows. *International Journal of Heat and Fluid Flow*, 16:194–201, June 1995.

[106] S. Wallin and S.S. Girimaji. Evolution of an isolated turbulent trailing vortex. *AIAA Journal*, 38(4):657–665, 2000.

[107] T. Siikonen. An application of Roe's flux-difference splitting for the $k-\epsilon$ turbulence model. *International Journal for Numerical Methods in Fluids*, 21(11):1017–1039, 1995.

[108] P. Kaurinkoski and A. Hellsten. FINFLO: the parallel multi-block flow solver. Report A-17, Helsinki University of Technology, Laboratory of Aerodynamics, 1998. ISBN 951–22–3940–X.

[109] A. Hellsten. On the solid-wall boundary condition of ω in the $k-\omega$-type turbulence models. Report B-50, Helsinki University of Technology, Laboratory of Aerodynamics, 1998. ISBN 951–22–4005–X; http://www.aero.hut.fi/Englanniksi/index.html.

[110] R.B. Dean. Reynolds number dependence of skin friction and other bulk flow variables in two-dimensional rectangular duct flow. *Journal of Fluids Engineering*, 100:215–223, 1978.

[111] A. Hellsten. Implementation of a one-equation turbulence model in the FINFLO flow solver. Report B-49, Helsinki University of Technology, Laboratory of Aerodynamics, 1996. ISBN 951–22–3219–7.

[112] V. Hämäläinen. Implementing an explicit algebraic Reynolds stress model into the three-dimensional FINFLO flow solver. Report B-52, HUT, Laboratory of Aerodynamics, 2001. ISBN 951–22–5605–3.

[113] J. Hoffren and A. Hellsten. Turbulence model tests in subsonic airfoil flows. In *Notes on Numerical Fluid Mechanics*, volume 58, 1997.

[114] S. Wallin and A. Johansson. Modelling of streamline curvature effects on turbulence in explicit algebraic Reynolds stress turbulence models. In *Second International Symposium on Turbulence and Shear Flow Phenomena*, Stockholm, Sweden, June 2001.

[115] W. Rodi and G. Scheuerer. Calculations of curved shear layers with two equation turbulence models. *Physics of Fluids*, 26:1422–1436, 1983.

[116] S.S. Girimaji. A Galilean invariant explicit algebraic Reynolds stress model for turbulent curved flows. *Physics of Fluids*, 9(4):1067–1077, April 1997.

[117] P.R. Spalart and M. Shur. On the sensitization of turbulence models to rotation and curvature. *Aerospace Science and Technology*, (5):297–302, 1997.

[118] A. Hellsten, S. Wallin, and S. Laine. Scrutinizing curvature corrections for algebraic Reynolds stress models. In *32nd AIAA Fluid Dynamics Conference*. AIAA, 2002. AIAA paper 2002–2963.

[119] D.J. Monson, H.L. Seegmiller, P.K. McConnaughey, and Y.S. Chen. Comparison of experiment with calculations using curvature-corrected zero and two-equation turbulence models for a two-dimensional U-duct. In *AIAA 21st Fluid Dynamics, Plasma Dynamics and Lasers Conference*, Seattle, Washington, June 1990. AIAA Paper 90–1484.

[120] D.J. Monson and H.L. Seegmiller. An experimental investigation of subsonic flow in a two-dimensional U-duct. Technical memorandum, NASA TM 103931, 1992.

[121] S. Wallin, A. Hellsten, M. Schatz, T. Rung, D. Peshkin, and A.V. Johansson. Streamline curvature corrected algebraic Reynolds stress turbulence modelling. In *Third International Symposium on Turbulence and Shear Flow Phenomena*, Sendai, Japan, June 2003.

[122] C. L. Rumsey, T.B. Gatski, K.W. Anderson, and W.J. Nielsen. Isolating curvature effects in computing wall-bounded turbulent flows. *Internal Journal of Heat and Fluid Flow*, 22:573–582, 2001.

[123] R.M.C. So and G.L. Mellor. Experiment on convex curvature effects in turbulent boundary layers. *Journal of Fluid Mechanics*, 60(1):43–62, 1973.

[124] C. L. Rumsey, T.B. Gatski, and J.H. Morrison. Turbulence Model Predictions of Strongly Curved Flow in a U-Duct. *AIAA Journal*, 38(8):1394–1402, 2000.

[125] G.H. Bech and H.I. Andersson. Turbulent plane couette flow subject to strong system rotation. *Journal of Fluid Mechanics*, 347:289–314, 1997.

[126] R. Roback and B.V. Johnson. Mass and momentum turbulent transport experiments with confined swirling coaxial jets. Technical report, NASA CR-168252, 1983.

[127] T. Rung, H. Lübcke, L. Xue, F. Thiele, and S. Fu. Assessment of explicit algebraic Reynolds-stress models in transonic flows. In W. Rodi and D. Laurence, editors, *Engineering Turbulence Modelling and Experiments 4*. Elsevier, 1999.

[128] S. Tavoularis and U. Karnik. Further experiments on the evolution of turbulent stresses and scales in uniformly sheared turbulence. *Journal of Fluid Mechanics*, 204:457–478, 1989.

[129] J.B. Cazalbou, P.R. Spalart, and P. Bradshaw. On the behavior of the two-equation models at the edge of a turbulent region. *Physics of Fluids*, 6:1797–1804, 1994.

[130] J.C. Kok. Resolving the dependence on freestream values for the $k-\omega$ turbulence model. *AIAA Journal*, 38(7):1292–1295, 2000.

[131] R. Ashworth, H. Bézard, A. Hellsten, M. Schatz, and F. Thiele. The length-scale equation and near-wall modelling in EARSM. HiAer project report D2.2-1, 2002. Unpublished.

[132] W.P. Jones and B.E Launder. The calculation of low-Reynolds-number-phenomena with a two-equation model of turbulence. *International Journal of Heat and Mass Transfer*, 16:1119–1130, 1973.

[133] M.B. Malone. Extension of a $k-\omega$ two-equation turbulence model to an algebraic Reynolds stress model. In *29th AIAA Fluid Dynamics Conference*. AIAA paper 98–2552, AIAA, 1998.

[134] K. Wieghardt and W. Tillman. On the turbulent friction layer for rising pressure. Tech. Memorandum 1314, NACA, July 1951.

[135] K.G. Winter and L. Gaudet. Turbulent boundary-layer studies at high Reynolds number at Mach numbers between 0.2 and 2.8. Report R & M 3712, Aeronautical Research Council, London, 1973.

[136] P.S. Klebanoff. Characteristics of turbulence in a boundary layer with zero pressure gradient. Report 1247, NACA, 1955.

[137] R. Abid, C. Rumsey, and T.B. Gatski. Prediction of nonequilibrium turbulent flows with explicit algebraic stress models. *AIAA Journal*, 33(11):2026–2031, 1995.

[138] T.B. Gatski. Prediction of airfoil characteristics with higher order turbulence models. Technical Report TM-110246, NASA, Langley Research Center, Hampton, Virginia, 1996.

[139] S.-H. Peng, L. Davidson, and S. Holmberg. A modified low-Reynolds number $k - \omega$ model for recirculating flows. *Journal of Fluids Engineering*, 119:867–875, Dec. 1997.

[140] D.C. Wilcox. *Turbulence modeling for CFD*. DCW Industries, Inc., La Canada, 1993. ISBN 0–9636051–0–0.

[141] J. Gullman-Strand. *Turbulence modelling using automated code generation applied to asymmetric diffuser flow*. Licentiate's thesis, Royal Institute of Technology, June 2002.

[142] F. Thivet, M. Daouk, and D.D. Knight. Influence of the wall condition on $k - \omega$ turbulence model predictions. *AIAA Journal*, 40(1):179–181, 2002.

[143] H. Grotjans and F. Menter. Wall functions for general applications CFD codes. In *Proceedings of the Fourth ECCOMAS Conference*, pages 1112–1117, Athens, Sep. 1998. John Wiley & Sons, Ltd.

[144] P. Rautaheimo and T. Siikonen. Improved solid-wall boundary treatment in low-Reynolds-number turbulence models. *AIAA Journal*, 39(5):824–830, May 2001.

[145] B. E. Launder and B. Spalding. The numerical computation of turbulent flows. *Computer methods in applied mechanics and engineering*, 3:269–289, 1974.

[146] H. Herring and J. Norbury. Some experiments on equilibrium turbulent boundary layers in favourable pressure gradients. *Journal of Fluid Mechanics*, 27:541–549, 1967.

[147] P. Bradshaw and D. Ferris. The response of a retarded equilibrium turbulent boundary layer to the sudden removal of pressure gradient. Technical Report 1145, NPL Aero, 1965.

[148] W.J. Glowacki and S.W. Chi. Effect of pressure gradient on mixing length for equilibrium turbulent boundary layers. In *AIAA 21st Fluid Dynamics, Plasma Dynamics and Lasers Conference*. AIAA, 1972. AIAA Paper 72–213.

[149] A.E. Perry, J.B. Bell, and P.N. Joubert. Velocity and temperature profiles in adverse pressure gradient turbulent boundary layers. *Journal of Fluid Mechanics*, 25:299–320, 1966.

[150] P. Bradshaw. The turbulent structure of equilibrium turbulent boundary layers. *Journal of Fluid Mechanics*, 29:625–645, 1967.

[151] L.F. East and W.G. Sawyer. An investigation of the structure of equilibrium turbulent boundary layers. In *Turbulent boundary layers: experiment theory and modelling AGARD CP-271*, pages 6.1–6.19, 1979.

[152] P. Bradshaw, D.H. Ferris, and N.P. Atwell. Calculation of boundary layer development using the turbulent energy equation. *Journal of Fluid Mechanics*, 28-3:593–616, 1967.

[153] J.C. Kok and S.P. Spekrejse. Efficient and accurate implementation of the $k-\omega$ turbulence model in the NLR multi-block Navier-Stokes system. In *ECCOMAS 2000*, Barcelona, Spain, September 2000.

[154] A. Hellsten and S. Laine. Extension of the $k-\omega$ Shear-Stress Transport Turbulence Model for Rough-Wall Flows. *AIAA Journal*, 36(9):1728–1729, 1998.

[155] S.-H. Peng and L. Davidson. New two-equation eddy viscosity transport model for turbulent flow computation. *AIAA Journal*, 38(7):1196–1205, July 2000.

[156] T.J. Coakley. Development of turbulence models for aerodynamic applications. In *28nd AIAA Fluid Dynamics Conference*, 1997. AIAA Paper 1997–2009.

[157] M.E. Olsen and T.J. Coakley. The lag model, a turbulence model for non-equilibrium flows. In *31st AIAA Fluid Dynamics Conference*, 2001. AIAA Paper 2001–2564.

[158] C.U. Buice and J.K. Eaton. Experimental investigation of flow through an asymmetric plane diffuser. *Journal of Fluids Engineering*, 122:433–435, 2000.

[159] T.J. Craft, B.E. Launder, and K. Suga. Development and application of a cubic eddy-viscosity model of turbulence. *International Journal of Heat and Fluid Flow*, 17:108–115, 1996.

[160] H.-J. Kaltenbach, M. Fatica, R. Mittal, T.S. Lund, and P. Moin. Study of flow in a planar asymmetric diffuser using large-eddy simulation. *Journal of Fluid Mechanics*, 390:151–187, 1999.

[161] P. Gendre. Brite-EURAM: EUROVAL, Task 2.1, "Maximum lift for single-element airfoils", 1990. CERFACS, France.

[162] W. Haase, F. Brandsma, E. Elsholz, M.A. Leschziner, and D. Schwamborn, editors. *EUROVAL: A European Initiative on Validation of CFD Codes*, volume 42 of *Notes on Numerical Fluid Mechanics*. Vieweg, Braunschweig, Germany, 1993.

[163] W. Haase, E. Chaput, E. Elsholz, M.A. Leschziner, and U.R. Müller, editors. *ECARP – European Computational Aerodynamics Research Project*, volume 58 of *Notes on Numerical Fluid Mechanics*. Vieweg, Braunschweig, Germany, 1997.

[164] R. Huddeville, O. Piccin, and D. Cassoudesalle. Opération décrochage—mesurement de frottement sur profiles AS 239 et A 240 à la soufflerie F1 du CFM. Technical Report TR RT-OA 19/5025 (RT-DERAT 19/5025 DN), ONERA, Paris, 1987.

[165] C. Gleyzes. Opération décrochage–résultats de la deuxieme campagne d'essais à F2–(mésures de presion et vélocimétrie laser). Technical Report TR RT-DERAT 55/5004, ONERA, Paris, 1989.

[166] D. Coles and A.J. Wadcock. Flying-hot-wire study of flow past an NACA 4412 airfoil at maximum lift. *AIAA Journal*, 17(4):321–329, 1979.

[167] R. Rudnik. *Untersuchung der Leistungsfähigket von Zweigleichungs-Turbulenzmodellen bei Profilumströmungen*. PhD thesis, Technische Universität Berlin, DLR Forschungsbericht 97-49, 1997.

[168] C.L. Rumsey, T.B. Gatski, S.X. Ying, and A. Bertelrud. Prediction of high-lift flows using turbulent closure models. In *15th AIAA Applied Aerodynamics Conference*, 1997. AIAA Paper 1997–2260.

[169] J. Wild. *Numerische Optimierung von zweidimensionalen Hochauftriebskonfigurationen durch Lösung der Navier-Stokes-Gleichungen*. PhD thesis, Technische Universität Carolo-Wilhelmina zu Braunschweig, DLR Forschungsbericht 2001-11, 2001.

A Transformation of the ω Model Equation into the Generalized ϕ-Form

Let us take the following length-scale-determining model equation as a starting point

$$\frac{\mathrm{D}\tilde{\omega}}{\mathrm{D}t} = \frac{\tilde{\omega}}{k}\left(C_{\tilde{\omega}1}P - C_{\tilde{\omega}2}\varepsilon\right) + \frac{\partial}{\partial x_j}\left(\nu_{\tilde{\omega}}\frac{\partial\tilde{\omega}}{\partial x_j}\right) + \frac{\nu_d}{k}\frac{\partial k}{\partial x_j}\frac{\partial\tilde{\omega}}{\partial x_j} \tag{A.1}$$

The generalized second-scale-determining model can be derived by first expressing the selected original variable as $\tilde{\omega} = k^{\tilde{m}}\varepsilon^{\tilde{n}}$ and transforming it for arbitrary operational variable $\phi = k^m\varepsilon^n$. The tilde-notation is used in order to emphasize that the $\tilde{\omega}$ is not necessarily the usual ω, but an arbitrary, yet undefined variable. For instance, the definition of $\tilde{\omega} = k^{\tilde{m}}\varepsilon^{\tilde{n}}$ can be varied by perturbing $\tilde{m}$ and $\tilde{n}$ around the ω-exponents $m = -1$ and $n = 1$. It must be noted that non-integer values can well be applied because the final m and n of the operational variable can be chosen as integers. In this study, a $k - \omega$ model of the from (6.2) – (6.3) is selected as the baseline model

Let us now define $\phi = k^m\varepsilon^n$ and $\tilde{\omega} = k^{\tilde{m}}\varepsilon^{\tilde{n}}$, with $n \neq 0$ and $\tilde{n} \neq 0$. Then

$$\varepsilon = \left(k^{-m}\phi\right)^{1/n} = k^{-m/n}\phi^{1/n} \tag{A.2}$$

$$\varepsilon^{\tilde{n}} = k^{-m\tilde{n}/n}\phi^{\tilde{n}/n} \tag{A.3}$$

$$\tilde{\omega} = k^{\tilde{m}}k^{-m\tilde{n}/n}\phi^{\tilde{n}/n} = k^{\tilde{m}-m\tilde{n}/n}\phi^{\tilde{n}/n} = k^{(\tilde{m}n-m\tilde{n})/n}\phi^{\tilde{n}/n} \tag{A.4}$$

$$\nu_k = \nu + \sigma_k\nu_T \tag{A.5}$$

$$\nu_{\tilde{\omega}} = \nu + \sigma_{\tilde{\omega}}\nu_T \tag{A.6}$$

$$\nu_d = \sigma_d\nu_T \tag{A.7}$$

Thus

$$\tilde{\omega} = k^{m'}\phi^{n'} \quad \text{where} \quad m' = \frac{\tilde{m}n - m\tilde{n}}{n} \quad \text{and} \quad n' = \frac{\tilde{n}}{n} \tag{A.8}$$

by substituting this into (A.1) we obtain the general ϕ-formulation term by term as follows.

The left hand side:

$$\frac{\mathrm{D}\tilde{\omega}}{\mathrm{D}t} = n'k^{m'}\phi^{n'-1}\frac{\mathrm{D}\phi}{\mathrm{D}t} + \underline{m'k^{m'-1}\phi^{n'}\frac{\mathrm{D}k}{\mathrm{D}t}} \tag{A.9}$$

The production and destruction terms can be written as

$$\begin{aligned}\frac{\tilde{\omega}}{k}\left(C_{\tilde{\omega}_1}P - C_{\tilde{\omega}_2}\varepsilon\right) &= k^{m'-1}\phi^{n'}\left[(C_{\tilde{\omega}_1}-m')P-(C_{\tilde{\omega}_2}-m')\varepsilon\right] \\ &\quad +\underline{m'k^{m'-1}\phi^{n'}\left(P-\varepsilon\right)} \end{aligned} \tag{A.10}$$

The transformation of the partial derivative of $\tilde{\omega}$ with respect to the spatial coordinates has the same form as (A.9), thus it can be applied. The diffusive term of (A.1) involves second-order differentation and therefore splits up into several terms as

$$\begin{aligned}\frac{\partial}{\partial x_j}\left(\nu_{\tilde{\omega}}\frac{\partial\tilde{\omega}}{\partial x_j}\right) &= n'k^{m'}\phi^{n'-1}\frac{\partial}{\partial x_j}\left(\nu_{\tilde{\omega}}\frac{\partial\phi}{\partial x_j}\right)+m'k^{m'-1}\phi^{n'}\frac{\partial}{\partial x_j}\left(\nu_{\tilde{\omega}}\frac{\partial k}{\partial x_j}\right) \\ &\quad +k^{m'}\phi^{n'}\left[n'(n'-1)\frac{\nu_{\tilde{\omega}}}{\phi^2}\left(\frac{\partial\phi}{\partial x_j}\right)^2+m'(m'-1)\frac{\nu_{\tilde{\omega}}}{k^2}\left(\frac{\partial k}{\partial x_j}\right)^2\right] \\ &\quad +k^{m'}\phi^{n'}\left[2m'n'\frac{\nu_{\tilde{\omega}}}{k\phi}\frac{\partial k}{\partial x_j}\frac{\partial\phi}{\partial x_j}\right]\end{aligned} \tag{A.11}$$

These can be rewritten as

$$\begin{aligned}\frac{\partial}{\partial x_j}\left(\nu_{\tilde{\omega}}\frac{\partial\tilde{\omega}}{\partial x_j}\right) &= n'k^{m'}\phi^{n'-1}\frac{\partial}{\partial x_j}\left(\nu_{\tilde{\omega}}\frac{\partial\phi}{\partial x_j}\right)+m'k^{m'-1}\phi^{n'}\frac{\partial}{\partial x_j}\left[(\nu_{\tilde{\omega}}-\nu_k)\frac{\partial k}{\partial x_j}\right] \\ &\quad \underline{+m'k^{m'-1}\phi^{n'}\frac{\partial}{\partial x_j}\left(\nu_k\frac{\partial k}{\partial x_j}\right)} \\ &\quad +k^{m'}\phi^{n'}\left[n'(n'-1)\frac{\nu_{\tilde{\omega}}}{\phi^2}\left(\frac{\partial\phi}{\partial x_j}\right)^2+m'(m'-1)\frac{\nu_{\tilde{\omega}}}{k^2}\left(\frac{\partial k}{\partial x_j}\right)^2\right] \\ &\quad +k^{m'}\phi^{n'}\left[2m'n'\frac{\nu_{\tilde{\omega}}}{k\phi}\frac{\partial k}{\partial x_j}\frac{\partial\phi}{\partial x_j}\right]\end{aligned} \tag{A.12}$$

Finally, the cross term must be transformed:

$$\frac{\nu_d}{k}\frac{\partial k}{\partial x_j}\frac{\partial\tilde{\omega}}{\partial x_j} = n'k^{m'-1}\phi^{n'-1}\nu_d\frac{\partial k}{\partial x_j}\frac{\partial\phi}{\partial x_j}+m'k^{m'-2}\phi^{n'}\nu_d\left(\frac{\partial k}{\partial x_j}\right)^2 \tag{A.13}$$

Now, the underlined terms form the k-equation multiplied by the factor $m'k^{m'-1}\phi^{n'}$ and they can thus be subtracted away. Next, all the terms are divided by $n'k^{m'}\phi^{n'-1}$ and the terms are combined yielding

$$\begin{aligned}\frac{\mathrm{D}\phi}{\mathrm{D}t} &= \frac{\phi}{k}\left[\left(\frac{C_{\tilde{\omega}_1}-m'}{n'}\right)P-\left(\frac{C_{\tilde{\omega}_2}-m'}{n'}\right)\varepsilon\right]+\frac{\partial}{\partial x_j}\left(\nu_{\tilde{\omega}}\frac{\partial\phi}{\partial x_j}\right) \\ &\quad +\frac{\phi}{k}\frac{\partial}{\partial x_j}\left[\frac{m'}{n'}(\nu_{\tilde{\omega}}-\nu_k)\frac{\partial k}{\partial x_j}\right]+\left[2m'\frac{\nu_{\tilde{\omega}}}{k}+\frac{\nu_d}{k}\right]\frac{\partial k}{\partial x_j}\frac{\partial\phi}{\partial x_j} \\ &\quad +\left[\frac{m'}{n'}(m'-1)\frac{\phi}{k^2}\nu_{\tilde{\omega}}+\frac{m'}{n'}\frac{\phi}{k^2}\nu_d\right]\left(\frac{\partial k}{\partial x_j}\right)^2 \\ &\quad +(n'-1)\frac{\nu_{\tilde{\omega}}}{\phi}\left(\frac{\partial\phi}{\partial x_j}\right)^2\end{aligned} \tag{A.14}$$

The term proportional to diffusion of k can be split into a more convenient form

$$\begin{aligned}\frac{\phi}{k}\frac{\partial}{\partial x_j}\left[\frac{m'}{n'}(\nu_{\tilde{\omega}}-\nu_k)\frac{\partial k}{\partial x_j}\right] &= \frac{\partial}{\partial x_j}\left[\frac{m'}{n'}\frac{\phi}{k}(\nu_{\tilde{\omega}}-\nu_k)\frac{\partial k}{\partial x_j}\right] \\ &+\frac{m'}{n'}(\nu_{\tilde{\omega}}-\nu_k)\frac{\phi}{k^2}\left(\frac{\partial k}{\partial x_j}\right)^2 - \frac{m'}{n'}(\nu_{\tilde{\omega}}-\nu_k)\frac{1}{k}\frac{\partial k}{\partial x_j}\frac{\partial \phi}{\partial x_j}\end{aligned} \tag{A.15}$$

After substituting this, the equation becomes

$$\begin{aligned}\frac{\mathrm{D}\phi}{\mathrm{D}t} &= \frac{\phi}{k}\left[\left(\frac{C_{\tilde{\omega}_1}-m'}{n'}\right)P - \left(\frac{C_{\tilde{\omega}_2}-m'}{n'}\right)\varepsilon\right] + \frac{\partial}{\partial x_j}\left[\nu_{\tilde{\omega}}\frac{\partial \phi}{\partial x_j} + \frac{m'}{n'}(\nu_{\tilde{\omega}}-\nu_k)\frac{\phi}{k}\frac{\partial k}{\partial x_j}\right] \\ &+ \left[\left(2m' - \frac{m'}{n'}\right)\nu_{\tilde{\omega}} + \frac{m'}{n'}\nu_k + \nu_d\right]\frac{1}{k}\frac{\partial k}{\partial x_j}\frac{\partial \phi}{\partial x_j} \\ &+ \left(\frac{m'^2}{n'}\nu_{\tilde{\omega}} - \frac{m'}{n'}\nu_k + \frac{m'}{n'}\nu_d\right)\frac{\phi}{k^2}\left(\frac{\partial k}{\partial x_j}\right)^2 \\ &+(n'-1)\frac{\nu_{\tilde{\omega}}}{\phi}\left(\frac{\partial \phi}{\partial x_j}\right)^2\end{aligned} \tag{A.16}$$

This can be expressed in a more compact way by introducing some new notation for the coefficients:

$$\begin{aligned}\frac{\mathrm{D}\phi}{\mathrm{D}t} &= \frac{\phi}{k}\left(C_{\phi 1}P - C_{\phi 2}\varepsilon\right) + \frac{\partial}{\partial x_j}\left(\nu_{\phi\phi}\frac{\partial \phi}{\partial x_j} + \nu_{\phi k}\frac{\phi}{k}\frac{\partial k}{\partial x_j}\right) \\ &+ \left(C_{\phi 3}^{(V)}\nu + C_{\phi 3}^{(T)}\nu_T\right)\frac{1}{k}\frac{\partial k}{\partial x_j}\frac{\partial \phi}{\partial x_j} + \left(C_{\phi 4}^{(V)}\nu + C_{\phi 4}^{(T)}\nu_T\right)\frac{\phi}{k^2}\frac{\partial k}{\partial x_j}\frac{\partial k}{\partial x_j} \\ &+ \left(C_{\phi 5}^{(V)}\nu + C_{\phi 5}^{(T)}\nu_T\right)\frac{1}{\phi}\frac{\partial \phi}{\partial x_j}\frac{\partial \phi}{\partial x_j}\end{aligned} \tag{A.17}$$

where

$$C_{\phi 1} = \frac{C_{\tilde{\omega}_1}-m'}{n'} \tag{A.18}$$

$$C_{\phi 2} = \frac{C_{\tilde{\omega}_2}-m'}{n'} \tag{A.19}$$

$$C_{\phi 3}^{(V)} = 2m' \tag{A.20}$$

$$C_{\phi 4}^{(V)} = \frac{m'}{n'}(m'-1) \tag{A.21}$$

$$C_{\phi 5}^{(V)} = n'-1 \tag{A.22}$$

$$C_{\phi 3}^{(T)} = \left(2m' - \frac{m'}{n'}\right)\sigma_{\tilde{\omega}} + \frac{m'}{n'}\sigma_k + \sigma_d \tag{A.23}$$

$$C_{\phi 4}^{(T)} = \frac{m'}{n'}(m'\sigma_{\tilde{\omega}} - \sigma_k + \sigma_d) \tag{A.24}$$

$$C_{\phi 5}^{(T)} = (n'-1)\sigma_{\tilde{\omega}} \tag{A.25}$$

$$\nu_{\phi\phi} = \nu_{\tilde{\omega}} \tag{A.26}$$

$$\nu_{\phi k} = \frac{m'}{n'}(\nu_{\tilde{\omega}}-\nu_k) \tag{A.27}$$

(A.28)

The auxiliary parameters m' and n' are defined as

$$m' = \frac{\tilde{m}n - m\tilde{n}}{n} \qquad \text{and} \qquad n' = \frac{\tilde{n}}{n} \qquad \text{where} \qquad n \neq 0 \tag{A.29}$$

HELSINKI UNIVERSITY OF TECHNOLOGY. LABORATORY OF AERODYNAMICS.
SERIES A

A-20	Risto Peltonen, A Numerical Method for Analysis and Design of Airfoils in Subsonic Flow, 2000.
A-19	Reijo Lehtimäki, On Structured Grid Generation, 2000.
A-18	Petri Kaurinkoski, Petteri Heino and Antti Hellsten, Implementation of a Time-Accurate Time-Integration Scheme to the FINFLO Flow Solver, 1999.
A-17	Petri Kaurinkoski and Antti Hellsten, FINFLO: the Parallel Multi-Block Flow Solver, 1998.
A-16	Jaakko Hoffren, A Numerical Method for Simulating Unsteady Flow Including Solid/Fluid Interaction, 1995.
A-15	Timo Siikonen, An Application of Roe's Flux-Difference Splitting for $k-\epsilon$ Turbulence Model, 1994.
A-14	Jaakko Hoffren, Time-Accurate Schemes for a Multi-Block Navier-Stokes Solver, 1992.
A-13	Petri Kaurinkoski and Timo Siikonen, Calculation of Transonic Laminar and Turbulent Flow Past a Delta Wing, 1992.
A-12	Timo Siikonen, A Three-Dimensional Multigrid Algorithm for the Euler and the Thin-Layer Navier-Stokes Equations, 1991.
A-11	Timo Siikonen and Jaakko Hoffren, Solution of the Thin-Layer Navier-Stokes Equations for Laminar Transonic Flow, 1989.
A-10	Timo Siikonen and Jaakko Hoffren, Multigrid Solution Method for the Euler Equations, 1989.

ISBN 951-22-6933-3 (print), 951-22-6934-1 (pdf, available at http://lib.hut.fi/Diss/)
ISSN 1456–6982